Shape Modelling of Bones

Application to the Primate Shoulder

by
Yuhui Yang

A Thesis submitted in fulfilment of requirements for the degree of
Doctor of Philosophy of Imperial College London

Department of Bioengineering and
Department of Computing
Imperial College London
2008

Abstract

The aims of this work were to develop techniques for describing morphological variations of shoulder bones and to test these on real datasets.

The robust measurement and description of anatomical geometry can provide accurate estimation and better understanding of bone morphology. Feature lines were detected automatically using crest line techniques and shape information from shoulder bones was extracted based on the extracted feature lines. Redefinition of local coordinate systems was proposed utilising the crest line technique.

Three dimensional statistical shape models (SSM) were built for a set of primate humeri and scapulae. Two types of models were constructed: one incorporated the maintained original scale whilst the other used scaled bones. Variations were captured and quantified by Principal Component Analysis (PCA). The application can be extended generally to long bones and other complex bones and was also tested on human femora.

Techniques to predict the shape of one bone from its neighbour at a joint were presented. PCA was used to reduce data dimensionality to a few principal components. Canonical Correlation Analysis (CCA) and Partial Least Square (PLS) Regression were applied to explore the linear morphological correlations between the two shoulder bones and to predict the shape of one segment given the shape of the adjoining segment.

List of publications

I Yuhui M Yang, Daniel Rueckert and Anthony M J Bull, A validation of the prediction of humeral shape using standard morphological measurement, to appear in *16$^{\sharp}$h European Society of Biomechanics Congress*, 2008 (Abstract)

II Yuhui M Yang, Daniel Rueckert and Anthony M J Bull, A validation of the prediction of shoulder bone shapes using standard morphological measurement: possible implications for arthroplasty, *Engineering the Upper Limb: Patient Specific Surgical Planning and Implementation*, 2008 (Abstract)

III Yuhui M Yang, Daniel Rueckert and Anthony M J Bull, Predicting the shapes of bones at a joint: application to the shoulder, *Computer Method in Biomechanics and Biomedical Engineering*, Volume 11, Issue 1, 2007

IV Yuhui M Yang, Adam M Hill, Anthony M J Bull and Daniel Rueckert, 3D statistical shape models of long bones, *Lecture Notes in Computer Science*, Volume 4057, 2006

V Yuhui M Yang, Adam M Hill, Anthony M J Bull and Daniel Rueckert, Describing the variation in complex bone shapes, *Journal of Biomechanics*, Volume 39, supplement 1, 2006 (Abstract)

VI Yuhui M Yang, Adam M Hill, Anthony M J Bull, Daniel Rueckert, Statistical shape modelling of long bones for biomechanical analysis, *Journal of Biomechanics*, Volume 39, supplement 1, 2006 (Abstract)

Acknowledgments

I would like to thank my supervisors, Dr Anthony Bull, for his guidance and encouragement through my years at IC. I am extremely lucky to be under his supervision as he always comes up with brilliant ideas. He is always there for his students, being patient and supportive. I am really grateful that he corrected this thesis during his Christmas holiday. I also thank my co-supervisor, Prof Daniel Rueckert, whose advice on various issues has been particularly important through my research. Without his guidance and help this work could not have been done. I have enjoyed working with them both, and what I have learnt from them has been far beyond my research topics.

I would like to thank everyone in the Musculoskeletal Biomechanics Group, who have created an enjoyable working environment. I am especially grateful to Adam Hill, who provided the invaluable primate datasets in this thesis; Dominic Southgate and Angelo Tardugno, who also contributed an indispensable part of the datasets. I am also grateful to my colleagues, Spyridon Masouros and Clarice Chung, for their discussions and company.

Finally, my special and deepest thanks to my parents for their love and support over the years.

Contents

List of Figures

List of Tables

Abbreviations

CAGD: Computer-aided geometric design

CCA: Canonical Correlation Analysis

CT: Computerised Tomography

DOF: Degrees of Freedom

FFD: Free Form Deformation

GHJ: Glenohumeral Joint

GM: Geometric Morphometrics

ICP: Iterative Closest Point algorithm

ISB: International Society of Biomechanics

JCS: Joint Coordinate System

MLR: Multiple Linear Regression

PCA: Principal Component Analysis

PCR: Principal Component Regression

PDM: Point Distribution Model

PLS: Partial Least Squares Regression

RPM: Robust Point Matching

SSM: Statistical Shape Models

SVD: Singular Value Decomposition

THA: Total Hip Arthroplasty

TKA: Total Knee Arthroplasty

TPS: Thin-Plate Spline

TSR: Total Shoulder Replacement

Abbreviations

(This is a duplication. Feel free to tear off for assisting reading)

CAGD: Computer-aided geometric design

CCA: Canonical Correlation Analysis

CT: Computerised Tomography

DOF: Degrees of Freedom

FFD: Free Form Deformation

GHJ: Glenohumeral Joint

GM: Geometric Morphometrics

ICP: Iterative Closest Point algorithm

ISB: International Society of Biomechanics

JCS: Joint Coordinate System

MLR: Multiple Linear Regression

PCA: Principal Component Analysis

PCR: Principal Component Regression

PDM: Point Distribution Model

PLS: Partial Least Squares Regression

RPM: Robust Point Matching

SSM: Statistical Shape Models

SVD: Singular Value Decomposition

THA: Total Hip Arthroplasty

TKA: Total Knee Arthroplasty

TPS: Thin-Plate Spline

TSR: Total Shoulder Replacement

Chapter 1

Introduction

1.1 Background

The accurate definition of the shapes of bones and the ability to predict the shape or alignment of one bone from its neighbour at a joint could be beneficial in many areas. For example, in palaeontology this could be used to predict incomplete skeletal components; in taxonomy it could provide parameters to categorise genera. In particular, morphological variations of primate humeri and scapulae are important in the analysis of loading effects on bone shapes due to significantly different locomotor types that upper limbs can be used for (brachiation and quadrupedalism to name two extremes in this thesis).

1.2 Motivations and Objectives

This thesis focuses on analysing shoulder bone shapes for better understanding of their bony morphology in a numerical way and proposing solutions for building accurate computer models for primate shoulder bone shapes. Three relating issues are to be addressed:

I A standardisation of the shoulder joint for description, measurement and clinical procedures is required. To be precise, a standardisation of joint motions using identical local coordinate systems (LCS) is very important for the enhancement of the study of motion biomechanics. Moreover, it expedites the

cycle of planning, navigation and analysis among researchers and clinicians. As such, a universally accepted standard is indispensable.

II Statistical shape models (SSM) are of considerable interest when studying shape variations in anatomical shapes. Two major difficulties in building a 3D SSM remain: firstly, segmentation of regions of interest from a series of images and, secondly, establishment of point-to-point correspondences throughout a training set. Although segmentation techniques are developing rapidly, many recent applications are still based on available manual or semi-manual segmentation tools, for example, *MRIcro* and *Amira*®. The accuracy of correspondences is important, because of the sensitivity of shape parameterisations, which may lead to difficulties in defining shape constraints. Manually labelling correspondences on each sample is time-consuming and inaccurate even for 2D shapes. Therefore, such a manual approach is impractical for 3D shapes.

III It is essential to comprehend relationships between bones of a joint in order to determine the location and the appropriate size of orthopaedic implants, for example, an understanding of these relationships can also be used as a tool for diagnosing abnormality, predicting bone growth and planning interventions. An intimate relationship between the humerus and the scapula of a subject is likely to exist and therefore, the hypothesis of this study is that the shape of one shoulder bone will be able to predict the shape of the other shoulder bone.

1.3 Contributions

In order to address the above issues for better comprehension of the shoulder joint, this work has developed methods to: 1) extract local bony morphological features automatically, 2) describe variations in shoulder bony morphology using a reduced set of variables, and classify a shoulder bone without taxonomical information based on these variables, 3) predict the shape of a bone from its neighbour at a joint, and quantify the accuracy in the morphological prediction using local morphological features. The main contributions

of this thesis are to solve the research problems described below.

Automatic parameterisations of the shoulder bony anatomy Traditional parameterisations of shoulder bone shape analysis is based on direct measurements taken from anatomical components. The present work developed an algorithm to extract distinctive surface features automatically in order to allow parameterisation. Instead of relying on some manually selected anatomical landmarks on an object, which may contain large variations, the method developed proposes an approximation of bony features with geometric forms, such as spheres and cylinders.

Recommendations of local coordinate systems for the glenohumeral joint Existing definitions of local coordinate systems for the glenohumeral joint are inconsistent and inaccurate. Therefore, more stable redefinitions were suggested and tested, and a recommendation of a local coordinate system on the distal humerus is proposed.

Training sets constructions A training set refers to a subset of a dataset. It is used to build a model for prediction or classification. The presented datasets are composed of nine different genera of primates. Point-to-point correspondences of the bone surfaces were identified across the humerus dataset and the scapula dataset. Two frameworks were proposed to build the training sets, one for the humerus shapes and the other for the scapula shapes. The frameworks developed can be extended generally to long bones and complex bones.

Morphological variation descriptions An SSM was constructed separately on the humerus training set and on the scapula training set. Due to the large variation of size among the genera, two shape models were built for each training set, one including size variation and the other excluding this variation. Principal variations of the shoulder bone shapes were captured and described by a few variables using principal component analysis (PCA). Visual simulations of how these variations change are presented.

Quantifications and classifications Based on the constructed shape models, shoulder bone shapes from different genera of the primates in the training sets were quantified. Given a humerus or a scapula shape, which is not in the training set, it can be classified to a certain genus. Leave-one-out validations were performed to demonstrate the accuracy of the classification method.

Bone morphing of a femur with statistical shape models A training set of human femur shapes was constructed for which two shape models were built. In the first model, the centres of the femoral heads were fixed. A simulation of selecting a sparse surface point set is provided. An optimisation algorithm to reconstruct the best fit complete surface for the selected point set was improved.

Prediction of a shoulder bone shape from the adjoining neighbour Canonical correlation analysis (CCA) was applied to extract linear morphological correlations between 28 humeri and their corresponding scapulae. A partial least square (PLS) regression algorithm was implemented to perform the shape prediction. Robustness was tested using leave-one-out validations. Prediction bias was estimated by calculating root mean square errors between all surface points on the predicted surface and on the real surface, and by comparing anatomical parameters obtained from the predicted shape and the real shape.

1.4 Thesis Overview

The thesis outline is as follows:

Chapter 2 is a literature review of bony anatomy of human and non-human primate shoulders, and techniques involved in shape analysis. The anatomy of the two major shoulder bones and the movement between them are briefly summarised. Some recommendations on the definitions of joint local coordinate systems are elaborated. Relevant techniques include crest line extractions, registration techniques, statistical shape models, CCA and PLS regression.

Chapter 3 describes and displays the datasets and method of acquisition of the shoulder bones from nine genera of primates.

Chapter 4 explains an improved method of extracting crest lines on a bony surface and suggests how the extracted lines can be used to obtain stable morphological features, for example the rim of a glenoid. Redefinitions of local coordinate systems on the gleno-humeral joint, and on the distal humerus, are proposed. These methods minimise errors caused by manual interventions such as labelling anatomical landmarks. The procedure of building the coordinate systems is also explained.

Chapter 5 describes the construction of SSMs for humeri and scapulae. Two shape models were constructed; one considers size variabilities across a training set whilst the other does not. Two SSMs for human femora were also constructed. An iterative optimisation method is described and the results of the bone morphing technique based on SSM and the optimisation method are presented.

Chapter 6 demonstrates how to extract linear morphological correlations between the shoulder bone shapes using CCA. The prediction of a shoulder bone shape from the adjoining bone shape using PLS regression is described. In order to assess accuracy of the prediction method with regards to morphology, some stable morphological features obtained from Chapter 4 are used to compare the predicted shapes and their corresponding real shapes.

Chapter 7 concludes this thesis with a discussion of the methodologies used and their further developments. A summary of future work on methodologies is presented.

Chapter 2

Literature Review

2.1 Introduction

The contributions of this thesis can be divided into three major parts. The first contributions are in understanding individual shoulder bone shapes and constructing local coordinate systems for these bones. Secondly, in building statistical shape models (SSM) for shoulder bones in order to describe their morphological variabilities so that a bone surface can be reconstructed given a set of sparse surface points. Thirdly, in identifying linear morphological correlations between the two main shoulder bones in order to predict the shape of one bone from the other. This chapter explores the related areas which are essential to this thesis and reviews relevant research topics. There are four main reviews: anatomy (Section 2.2), bony coordinate frames (Section 2.3), geometric morphometrics (Section 2.4) and computational and statistical techniques (Sections 2.5, 2.6 and 2.7).

2.2 Primate Shoulder Bony Anatomy

This section describes the anatomy of primate shoulder bones in order to identify the anatomical parameters within which to study shoulder bony morphology. The scapula and the humerus come together at the shoulder to form the glenohumeral joint in which the humeral head meets the scapular glenoid to form a highly incongruent glenohumeral cavity (Figure 2.1). The glenohumeral joint, which has six degrees of freedom, is regarded

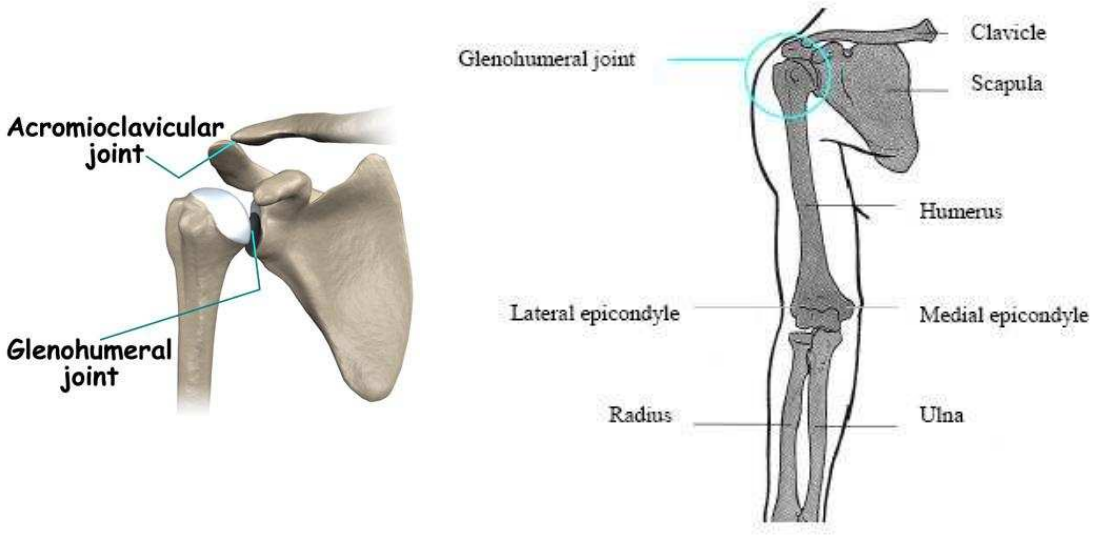

Figure 2.1: Human upper limb bony anatomy (left from [mmg03], right from [Ama06])

as a synovial ball and socket joint made up of the glenoid fossa of the scapula, the head of the humerus and soft tissues, such as cartilages, ligaments and tendons. The geometry of this articulation allows great freedom of movement in all directions, but provides little passive stabilising effect to the joint. An additional osteological constraint is provided superiorly by the acromion and the coracoid process of the scapula (Figure 2.4).

2.2.1 Humerus

The humerus is a long bone maintaining the distance between two synovial articulations, the glenohumeral joint and the elbow joint (Figure 2.2). At the proximal end, the spheroid humeral head articulates with the glenoid fossa, whilst distally, the humerus has two epicondyles, the medial and the lateral epicondyles, articulating with the proximal radius and the proximal ulna. In between the proximal and distal extremes of the humerus lies the long middle portion of its body, the humeral shaft. The shaft of the humerus varies in degrees of torsion amongst non-human primates. It is hypothesised that humeral torsion has played a significant role in evolutionary developments [ISDA44].

In humans, the radius of the humeral head in the coronal plane ranges from $21mm$ to $26.5mm$ [HK02]. The humeral head retroversion in relation to the plane of the articular

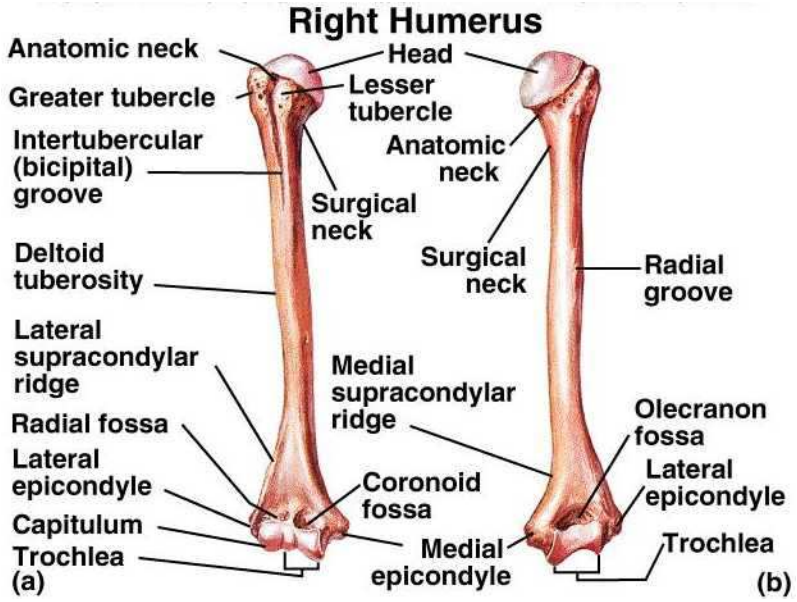

Figure 2.2: Human humerus bony anatomy. (a) Anterior view, (b) Posterior view [MH02]

surface and the trochlear axis ranges from 10° to 55° with mean 29.8° [PV95]. The inclination angle (the angle between the long axis through the humeral shaft and the axis through the neck of the humeral head) is between 132° and 142° [HK02].

2.2.2 Scapula

The primate scapula consists of an undulating concavoconvex blade divided into two fossae on the dorsal surface by the scapula spine; a ridge grossly perpendicular to the blade conferring considerable mechanical rigidity to the structure [Rob74]. In humans, both the scapular blade and the spine are thickened along their free margins, enclosing thinner bone that is occasionally fenestrated, suggesting a complex arrangement adapted to distribute stress patterns across the structure to muscular insertions [Hil06] (Figure 2.3).

The human scapula is a large triangular bone with two surfaces, the anterior surface and the posterior surface. There are three edges of the scapula blade: the lateral, the medial and the superior borders, with the sides meeting each other at the scapula's inferior, superior and lateral angles, respectively (Figure 2.4). The acromion is a flat triangular lateral projection over the glenoid fossa, which meets the lower lip of the spine at the

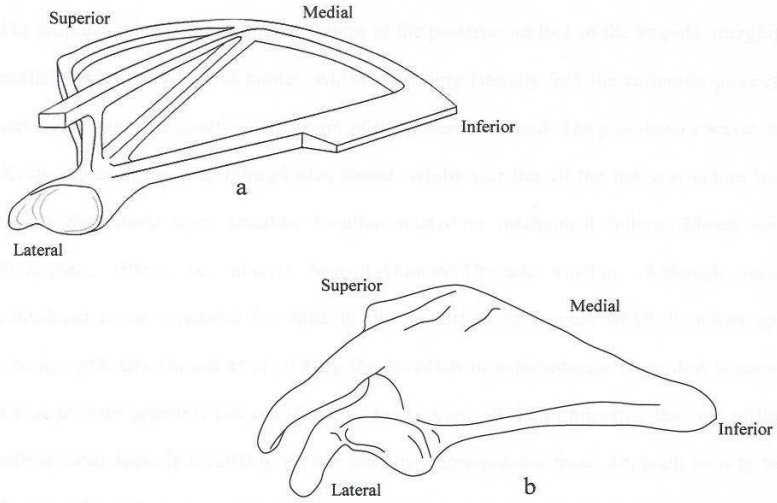

Figure 2.3: Comparison of stylised (a) and anatomical (b) scapulae [Hil06]

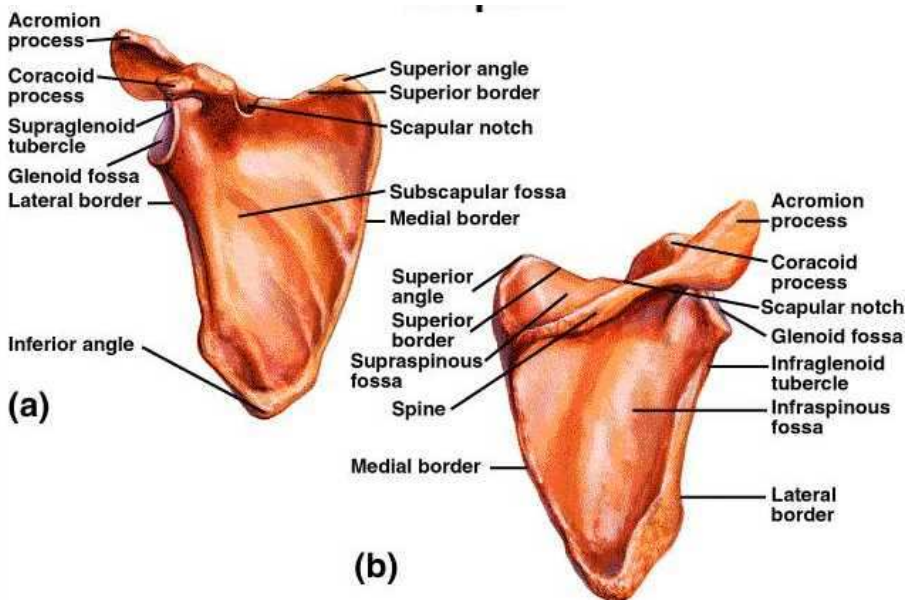

Figure 2.4: Bony anatomy of the human scapula. (a) anterior view, (b) Posterior view [MH02]

acromial angle, and acts as a partial insertion of both Deltoid and Trapezius.

2.3 Shoulder Local Coordinate Systems

Now that the anatomical framework is established, it is necessary to relate morphology to local coordinate frames or systems for engineering analysis.

2.3.1 Joint Coordinate Systems

Grood and Suntay first proposed the joint coordinate system (JCS) to eliminate the temporal sequence dependency of Euler angle techniques in the study of human biomechanics of joint motions and to encourage the use of clinically relevant models [GS83]. Thereafter, many studies have been carried out to define and describe joint motions using their own adjustments based on Grood and Suntay's JCS definitions [vdH97a, EBN00, Hil06, Ama06]. A standardisation for the shoulder was initialised by van der Helm [vdH97b]. The JCS is now widely accepted and used in the Biomechanics field and is widely used in clinical situations. For the purpose of better communications among people involved, the Standardisation and Terminology Committee (STC) of the International Society of Biomechanics (ISB) proposed definitions of the JCS for the shoulder [vdHCM$^+$04] (see Appendix A), proposing the usage of a common set of bony landmarks and an identical local coordinate system (LCS).

A JCS, described by two segment-fixed axes $\mathbf{u}_x$ and $\mathbf{u}_v$, and their mutually orthogonal floating axis $\mathbf{u}_f$ (Figure 2.5), was introduced by Grood and Suntay [GS83] to define the relative motions of two rigid body segments. Most of the proposed systems for the glenohumeral joint only consider three degrees of rotation of the humeral head [Cha03, BF04], which are insufficient to understand the full normal kinematics of the glenohumeral joint. A more clinically relevant model should allow six degrees of freedom (DOF), including three additional degrees of translations that relates the stability of the glenohumeral joint. However, there is yet to be a generally accepted definition. Different research groups tend to define their own JCSs depending on individual's choice and convenience [Ama06].

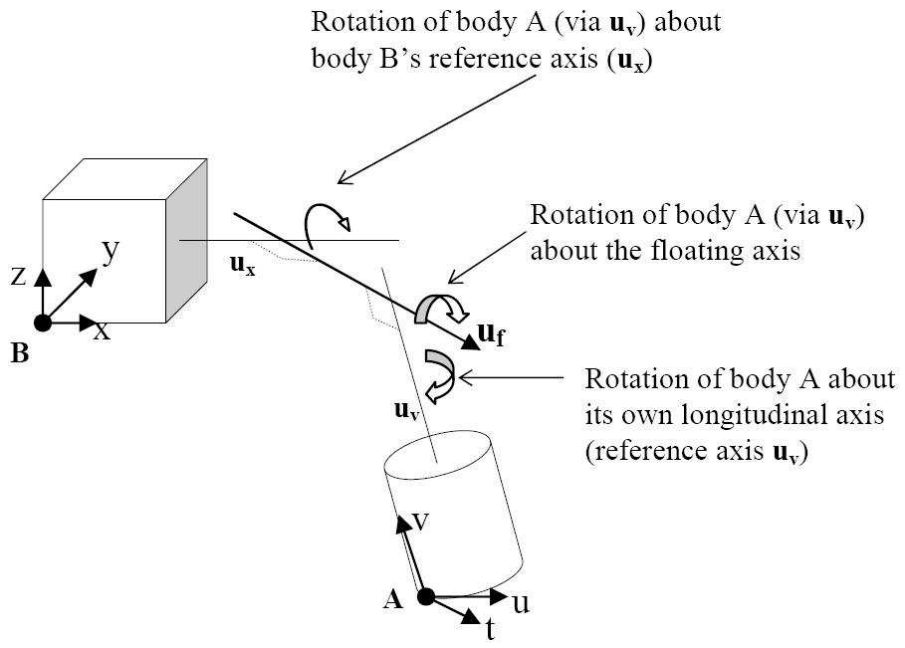

Figure 2.5: The three-cylinder open chain mechanism for the description of joint kinematics [GS83]

It is essential to define an orthogonal Cartesian coordinate system (also called *body coordinate frame*) that is fixed to an individual bone so as to specify the $\mathbf{u}_x$, $\mathbf{u}_v$ and $\mathbf{u}_f$ axes. The JCS defines how the orientation of one body coordinate frame is related to another. Hill applied the three-cylinder open chain mechanism [Hil06], as shown in Figure 2.5, to the glenohumeral joint with two frames locally fixed on the humerus and the scapula and their mutual interaction as the *floating* axis $\mathbf{u}_f$. The ISB's recommendation on definitions of the local frames on the humerus and the scapula, which utilises anatomical landmarks on the bone surfaces, potentially increases variations contained by the morphological features of the bones. To construct stable coordinate frames for the shoulder bones, Amadi redefined the frames for the two bones and developed methodologies to build stable coordinate frames [Ama06]. The major drawback of his method is the involvement of a significant amount of manual labelling work that can result in variability.

More automatic techniques will need to be explored to remove this dependence on manual labelling. The use of crest lines automates the decision of feature areas on shoulder bones.

2.3.2 Crest Lines

Crest lines are 3D lines on a surface corresponding to the successive loci of the surface whose principal curvature is locally maximal, providing a satisfactory geometrical representation of important physical properties such as anatomical features in medical images [KMG98, TG96] and ridge-valley lines in satellite data [MAM97]. These properties have enabled widespread use in many fields in image processing and computer vision, for instance registrations [STA98, GA92, SF04], face recognitions [GFP06] and growth simulations [ANK98].

Various methodologies of crest lines extraction have been proposed. Thirion and Gourdon developed a marching lines algorithm to extract characteristic lines based on implicit representations of the iso-intensity surfaces of 3D images without extracting any surface in the first place [TG93]; Ohtake *et al* detected view and scale independent ridge-valley lines via first and second order curvature derivatives on shapes approximated by dense triangle meshes [OBS04]; Stylianou and Chrysanthou approximated curvatures and derivatives on every point of a point cloud to classify crest points followed by crest line linkage and noise pruning [SC05]. Extraction methods on mesh surfaces have been developed by employing a number of methods, including a local moving-least-squares approximation technique [KK06], a bivariate polynomial [SF03] and morphological operators [RKS00].

Differential Geometry for Parametric Surfaces

This section describes the background of differential geometry relating to principal curvatures and principal directions, which are essential for crest lines extraction. Surfaces in this section are described in the classical form of mesh grids.

In computer-aided geometric design (CAGD), a surface is usually given by its parametric form

$$\begin{aligned} \mathbf{x} &= \mathbf{x}(u,v) = (x(u,v), y(u,v), z(u,v))^T \\ \mathbf{u} &= (u,v)^T \in [\mathbf{a}, \mathbf{b}] \subset R^2 \end{aligned} \tag{2.1}$$

where the cartesian coordinates x, y and z are differentiable functions of the parameters u and v; $[\mathbf{a}, \mathbf{b}]$ indicates the area (e.g. rectangle, triangle) of the $u - v$ plane (Figure 2.6). For all $\mathbf{u} \in [\mathbf{a}, \mathbf{b}]$, assume $\mathbf{x}_u \times \mathbf{x}_v \neq (0, 0, 0,)^T$ so as to avoid potential problems with undefined normal vectors.

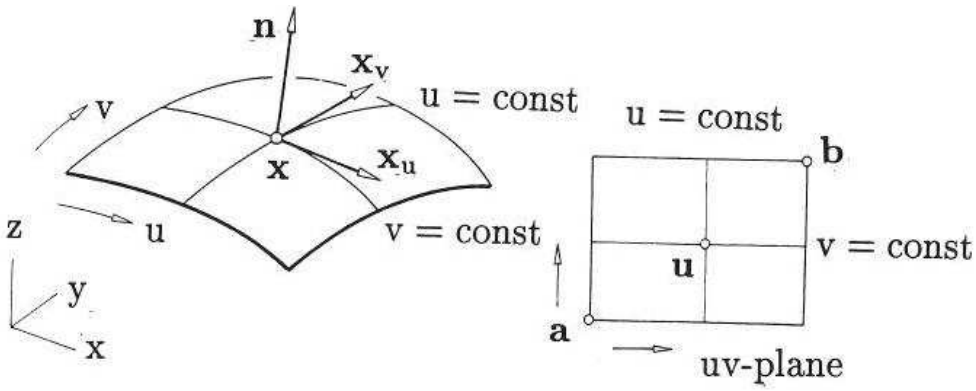

Figure 2.6: A parametric surface [Boe]

The tangent plane of the surface which intersects with point $\mathbf{x}_0 = \mathbf{x}(\mathbf{u}_0)$ has its outward unit normal vector $\mathbf{n}_0 = \mathbf{n}(\mathbf{u}_0)$ (for example, $\mathbf{n}$ in Figure 2.6):

$$\mathbf{n}_0 = \frac{\mathbf{x}_u(\mathbf{u}_0) \times \mathbf{x}_v(\mathbf{u}_0)}{\|\mathbf{x}_u(\mathbf{u}_0) \times \mathbf{x}_v(\mathbf{u}_0)\|} = \frac{\mathbf{x}_u \times \mathbf{x}_v}{\|\mathbf{x}_u \times \mathbf{x}_v\|} \tag{2.2}$$

First Fundamental Form Let $\mathbf{u}(t)$ be a curve on the surface $\mathbf{x}(\mathbf{u})$ with tangent $\mathbf{t}$ and normal $\mathbf{m}$ (the osculating circle of the curve is shown in Figure 2.7). According to curve theory, the *arc length* of the curve s, which is an invariant parameter, can be obtained from $s = s(t) = \int_a^t \|\dot{\mathbf{x}}\| dt$ where dot denotes the derivative with respect to t. Having $\dot{\mathbf{x}} = \mathbf{x}_u \dot{u} + \mathbf{x}_v \dot{v}$, the squared arc element ds^2 equals to

$$\begin{aligned} \|\dot{\mathbf{x}}\|^2 dt^2 &= \mathbf{x}_u \cdot \mathbf{x}_u du^2 + 2\mathbf{x}_u \cdot \mathbf{x}_v du dv + \mathbf{x}_v \cdot \mathbf{x}_v dv^2 \\ &= E du^2 + 2F du dv + G dv^2 \end{aligned} \tag{2.3}$$

The second degree polynomial (Equation 2.3) is called the *first fundamental form* of a regular parametric surface; E, F and G are called the *first fundamental coefficients*.

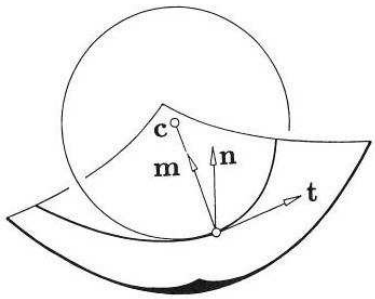

Figure 2.7: Osculating circle [Boe]

Second Fundamental Form The *normal curvature vector* to $\mathbf{u}(t)$ at point $\mathbf{x}_0$ is the projection of the curvature vector, $\mathbf{k} = \dot{\mathbf{t}}/\|\dot{\mathbf{t}}\|$ where $\mathbf{t} = \dot{\mathbf{u}}/\|\dot{\mathbf{u}}\|$, onto the unit surface normal vector $\mathbf{n}$. The proportionality factor $\mathbf{k} \cdot \mathbf{n}$ is called the *normal curvature*, denoted by κ. κ is defined by $\mathbf{t}' = \kappa\mathbf{m}$ where prime denotes the differentiation with respect to the arc length of the curve; $\mathbf{t}'$ is equal to $\mathbf{x}'' = \mathbf{x}_{uu}u'^2 + 2\mathbf{x}_{uv}u'v' + \mathbf{x}_{vv}v'^2 + \mathbf{x}_u u'' + \mathbf{x}_v v''$. Let ϕ be the angle between the curve normal $\mathbf{m}$ and the surface normal $\mathbf{n}$ at point $\mathbf{x}_0$. Since $\mathbf{n}\mathbf{x}_u = \mathbf{n}\mathbf{x}_v = 0$ and consequently $\mathbf{n}_u\mathbf{x}_u + \mathbf{n}\mathbf{x}_{uu} = 0$, we have

$$\begin{aligned} \kappa\cos\phi &= \kappa\mathbf{m}\mathbf{n} = \mathbf{t}'\mathbf{n} \\ &= \mathbf{n}\mathbf{x}_{uu}u'^2 + 2\mathbf{n}\mathbf{x}_{uv}u'v' + \mathbf{n}\mathbf{x}_{vv}v'^2 \\ &= -\mathbf{x}_u \cdot \mathbf{n}_u u'^2 - (\mathbf{x}_u \cdot \mathbf{n}_v + \mathbf{x}_v \cdot \mathbf{n}_u)u'v' - \mathbf{x}_v \cdot \mathbf{n}_v v'^2 \\ &= Lu'^2 + 2Mu'v' + Nv'^2 \end{aligned} \tag{2.4}$$

where L, M and N are called the *second fundamental coefficients*. The second degree polynomial (Equation 2.5) is called *second fundamental form* of a regular parametric surface

$$\kappa\cos\phi ds^2 = Ldu^2 + 2Mdudv + Ndv^2 \tag{2.5}$$

Principal Curvatures The extreme values κ_1 and κ_2 of κ are called *principal curvatures* of the surface at point $\mathbf{x}_0$. Their values and their corresponding *principal directions* correspond to the eigenvalues and the eigenvectors respectively of the following matrix,

which is called the *Gauss-Weingarten map*:

$$W = \begin{pmatrix} L & M \\ M & N \end{pmatrix} \begin{pmatrix} E & F \\ F & G \end{pmatrix}^{-1} = - \begin{pmatrix} \frac{(MF-LG)}{EG-F^2} & \frac{(LF-ME)}{EG-F^2} \\ \frac{(NF-MG)}{EG-F^2} & \frac{(MF-NE)}{EG-F^2} \end{pmatrix} \tag{2.6}$$

Alternatively, κ_1 and κ_2 are the (real) roots of the characteristic polynomial of matrix 2.6. The quadratic polynomial is $\kappa^2 - (\kappa_1 + \kappa_2)\kappa + \kappa_1\kappa_2 = 0$, which yields

$$\begin{aligned} \kappa_1\kappa_2 &= \frac{LN - M^2}{EG - F^2} \\ \kappa_1 + \kappa_2 &= \frac{NE - 2MF + LG}{EG - F^2} \end{aligned} \tag{2.7}$$

The term $K = \kappa_1\kappa_2$ is called *Gaussian curvature*, while $H = \frac{1}{2}(\kappa_1 + \kappa_2)$ is called *mean curvature*.

Curvature Approximation for Triangulated Mesh Surfaces

The problem with a triangulated mesh is that we cannot explicitly calculate derivatives and curvatures on every vertex [SF04]. Therefore, prior to the crest point classification, a quadric on the neighbourhood of every vertex should be fitted as to parameterise the surface.

Based on the theory of surface curvature, the graph of an explicit bivariate function $f(x, y)$ for a triangulated 2D surface can be defined as a parametric surface in the form of

$$\mathbf{x}(\mathbf{u}) = (u, v, f(u, v))^T, \quad (u, v) \in D \subset R^2 \tag{2.8}$$

The normal of the tangent plane of this surface is therefore represented by

$$\mathbf{n}(\mathbf{u}) = \frac{\mathbf{x}_u \times \mathbf{x}_v}{\|\mathbf{x}_u \times \mathbf{x}_v\|} = \frac{(-f_u, -f_v, 1)^T}{\sqrt{1 + f_u^2 + f_v^2}} \tag{2.9}$$

The first and the second fundamental coefficients are respectively calculated as

Equations 2.10 and 2.11

$$E = 1 + f_u^2, \quad F = f_u f_v, \quad G = 1 + f_v^2 \tag{2.10}$$

$$L = \frac{f_{uu}}{\sqrt{1 + f_u^2 + f_v^2}}, \quad M = \frac{f_{uv}}{\sqrt{1 + f_u^2 + f_v^2}}, \quad N = \frac{f_{vv}}{\sqrt{1 + f_u^2 + f_v^2}} \tag{2.11}$$

The Gauss-Weingarten map (Equation 2.6) is consequently formed as

$$W = \begin{pmatrix} L & M \\ M & N \end{pmatrix} \begin{pmatrix} E & F \\ F & G \end{pmatrix}^{-1} = \frac{1}{l} \begin{pmatrix} f_{uu} & f_{uv} \\ f_{uv} & f_{vv} \end{pmatrix} \begin{pmatrix} 1 + f_u^2 & f_u f_v \\ f_u f_v & 1 + f_v^2 \end{pmatrix}^{-1} \tag{2.12}$$

where $l = \sqrt{1 + f_u^2 + f_v^2}$.

Classification of Crest Points

A crest point is defined by Monga *et al* as the point on a surface where the magnitude of the maximum curvature is maximum along the maximum curvature direction [MB92]. They derived the two *extremalities* (or *extremality coefficients*), e_{max} and e_{min} (derivatives of the maximum and the minimum curvatures, κ_1 (κ_{max}) and κ_2 (κ_{min})), along their principal directions, t_1 (t_{max}) and t_2 (t_{min}). Zero crossings of the extremalities, which involve also the third partial derivatives of the surface, correspond to the crest lines. Following Yoshizawa *et al* [YBS05], the crest points consist of perceptually salient ridge points. They distinguish convex and concave crest points, respectively, by

$$\begin{aligned} e_{max} &= 0, \quad \partial e_{max}/\partial \mathbf{t}_{max} < 0, \quad \kappa_{max} > |\kappa_{min}| \\ e_{min} &= 0, \quad \partial e_{min}/\partial \mathbf{t}_{min} > 0, \quad \kappa_{min} < -|\kappa_{max}| \end{aligned} \tag{2.13}$$

Without using zero crossings of the extremalities that require the third partial derivatives, Stylianou and Farin [SF03, SF04] proposed a more computationally convenient method to classify vertices as crest points using *local domain* values on the surface patch. Let $star(\mathbf{x}_0)$ denote all the vertices of the triangulated mesh that share an edge with $\mathbf{x}_0$; the local domain values of $\mathbf{x}_0$ and $star(\mathbf{x}_0)$ are calculated by projecting vertices $\mathbf{x}_0$, which

will remain as $\mathbf{x}_0$, and $star(\mathbf{x}_0)$ on the plane (P). The procedure [SF03] of classifying the i^{th} $(i = 1, 2, \cdots, n)$ point is as following: $\mathbf{y}$ is the projection of $star(\mathbf{x}_0)$ on plane P. ϵ is the pre-defined threshold determining crest points.

I Find the edge $(\mathbf{x}_0, \mathbf{y}_m)$, $m \in [1, n]$ closest to $\mathbf{t}_1^i$.

II Find the edge $(\mathbf{x}_0, \mathbf{y}_j)$, $j \in [1, n]$ and $j \neq m$ closest to $-\mathbf{t}_1^i$.

III Get the largest curvature of the corresponding vertices κ_1^m and κ_1^j.

IV If $(\kappa_1^i)^2 - (\kappa_1^m)^2 > \epsilon$ and $(\kappa_1^i)^2 - (\kappa_1^j)^2 > \epsilon$ then $\mathbf{x}_0$ is a crest point.

Construction of Crest Lines

Two major problems remain after extracting the crest points. Firstly, they are unstructured and unconnected. Secondly, the calculation is noise-sensitive in that it may produce unwanted short and poorly connected line segments. Only when the surface is really smooth will the crest points have implicitly created all the crest lines.

To address the first problem, Stylianou and Farin provided an algorithm to trace a crest line by adding an accordant point to a line [SF03]. In their other work, they proposed a solution using region growing followed by a skeletonisation [SF04]. Instead of using a skeletonisation, Stylianou and Chrysanthou [SC05] utilised the minimum spanning tree (MST) to skin the grown regions.

To address the second problem, various approaches have been proposed to truncate unwanted line segments [HG01, RKS00, OBS04, PK03]. A more sophisticated approach is to use a threshold considering both the curvatures κ_{max} and the lengths of the feature lines [KK06].

2.4 Geometric Morphometrics

Traditionally, morphometrics is the field of multivariate statistical analysis concerned with the methods necessary to rigorously address questions relating to shapes. It has involved

the analysis of arbitrary collections of distance measures, ratios and angles, which fail to capture the complete spatial arrangement of the anatomical landmarks on which the measurements are based. They represent only a small part of information that may be obtained from relative positions of the landmarks.

In the late 1980's, the focus of morphometric procedures was shifted to emphasise methods that captured the geometry of the morphological structures of interest and to preserve the geometry throughout the analysis. These methods include *outline methods*, which were the first geometric morphometric methods to be used, and *landmark methods*, which begin with the collection of two or three dimensional anatomical landmarks. Rohlf and Marcus suggested that this paradigm shift signaled a *revolution on morphometrics* [RM93], whilst Bookstein referred to this as the *morphometric synthesis* [Boo96a]. Most of this change has been due to the development and adoption of methods to analyse the Cartesian coordinates of anatomical landmarks. The direct study of landmark coordinates requires special techniques but yields powerful, concise, and comprehensive analysis [Sli07]. Coordinates of these same landmarks concisely encode all information in any subset of distances (or ratios or angles) among them.

The fundamental advances of geometric morphometrics (GM) over traditional approaches include the way one measures the amount of difference between shapes, the elucidation of the properties of the multidimensional shape space defined by this distance coefficient, the development of specialised statistical methods for the study for shapes, and the development of new techniques for the graphical representations of the results [RC02]. GM methods have found wide applications in the biological sciences, where comparing anatomical features of organisms has been a central element for centuries. In particular, anthropology has played an essential role in the development and adoption of these new methodologies [BSP$^+$99, Har89, OJ98, SLM$^+$06].

General reviews of the entire morphometrics field and its development include [RC90, RM93, Boo96a, O'H00]. Bookstein supplies a more technical review [BSP$^+$91]. Adam *et al* [ARS04] address the influence of morphometrics beyond the field of anthropology, and Bookstein *et al* [BSGM04] explain the role of anthropology in contemporary

morphometrics.

2.4.1 Definition of Shapes

Kendall defined a shape as all the geometrical information that remains when location, scale and rotational effects are filtered out from an object [Ken77]. The entire theory of GM follows from this definition of shapes. A direct analysis on landmark data is invalid since there are position, scale, and orientation effects on the object. These effects should be removed prior to the analysis of the landmarks.

There are no precise definitions of scale (or size) effects. Different studies have their specific surrogates for size and the choice of the size measurement cannot be applied to all datasets or to other studies [Cor87, JFW95]. Since the definition of size is nonunique, a shape can be independent of only the choice of the size measurement, which will affect the results of any analysis of shape variations. A commonly used method to remove size variation is to scale all the objects to a unit centroid size, the square root of the sum of their squared coordinates [BSP+91].

The landmarks must be located on the same coordinate system, and their coordinates must reflect the unique location and orientation of each object with respect to those coordinate axes. The most popular methods, with most thorough theoretical developments, are the Procrustes methods [Gow75, RC90, DM98, GD04]. Other methods include the conversion of the coordinates [LR04, RS98] and registration techniques (see Section 2.6 for a review).

Once all the objects are scaled to the unit centroid size, and translated and rotated to the same coordinate system, the remaining variables become shape variables. They can be used as data in multivariate comparisons of shape variations [Boo96b]. The two most important parameters to be estimated are the mean (or average) and the variability around it.

2.4.2 Morphometric Methods

A number of methods have been proposed to eliminate the location, scale and rotational effects of landmarks, including superimposition methods, deformation methods, Euclidean distance matrix analysis, finite element scaling analysis and methods based on interior angles.

Generalised procrustes analysis is a widely used superimposition method. It superimposes landmarks using translations and rotations obtained in a least square sense. A landmark set is firstly translated to the origin and then scaled to a common size (by dividing by centroid size); rotations are estimated by minimising the least square differences between the corresponding landmarks. The thin-plate spline (TPS) method was originally developed in the field of approximation [Boo89]. In GM, it is a deformation technique that uses chosen functions to map the landmarks to their corresponding landmarks and it can be used to visualise the localised shape phenomena. Procrustes method and TPS are both well described in [Boo97, RDL02]. Details about other superimposition methods can be found in [ARS04].

While most of the recent morphometric methods were developed for landmark data, Bookstein proposed the sliding semilandmark method for outline data [Boo97]. He combined the procrustes method and the TPS method to perform a multivariate analysis of curving outlines in samples of biomedical images. In addition to optimally translating, scaling and rotating the landmarks, the semilandmarks are slid along the outline curves until they match the positions of the corresponding points along the outlines in another object.

The difference between the approach proposed in this thesis and the traditional morphometrics methods will be demonstrated in Chapter 5. Advantages and limitations of the present approach will also be discussed in Section 5.7.

2.5 Statistical Shape Models

Accurate definitions of anatomical structures and morphological variations of bones are of importance in the fields of palaeontology, taxonomy and anthropology. They also play an important role in subject-specific pre-clinical planning, intraoperative navigation and musculoskeletal modelling. With the development of mathematical models and computational tools in medical imaging, a number of approaches have emerged to quantify shapes and size of anatomical structures of bones. Model-based image analysis techniques such as active shape models [CCTG95] and active appearance models [CBET99] have been recently developed and widely used in computer vision.

Statistical shape modelling (SSM) is the underlying basic technology, showing considerable promise to study the variations in anatomical shapes and acting as a basis for the segmentation and the interpretation of images. Its basic idea is to establish, from a training set, the pattern of variations in the shapes and the spatial relationships of structures for a given class of images. It is used to provide an efficient parameterisation of the studied variability, producing a compact representation of shape and allowing shape constraints to be applied effectively during image interpretation [CCTG95].

One of the major difficulties in building an SSM is the determination of surface point correspondences between shapes over a large set of training shapes. Although manual labelling in 2D images is still being used in many applications, it is very time-consuming. 3D landmarking becomes impractical due to the significant number of landmarks required to describe the structure and by definition limits information that can be obtained. Also, it is tedious and error-prone.

Numerous attempts have been made to automate the construction of training sets with correspondences. The use of local shape features (e.g. high curvatures) has been proposed to establish correspondences between shapes [BHT99, BT00a, Tag99, WPS00]. As pointed out by Davies, the method does not guarantee optimal correspondences although it corresponds with human intuition [DCT01]. Alternatively, correspondences of the training shape boundaries are defined through the parameterisation of each shape

[BGK95, Boo97, KT98]. Davies and colleagues defined the *best* model as that which minimises the *minimum description length* of the training set [DTA+03]. They utilised the SPHARM approach introduced by Brechbuhler to find the initial parameterisation of each shape [BGK95]. Approaches using non-rigid registration have also been used in a number of applications [FL98, BT00b, FRSN02]. Correspondences were identified by deforming each training sample to the reference (also called *atlas*). The resulting deformation fields can then be used to build the model. Splines, more specifically methods including B-spline [RSH+99, LWS97, LV95] and thin-plate spline [Boo89, LK00, LP00], are common mathematical models for non-rigid registrations.

Given a training set of n shapes which are represented by m corresponding surface points and given that those shapes are already aligned to a common coordinate system, each shape in the training set is denoted by a $3m$-element column vector of point coordinates

$$\mathbf{x} = (x_1, y_1, z_1, x_2, y_2, z_2, \cdots, x_m, y_m, z_m)^T$$

2.5.1 Principal Component Analysis

PCA is a projection-based dimensionality reduction method to reduce data dimensionality by linearly transforming the data to a new coordinate system such that the greatest variance by any projection of the data comes to lie on the first coordinate (called the first principal component), the second greatest variance on the second coordinate, and so on. The main advantage of using PCA in a study on the morphology of bones is that the patterns or the major variations within high dimensional 3D surface data can be captured and that the data can be compressed without losing patterns of the data. PCA is closely related to SSM. It decomposes the training set in eigen space as well as restricts the shape variations of the model close to the known variations.

Given a $n \times 3m$ data matrix $\mathbf{x}$ of n shapes consisting of m surface points ($3m$ dimensional), the computation of PCA starts with a mean-centred matrix $\mathbf{y}$ obtained from the empirical mean $\overline{\mathbf{x}}$ ($\overline{\mathbf{x}} = \sum_{i=1}^{n} \mathbf{x}_i/n$) of the distribution being subtracted from the variables: $\mathbf{y} = \mathbf{x} - \overline{\mathbf{x}}$. Two approaches are mostly used to calculate the principal

axes (eigenvectors). The first one is comparatively computationally expensive due to the computation of the covariance matrix $C_{3m\times 3m}$ of $\mathbf{y}$. The solution of equation $C\phi = \lambda\phi$ provides the eigenvectors ϕ ($\phi^T\phi = 1$) and eigenvalues λ of covariance matrix C. The second approach utilising singular value decomposition (SVD) is numerically more stable. Decomposing $\mathbf{y}$ as $U\Sigma D^T$, the right singular vectors contain the eigenvectors whilst the squared diagonal elements of Σ contain the eigenvalues.

By arranging the eigenvalues in descending order and their corresponding eigenvectors so that $\lambda_i > \lambda_{i+1}$ makes λ_j nearly zero at a certain point j. The first corresponding j eigenvectors form the principal axes describing the most important modes of variabilities of the data in eigen space. The proportion of the total variability f_i explained by each principal mode is equal to its eigenvalue divided by the sum of all n eigenvalues: $f_i = \lambda_i / \sum_i \lambda_i$. The eigenvectors ϕ provide the so-called *modes of shape variations*, and the eigenvector corresponding to the largest eigenvalue accounts for the largest variation. The magnitude of eigenvalue shrinkage is a function of the type of shrinkage, sample size, the number of variables in the correlation matrix, the ordinal root position, the population eigenstructure, and the choice of PCA or principal factors analysis [BS84].

The n (when $3m > n$) largest eigenvalues and their corresponding eigenvectors of the covariance matrix $C_{3m\times 3m}$ can be determined from the n eigenvalues and eigenvectors of $\widetilde{C}_{n\times n} = \mathbf{y}_{n\times 3m}\mathbf{y}^T_{n\times 3m}$. The cumulation of the first few eigenvalues has such a large proportion of the cumulation of all eigenvalues that the rest of the eigenvalues approximate a zero proportion. Let $\widetilde{\lambda}_i (i = 1, 2, ..., n)$ be the eigenvalues of $\widetilde{C}_{n\times n}$ and $\widetilde{\phi}_i$ be the eigenvectors, the first j eigenvalues λ_j and corresponding eigenvectors ϕ_j of $C_{3m\times 3m}$ can be calculated as

$$\lambda_j = \widetilde{\lambda}_j \tag{2.14}$$

$$\phi_j = \frac{1}{\sqrt{\widetilde{\lambda}_j}}\mathbf{y}\widetilde{\phi}_j \tag{2.15}$$

By far the most common form of factor analysis, PCA is a large-sample procedure (another main type of factor analysis is *common factor analysis*, which is what people

generally mean when they say *factor analysis*). The question of sample size in factor analysis and PCA has been studied for decades: some statisticians have argued that a large sample size N improves the precision of estimates from PCA [Cli70, Bag83]; others have shown that the ratio of samples to variables is more important in interpreting outcomes of PCA [GV88]. The commonly accepted minimal number of samples for the analysis should be larger than 100 or five times the number of variables being analysed. However, it is fair to say that there are no absolute rules for deciding sample size.

MacCallum *et al* suggested that the minimum sample size depended on the nature of the data, most notably its *strength* [MHW01]. Strong data are data in which variable communalities are consistently high and many variables are expected to have high load (or weight) on at least three or four components. Communality represents the proportion of the variance of a particular variable that is shared with other variables. The values are calculated as the sum of squared component weights for a given variable [Try98]. The meaning of load (or weight) of PCA is the same as for point distribution models, which will be explained in the following section.

The reliability of applying PCA to the shoulder bone shapes is not validated in this thesis. Instead, all applications based on PCA results in the present work are tested using leave-one-out validations.

2.5.2 Point Distribution Models

A widely acknowledged SSM is the Point Distribution Model (PDM) introduced by Cootes *et al* [CTCG92]. PDM is built from a set of training samples which are given in the form of boundary or surface points. It models the shape probability distribution as a multivariate Gaussian in a subspace of reduced dimensionality. SSM is a larger concept as it can be also built from lines (e.g. sutura, crista) or areas (e.g. pars, foramen).

Correlations between shape (vector) elements can be obtained from the covariance matrix

$$C = \frac{1}{3m}\sum_{i=1}^{3m}(\mathbf{x}_i - \overline{\mathbf{x}})(\mathbf{x}_i - \overline{\mathbf{x}})^T (i = 1, 2, \cdots, n)$$

where $\overline{\mathbf{x}}$ is the vector of the mean shape. Let P_k be the first $k(k \leq 3m)$ eigenvectors of C, the dominant shape variations can be modelled using factor analysis

$$S = \overline{\mathbf{x}} + P_k b \tag{2.16}$$

b is the latent variable (also known as the factor loadings for the principal axes) describing shape deformations and the number of eigenvectors k is chosen to explain a given proportion of the variance exhibited in the training set such that $\sum_{i=1}^{k} \lambda_i \geq f V_{3m}$. λ_i is the i^{th} eigenvalue of covariance matrix C, the larger the i^{th} eigenvalue the greater the shape of change associated with the i^{th} principal mode; $V_{3m} = \sum_{3m} \lambda_i$ is the total variance in the training set and f defines the proportion of the variation we wish to obtain.

New plausible shapes S are generated by varying the values of vector b within suitable limits, which are derived by examining the distribution of the parameter values required to generate the training sets. The method relies on the assumption that the shape variations across the population have normal distributions. Since 99.7% of the population lies within three standard deviations of the mean, the suitable limit for b_i is thus typically in the range $\pm 3\sqrt{\lambda_i}(i = 1, 2, \cdots, k)$. This assumes that the important shape data and key variability in shape data is wholly contained within this 99.7% of the population. The approximate variance described by the first k principal components is estimated by $\sum_{i=1}^{k} \lambda_i$.

2.5.3 Neighbour-Conditional Shape Model

A pairwise conditional shape model is proposed by Bruijne *et al* for vertebral fracture quantification from X-ray images [BLT+06]. The method does not only model the shape variations over a population for individual vertebrae, but can also model the interrelations between vertebrae in the same subject. It is able to predict the most likely shape of a joint given the known shape of the adjoining segment, and to estimate the variations of the estimation.

The maximum likelihood estimate of shape $\mathbf{x}_y$ given the neighbour shape $\mathbf{x}_x$ is

calculated as

$$\mu = \mu_y + C_{yx}C_{xx}^{-1}(\mathbf{x}_x - \mu_x) \tag{2.17}$$

where μ_x and μ_y are the mean shapes of the training sets for $\mathbf{x}_x$ and $\mathbf{x}_y$, respectively, and covariance C_{ij} is constructed as

$$C_{ij} = \frac{1}{n-1}\sum_n (\mathbf{x}_{in} - \mu_i)(\mathbf{x}_{jn} - \mu_j)^T \tag{2.18}$$

C_{xx} in Equation 2.18 is not always invertible owning to multi-collinearity and unreliability due to insufficient number of training samples. Ridge regression [HK70] provides a solution which replaces C_{xx} by $C_{xx} + \gamma I$, where γ is a positive and extremely small constant. The relationship between $\mathbf{x}_x$ and $\mathbf{x}_y$ tends to decrease as γ increases.

The probability distribution $P(\mathbf{x}_y|\mathbf{x}_x)$ of shape $\mathbf{x}_y$ given shape $\mathbf{x}_x$ is modelled as the Gaussian conditional density with expectation μ and variance K:

$$K = C_{yy} - C_{yx}C_{xx}^{-1}C_{xy} \tag{2.19}$$

2.5.4 Bone Morphing

CT-free methods of guiding surgery without acquisition of CT data are desirable. These are explored here for image-free surgical planning. Current normal practice requires a three-dimensional patient-specific model to be generated from volume CT scans obtained pre-operatively and surgical strategies are planned using all available information. For many cases, very detailed and precise 3D models are unnecessary and the reconstructed 3D shapes of the articulating bones are sufficient.

Bone morphing is a procedure of extrapolating extremely sparse 3D surface points on a bone to obtain a complete surface representation. It is important for intra-operative visualisation of bone structures in image-free surgeries (examples include visualising bone defects, planning surgical cuts, choosing implant size, choosing the implant position and rotations with respect to bone cortical surfaces, and estimating distances between bones and components prior to making any real cut [SBM+02]).

Fleute and Lavellee proposed using an SSM to reconstruct a complete surface model of the femur by manually digitising a few points on the femoral surface [FL98], in order to improve visualisation of a system developed by the TIMC laboratory (France) for computer assisted anterior cruciate ligament (ACL) reconstruction. The femora were registered using an elastic registration method based on the multi-resolution octree-spline method. Non-linear optimisation was performed to fit the statistical model to a few digitised surface points so that the distance between the surface points and the model were minimised. The objective function to be minimised is

$$f = \sum_{i=1}^{D} \min_{1 \leq j \leq M} \|\mathbf{d}_i - \mathbf{m}_j\|^2 \tag{2.20}$$

where $\mathbf{m}_j = R(\overline{m} + \sum_{i=1}^{t} \omega_i \mathbf{e}_i) + T$, D is the number of surface points, $\mathbf{d}_i$ is the i^{th} surface point, R is the rotation function and T is the translation function.

Stindel *et al* presented a method for performing a total knee arthroplasty (TKA) based on bone morphing using the octree-spline deformation, published by Szeliski and Lavallee [SL96], to build an SSM of the femora or the tibiae [SBM+02]. Yao and Taylor developed a non-rigid registration method to deform a pelvis shape model to match with the anatomical structures in a CT image [YT03]. A leave-one-out validation was performed and it showed the method could achieve about 94% volume overlap and 5.5% density error between the registered model and the ground truth model. Chan *et al* presented a cadaveric validation of their method that used tracked ultrasound to instantiate and register the SSM. Surface points were matched to the corresponding SSM surface using the ICP algorithm with the mean shape of the model as the starting estimation [CBE+04]. Optimisation was based on the golden section search method [PTVF92].

Rajamani *et al* developed a morphing scheme operating directly in PCA shape space incorporating the full set of possible variations including additional information such as patients' height, weight and age [RNS04]. In each iteration, they first calculated the most probable shape that is related to the three initially digitised landmarks, and then used statistical shape analysis to examine the remaining shape variability after surface information coded by the digitised points was progressively subtracted. They also proposed

a method to extrapolate 3D shapes by computing a Mahalanobis distance weighted least squares fit of the constructed SSM to minimal sparse 3D data [RTSGB05]. The morphing computation was formulated as a linear equation system and then solved for the shape parameters that best describe the unknown shapes. The objective function that was minimised is

$$f = \sum_{k=1,j=index(x_k)}^{N} \omega_k \|\vec{Y}_k - (\vec{X}_j + \sum_{i=1}^{m} \alpha_i \vec{p}_i(j))\|^2 + \rho \sum_{i=1}^{m} \frac{\alpha_i^2}{\lambda_i} \tag{2.21}$$

with N the number of points that were digitised, $\vec{Y}_k$ the k^{th} digitised point, $\vec{X}_j$ a point on the mean shape that is closest to $\vec{Y}_k$, $\vec{p}_i(j)$ the j^{th} tuple of the i^{th} basis vector of the shape, λ_i the i^{th} eigenvalue and α_i scalar weights which are the m shape parameters that describe the shape.

2.6 Registration Techniques

As mentioned above, one of the major difficulties in building an SSM is the determination of surface point correspondences between shapes over a training set. The present work identifies point-to-point correspondences using non-rigid registration. Rigid registration is also utilised in automatic shape alignment. This section summarises the registration techniques and describes the related methods in detail.

2.6.1 Types of Registration

In the recent decades, image acquisition devices have been developing rapidly. Images are acquired faster with higher resolution and improved image quality, which has invoked research on automatic image registration. Being first applied in image guided surgery but perceived as a minor precursor to some medical applications at its early stage, image registration is now widely used with applications in the context of industrial computer vision, medical imaging, remote sensing and so on. Its potential applications include [Haw00]:

- Combining information from multiple imaging modalities
- Monitoring changes in size, shape or image intensity over time intervals
- Relating pre-operative images and surgical plans to the physical reality of the patient in the operating room
- Relating individual anatomy to a standardised atlas

A classification of registration was proposed by van den Elsen and Viergever using nine basic criteria [vdEV93]: (a) Dimensionality, (b) Nature of registration basis, (c) Nature of transformation, (d) Domain of transformation, (e) Interaction, (f) Optimisation procedure, (g) Modalities involved, (h) Subject and (i) Object. The description of registration in this chapter is based on criterion (c), Nature of transformation. This primarily includes rigid, affine, projective and curved registration. Applications mostly relate to rigid registration and, specially, curved registration, which is referred to as non-rigid registration in this thesis.

In order to align a 3D shape (or image), B (source), to its comparator shape, A (target), to relate their corresponding position of features or coordinate space x, shape B is *transformed* using a transformation algorithm. T is used to represent this registration transformation and it is performed as

$$T : x_B \mapsto x_A \Longleftrightarrow T(x_B) = x_A \tag{2.22}$$

Rigid Transformation

Rigid transformation consists of only rotations and translations, and leaves given arrangements unchanged. In 3D space, rigid registration has six DOF consisting of three translations and three rotations. Rigid transformation is regarded as a global transformation because it only changes the position of an image whilst it preserves the overall geometric relationships between points of the image. The technique is particularly useful in image-guided surgery for fiducial registration and calibration, by computing a rigid transformation that minimises fiducial registration errors [FWMJ98].

Denote the translation vector along x, y and z axes as t ($t = (t_x, t_y, t_z)^T$), and the rotation matrix as R ($RR^T = I$), a rigid transformation that maps any point $\mathbf{x}_B = (x_B, y_B, z_B)^T$ of shape B to its corresponding point $\mathbf{x}_A = (x_A, y_A, z_A)^T$ of shape A can be written in homogeneous coordinates:

$$T_{rigid}(\mathbf{x}_B) = \begin{pmatrix} & R & & t \\ & & & \\ 0 & 0 & 0 & 1 \end{pmatrix} \begin{pmatrix} x_B \\ y_B \\ z_B \\ 1 \end{pmatrix} \tag{2.23}$$

The most popular representation of rotation matrix R uses Euler angles corresponding to three successive rotations with angles α, β and γ around x, y and z axes.

$$R = \begin{pmatrix} \cos\beta\cos\gamma & \cos\alpha\sin\gamma + \sin\alpha\sin\beta\cos\gamma & \sin\alpha\sin\gamma - \cos\alpha\sin\beta\cos\gamma \\ -\cos\beta\sin\gamma & \cos\alpha\cos\gamma - \sin\alpha\sin\beta\sin\gamma & \sin\alpha\cos\gamma + \cos\alpha\sin\beta\sin\gamma \\ \sin\beta & -\sin\alpha\cos\beta & \cos\alpha\cos\beta \end{pmatrix} \tag{2.24}$$

Affine Transformation

Affine transformation is an extension of rigid transformation allowing 12 DOF in 3D space: translations, rotations, scalings and shears. It maintains co-linearity by mapping parallel lines onto parallel lines whilst it does not preserve the geometric relationships between points.

Scaling allows a shape to stretch or shrink along at least one axis or dimension, but not necessarily all axes. Shear preserves a homothety (a similarity transformation which preserves orientation) and an isometry by pushing a shape to one direction parallel to a 3D coordinate plane or a 2D coordinate axis with a shearing factor determining how far the direction is pushing (Figure 2.8). In 3D space, a shape can be pushed in two coordinate axis directions with the third direction fixed.

As for rigid transformations, an affine transformation is described by a single constant matrix equation, which can be obtained by replacing the rotation matrix R in Equa-

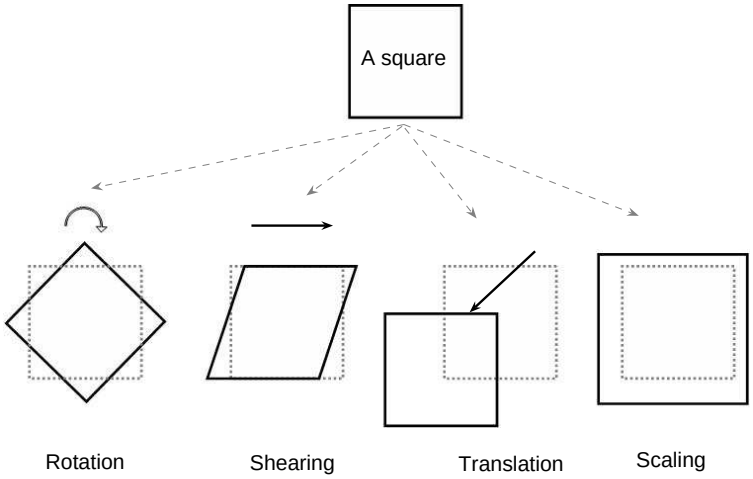

Figure 2.8: A demonstration of 2D affine transformations

tion 2.23 with matrix M. M can be decomposed into components representing 3D rotations, scalings and shears (Equation 2.25):

$$M = R(\alpha, \beta, \gamma) \begin{pmatrix} 1 & S_{xy} & S_{xz} \\ 0 & 1 & S_{yz} \\ 0 & 0 & 1 \end{pmatrix} \begin{pmatrix} S_x & 0 & 0 \\ 0 & S_y & 0 \\ 0 & 0 & S_z \end{pmatrix} \tag{2.25}$$

where S_{xy}, S_{xz}, S_{yz} are shear parameters and S_x, S_y, S_z are scale factors in three orthogonal directions.

An affine transformation cannot be simply taken as a linear transformation because it does not satisfy the linear equation

$$L(\phi x + \theta x') = \phi L(x) + \theta L(x') \qquad \forall x, x' \in R^D \tag{2.26}$$

Non-rigid Transformation

When a shape tends to deform in much more complicated ways, an affine transformation is insufficient and more DOF are required to describe deformations with adequate accuracy. By adding additional DOF, a linear or a nearly linear transformation model with few DOF

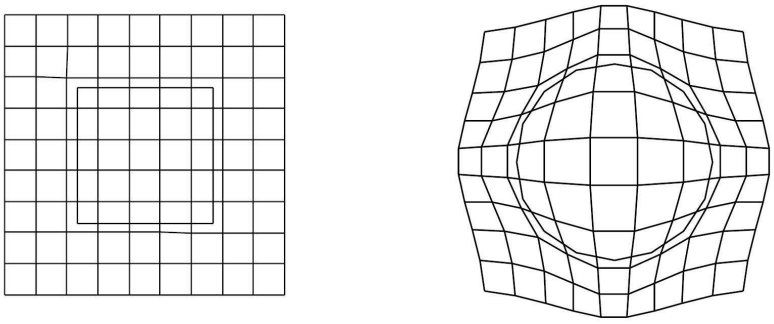

(a) Before transformation (b) After transformation

Figure 2.9: An example of 2D non-rigid transformations [Haw00]

can be extended to non-rigid transformation models (Figure 2.9), giving over a million DOF for typical images. Any non-rigid registration technique can be described by three components [Haw00]: (a) a transformation which relates the target and source images; (b) a similarity measure which measures the similarity between the target and source images and (c) an optimisation method which determines the optimal transformation parameters as a function of the similarity measure.

The most common mathematical or physical models that are used in non-rigid registration include basic functions, spline, elastic-solid registration, viscous-fluid registration and smoothed displacement fields. In spline models (for example B-spline [RSH+99, SRQ+01, LWS97] and thin-plate spline [Boo89, LK00, LP00]), the transformation can be separated into piecewise terms which are specified by local knots or control points. Its DOF are decided by the number of control points and smoothness of the transformed image is affected by the spacing of the control points. The theory is based on the assumption that correspondent points can be identified in a source image and its target image, and that the locations of the control points in the target can be mapped onto its corresponding counterpart in the source.

2.6.2 Feature-based Registrations

In contrast to registration based on voxel intensities, which uses intensities of an image alone without any requirement to segment or delineate corresponding structures of the

object in the image, the majority of feature-based registration techniques, which use features of the object in the image such as landmarks, surfaces and curves, can be divided into four steps: feature detection, feature matching, transform model estimation and final transformation. Correspondences and transformations are the two unknown variables desirable in this type of registration. This section discusses two types of feature-based registration methods, landmark-based registration and surface-based registration.

Landmark-based Registrations

A pair of specified 3D points, which could be point landmarks (such as surface points), anatomical landmarks and markers (fiducials) attached to structures on a body which would be made visible in imaging modalities, in a shape A and a shape B are the representations of the same features of the object in both shapes. Registration using corresponding point sets is referred to as *landmark based* registration in the present work. The transformation of shape B to shape A can be performed by transforming all of the arbitrary points using the transformation of those landmarks.

The Procrustes Algorithm Drawing its name from the Procrustes area of statistics, the Procrustes problem is widely used for determining rigid and affine transformations. It is an optimal least square fitting problem. Given two sets of n corresponding points, $\mathbf{x}_B = \{x_{Bi}\}$ and $\mathbf{x}_A = \{x_{Ai}\}$ $(i = 0, 1, \cdots, n)$, the Procrustes algorithm is able to seek the transformation T which minimises $G(T) = |T(\mathbf{x}_B) \Leftrightarrow \mathbf{x}_A|^2$. As such, parameters for the rigid transformation matrix T_{rigid} can be estimated.

When T represents a rigid transformation, the classical Procrustes problem has known solutions using SVD [DM98, FWMJ98]. A minimisation function is set as Equation 2.27 and the differentiation of this equation concerning transformation T_{rigid} is set to zero.

$$G(T_{rigid}) = \sum_{i=1}^{n} |\mathbf{x}_{Ai} - T_{rigid}(\mathbf{x}_{Bi})|^2 = \sum_{i=1}^{n} |\mathbf{x}_{Ai} - R\mathbf{x}_{Bi} - t|^2 \tag{2.27}$$

Suppose a set of points $\mathbf{x} = \{\mathbf{x}_1, \mathbf{x}_2, \cdots, \mathbf{x}_n\}$ is to be rigidly transformed to its corresponding target set of points $\mathbf{y} = \{\mathbf{y}_1, \mathbf{y}_2, \cdots, \mathbf{y}_n\}$, the rigid registration algorithm

aligns $\mathbf{x}$ to $\mathbf{y}$ as close as possible by minimising the least squares of their distances: $C = \sum_{i=1}^{n} |\mathbf{y}_i - T_{rigid}(\mathbf{x}_i)|^2$. Substituting the rotation matrix R and the translation matrix T for the rigid registration transformation matrix T_{rigid} and setting the differential of C relating to the translation matrix T as zero, we have

$$\begin{aligned} \frac{\partial C}{\partial T} &= \partial \sum_{i=1}^{n} |\mathbf{y}_i - R\mathbf{x}_i - T|^2 / \partial T \\ &= -2\sum_{i=1}^{n} \mathbf{y}_i + 2R\sum_{i=1}^{n} \mathbf{x}_i + 2T\sum_{i=1}^{n} 1 \\ &= 0 \end{aligned} \tag{2.28}$$

Solving the above equation gives $T = \overline{\mathbf{y}} - R\overline{\mathbf{x}}$, where $\overline{\mathbf{x}}$ is the mean point of point set $\mathbf{x}$, and $\overline{\mathbf{y}}$ is the mean point of point set $\mathbf{y}$. The mathematical solution for $T = \overline{\mathbf{y}} - R\overline{\mathbf{x}}$ is known as the solution to the *orthogonal procrustes problem* involving the use of SVD. Decomposing the covariance matrix K of $\mathbf{x}$ and $\mathbf{y}$ gives

$$K = \sum_{i=1}^{n} (\mathbf{y} - \overline{\mathbf{y}})(\mathbf{x} - \overline{\mathbf{x}})^T = UVD^T \tag{2.29}$$

The rotation matrix R can then be obtained by

$$R = VU^T \tag{2.30}$$

Non-rigid Transformation Models Using B-spline Sederberg and Parry presented a technique for deforming solid geometric models in a free-form manner based on trivariate Bernstein polynomials [SP86]. Its basic idea was to embed an object in a control grid which defines the continuous deformation field. Lee *et al* used B-spline to model the deformations of multilevel control grids [LWCS96]. The mesh nodes were taken as the control points that were interpolated by a set of B-spline basis functions. Frangi *et al* [FRSN02] proposed a method to establish shape correspondences via a volumetric non-rigid registration technique using multi-resolution B-spline free form deformation (FFD). The study shape was non-rigidly registered in a coarse-to-fine manner by deforming its control points at different resolution levels. Schnabel *et al* [SRQ+01] further developed

an image-based registration algorithm proposed by Rueckert *et al* [RSH+99] to generate a framework for non-rigid registration.

Even though a bone itself is a relatively rigid body that deforms little compared to variations in shapes between individuals, rigid or even affine registration is not enough to model the local differences. Non-rigid deformation is required to model the global as well as the localised differences. The transformation function $T_{non-rigid}$ that registers a source shape to its target shape is combined by a global transformation T_{global}, specifically a rigid and affine transformation, and all local transformations T_{local} that transform localised points of the source shape by deforming their respective surrounding mesh nodes:

$$T_{non-rigid} = T_{global} + T_{local} \tag{2.31}$$

Assuming a shape I is in domain $\Omega = \{(x, y, z)|0 \leq x \leq X, 0 \leq y \leq Y, 0 \leq z \leq Z\}$, where X, Y and Z are the image dimensionalities, with $n_x \times n_y \times n_z$ uniform spacing control points ϕ, the local transformation in the form of cubic B-spline function can be written as

$$T_{local}(x, y, z) = \sum_{l=0}^{3} \sum_{m=0}^{3} \sum_{n=0}^{3} B_l(u) B_m(v) B_n(w) \phi_{i+l,j+m,k+n} \tag{2.32}$$

where $i = \lfloor x/n_x \rfloor - 1$, $j = \lfloor y/n_y \rfloor - 1$, $k = \lfloor z/n_z \rfloor - 1$, $u = x/n_x - \lfloor x/n_x \rfloor$, $v = y/n_y - \lfloor y/n_y \rfloor$, $w = z/n_z - \lfloor z/n_z$ and $B(a)$ is defined as

$$\begin{aligned} B_0(a) &= (1-a)^3/6 \\ B_1(a) &= (3a^3 - 6a^2 + 4)\ 6 \\ B_2(a) &= (-3a^3 + 3a^2 + 3a + 1)\ 6 \\ B_3(a) &= a^3/6 \end{aligned} \tag{2.33}$$

With the ability to have locally controlled functions, computational efficiency and general applicability, non-rigid registration using B-spline is a powerful tool for modelling deformable objects such as patients' bone shapes.

Multi-resolution B-spline Free Form Deformation In single level deformation, size of a control volume largely influences the deformation results. Large size control volumes lead to a smooth effect while small size volumes generate accurate point-to-point deformation. To circumvent this trade-off, multi-resolution B-spline approximation was devised so that the size of the control volume can be subdivided progressively at each resolution level. Through defining a sequence of control meshes $\Phi^0, \Phi^1, \cdots, \Phi^H$, the local transformation is the sum of the transformations at all levels of resolution.

$$T_{local}(x, y, z) = \sum_{h=0}^{H} T_{local}^{h}(x, y, z) \tag{2.34}$$

Surface-based Registration

Instead of using corresponding points of the shapes (or boundaries, surfaces), corresponding anatomical structures can be used to register two shapes.

One of the surface fitting techniques to match a source surface to the target surface is called the head and hat algorithm. It was proposed by Pelizzari and colleagues [LPC+88]. The algorithm tries to find the best transformation between *a stack of disks* being referred to as the head and a list of unconnected 3D points on the other surface (the hat surface). The hat surface is iteratively transformed with respect to the head surface until the best fit of them is found. The performance of the algorithm was improved by using a distance transform to pre-process the head. A widely used distance transform is the chamfer filter proposed by Borgefors [Bor84]. This approach has been used for rigid registration [JRH92, VHK94].

Iterative closest point algorithm The Iterative Closest Point (ICP) algorithm proposed by Besl and McKay is a widely used surface matching algorithm [BM92]. It is applied in a large range of representations that cover most applications of 3D shape registration: point sets, line segment sets (polylines), implicit curves, parametric curves, triangle sets, implicit surfaces and parametric surfaces. The algorithm always converges monotonically to a close minimum of a mean square distance metric at a rapid rate during the first few

iterations.

Given two surfaces described by two sets of surface points without correspondences, $P\{p_1, p_2, \cdots, p_m\}$ and $Q\{q_1, q_2, \cdots, q_n\}$, the Euclidean distance between point $p_i \in P(i = 1, 2, \cdots, m)$ and point $q_j \in Q(j = 1, 2, \cdots, n)$ is denoted as $d(p_i, q_j)$. In each of the iterations, find the closest point c_j to every point q_j in P so that $d(p_j, c_j) = \min_{i \in \{1,2,\cdots,n\}} d(q_j, p_i)$. Taking c_j as the corresponding point to q_j, Q's corresponding point set $C\{c_1, c_2, \cdots, c_q\}$ can be constructed. ICP estimates the rigid or non-rigid transformation that best maps P and Q and the estimated transformation is then applied to all points in P. A new corresponding point set C' is then further extracted from the transformed P. The algorithm iterates until convergence or the maximum number of iterations is achieved.

The ICP algorithm is simple and relatively easy to implement, and with a reasonably good starting estimation, the algorithm converges quickly. However, it is prone to find a local minimum if the starting estimation is not good enough.

2.6.3 Point Matching Techniques

Identifying correspondences between features is a major problem frequently encountered by feature-based registration techniques. Noise arising from image acquisition and feature detection, as well as outliers - feature points that exist in one image but not in others, degenerate the automatic correspondences establishment. ICP's crude way of assigning correspondence generates a lot of local minima and does not usually guarantee that the correspondences are one-to-one [CR03].

Only a few methods have been developed to deal with identifying correspondences and matching shapes at the same time. Jagannathan and Miller presented a thermodynamically inspired graph theoretical algorithm to address the problem of matching a scene and a point cloud [JM05]. A thermodynamically inspired objective function was proposed to capture the structural nuances between a pair of graphs and the spatial differences between the underlying point sets. Correspondences are obtained by tackling a sequence of inexact graph matching problems that optimise the proposed objective func-

tion. Rangarajan *et al* presented an extension of the Procrustes method to the point sets of different point clouds without correspondences. The method iteratively combines the search for correspondences, spatial mapping and Procrustes rescaling. Correspondences are parameterised via a binary match matrix that assigns points in one set to points in the other and discards non-homologies as outliers.

Following the work on the joint estimation of pose and correspondences using softassign [GRL$^+$98] and deterministic annealing [GG91], Chui and Rangarajan developed a robust point matching algorithm with thin-plate spline (TPS-RPM) as the parameterisation of non-rigid spatial mapping [CR03]. Given two sets of unstructured points, x_i $(i = 1, 2, \cdots, n_1)$ and y_j $(j = 1, 2, \cdots, n_2)$, the robust point matching (RPM) algorithm minimises the following objective function.

$$\min_{M,\theta,t,s} E(M, \theta, t, s) = \sum_{i=1}^{n_1}\sum_{j=1}^{n_2} M_{ij}\|x_i - t - sR(\theta)y_j\|^2 + \frac{\gamma}{2}(\log s)^2 - \alpha\sum_{i=1}^{n_1}\sum_{j=1}^{n_2} M_{ij} \quad (2.35)$$

subject to $\sum_{i=1}^{n_1+1} M_{ij} = 1$ $(\forall j \in 1, 2, \cdots, n_2)$, $\sum_{j=1}^{n_2+1} M_{ij} = 1$ $(\forall i \in 1, 2, \cdots, n_1)$ and $M_{ij} \in 0, 1$. M_{ij} is the $n_1 + 1 \times n_2 + 1$ match matrix that indicates when homologies have been found or outliers are discarded. The minimisation function gives solutions for the transformation parameters: rotation θ, translation t and scaling factor s. γ is a regularisation parameter.

Instead of finding the closest point as the part counter in ICP algorithm, the robust point matching algorithm iteratively updates the match matrix, which is called *softassign*, to map the correspondences between two point sets.

The name *thin-plate spline* refers to a physical analogy involving bending of a thin sheet of metal. When applied in a registration scenario, it fits a mapping function $f(x_a)$ between corresponding point sets x_a and y_a by minimising the energy function 2.36.

$$E_{TPS}(f) = \sum_{a=1}^{K} \|y_a - f(x_a)\|^2 + \lambda \int\int [(\frac{\partial^2 f}{\partial x^2})^2 + 2(\frac{\partial^2 f}{\partial x \partial y})^2 + (\frac{\partial^2 f}{\partial y^2})^2] dxdy \quad (2.36)$$

The TPS-RPM algorithm has been successfully applied to align autoradiographs and to compute registration of cortical anatomical structures. However, the algorithm has

limitations in that it works generally on simple and clear data, not on complex and noisy data.

2.7 Multiple Linear Regression

Both PCA and SSM only capture variabilities and inner relationships within a training set as a whole. To model intrinsic morphological correlations between the bones of the glenohumeral joint, multiple linear regression (MLR) will be used. The general purpose of MLR is to model the relationship between several independent or predictor variables and dependent or criterion variables by fitting a linear equation to observed data. To address more sophisticated data analysis problems, MLR has been extended in a number of multivariate methods, such as discriminant analysis, canonical correlation analysis (CCA), principal components regression (PCR) and partial least square (PLS) regression.

Discriminant analysis is used to determine which variables discriminate between two or more naturally occurring groups. Its aim is to determine the group of an observation based on a set of variables (predictors). The discriminant model is built based on a set of observations for which the groups are known. CCA is a procedure for assessing and investigating linear relationships between variables. PCR estimates the values of a response variable at the basis of selected principal components of the explanatory variables. PLS regression is a method for modelling relations between sets of observed variables by means of latent variables. It comprises regression and classification tasks as well as dimension reduction techniques and modelling tools [RK06].

Two constraints are imposed to discriminant analysis, CCA and PCR: firstly, factors underlying the predictor variables and the criterion variables are extracted from inner-product matrices but not their cross-product matrix; secondly, the number of observations can never be less than the minimum number of the variables. PLS regression is less restrictive since it does not have the above two constraints.

This section discusses two MLR extensions, CCA and PLS, in details and summarises the PCR method briefly.

2.7.1 Canonical Correlation Analysis

CCA is a method to correlate linear relationships between two multidimensional variables. It finds two basis vectors (bases), one for each variable, so that the projections of these variables onto the basis vectors are maximally linearly correlated. Thus the invisible correlation between two variables can be obtained by loading these two bases.

Let $X_{n\times p}$ and $Y_{n\times q}$ be mean-centred matrices of p variables and q variables over n representations. CCA seeks a pair of linear transformations w_x and w_y such that when the X and Y are projected onto w_x and w_y, respectively, the correlations between the projections (scores or canonical variates) $S_x = Xw_x$ and $S_y = Yw_y$ are maximized:

$$\begin{aligned}\rho &= \max_{\mathbf{w_x},\mathbf{w_y}} \frac{\langle S_x, S_y\rangle}{\|S_x\| \cdot \|S_y\|} \\ &= \max_{\mathbf{w_x},\mathbf{w_y}} \frac{E[w_y^T Y^T X w_x]}{\sqrt{E[w_x^T X^T X w_x] E[w_y^T Y^T Y w_y]}} \\ &= \max_{\mathbf{w_x},\mathbf{w_y}} \frac{{w_y}^T C_{xy} w_x}{\sqrt{{w_x}^T C_{xx} w_x {w_y}^T C_{yy} w_y}} \end{aligned} \tag{2.37}$$

where the maximum of ρ with respect to w_x and w_y is the maximal canonical correlation. Maximizing Equation 2.37 is subjected to the constraints ${w_x}^T C_{xx} w_x = 1$ and ${w_y}^T C_{yy} w_y = 1$. The maximization problem can be written in Lagrangian form as following:

$$L(\lambda_x, \lambda_y, w_x, w_y) = {w_y}^T C_{xy} w_x - \frac{\lambda_x}{2}({w_x}^T C_{xx} w_x - 1) - \frac{\lambda_y}{2}({w_y}^T C_{yy} w_y - 1) \tag{2.38}$$

The derivatives with respect to w_x and w_y of the Lagrangian form result in the generalized eigenproblems which can be solved by finding the eigenvalues for the correlation coefficients and eigenvectors for the scores vectors of Equations 2.39 and 2.40

$$C_{xx}^{-1} C_{xy} C_{yy}^{-1} C_{yx} w_x = \rho^2 w_x \tag{2.39}$$

$$C_{yy}^{-1} C_{yx} C_{xx}^{-1} C_{xy} w_y = \rho^2 w_y \tag{2.40}$$

The above calculations involve within-sets covariance matrices inversions, which may not be numerically stable. In order to solve the generalized eigenproblems in a robust

manner and reduce the imprecision caused by matrix inversions and multiplications, the SVD method can be used as an alterative solution. Let $X = U_x W_x {T_x}^T$ and $Y = U_y W_y {V_y}^T$; the decompositions of their covariance matrices and their cross-covariance matrix are

$$\begin{aligned} C_{xx} &= X^T X = V_x {W_x}^2 {V_x}^T \\ C_{yy} &= Y^T Y = V_y {W_y}^2 {V_y}^T \\ C_{xy} &= Y^T X = V_y W_y {U_y}^T U_x W_x {V_x}^T \end{aligned} \tag{2.41}$$

Substituting the generalized eigenproblems (Equations 2.39 and 2.40) with the Equation set 2.41, $(W^2 - \rho^2) U^T W_x {V_x}^T w_x = 0$ can be derived, where W and U are the singular values and the left singular vectors, respectively, for $U_{xy} = {U_x}^T U_y$. This equation has eigenvalues $\rho^2 = W^2$ and eigenvectors w_x obtained from the columns of $(U^T W_x {V_x}^T)^{-1} = V_x {W_x}^{-1} U$. Similarly, the canonical scores for Y can be estimated by finding the eigenvectors w_y for $(W^2 - \rho^2) V^T W_y {V_y}^T w_y = 0$.

2.7.2 Partial Least Squares Regression

The PLS regression method is a prediction technique based on correlations between two sets of variables. It projects the independent variables onto a set of weighted vectors to extract the latent vectors which are supervised by the desired response variables. It is capable of predicting a set of response variables from a set of predictor variables. This method has become a standard tool for processing a wide spectrum of problems and has been applied in medicine [SBSB93], biology [RC00], and medical imaging [AGK+04] amongst many other fields, because it comprises multiple regression, classification tasks, dimension reduction techniques and modelling tools.

PLS has many variants which can be run in Mode A and Mode B with applications to data that can be divided into two or more blocks [Wol84]. Most current work using the PLS method is based on two-block PLS when data is divided into two sets of variables (predictor variables and response variables). Its basic idea is to extract a set of orthogonal score vectors (latent vectors) that explain as much as possible of the covariance between

the two sets of variables, X and Y. The difference between Mode A and Mode B lies in the way the coefficients are updated which relates an indicator variable to its latent variable [Weg00]. In Mode A, each coefficient is computed by a simple linear model; in Mode B, coefficients are computed by a multiple regression model. In contrast to various multivariate extensions of the multiple linear regression models, PLS regression is probably the least restrictive method.

Let X denote the first block and Y the second block of variables. X is a $n \times m_x$ matrix with m_x predictor variables over n data vectors, Y is a matrix with m_y response variables over n data vectors corresponding to X's n data vectors. Both X and Y are zero-mean. Although PLS has many forms (reviewed by Rosipal and Kramer [RK06]), it generally models the relations between these two blocks by finding latent vectors from X that are also relevant for Y. The two data matrices are decomposed simultaneously as $X = TP^T + E$ and $Y = UQ^T + F$ so that the extracted latent vectors explain the maximum covariance between them. T ($T^TT = I$) and U are $n \times k$ matrices of the k latent vectors of X and Y, respectively; $P_{m_x \times k}$ and $Q_{m_y \times k}$ are the loading vectors; E and F are residuals having the same dimensions as X and Y, respectively. PLS regression selects components that give maximal reduction in the covariance E^TF instead of using the kernel method or penalties.

The latent vectors are selected as the linear combinations of the columns of X and Y on their weight vectors W and C. The first pair of latent vectors t and u are obtained from the first pair of weight vectors w and c such that $t = Xw$ and $u = Yc$, with constraints $w^Tw = 1$, $t^Tt = 1$ and t^Tu being maximal. The approximations of X based on t is subtracted from X and the iteration continues until the residual of X become a null matrix.

PLS Regression Algorithm

The classical algorithm for PLS is the nonlinear iterative partial least squares (NIPALS) algorithm which contains two iterations. The inner iteration is to calculate the latent vectors and the outer iteration is to decompose X until its residual becomes a null matrix.

The algorithm presented here is known as PLS2.

Algorithm 1 Nonlinear iterative partial least squares algorithm

1: **Initialization** $E = X$, $F = Y$, $u =$ a column vector with n random values.
2: $i = 0$.
3: $u_i = u$, $w_i = E^T u_i/({u_i}^T u_i)$.
4: $t_i = Ew_i$.
5: $c_i = F^T t_i/({t_i}^T t_i)$.
6: $u_i = Fc_i$.
7: **if** convergence **then**
8: goto 12
9: **else**
10: goto 3
11: **end if**
12: $p_i = E^T t_i/({t_i}^T t_i)$.
13: $b_i = {u_i}^T t_i/({t_i}^T t_i)$.
14: subtract the effect of latent vector t. $E = E - t_i {P_i}^T$, $F = F - b_i t_i {c_i}^T$.
15: **if** X becomes a null matrix or the algorithm meets the stopping criteria **then**
16: exit
17: **else**
18: goto 3, $i = i + 1$
19: **end if**

The proportions of the variance explained by a latent vector $t_i (i = 1, 2, ..., k)$ for X and u_i for Y are estimated by ${p_i}^T p_i/S_x$ and b^2/S_y, respectively, where S_x is the sums of squares of X and S_y of Y. When the residual matrix E becomes a null matrix, all latent vectors are found and the cumulated proportion of variance explained by these latent vectors is 100%.

Prediction

The upgraded residual matrices are defined in different ways depending on the PLS variants being used. In PLS-W2A variant [Wol84], the residual matrix of Y is upgraded as $F = F - uq^T (q = F^T u/(u^T u))$. In the PLS-SVD variant reported by Sampson *et al* [SSBB89] in the use of modelling, the outer iteration starts with upgrading $E^T F$ instead of upgrading E and F separately. Among the available variants, the PLS2 variant is used most widely.

The goal of PLS is to predict the response variables Y from the predictor variables X. The estimation of Y is $\widehat{Y} = TBC^T$ where $T = [t_1, t_2, ..., t_k]$ is the latent vector of X, B is the diagonal matrix with diagonal elements b_i $(i = 0, 1, ..., k - 1)$, and $C = [c_1, c_2, ..., c_k]$

is the weight vector of Y. Since $X = TP^T$, we have $\widehat{Y} = X(P^{T+})BC^T$. When the number of variables is greater than the number of observations, we can always have an estimated $\widehat{Y}$ being very close to the real Y (this proportion being nearly 100%). However, PLS does not necessarily give satisfactory prediction results when the regression coefficient matrix ($B_{pls} = (P^{T+})BC^T$) is applied to the new predictor variables. Statistically speaking, the common structures between a small numbers of observations are easy to derive but become difficult to describe as more observations are added.

2.7.3 Principal Components Regression

PCR is a two-step multivariate method. In the first step, PCA of the predictor data matrix $X_{n\times m}$ is performed. Assuming P_k ($k \leq m$) is the matrix of the eigenvectors corresponding to the first k eigenvalues that account for the desired variations, the important features of X have been retained by b_k, the score matrix corresponding to P_k. The second step is followed by an MLR model between the PCA scores obtained, b_k, and the criterion variables, Y.

2.8 Summary

This chapter has reviewed the bony anatomy of the primate humerus and scapula, the definitions of the shoulder bony coordinate frames, the development and methodologies of geometric morphometrics, and computational and statistical techniques applied or developed in this thesis. The crest line technique is modified in Chapter 4 to obtain the geometrical features of the bone shapes; the registration methods, SSM and the bone morphing are used in Chapter 5; multiple linear regression methods and the neighbour-conditional models are applied in Chapter 6 to understand the morphological relationships between the two shoulder bones.

Chapter 3

Data Description

3.1 Specimen Selection

The humeri and scapulae analysed in this thesis were selected within a group of primates from the osteological collection at the Natural History Museum, London. Briefly described, they are shoulder bones from nine genera of primates, including *Homo* (human): *Cebus* (Capuchin monkey), *Colobus*, *Macaca* (Rhesus monkey), *Papio* (baboon), *Presbytis* (Leaf monkey), *Pan* (chimpanzee), *Gorilla* and *Pongo* (orangutan). These genera encompass various locomotor types, such as quadrupedalism, bipedalism, and brachiation. The selection and acquisition formed a significant part of a previous thesis [Hil06] and these are described only briefly here.

3.1.1 Data Comprehension

Primates make up one of the *orders* of mammals. It can be divided informally into three main groupings: prosimians, monkeys of the New World, and monkeys and apes of the Old World. At present, monkeys and apes are believed to be genetically related to humans as our closest relatives. Scientists have learned that chimpanzees are closest related to humans with over 95% shared genes in general [Bri02], whilst gene similarities between mice and humans range from 70% to 90% with an average of 85% [CCD$^+$02].

Due to their phylogenetic proximity to humans, primates have been used in or-

thopaedic related studies of limb anatomy [SF86, Ane93], gait [Kim92, SL92] and age related bone loss [SML89, CLJ+94, JCR+94]. Kuo *et al* compared various external morphological features between adult human, *Pan* and canine femora to assess the limitations and benefits of canines and primates as the models for human total hip arthroplasty (THA) [KSB98]. They found that the large morphological differences might be biomechanically significant for interpreting stress transfer across the hip. Limited use of non-human primates in THA-related research can be attributed to the differences in locomotion and bone physiology when compared to humans. Discretion must be exercised when extrapolating experimental results using non-human models, even with primates.

Modern humans are more similar to apes in upper limb than in lower limb bony morphology [WR00]. Kimura concluded that evolutionary developments from quadrupedalism to bipedalism have caused the forelimbs of non-human primates to be primarily used for steering and braking while the hindlimbs used for support and acceleration [Kim85]. Studies have suggested that differences between hindlimbs of modern humans and apes are largely attributable to the bipedal locomotion of the former whilst differences between forelimbs can be related to the loss of habitual weight-bearing function [WR00].

3.1.2 Selection Criteria

Table 3.1 displays the collection of the non-human primates and their available information. All specimens examined have a specific catalogue identification often indicating provenance of the primate with a limited history. The collection is thought to be a significant representation of primate taxonomy [Hil06]. Apart from the described primate specimens, the datasets in this thesis also contain four *Homo* humeri, four *Homo* scapulae, and one complete articulating *Pongo* shoulder bone pair. Some of these shoulder bones in the present datasets do not have the adjoining segments. There are a total of 28 pairs of adjoining humeri and scapulae in this thesis (Table 3.2).

Species in Table 3.1 can be categorised into three groups according to their locomotor types (Table 3.3). *Papio* has the fewest locomotor types: quadrupedalism and vertical climbing; *Cebus*, *Colobus*, *Macaca* and *Presbytis* have quadrupedalism, non-vertical sup-

Species	Sex	Specimen Number	Country of Origin	Locomotor Type [a]	Segment [b]	Provenance
Cebus apella xanthosternos	N/A	1948.10.20.1	N/A	q nvc vc	S & H	Wild
Cebus apella	N/A	1948.10.20.3	N/A	q nvc vc	S & H	Wild
Cebus apella xanthosternos	N/A	1948.10.20.2	Brazil (South East)	q nvc vc	S & H	Wild
Colobus bodius kirkii	F	72.132	Zanzibar	q nvc vc	S & H	Wild
Colobus bodius tephrosceles	M	72.133	Uganda	q nvc vc	S & H	Wild
Colobus guereza kikuyuensis	M	72.134	Kenya	q nvc vc	H	Wild
Colobus guereza uellensis	F	72.153	Uganda	q nvc vc	S & H	Wild
Gorilla	M	1948.436 (Box 1 & 2)		q nvc vc br bi	S & H	Wild
Gorilla	F	1948.12.20.2 (Box 1)	French Congo	q nvc vc br bi	S & H	Wild
Gorilla	M	1948.5.4.1 (Box 1 & 3)	French Congo	q nvc vc br bi	S & H	Wild
Macaca sylavana	F	1854.3.20.1	N/A	q nvc vc	S & H	Wild
Macaca mulatta	M	30.g	N/A	q nvc vc	S & H	Wild
Macaca arctoides	M	1866.4.25.3	N/A	q nvc vc	S & H	Wild
Macaca [IRUS] rascicularis	F	1894.6.12.13	N/A	q nvc vc	S & H	Wild
Pan troglodytes	F	39.3367	Gabon	q nvc vc br bi	S & H	Wild
Pan troglodytes	N/A	1948.7.8.2	Uganda	q nvc vc br bi	S & H	Wild
Pan troglodytes	N/A	1968.6.27.1	Cameroon	q nvc vc br bi	S & H	Wild
Papio doguera	M	1862.6.26.1	Angola (Benguela)	q vc	S & H	Wild
Papio anubis furax	F	1901.8.9.23	Kenya (Baringo)	q vc	S	Wild
Papio cynocephalus	M	1962.7.6.13	Kenya (Tsaro Park)	q vc	S & H	Wild
Papio cynocephalus	M	1972.129	Kenya (Kwale, Coast Province)	q vc	H	Wild
Papio hamadryas anubis	N/A	1972.127	N/A	q vc	S & H	Wild
Presbytis obscura	N/A	1882.12.15.2	N/A	q nvc vc	S & H	Wild
Presbytis obscura	N/A	1971.721	N/A	q nvc vc	S & H	Wild
Presbytis obscura	N/A	1971.722	N/A	q nvc vc	S & H	Wild
Presbytis obscura	N/A	1971.724	N/A	q nvc vc	S & H	Wild
Presbytis obscura	N/A	1971.736	N/A	q nvc vc	S & H	Wild

[a] q - quadrupedalism; nvc - climbing with non-vertical supports; vc - vertical climbing; br - brachiation; bi - bipedalism

[b] S - scapula; H - humerus

Table 3.1: Collection of specimens used for development of the models [Hil06]. Property of Natural History Museum, London

Genus	Number of Pairs
Cebus	3
Colobus	3
Gorilla	3
Macaca	4
Pan	3
Papio	3
Presbytis	5
Pongo	1
Homo	3

Table 3.2: Number of shoulder bone pairs from the same articulations

	Group One	Group Two	Group Three
Genus	*Papio*	*Cebus* *Colobus* *Macaca* *Presbytis*	*Gorilla* *Pan*
Locomotor Types	quadrupedalism vertical climbing	quadrupedalism non-vertical climbing vertical climbing	quadrupedalism non-vertical climbing vertical climbing brachiation bipedalism

Table 3.3: Groups of locomotor types in the present dataset

port climbing and vertical climbing locomotor types; *Gorilla* and *Pan* have two additional locomotor types compared to the second group: brachiation and bipedalism. *Pongo* is primarily arboreal. Quadrupedal locomotion on the ground is rare and usually short in duration. Bipedal locomotion forms 7% of locomotion is rare. The genera used in this thesis can also be categorised using Linnean classification (taxonomy [Mye]) (Table 3.4).

In order to choose suitable specimens for morphometric analysis, a bone survey of the mammalian osseous collection at the museum was conducted and documentation of

Family	Cercopithecidae (Old World monkeys)		Cebidae (New World monkeys)	Hominidae (great apes and humans)	
Subfamily	Cercopithecinae	Colobinae	Cebinae	Homininae	Ponginae
Genus	*Macaca* *Papio*	*Colobus* *Presbytis*	*Cebus*	*Gorilla* *Pan* *Homo*	*Pongo*

Table 3.4: Linnean classification of the species

the reliability of this collection was also obtained.

To remove confounding factors due to developmental changes in morphology from analysis and to ensuing interpretation, specimens must be chosen from an extended period of relative morphological continuity within the life span of a species. Commonly, adulthood is chosen to best suit this requirement prior to a decline in old age [Kir85]. The full development of secondary sexual characteristics is often cited as proof of adulthood. Smith and Jungers have shown that it is a reliable basis for characterising adulthood [SJ97], along with epiphyseal fusion and eruption of complete permanent dentition.

Bones with previous fractures were excluded from the study. All bones in the analysis were from wild specimens with a known provenance, as zoo specimens are prone to captivity related disorders such as vitamin-D deficiency, stemming from relative inactivity and poor diet, and cage-bound trauma [Hil06]. Attention was confined to those adult specimens devoid of apparent pathology which may have altered the osteological morphology. This includes scurvy, demonstrable by observing gross curvature or deformation of the bony shaft axes.

No sex-based selection bias was used since, firstly, the sex of only a few specimens was known from field records, and secondly, previous work has demonstrated insignificant differences between male and female morphology within the same species [AOS65].

3.2 Data Acquisition

The bones previously detailed in Table 3.1, including 32 humeri and 30 scapulae, were CT scanned while mounted upon wooden rigs (Figure 3.1) in order to standardise spatial variables. Imaging parameters are as follows: slice thickness $1mm$; image matrix dimension 512×512; the in-plane resolution $0.35mm \times 0.35mm$. The outline of each bone was segmented manually using the commercial software *Amira*® (Visage Imaging of Mercury Computer Systems, Inc.) and then converted into a 3D triangulated mesh surface (see Figure 3.2 for a mesh surface example) using the marching cubes algorithm in software *Image Registration Toolkit* (Visual Information Processing Group in Imperial College London).

Decimation and smoothing were both implemented using *Amira*®.

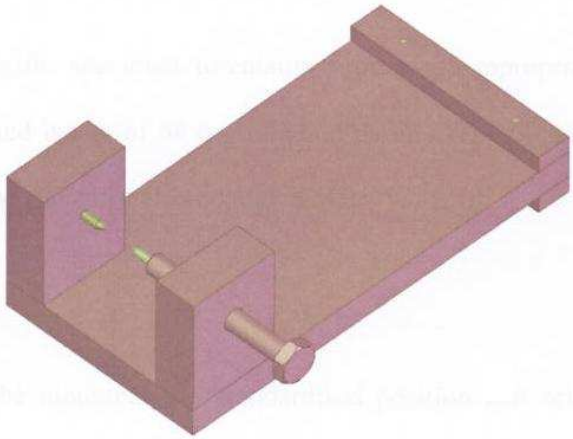

Figure 3.1: Humeral and scapular CT mounting rig [Hil06]

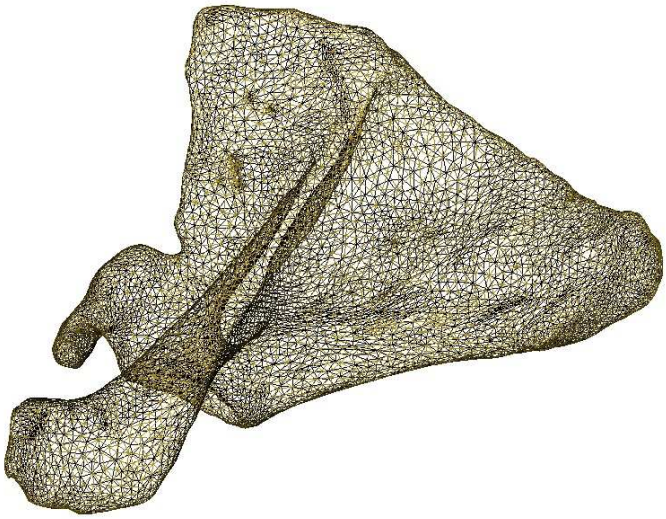

Figure 3.2: A triangulated mesh surface

The generated bone surfaces at this stage have no point-to-point correspondences across the datasets and they contain a great deal of artifacts and noise in the form of excessive surface points. Mesh decimation, which reduces redundant points, and smoothing were therefore applied to all surfaces. A comparison before the decimation and smoothing and after can be seen in Figure 3.3. In this demonstration, the decimated and smoothed scapula can be seen not to vary in morphology when the number of surface points of the

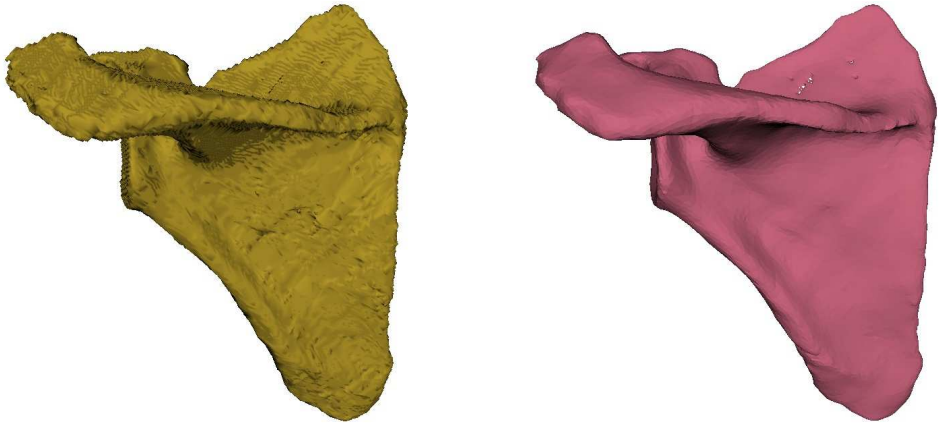

(a) Before decimation and smoothing

(b) After decimation and smoothing

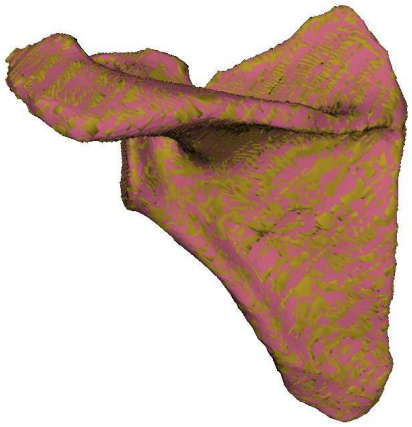

(c) Comparison between (a) and (b)

Figure 3.3: Comparison of a surface before and after decimation and smoothing. The decimated and smoothed scapula is not changed in terms of morphology.

displayed humerus was reduced significantly from 30,007 to 8,977.

Figure 3.4 displays all the 32 scanned, segmented, reconstructed, decimated and smoothed humeri in this thesis. They were aligned to the displaying position using a semi-automatic method which will be discussed in Chapter 5, Section 5.3.1. It can be seen that sizes vary largely from monkeys to great apes and humans. Although they were chosen from adulthood, there is still size difference even within the same genus. For example, the third *Macaca* humerus and the first *Gorilla* humerus are much smaller than the other humeri in their same genera.

Figures 3.5 and 3.6 show all the 30 scapulae in this thesis. Size is also a major variation from monkeys to great apes and humans. In addition, bending of the scapular spine

(a) *Cebus* (b) *Colobus* (c) *Macaca*

(d) *Papio* (e) *Presbytis* (f) *Pan*

(g) *Gorilla* (h) *Homo* (i) *Pongo*

Figure 3.4: All the humeri in the present dataset

and the shapes of the two fossae are distinct within and among the genera (for example, the infraspinous fossa difference between *Cebus* 2 and *Cebus* 3, and the supraspinous fossa difference between *Gorilla* 1 and *Gorilla* 3; the spine difference between the *Pongo* and other great apes).

3.3 Summary

In this chapter the Imperial College / Natural History Museum shoulder morphology datasets were presented. These consist of 32 humeri and 30 scapulae, 28 pairs of which are from the same shoulder articulations. Two shoulder bones from the *Pongo* were collected for this thesis, and all the remainders were collected as part of a previous thesis [Hil06]. These imaged, segmented, reconstructed, decimated and smoothed shoulder bone shapes form the dataset on which the remainder of this thesis is based.

(a) *Cebus* 1

(b) *Cebus* 2

(c) *Cebus* 3

(d) *Colobus* 1

(e) *Colobus* 2

(f) *Colobus* 3

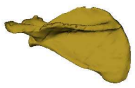

(g) *Macaca* 1

(h) *Macaca* 2

(i) *Macaca* 3

(j) *Macaca* 4

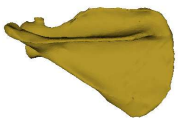

(k) *Papio* 1

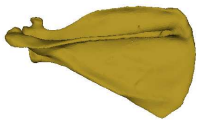

(l) *Papio* 2

(m) *Papio* 3

(n) *Papio* 4

(o) *Presbytis* 1

Figure 3.5: Scapulae in the present dataset (Part I)

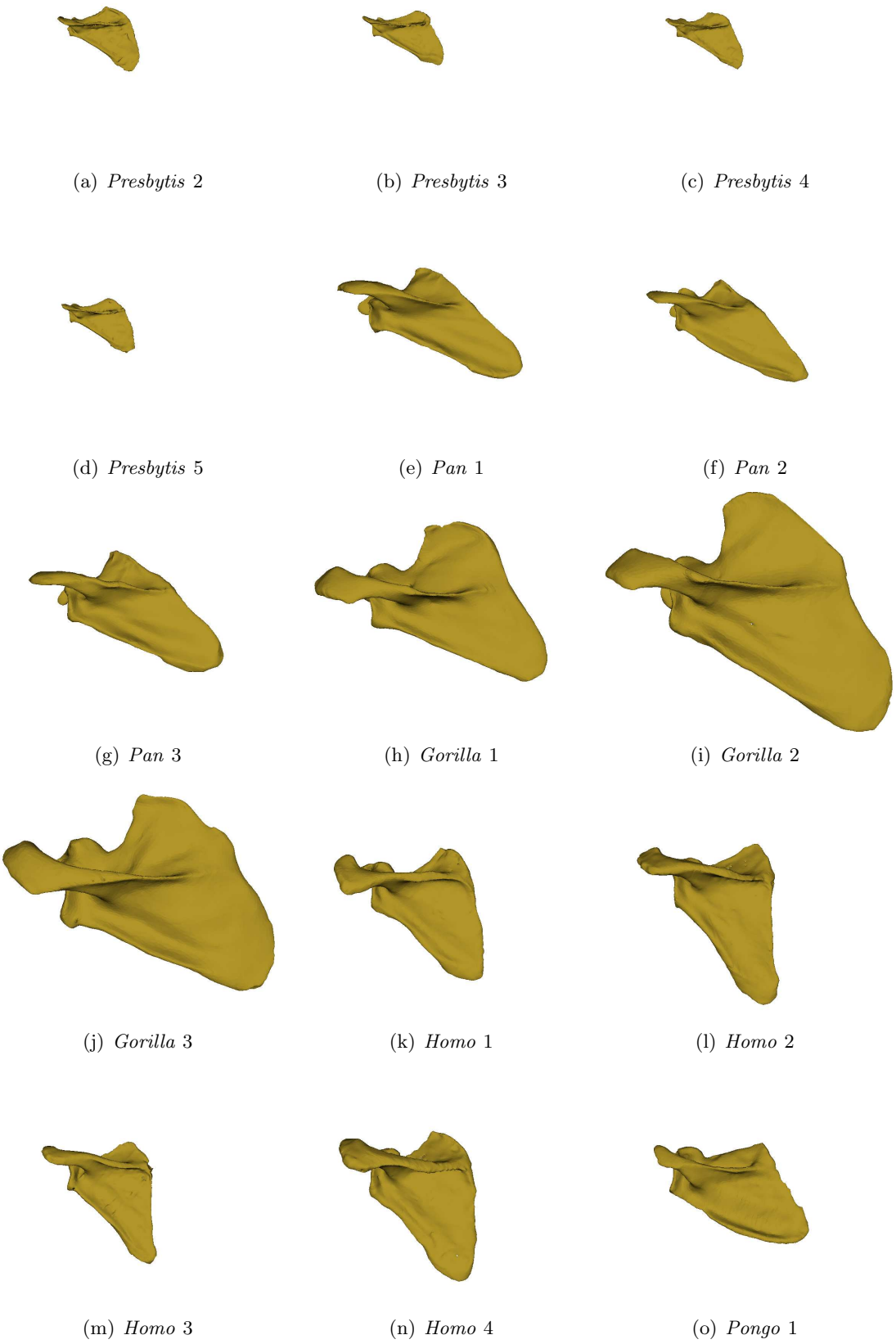

(a) *Presbytis* 2 (b) *Presbytis* 3 (c) *Presbytis* 4

(d) *Presbytis* 5 (e) *Pan* 1 (f) *Pan* 2

(g) *Pan* 3 (h) *Gorilla* 1 (i) *Gorilla* 2

(j) *Gorilla* 3 (k) *Homo* 1 (l) *Homo* 2

(m) *Homo* 3 (n) *Homo* 4 (o) *Pongo* 1

Figure 3.6: Scapulae in the present dataset (Part II)

Chapter 4

Describing Shoulder Bone Shapes and Redefinition of Local Coordinate Frames

4.1 Introduction

Shape is all the geometrical information that remains when location, scale and rotational effects are filtered out from an object (for a definition of shapes, see Section 2.4.1 in Chapter 2). Two objects that have a similar or the same shape can be matched to each other by translations, scalings and rotations. It is essential not only to identify bones that have similar shapes, but also to recognise their individual anatomical properties. For example, the shaft of the humerus varies in the degree of torsion and bending amongst the primate genera in this thesis dataset. These have played a significant role in evolutionary adaptation and development [Mil32, ISDA44]. Robust measurements of the anatomical properties can provide accurate estimation and help better understanding of shoulder bony morphology.

Mathematical landmarks according to mathematical or geometrical properties are particularly useful in shape analysis and automatic recognition. Feature lines connecting those landmarks that carry the most prominent characteristics are also called ridges.

These have numerous applications in image analysis [MB92, SF04], quality control of free-form surfaces [Hos92], human perception [HR85], analysis and registration of anatomical structures [PAT00] and non photorealistic rendering [DFS03]. Mathematical landmarks have distinctive mathematical properties and can be identified automatically.

This chapter describes the implementation designed to detect feature lines automatically using the *crest line* techniques, and presents a method to extract shape information from shoulder bones based on the extracted feature lines. Redefinitions of the local coordinate systems for shoulder bones are proposed utilising the crest line technique.

4.2 Crest Lines Extraction

Hamann proposed a sequence to compute the principal curvatures of a point $\mathbf{x}_0$ [Ham93], using the fact that a 2D surface can locally be represented explicitly. The principal curvature calculation here is based on Hamann's sequence, in combination with, and with modification of, some of the approaches that are involved in the crest line technique. Implementations of the two main steps in the sequence, including the calculation of local surface normals and the approximation of bivariate polynomials, were improved by applying more sophisticated and more stable methodologies, which were developed in other techniques (details will be explained in Section 4.2.1).

Crest points can be classified after calculating the principal curvatures for each surface point. Computational details were explained in Chapter 2, Section 2.3.2. The discrete crest points were linked to form the crest lines, and short line branches were truncated as noise. These two steps were implemented using different methods proposed by different authors (a review in Chapter 2, Section 2.3.2). Among those methods, this thesis utilises and combines the methods that provide the best results for the present datasets. The implementation details will be described in Section 4.2.2.

To sum up, Figure 4.1 demonstrates the procedure for extracting crest lines.

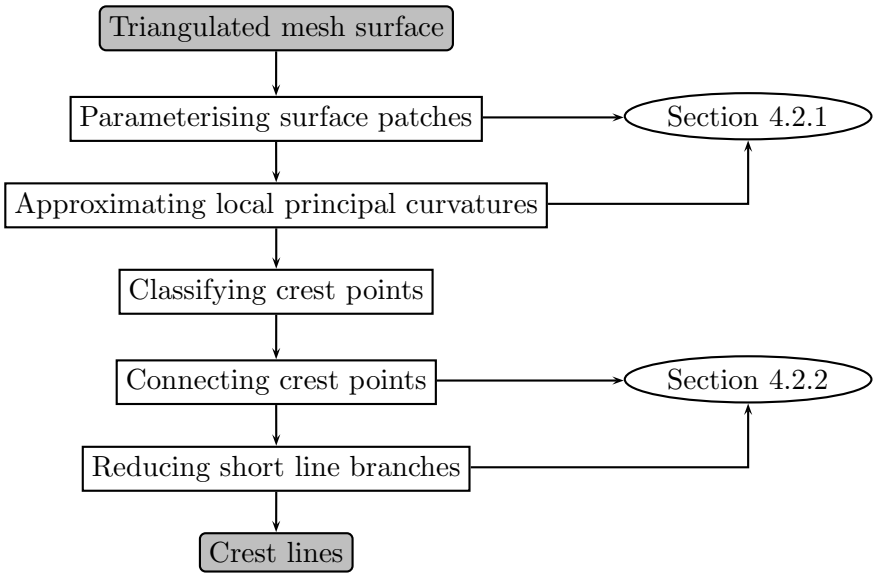

Figure 4.1: Flowchart of the extraction of crest lines

4.2.1 Approximating Principal Curvatures

The computational sequence resembling Hamann's sequence to calculate the principal curvatures is listed below:

- Determine the platelet points (first-order neighbours) associated with point $\mathbf{x}_0$ (black solid points in Figure 4.2(a)).
- Compute the plane, P, passing through point $\mathbf{x}_0$ and with normal $\mathbf{n}_0$, where $\mathbf{n}_0$ is the normal of the surface patch formed by point $\mathbf{x}_0$ and its platelet points (also called the normal of vertex $\mathbf{x}_0$).
- Define an orthogonal coordinate system in plane P, with $\mathbf{x}_0$ as its origin and two arbitrary orthogonal unit vectors. The graph of a fitted bivariate polynomial is independent of the orientation of the two unit vectors which determine the coordinate system of the plane.
- Compute the distances of all platelet points from plane P.
- Project all platelet points onto plane P and calculate their projections with respect

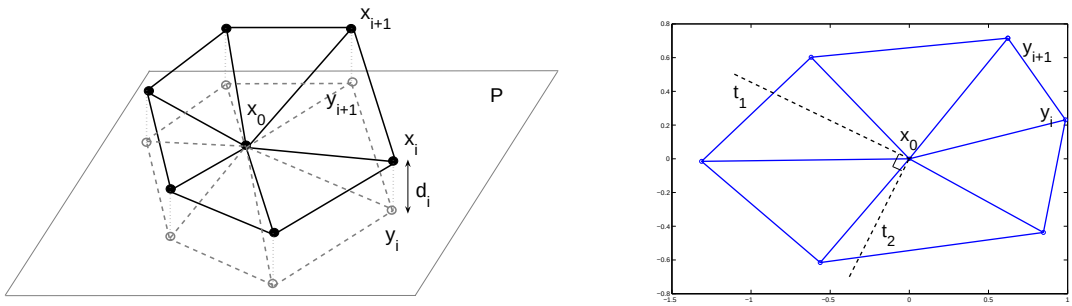

(a) Projecting the platelet points to the tangent plane (b) Projection on the tangent plane

Figure 4.2: Demonstration of constructing a bivariate polynomial for the platelet points in a patch of the triangulated mesh surface

to the orthogonal coordinate system in plane P.

- Interpret the projections in plane P as abscissae values and the distances of the original platelet points from plane P as ordinate values. Construct a bivariate polynomial f approximating these ordinate values.

- Compute the principal curvatures at each platelet point $\mathbf{x}_i$ using the bivariate polynomial.

Assuming there are n first-order neighbours of point $\mathbf{x}_0$, the platelet points are denoted as $\mathbf{x}_i = \{\mathbf{x}_1, \mathbf{x}_2, \cdots, \mathbf{x}_n\}$, and their projections on plane P are denoted as $\mathbf{y}_i = \{\mathbf{y}_1, \mathbf{y}_2, \cdots, \mathbf{y}_n\}$. The implicit equation for plane P is thus written as

$$\mathbf{n}_0 \cdot (\mathbf{y} - \mathbf{y}_0) = n_x(x - x_0) + n_y(y - y_0) + n_z(z - z_0) = 0 \tag{4.1}$$

The projection $\mathbf{y}_i$ of $\mathbf{x}_i$ is estimated as $\mathbf{x}_i - d_i\mathbf{n}_0$, where d_i is the distance between $\mathbf{x}_i$ and $\mathbf{y}_i$. d_i equals to $(n_x x_i + n_y y_i + n_z z_i + D)/\sqrt{n_x^2 + n_y^2 + n_z^2}$, where $D = -(n_x x_0 + n_y y_0 + n_z z_0)$. An arbitrary vector $\mathbf{a}_1$, lying on plane P and perpendicular to normal $\mathbf{n}_0$, is first calculated as one of the orthogonal vectors on plane P. It can be obtained by one

of the following three possibilities:

$$\mathbf{a}_1 = \begin{cases} (-(n_y + n_z), n_x, n_x)^T / n_x, & n_x \neq 0 \\ (n_y, -(n_x + n_z), n_y)^T / n_y, & n_y \neq 0 \\ (n_z, n_z, -(n_x + n_y))^T / n_z, & n_z \neq 0 \end{cases} \tag{4.2}$$

The normalisation of $\mathbf{a}_1$ forms the first unit basis vector $\mathbf{b}_1$. Consequently, the second unit basis vector $\mathbf{b}_2$ is defined as the cross product of $\mathbf{n}_0$ and $\mathbf{b}_1$. Now that we have $\mathbf{x}_0$ as the origin, $\mathbf{b}_1$ and $\mathbf{b}_2$ as the two unit basis vectors of a local orthogonal coordinate system on plane P, the local coordinates $(u_i, v_i)^T$ of a point $\mathbf{x}_i$ in terms of $\mathbf{b}_1$ and $\mathbf{b}_2$ is

$$(u_i, v_i)^T = (\mathbf{d}_i \cdot \mathbf{b}_1, \mathbf{d}_i \cdot \mathbf{b}_2)^T \tag{4.3}$$

where $\mathbf{d}_i = \mathbf{y}_i - \mathbf{x}_i$ is the difference vectors between points $\mathbf{y}_i$ and point $\mathbf{x}_i$.

Normal Calculation for a Surface Patch

Construction of the tangent plane, P, of a surface patch is sensitive to the calculation of its normal vector, $\mathbf{n}_0$. Different normal vectors will consequently result in different projections $(u_i, v_i)^T$ on the plane as well as the distances d_i. A vertex normal is usually taken as a weighted sum of the normals of the adjacent triangles (or facets sharing that vertex). Gouraud suggested equal weights [Gou71]; Thurmer and Wuthrich suggested weighting by the facet angles at the vertex [TW98]; Max proposed a set of weights depending on size of the facets [Max99]. Figure 4.3 compares the projections on the tangent plane defined by the normal vectors calculated using Gouraud's method (Figure 4.3(a)) and Max's method (Figure 4.3(b)). The latter method, with the weight for facet i estimated as Equation 4.4, is used in the present work.

$$w_i = sin(\alpha_i)/(|V_i||V_{i+1}|) \tag{4.4}$$

where V_i is the vector between vertex $\mathbf{x}_0$ and platelet point $\mathbf{x}_i$, α_i is the angle between vector V_i and vector V_{i+1}.

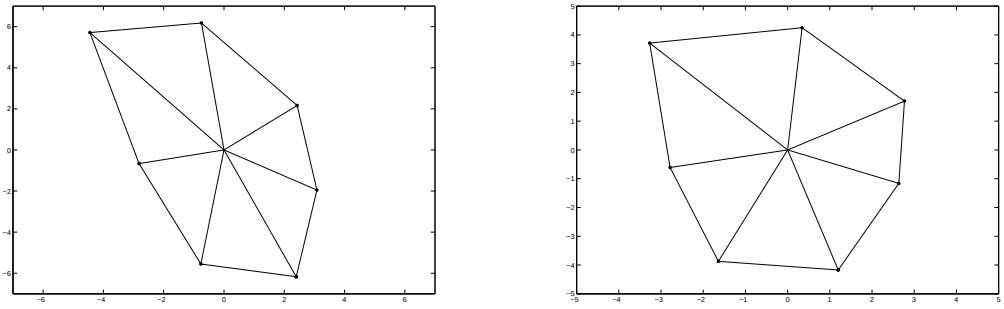

(a) Equal weights (b) Weighted by size

Figure 4.3: Platelet points projected on the tangent plane

Smoothness of a surface largely affects the normal calculation and, consequently, the crest point classification. All surfaces analysed in this thesis were smoothed using the commercial software *Amira*®.

Normal Cubic Approximation Method

Methods for calculating and approximating curvatures affect the classification of crest points. Therefore, appropriate calculations of a local surface normal and a parameterisation of a surface patch are essential. Three methods approximating principal curvatures and principal directions are compared by Goldfeather and Interrante [GI04], including the normal curvature approximation method, the quadratic surface approximation method, and the adjacent normal cubic approximation method which can be further extended to higher order methods. The construction of the corresponding Gauss-Weingarten map (Equation 2.12, page 35) in the present work utilises the adjacent normal cubic approximation method, which fits a surface patch to a platelet point set using the approximation function f:

$$f(u,v) = \frac{A}{2}u^2 + Buv + \frac{C}{2}v^2 + Du^3 + Eu^2v + Fuv^2 + Gv^3 \tag{4.5}$$

The normal vector to the surface patch is given by

$$\begin{aligned} N(u,v) &= (f_u(u,v), f_v(u,v), -1) \\ &= (Au + Bv + 3Du^2 + 2Euv + Fv^2, Bu + Cv + Eu^2 + 2Fuv + 3Gv^2, -1) \end{aligned} \tag{4.6}$$

Assuming that a platelet point (u_i, v_i, d_i) $(i = 1, 2, \cdots, m)$ has a normal vector (n_{ui}, n_{vi}, n_{di}) in the local coordinate system, we can rewrite the normal vector as $(-\frac{n_{ui}}{n_{di}}, -\frac{n_{vi}}{n_{di}}, -1)$. The linear equation to be solved is thus

$$\begin{pmatrix} \frac{1}{2}u_1^2 & u_1v_1 & \frac{1}{2}v_1^2 & u_1^3 & u_1^2v_1 & u_1v_1^2 & v_1^3 \\ u_1 & v_1 & 0 & 3u_1^2 & 2u_1v_1 & v_1^2 & 0 \\ 0 & u_1 & v_1 & 0 & u_1^2 & 2u_1v_1 & 3v_1^2 \\ & & & \vdots & & & \\ \frac{1}{2}u_m^2 & u_mv_m & \frac{1}{2}v_m^2 & u_m^3 & u_m^2v_m & u_mv_m^2 & v_m^3 \\ u_m & v_m & 0 & 3u_m^2 & 2u_mv_m & v_m^2 & 0 \\ 0 & u_m & v_m & 0 & u_m^2 & 2u_mv_m & 3v_m^2 \end{pmatrix} \begin{pmatrix} A \\ B \\ C \\ D \\ E \\ F \\ G \end{pmatrix} = \begin{pmatrix} n_{d1} \\ -\frac{n_{u1}}{n_{d1}} \\ -\frac{n_{v1}}{n_{d1}} \\ \vdots \\ n_{dm} \\ -\frac{n_{um}}{n_{dm}} \\ -\frac{n_{vm}}{n_{dm}} \end{pmatrix} \tag{4.7}$$

The Gauss-Weingarten map W (Equation 4.8) can be produced using the values A, B and C calculated from the above linear equation (see Equation 4.8 for the calculation of the Gauss-Weingarten map). Once the eigenvalues of matrix W are calculated, eigenvectors corresponding to the largest and second largest eigenvalues, $\mathbf{t}_1$ and $\mathbf{t}_2$, can be estimated for the purposes of crest point classification and crest line linkage.

$$W = \begin{pmatrix} A & B \\ B & C \end{pmatrix} \tag{4.8}$$

4.2.2 Crest Point Classification and Tracing

Generally speaking, the crest points identified are surface points that have strong local curvatures. Although the surfaces of the shoulder bones were smoothed before calculating surface curvatures, noise and irregularities of the triangulated mesh surfaces still play an important role in the calculation. Some points were identified as crest points that do not

represent any prominent characteristics on a surface. However, some points lying on the feature lines were not classified as crest points. To solve these problems, region growing followed by a skeletonisation was performed. A line tracing algorithm to connect all the skeleton points was developed. Short line segments and single points, with a small weight under a defined threshold, were pruned as noise.

Region Growing

Region growing is able to implicitly connect many of the unconnected crest points to create *crest regions*. If a crest point is grown with its k^{th} order of neighbourhood, it means that all points within the k-link neighbourhood would be classified as a crest point in the crest region.

Skeletonisation

Skeletonisation (or *Medial Axis Transformation*) is the procedure to extract a region-based shape feature representing the general form of an object. The extent and connectivity of the original regions are preserved whilst the *foreground* regions are thrown away. There are three major skeletonisation techniques: detecting ridges in distance map of the boundary points, calculating the Voronoi diagram generated by the boundary point, and the layer-by-layer erosion called *thinning*. Rossl *et al* presented a method to determine the skeleton of the feature regions by morphological operators [RKS00].

All surface points of a bone are assigned binary values, with 1 denoting crest points and 0 otherwise. A surface is thus represented by a feature vector $F \in \{0,1\}^N$ containing N vertices. Let $v_i \in F$ be any of the vertices with m_i neighbour vertices $(u^i_\mu)^{\mu=m_i-1}_{\mu=0}$ ordered clockwise, v_i is defined as *complex* if $F_i = 1$ and $c_i \geq 4$, where c_i is the complexity of v_i defined as

$$c_i := \sum_{\mu=0}^{\mu=m_i-1} |F_{u^i_\mu} - F_{u^i_{(\mu+1)mod(n_i)}}| \tag{4.9}$$

v_i is said to be a *centre* if $F_i = 1$ and all its neighbour vertices $(u^i_\mu)^{\mu=m_i-1}_{\mu=0}$ have value 1. Neighbour vertices surrounding the centres are defined as *disk* if they themselves are not

centres. With the above definitions, the skeletonisation operator is thus defined as

$$skeletonise(F) := \mathcal{F} \backslash (\bigcirc \cap \overline{C \cup \odot}) \tag{4.10}$$

$\mathcal{F}$ is an alternative notation for the feature vector F with definition $\mathcal{F} := \{i \in \{1, \cdots, N\} | F_i = 1\}$; $C \in \mathcal{F}$ is the set of all complex vertices; $\bigcirc \in \mathcal{F}$ is the union of all disks and $\odot \in \mathcal{F}$ is the union of corresponding centres. The skeletonisation is an iterative procedure. With every iteration of the operator, the outmost layer is scratched off from the feature regions except for complex vertices. The complex vertices, the disks and the centres have to be recalculated in each iteration. The procedure iterates until the feature vector remains unchanged.

Line Tracing

Region growing and a skeletonisation only provide point clouds without point-to-point linkage. The next step is to connect all those obtained skeleton points.

Some algorithms connecting all available crest points have been proposed but these do not consider any geometrical property [SF03, OBS04, YBS05]. More sophisticated methods have been suggested, such as the use of minimum spanning tree (MST) [PK03, SC05] and principal directions [KK06]. The idea of the MST method is to assign three types of weights to all edges connecting any two vertices. The edges with the smallest weight are forced to form the spanning tree, which will be used to represent the crest lines. This method does not take the local curvatures into account, and the weights are determined empirically.

In this thesis, the method using principal directions, suggested by Kim [KK06], was applied to link the skeleton points. Assuming the crest points are skeletonised, Algorithm 2 explains the implementation details of defining directions of the discrete skeleton points. The direction of a skeleton point is the index of the next skeleton point on the same line. Once the linkage of the skeleton points are defined, crest lines can be extracted. Algorithm 3 shows the pseudo-code of tracing crest lines using the defined directions.

Algorithm 2 Defining the tracing directions of the skeleton points

Initialisation: create an N dimensional vector D. Its initial values are -1. N is the number of surface points.
for each surface point v^i **do**
  calculate the number of feature points (n^i) that are adjoining to v^i
  if there is only one adjoining feature point ($n^i == 1$) **then**
    set the direction pointing to this feature point: $D[i] = j$ (j is the index of this feature point)
  else if there are at least two adjoining feature points ($n^i \geq 2$) **then**
    obtain minimum principal direction t_2^i
    for each adjoining feature point u^j **do**
      calculate the dihedral angle θ_j between edge $|v^i - u^j|$ and t_2^i
    end for
    get the smallest dihedral angle $\theta_\sigma = \min\{\theta_j\}$
    set the direction pointing to the adjoining feature point with θ_σ: $D[i] = \sigma$ (σ is the index of this feature point)
  else
    do nothing
  end if
end for

Algorithm 3 Tracing the discrete skeleton points to form crest lines

for each surface point v^i **do**
  Initialisation: $traceID = D[i]$ (D is the N dimensional vector defined in Algorithm 2)
  if v^i is a feature point && v^i is not visited && its next point is not pointing at itself **then**
    create a line starting with v^i
    while there is point to trace ($traceID! = -1$) **do**
      if there is a line starting with $v^{traceID}$ **then**
        append this line to the current line starting with v^i
        set point $v^{traceID}$ as *visited*, and clear the line starting with $v^{traceID}$
        stop the while loop (let $traceID = -1$)
      else
        append point $v^{traceID}$ to the line starting with v^i
        set point $v^{traceID}$ as *visited*
      end if
    end while
  end if
end for

Thresholding for Simplification

To clear small line segments, a threshold that considers both curvatures κ_{max} and the lengths of the crest lines l is set [KK06]. It is defined as

$$T = \frac{1}{l} \sum_{i=1}^{l} |v_{i+1} - v_i|^2 \kappa_{max}(v_i) \quad (1 \leq i \leq l) \tag{4.11}$$

Lines having a smaller T than the pre-defined threshold, $\mathcal{T}$, are truncated.

4.2.3 Results

Figure 4.4 shows the extracted crest points on a *Homo* humerus, with a threshold $\epsilon = 0.01$ (refer to page 36, Chapter 2, for definition of ϵ); Region growing was performed with second-order neighbourhood, and the skeleton (shown in blue) was obtained from these grown surface points, which are in red. Figure 4.5(a) illustrates the linkage directions of the discrete skeleton points on the distal *Homo* humerus, which were obtained by using Algorithm 3. Figure 4.5(b) illustrates the crest lines extracted after thresholding (the threshold for truncating line fractions is $\mathcal{T} = 1.5$).

Figure 4.6 shows the extracted crest lines from a *Homo* scapula. The threshold determining a crest point is 0.01; region growing expands to first-order neighbourhood; the threshold for truncating line fractures is $\mathcal{T} = 1.5$.

Figures 4.4 to 4.6 show that the extracted crest lines are able to capture the loci of the surface where there are anatomical meanings, such as the medial edge of the trochlea and the two epicondyles on a humerus, and the glenoid rim and the three borders on a scapula.

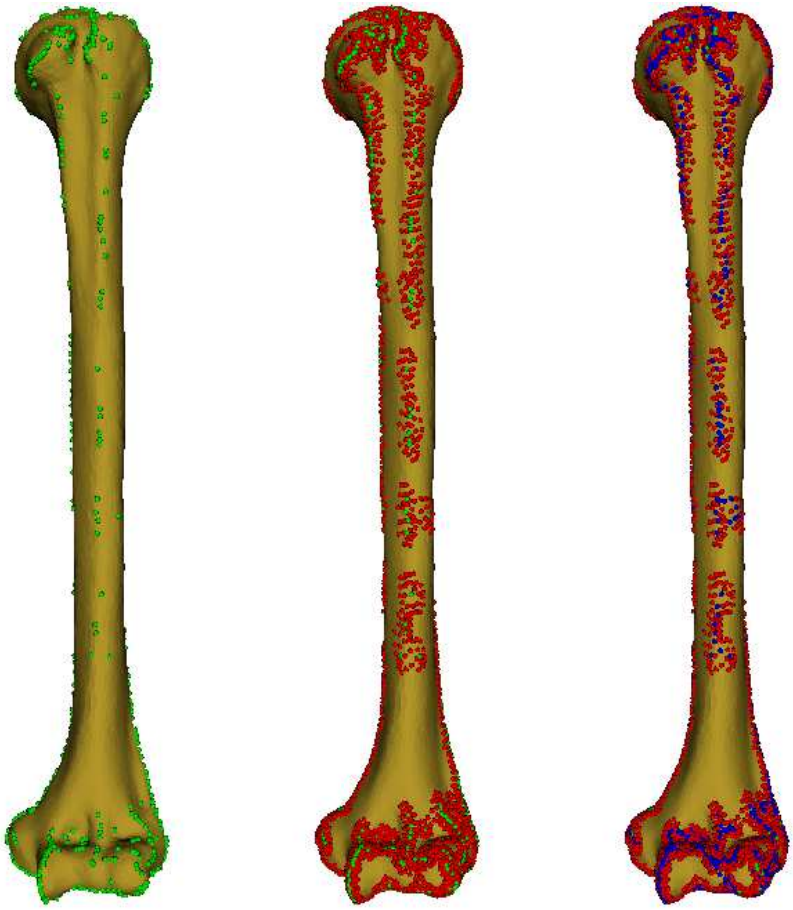

(a) Crest points

(b) Region growing (to second-order neighbourhood)

(c) Skeleton (in blue)

Figure 4.4: The skeleton on a *Homo* humerus surface

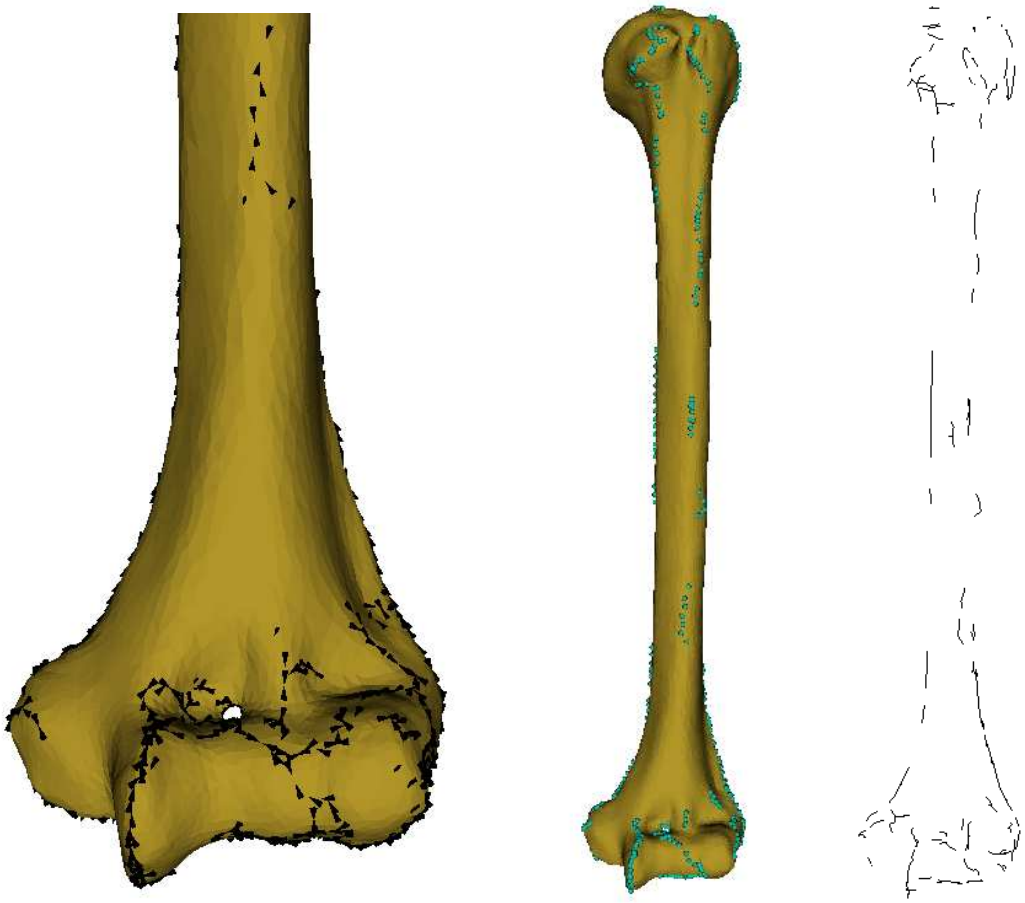

(a) Directions (pointed by arrow marks) of skeleton points on the distal *Homo* humerus

(b) Extracted crest lines shown in points (left) and shown in lines (some lines on the right figure are invisible on the left figure because they lie on the other side of the humerus)

Figure 4.5: Connecting crest lines from the discrete crest points on a *Homo* humerus

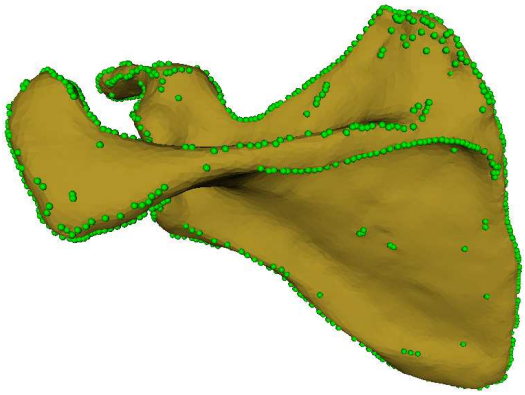

(a) Crest points

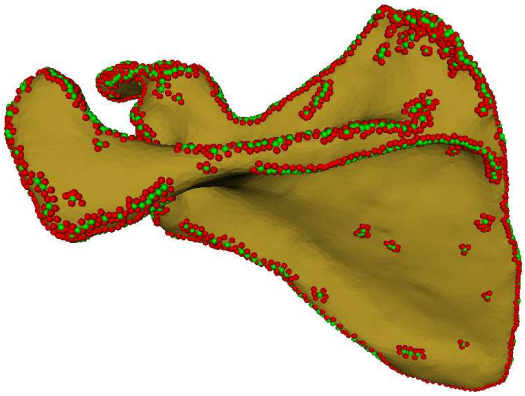

(b) Region growing (to first-order neighbourhood)

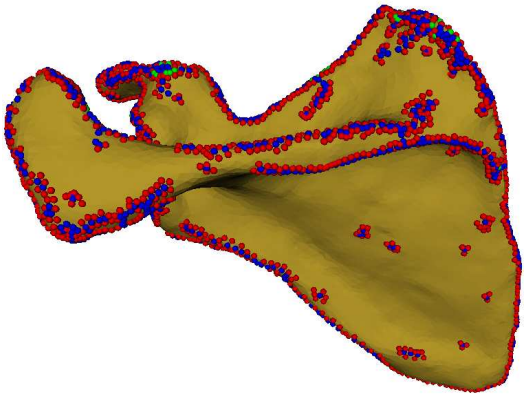

(c) Skeleton

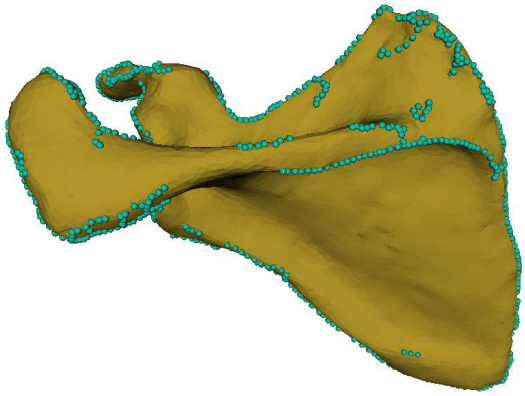

(d) Crest lines shown in points

(e) Crest line set (some lines on this sub-figure are invisible in (d) because they lie on the other side of the scapula)

Figure 4.6: Extracted skeleton on a *Homo* scapula, the linkage of the skeleton points, and the crest lines constructed

4.3 Geometrical Variation of the Humerus

Some morphological features of the humeri are very different with great visual variations in the presented datasets, for example bending of the humerus shaft and torsion between the humeral head and the trochleae. However, these variations are difficult to measure and to quantify. An automatic and stable method that involves little manual intervention is proposed in this section. This reduces variability that is induced by the measurement procedure.

4.3.1 Bending and Torsion

In the literature, the shaft of the human humerus is always described by an axis passing through the humeral shaft. This measurement ignores the bending of the humerus and, therefore, is less accurate for, and is not applicable to, the humeri from non-human primates, which have much greater bending (Figure 4.7). Two axes, L_{h1} and L_{h2}, were defined, one approximating the proximal humeral shaft and the other approximating the distal humeral shaft. The angle between the two axes is considered as the degree of bending. The grey line in Figure 4.8 is obtained from the humeral shaft to approximate the long axis of the humeral shaft; the two black lines are the two redefined axes, L_{h1} and L_{h2}. Angles can be seen between the grey line and the black lines and the angles become larger on non-human primate humeri. These angles can be also used to measure proximal and distal bending on a humerus.

If the humeral heads of the different genera are fixed in a certain position, the positions of their trochlea and capitulum do not remain the same (Figure 4.9). Hertel measured retrotorsion by projecting a humerus onto a equatorial plane [HK02]. The orientation difference between the humeral head and the axis through the trochlea and the capitulum was measured to describe torsion.

The axis through the trochlea and the capitulum was defined differently according to different circumstances. Functionally speaking, the trochlea is sometimes considered as a spiral and its spiral orientation allows flexion and extension about an oblique axis,

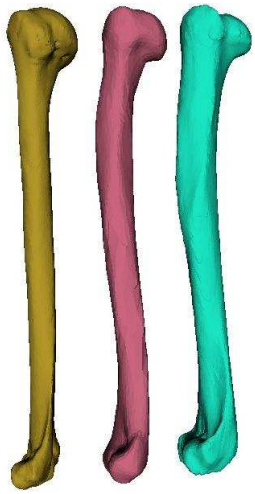

Figure 4.7: Differences in bending of three scaled humeri. From left to right: *Homo*, *Colobus* and *Papio*.

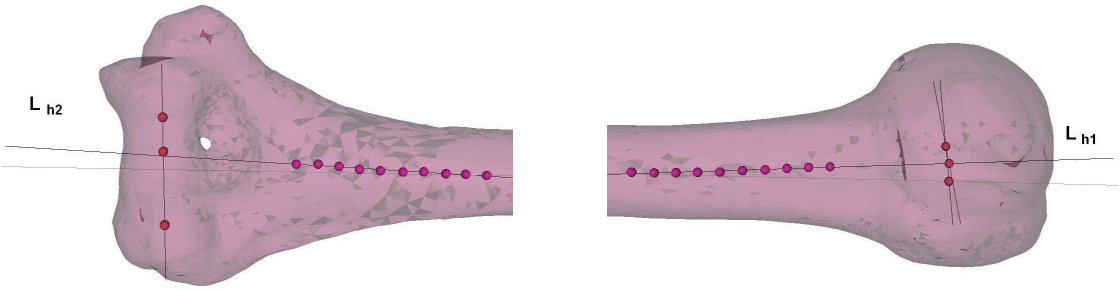

(a) Distal segment (b) Proximal segment

Figure 4.8: Distal axis (L_{h2}) and proximal axis (L_{h1}) on a *Homo* humerus. They were fitted to the two point sets in the humeral shaft.

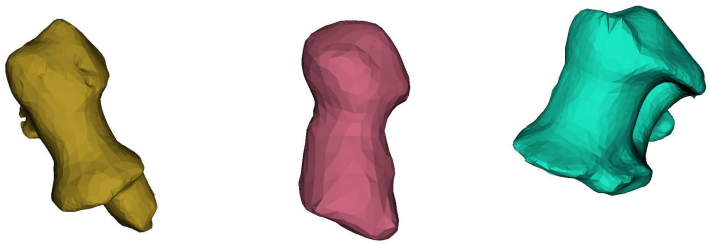

(a) *Homo* (b) *Colobus* (c) *Papio*

Figure 4.9: Transverse view of three humeri with their humeral heads fixed in a certain position

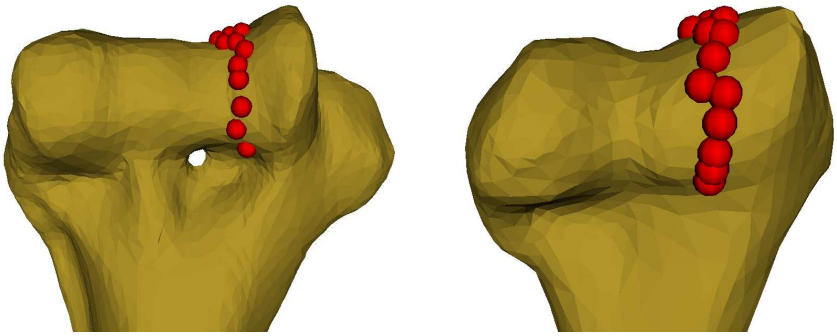

(a) *Homo* (b) *Colobus*

Figure 4.10: Manually selected surface points on the trochlea

which brings the forearm from a position parallel to the humerus in full flexion to a valgus carrying angle of 15° in extension [RPW05]. In fact, the direction of the axis of flexion and extension changes progressively between the two extreme positions of flexion and extension [Kap82]. Some authors simply define the humeroulnar joint as a hinge joint with a rotation axis passing through the medial epicondyle and the lateral epicondyle [WvdHV$^+$05, OL07]. The humerus is articulated by the radius and the ulna at the trochlea and the capitulum, it is intuitively more suitable to approximate the rotation axis using the trochleae and the capitulum instead of simply connecting the epicondyles. Since this thesis is focussed on the description of morphology of a humerus as a whole and the validation of the shape prediction method (the prediction model will be explained in Chapter 6) rather than finding a mechanical way to describe elbow function, the axis of flexion and extension is defined as one fixed axis through the trochlea instead of an oblique axis.

The rotation axis of the elbow joint is sometimes defined as a line that passes through the centre of the capitulum and the centre of the deepest points on the trochlea (these deepest points form a concave ring on the trochlea) [DDKJ03]. To construct this axis, a plane P was firstly fitted using the manually selected surface points on the concave area on the trochlea (Figure 4.10(a)) and a circle was then fitted to the projections of these surface points on the plane P. However, the monkey humeri do not have this concave ring. A comparison between a *Homo* trochlea and a *Colobus* trochlea can be seen in Figure 4.10. The points on both bones were labelled manually to approximate the trochlea rings.

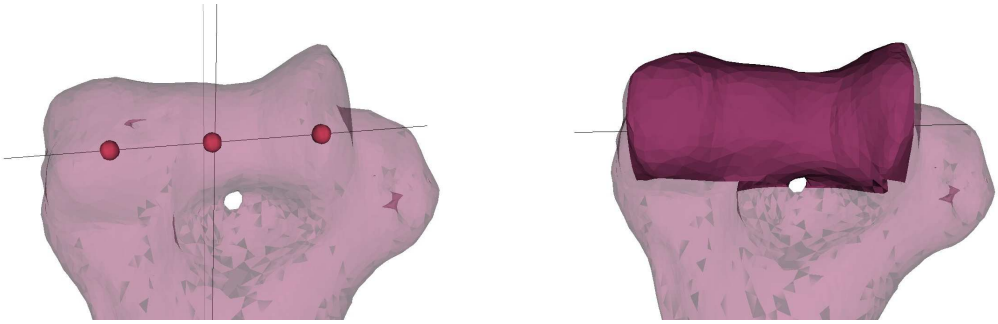

(a) Method one (b) Method two

Figure 4.11: Two methods defining the rotation axis of the elbow joint

To obtain the rotation axis in a stable way, two methods were proposed. Method one is similar to Dunning's method [DDKJ03]. It fits a sphere to the capitulum and a circle to the medial edge of the trochlea instead of the deepest points on the trochlea (Figure 4.11(a)). The rotation axis is defined as that which passes through the centre of the sphere fitted to the capitulum and the centre of the circle fitted to the medial edge of the trochlea. Method two considers the whole hinge area by fitting a cylinder to the region combined by the trochlea and the capitulum (the area with darker colour in Figure 4.11(b)). The medial axis of the cylinder is calculated as the rotation axis.

4.3.2 Methodology

Figure 4.12 is a flowchart demonstrating how to obtain the geometrical parameters (e.g. size of the humeral head) and the anatomical axes on the distal humerus.

To fit a sphere to the humeral head, manual selections of a few seed points were conducted. The seed points are grown with a certain degree of neighbourhood to cover the region of fitting using region growing. The degree of growing was determined so that the grown points cover as much of the region of interest as possible. Figure 4.13(a) shows the selected seed points and their grown points. The centre of the sphere fitted to the grown points can be calculated.

To obtain the rotation axis on the distal humerus, by method one - sphere and circle fitting - two centres should be calculated to form the axis on the distal humerus. A least

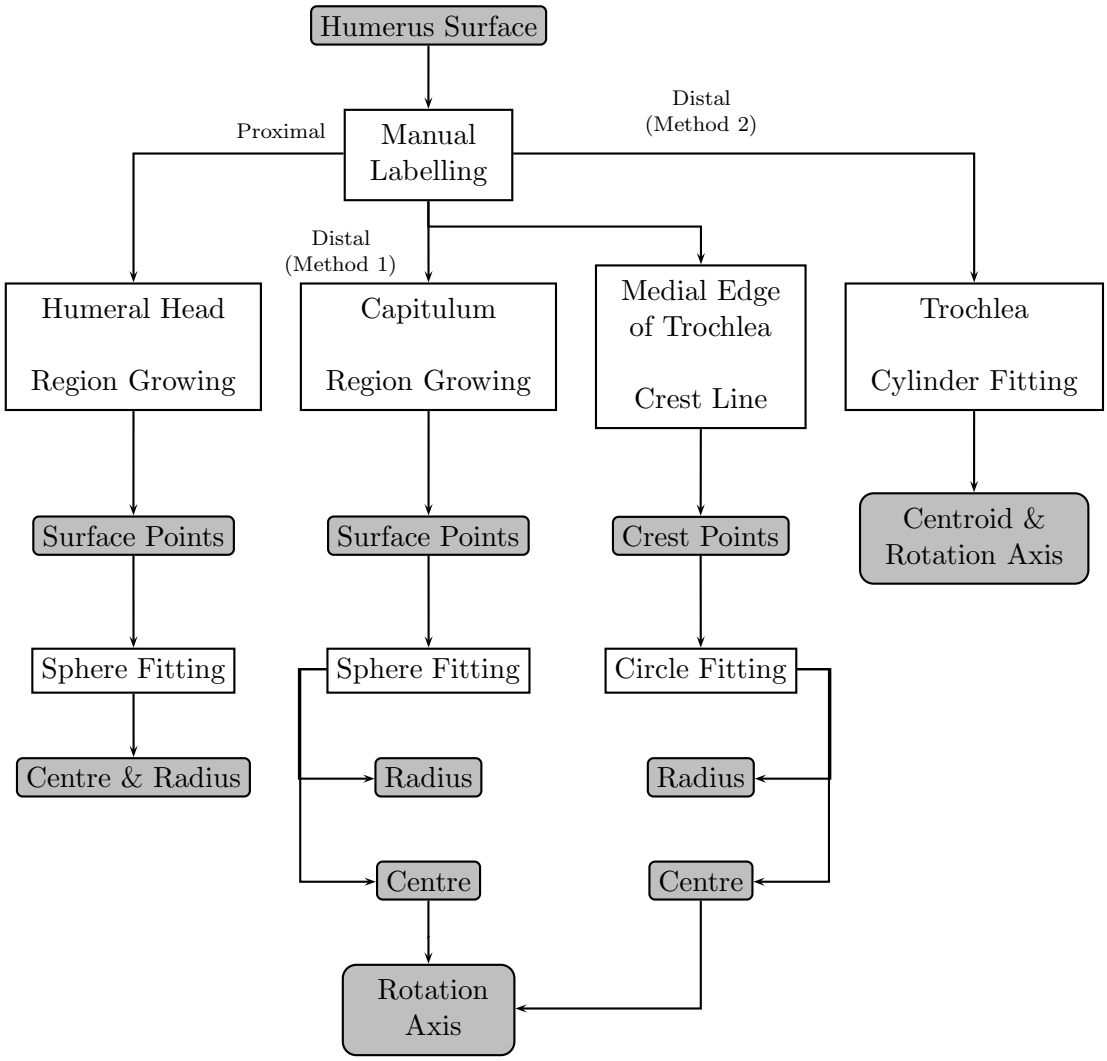

Figure 4.12: Obtaining the centre and size of the humeral head, and the rotation axis on the distal humerus

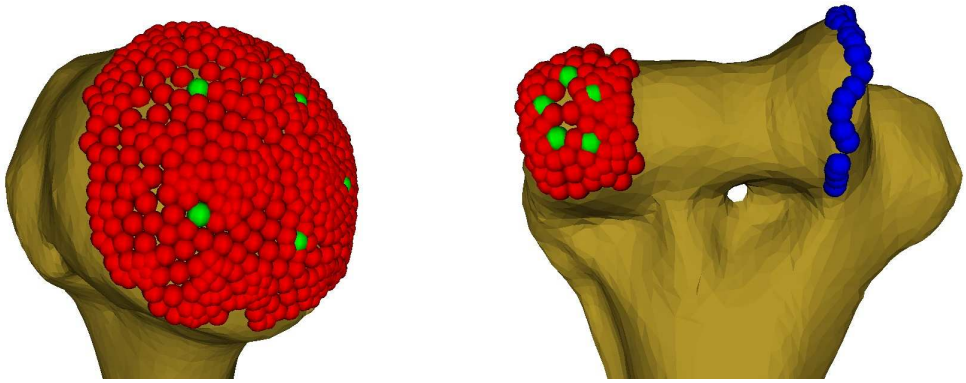

(a) Five seed points on the humeral head (in green); five degrees of region growing.

(b) Five seed points on the capitulum (in green); three degrees of region growing. Blue points are the crest line on the trochlea.

Figure 4.13: Selected seed points and their grown surface points

square best-fit sphere was firstly fitted using the grown points on the capitulum (Figure 4.13(b)) and the centre of the fitted sphere was obtained as one point defining the axis. A least square best-fit plane was then fitted to the nodes on the extracted crest lines on the trochlea. Points lying on the edge of the trochlea in Figure 4.13(b) are the nodes of crest lines extracted in this area, with parameters $\epsilon = 0.01$, first-order neighbourhood for region growing and $\mathcal{T} = 1.5$. These automatically-extracted crest points are able to capture anatomical features accurately such that manual labelling is not required. Projections of the nodes onto the plane were fitted by a least square best-fit circle, and the centre of the circle was obtained as another point defining the rotation axis.

Alternatively, by method two - cylinder fitting, the region of interest (the area of darker colour in Figure 4.11(b)) was clipped manually using the open source software *ParaView* and the axis was approximated by the medial axis of the cylinder fitted to the area of interest. Instead of fitting a cylinder using a least square method, principal component analysis (PCA) was applied to initiate the axis through the centre of the clipped surface. The medial axis construction method here is similar to the method to approximate the long axis through the humeral shaft, which will be described in the following paragraphs. The initial axis was further refined using another PCA based on the extracted centre points through the cylinder.

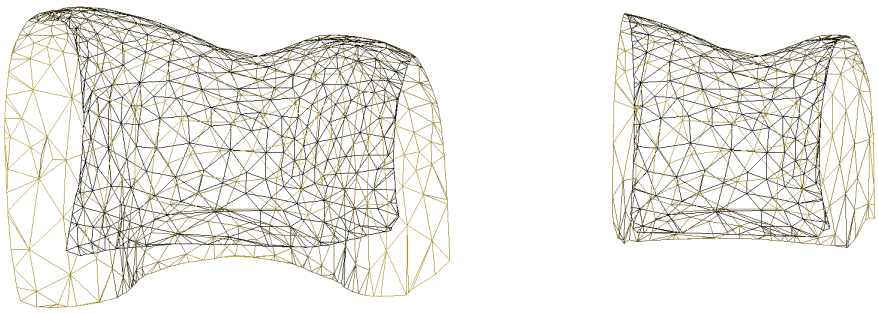

(a) Two surfaces clipped from a *Colobus* humerus

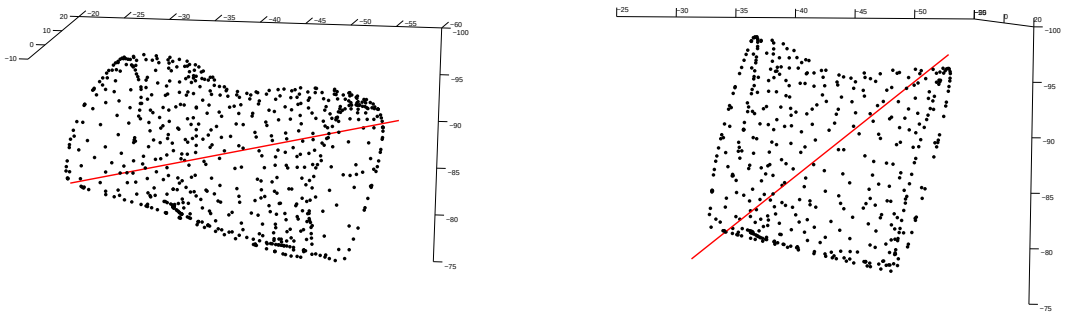

(b) Principal axes of the surface points (obtained using PCA)

Figure 4.14: Two clipped surfaces

A critical issue of the cylinder fitting method is that the cylinder has to be clipped in a way such that the principal axis of its surface points traverses through the centre of the cylinder. If the height of the clipped cylinder is not long enough, the principal axis constructed by PCA is unlikely to lie along the median of the cylinder. An example can be seen in Figure 4.14, which shows two surfaces clipped from the same *Colobus* humerus and their principal axes. The resulting initial principal axis in the right figure in Figure 4.14(b) does not lie along the cylinder median.

Having the centre of the humeral head and the rotation axis of the distal humerus, obtained from either method one or method two, allows the two axes in Figure **??**, L_{h1} and L_{h2}, to be estimated by the steps described below.

Initialise layers Let p_m be the middle point between the centre of capitulum and the centre of the circle (or the mean point of all surface points on the clipped surface). p_m

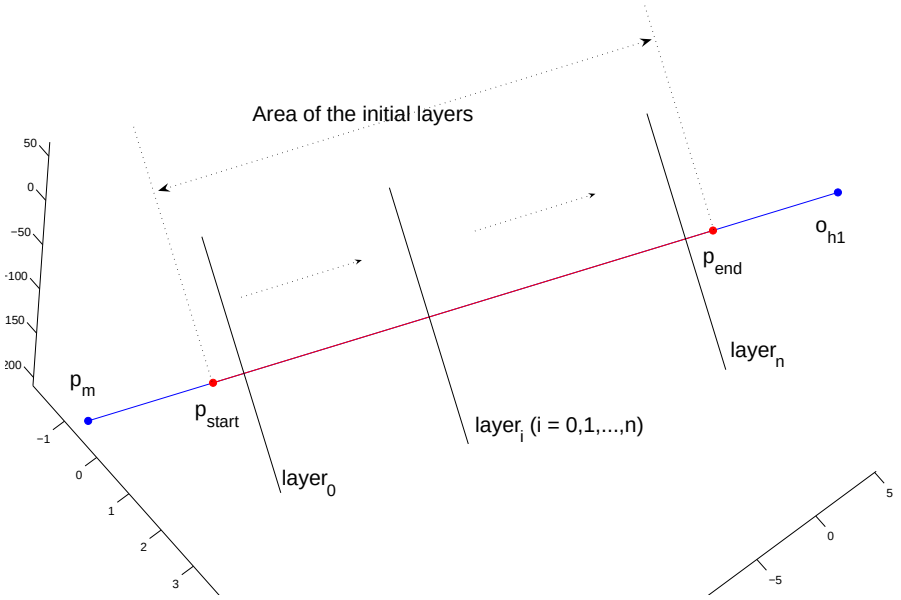

Figure 4.15: The construction of the initial layers along the humeral shaft. Layer$_i$ is perpendicular to ling segment p_{start} - p_{end}

is on the rotation axis of the distal humerus. Two-thirds of the line segment p_m - $\mathbf{o}_{h1}$, shown as the line segment p_{start} - p_{end} in Figure 4.15, was computed to construct the initial layers. Line segment p_{start} - p_{end} lies on the middle of p_m - $\mathbf{o}_{h1}$. Figure 4.16(a) shows the first and the fourth layers constructed perpendicular to p_{start} - p_{end}. There are 30 of these initial layers along line segment p_{start} - p_{end} in this thesis.

Extracting the centres of layers A plane was fitted to each layer using all surface points belonging to this layer. These were projected to this plane and a circle was fitted to the projection points; the centre of the fitted circle is calculated as the centre of the current layer (Figure 4.16).

Layers reconstruction Line L_{shaft} was fitted to the centres of all layers using PCA to approximate the medial axis (Figure 4.17). This line is the new direction to reconstruct the layers on the humeral shaft. In Figure 4.18, point P_m and point $\mathbf{o}_{h1}$ are the projected axis L_{shaft}. r_h is the radius of the approximated sphere for the humeral head and r_c is the radius of the approximated circle or the radius of the approximated cylinder. a_3 and a_4 ($a_3 = 2$ and $a_4 = 1$ in this thesis) are constants deciding the areas of axis reconstruction.

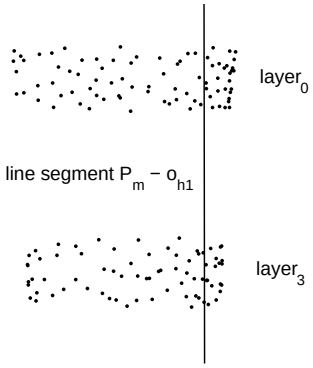

(a) Two layers

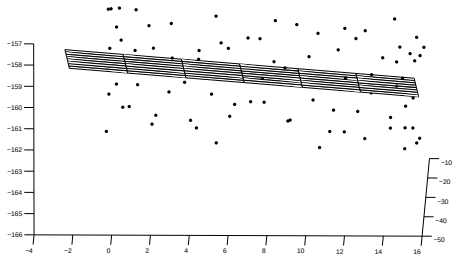

(b) Fit a plane to the current layer

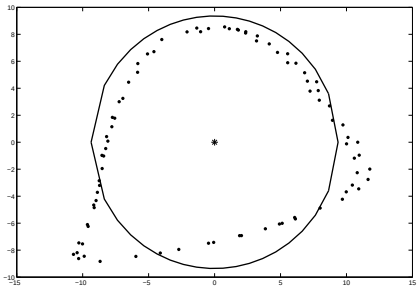

(c) Fit a circle to the projected points

Figure 4.16: Steps to obtain the centre of a layer on the humeral shaft

Figure 4.17: Construction of the long axis using the centres of all layers

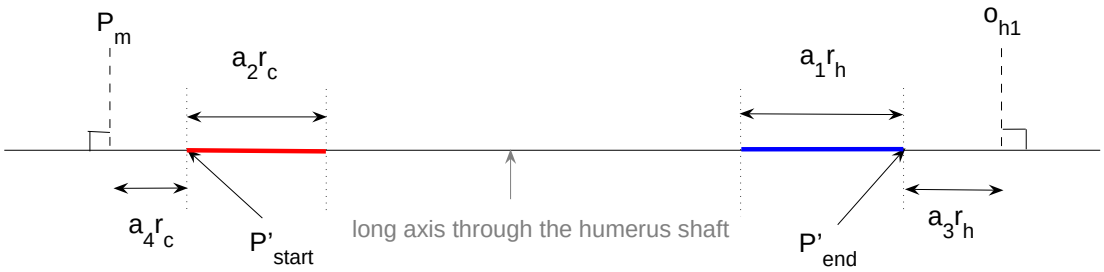

Figure 4.18: Axis reconstruction areas. $a_1 r_h$ and $a_2 r_c$ are the ranges to construct the proximal axis and the distal axis.

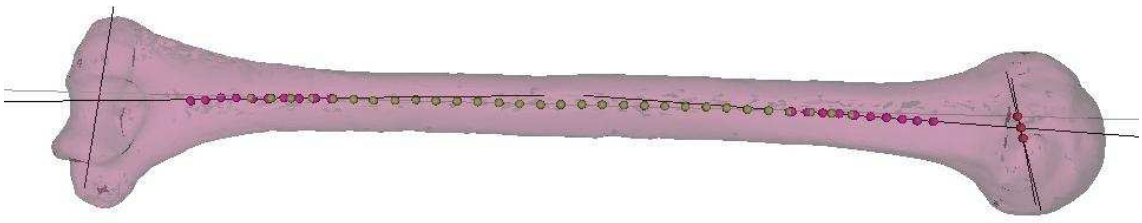

(a) *Homo*

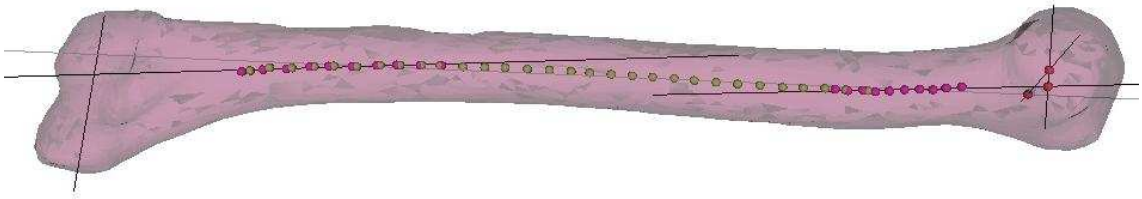

(b) *Colobus*

Figure 4.19: Centre points of the humerus shaft and all the constructed axes

a_1 and a_2 are determined so that $a_1 r_h$ and $a_2 r_c$ are both equal to one quarter of the length between P'_{start} and P'_{end}. The areas marked by $a_1 r_h$ and $a_2 r_c$ are the ranges of reconstruction of the layers for the proximal and distal humerus, respectively.

Constructing L_{h1} and L_{h2} Given the reconstruction ranges $a_1 r_h$ and $a_2 r_c$, axes L_{h1} and L_{h2} can be constructed using the same procedure as for L_{shaft} in Figure 4.17. For each line segment, ten layers were divided for reconstruction.

4.3.3 Results

A demonstration of all the axes estimated on a *Homo* humerus and a *Colobus* humerus using the described method is shown in Figure 4.19. Let L_r denote the elbow rotation axis (Figure 4.11), L_c a line passing the centre of the humeral head, $\mathbf{o}_{h1}$, and perpendicular to axis L_{h1}. Morphological parameters calculated on this *Homo* humerus are shown in Table 4.1.

All humeri in the present work were analysed. The average morphological parameters for each genus, and the standard deviations (std), are shown in Table 4.2. Since there is only one pair of *Pongo* shoulder bones in the datasets, parameters in the *Pongo* column

Size of the humeral head (S_h) - radius of the fitted sphere	16.10mm
Radius of the elbow hinge (S_r) - average distance of points on the clipped area to axis L_r	7.07mm
Degree of bending (D_b) - angle between L_{h1} and L_{h2}	7.10°
Degree of torsion (D_t) - angle between L_r and L_c	48.87°
Offset of axis L_{h2} (D_{h2}) - distal bending - angle between L_{h2} and L_{shaft}	6.39°
Offset of axis L_{h1} (D_{h1}) - proximal bending - angle between L_{h1} and L_{shaft}	4.24°

Table 4.1: Morphological parameters of a *Homo* humerus (*Homo* 1 in Figure 3.4, page 71)

are calculated from only one *Pongo* humerus. It can be seen that the great apes have much larger humeral heads compared to the monkeys (greater radius of the fitted sphere), whilst they are less twisted between the humeral head and the epicondyle (torsion) and less bent at the proximal end (D_{h1}).

4.3.4 Validation

In order to assess the accuracy of size of the humeral head, ten sets of seed points were selected on a *Colobus* humeral head and ten sets of corresponding surface points were generated by the seed points. The average distance between each approximated sphere centre and the mean centre from all approximated spheres is $0.36mm$ with standard deviation $0.33mm$. The average radius of the fitted spheres is $13.25mm$ with standard deviation $0.37mm$.

The trochlea is a very smooth structure, which can be seen in Figure 2.2, page 27, and therefore it has no distinct concave feature to be identified automatically using the crest line technique. Manual manipulation of landmark data is tedious and time consuming, and it has both inter- and intra- observer reliability problems. Apart from the above facts, the main reason why Dunning's method [DDKJ03] cannot be used here is because of the trochlear differences between the great apes and the monkeys. The methodologies developed here reduce manual involvement and also lessen these types of

Monkeys	*Cebus*		*Colobus*		*Macaca*		*Papio*		*Presbytis*	
	mean	std	mean	std	mean	std	mean	std	mean	std
$S_h(mm)$	7.5	2.6	8.9	0.3	9.9	2.6	12.3	0.4	8.2	0.8
$S_r(mm)$	3.4	0.2	5.6	0.4	6.0	1.2	9.0	0.6	4.9	0.4
$D_b(^\circ)$	28.1	3.8	11.9	1.6	14.2	2.9	13.6	2.9	10.7	4.3
$D_t(^\circ)$	73.3	7.3	81.4	6.9	70.9	14.8	82.8	4.9	81.4	7.7
$D_{h2}(^\circ)$	29.8	5.7	7.7	0.2	6.5	3.2	4.6	1.7	7.3	1.9
$D_{h1}(^\circ)$	9.6	0.4	11.2	2.8	12.8	1.8	13.4	3.3	11.8	2.6
Great apes	*Pan*		*Gorilla*		*Homo*		*Pongo*			
	mean	std	mean	std	mean	std				
$S_h(mm)$	20.0	3.6	30.3	3.7	21.0	1.6	18.3			
$S_r(mm)$	10.2	1.1	16.1	2.8	9.6	0.8	10.7			
$D_b(^\circ)$	6.8	1.7	11.0	0.8	6.2	1.4	15.7			
$D_t(^\circ)$	22.1	14.6	33.0	16.8	42.6	11.3	70.4			
$D_{h2}(^\circ)$	6.4	1.6	7.9	2.1	7.7	1.3	12.9			
$D_{h1}(^\circ)$	2.0	1.9	3.9	1.3	2.7	0.8	4.9			

Table 4.2: Average morphological parameters of humeri of the present genera

variations. Moreover, they are applicable to the present primate-humerus dataset.

To investigate robustness of Dunning's method and the cylinder fitting method, the two measurements were repeated on the same *Colobus* humerus. Ten cylinders were clipped; ten sets of seed points on the capitulum (as shown in Figure 4.13(b)) and ten sets of surface points on the trochlea (points in Figure 4.10(b)) were selected. The average distance between the centres of the fitted spheres on the capitulum and the mean centre of those spheres is $0.43mm$, with standard deviation $0.33mm$. The average distance between the centres of the fitted circles on the trochlea and the mean centre of those circles is $0.42mm$, with standard deviation $0.12mm$. These values indicate that the circle fitting on the concave ring of the trochlea is slightly more stable when approximating geometrical parameters on this *Colobus*.

Ten axes were fitted to the clipped cylinders, and ten axes were constructed to connect the sphere centres of the capitulum and the circle centres of the trochlea. Figure 4.20 shows the mean axes of these two repeated measurements on the *Colobus* humerus shown in Figure 4.10(b). The 3D angle between them is 6.6° and their direction difference is more obvious at the medial side of the humerus. The angle between the constructed axes in the measurements and the mean axes of the measurements were calculated to assess

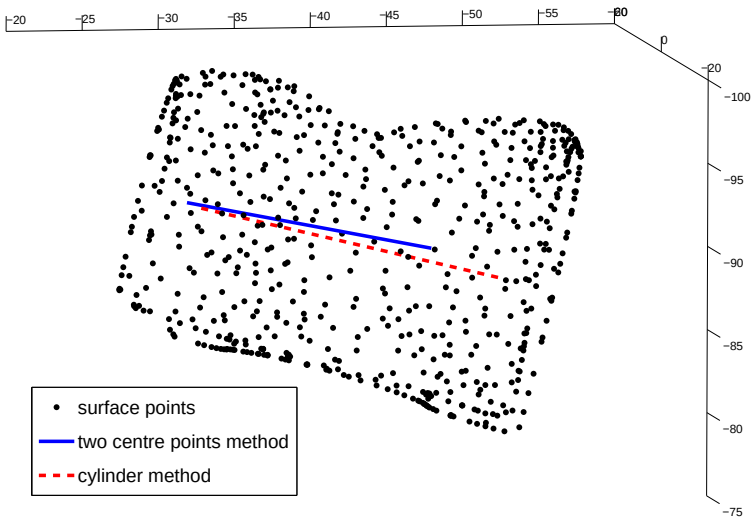

Figure 4.20: Mean axes of ten repeated measurements on a *Colobus* distal humerus

Parameters	Cylinder method		Dunning's method	
	mean	std	mean	std
$D_b(^\circ)$	10.76	0.21	10.46	0.27
$D_t(^\circ)$	79.61	1.12	85.83	1.77
$D_{h2}(^\circ)$	8.31	0.15	8.71	0.25
$D_{h1}(^\circ)$	10.88	0.02	10.86	0.03
$d_b(mm)$	13.86	0.19	14.65	0.46

Table 4.3: Morphological parameters of a *Colobus* humerus from ten measurements. Definitions of the parameters are in Table 4.1.

the stability of the two methods. The average values of the angle differences are 2.2° and 2.5° in the cylinder fitting method and in Dunning's method, respectively, with standard deviations 0.4° and 0.7°. Both methods are stable and the cylinder fitting method shows more statistical stability.

Morphological parameters in Table 4.1 were estimated based on the constructed anatomical axes and they are the parameters to be validated. Table 4.3 shows the average values of these parameters and the standard deviations of them (d_b is the distance between the two axes approximating the proximal and distal humeral shaft). Dunning's method shows more variability for all the estimated parameters.

The remainder of this thesis estimates the rotation axis using the cylinder fitting

method (method two in Figure 4.11).

4.4 Geometrical Variation of the Scapula

The scapula is a complex bone with very complicated structures that are difficult to describe. Its inferior and medial angles, spine, acromion process and glenoid vary largely even within the same genus. Three axes were constructed on each scapula in the present work: one describing the orientation of the glenoid, one describing the orientation of the infraspinous fossa, and one approximating the lateral border.

Another axis can be constructed to approximate reliably the scapular spine of great apes (Figure 4.28 shows the spine axis on a *Homo* scapula). The basic idea of the construction method is to extract surface points on the spine satisfying some predefined conditions (Section 4.4.1 describes how to choose these surface points), and to fit a line to these surface points using PCA. Due to the large difference between the great apes and the monkeys on the spine, this axis is not utilised to measure the geometrical feature in this thesis.

Amadi and Hill describe the glenoid as a plane [Ama06, Hil06]. The normal of this plane was suggested as the orientation of the scapula. However, as described in Chapter 2, Section 2.2, the glenohumeral joint is regarded as a synovial ball and socket joint. It is inaccurate to describe the glenoid simply as a plane. Amadi proposed fitting an ellipse to the cross section of the lateral border (highlighted area in Figure 4.21(a)) [Ama06]. An axis approximating the lateral border was then fitted to all the centres of the fitted ellipses. The non-human primate humeri do not have the same discrete anatomical properties as the human humeri. It is obvious from Figure 4.21 that the cross section of the lateral border of a *Colobus* scapula could not appropriately usefully be fitted by an ellipse (highlighted area in Figure 4.21(b)).

This section suggests the description of the glenoid by a sphere and proposes a semi-automatic method to estimate the geometrical axes on a primate scapula. These axes can be used to describe the spatial relationships between the glenoid, the infraspinous fossa

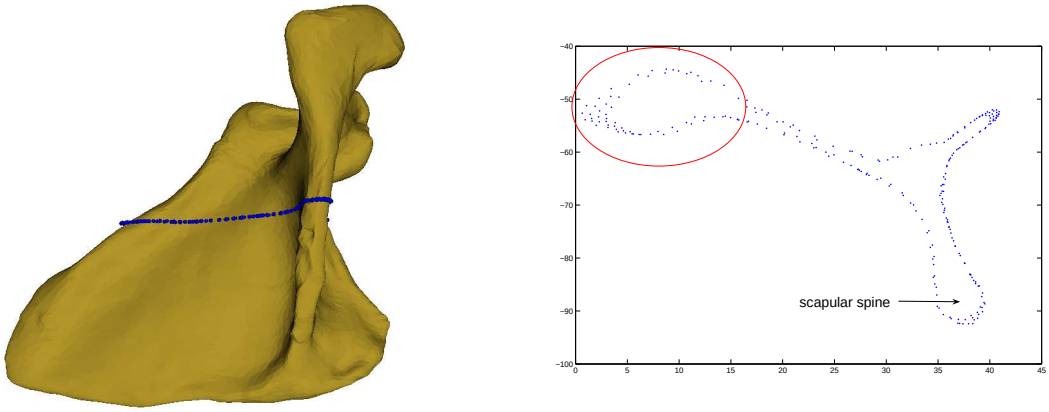

(a) *Homo*

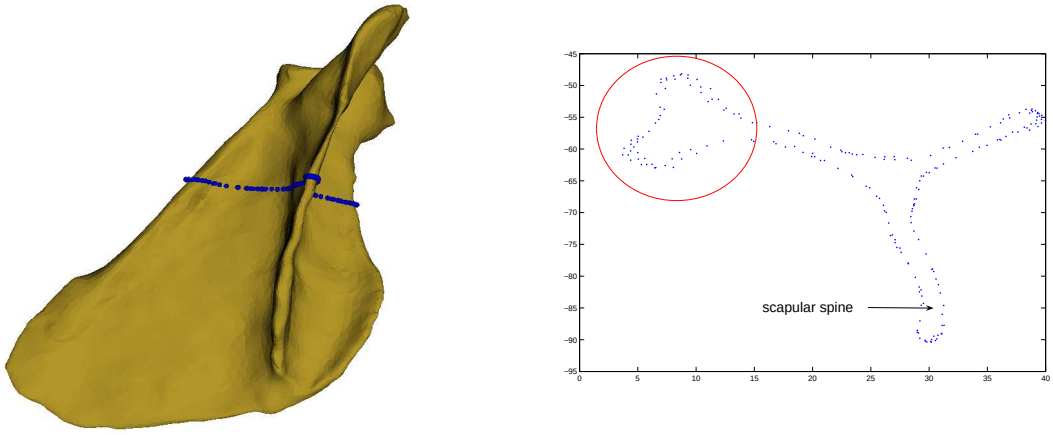

(b) *Colobus*

Figure 4.21: Cross sections of two scapulae

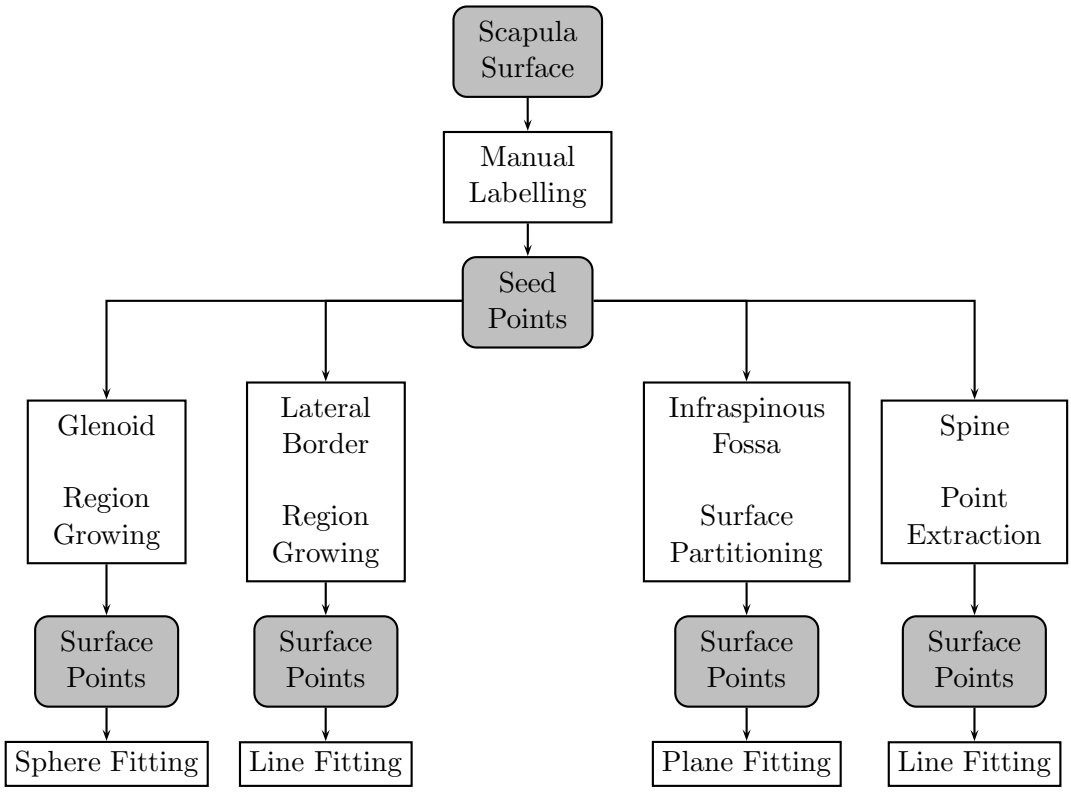

Figure 4.22: Obtaining geometrical variation of the scapula

and the lateral border. The implementation procedure is explained below.

4.4.1 Methodology

The computational procedure can be summarised in the flowchart in Figure 4.22. A suggestion for obtaining the axis of the scapular spine on great ape scapulae is presented. Although the method was applied to monkey scapulae in the dataset, a more general and reliable approximation of this axis is required in the future.

Manual labelling

Five surface points were labelled manually on a *Homo* scapula (Figure 4.23): two of them are on the glenoid surface, three are on the lateral border and one is on the intersection between the scapular spine and the medial border.

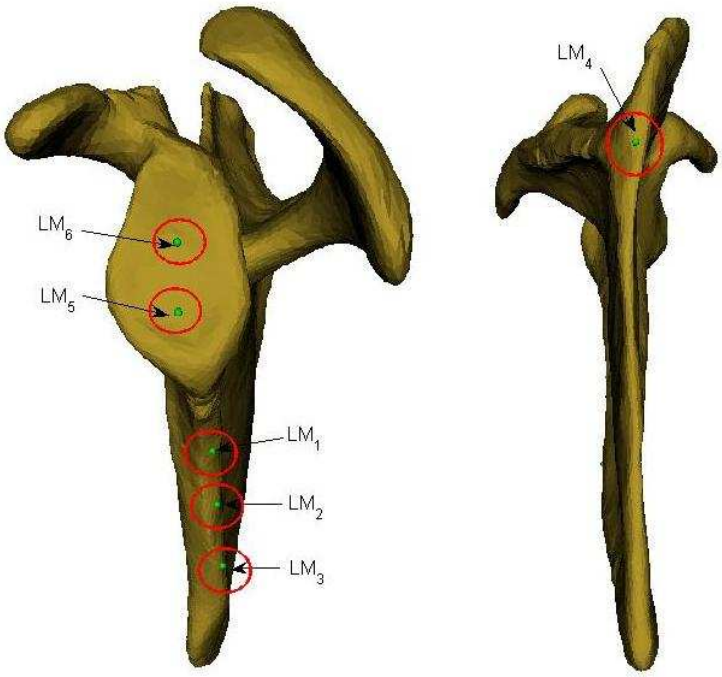

Figure 4.23: Manually labelled surface points on a *Homo* scapula

Fitting a sphere to the glenoid

A least square best-fit sphere, instead of a plane, was fitted to the surface points of the glenoid. The radius of the fitted sphere is calculated as a surrogate measure of size for the socket of the three-degree of freedom (DOF) spherical joint. The surface points were extracted by region growing starting from two seed points, LM_5 and LM_6, as shown in Figure 4.24.

Since the crest lines obtained on the glenoid rim may be unclosed (there may be gaps between crest lines such that the grown points would leak out of the region of interest), a modified region growing algorithm (Algorithm 4) was developed. In Figure 4.24, the green points on the glenoid are the grown points from the two seed points. They are to be used to represent the glenoid surface. Let $\mathbf{o}_s$ be the average point of all points on the glenoid surface, and c be the centre of the fitted sphere, the direction of vector $|\overrightarrow{\mathbf{o}_s - c}|$ defines the orientation of the glenoid and, consequently, the orientation of the scapula. The degree of growing is restricted by the crest lines on the rim of the glenoid (blue points in Figure 4.24).

Algorithm 4 Region growing on the glenoid, constrained by the crest lines on the glenoid rim

Initialisation: create a column vector to record the indexes of the grown surface points on the glenoid ($g_{i=0,1,\cdots,n-1} = false$); create a column vector to record the stopping point of region growing ($f_{i=0,1,\cdots,n-1} = false$); set the maximum degree of region growing ($m = 6$)
for each degree of region growing ($it = 0$ to $m - 1$) **do**
  for each surface point ($id = 0$ to $n - 1$) **do**
    if the surface point v^{id} is on a crest line ($F_{id} == true$) && it is not a stopping point ($f_{id} == false$) **then**
      set this point as a grown point ($g_{id} = true$)
      let l equals to the number of first-order neighbour vertices of vertex v^{id}
      for each first-order neighbour vertex u_i^{id} ($i = 0$ to $l - 1$) **do**
        if u_i^{id} is not on a crest line **then**
          set this neighbour vertex as a grown point ($f_{index(u_i^{id})} = true$)
        else
          set point v^{id} as a stopping point ($f_{id} = true$)
          stop the current *for* loop
        end if
      end for
      if point v^{id} is a stopping point ($f_{id} == true$) **then**
        set each of its first-order neighbour vertex as a stopping point ($g_{index(u_i^{id})} = true$)
      end if
    end if
  end for
end for

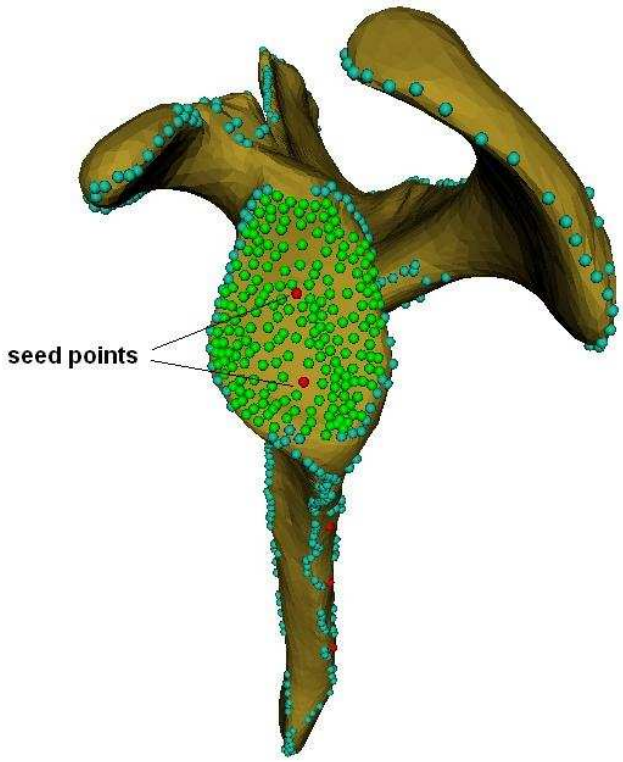

Figure 4.24: Surface points extracted from the glenoid (in green). They were grown from the two seed points which were manually labelled (in red), and were constrained by the crest lines on the glenoid rim. The light blue points are crest points on all crest lines.

Fitting an axis to the lateral border

The lateral border is approximated by an axis constructed from applying PCA to the surface points on the lateral border, which are extracted by region growing the crest lines obtained on the border (Figure 4.25). They are the closest crest lines to points LM_1, LM_2 and LM_3. The degree of region growing is determined so that the grown points only cover the thickened area of the border. The angle between this axis and the vector $|\overrightarrow{\mathbf{o}_s - c}|$ (direction of the glenoid) describes the orientation of the lateral border with regard to the glenoid.

Fitting a plane to the infraspinous fossa

The scapular fossa is approximated by a plane, which is the least square best-fit plane to the surface points on the infraspinous fossa (on both the costal and dorsal surfaces, Figure

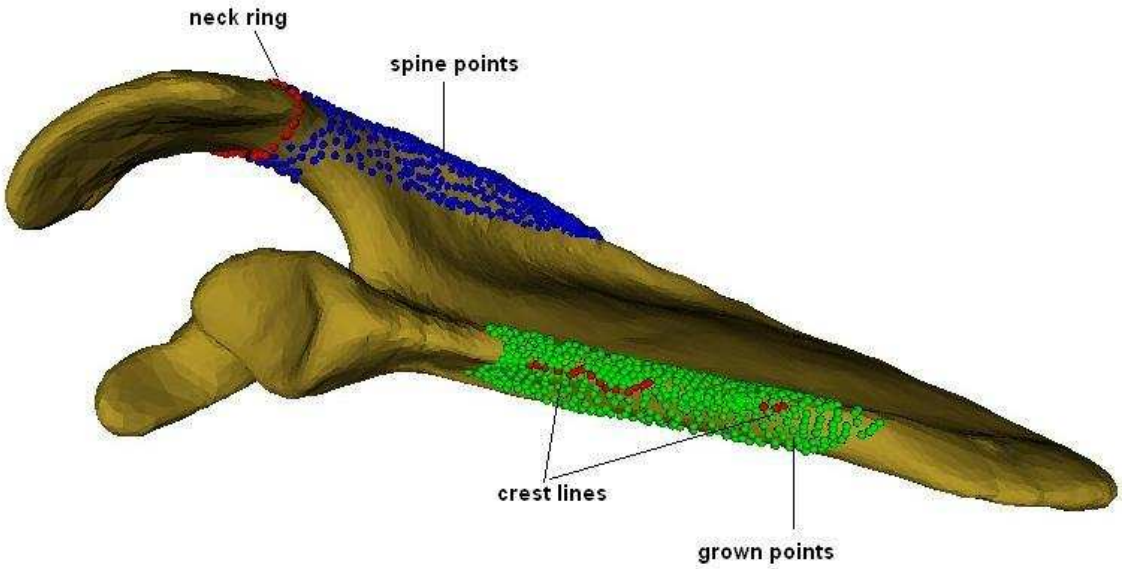

Figure 4.25: Surface points extracted from the lateral border (in green) and the spine (in blue)

4.26). The angle between the normal vector of the fitted plane and the direction of the glenoid, $|\overrightarrow{\mathbf{o}_s - c}|$, defines the orientation of the fossa with regard to the glenoid.

Fitting an axis to the spine

The direction of the scapular spine is estimated by an axis fitted to the surface points (shown as the blue points in Figure 4.25) on the spine using PCA. These surface points are within a right circular cone, whose radius and height were determined individually.

The neck points in Figure 4.25 were firstly extracted and a circle was fitted to the points. A right circular cone was generated with its base radius equal to $2r_n$, where r_n is the radius of the fitted circle, and its peak point lying on the intersection between the medial border and the scapular spine. Surface points of the scapula inside this cone were extracted to construct the spine axis.

Figure 4.27 shows the extracted surface points on a *Papio* scapular spine. The surface points extracted are on a different area of the spine compared to those points in Figure 4.26. A more general and reliable method is required to describe the scapular spine

Figure 4.26: Surface points extracted from the infraspinous fossa

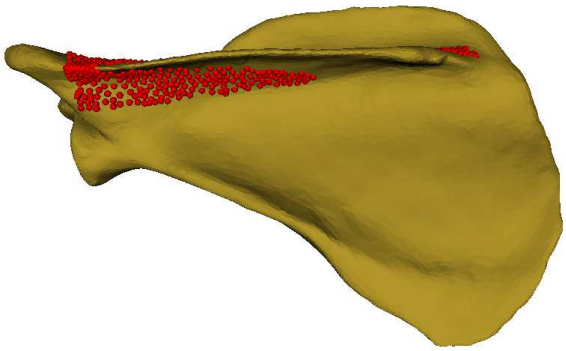

Figure 4.27: Surface points on a *Papio* scapular spine

in this primate dataset, or more manual manipulation should be involved to identify the feature.

4.4.2 Results

Figure 4.28 shows the sphere fitted to the glenoid of a *Homo* scapula, and the axes approximating the scapular spine and the lateral border. A demonstration of the estimated axes on this scapula can be seen in Figure 4.29. Table 4.4 shows the calculated anatomical parameters from this scapula.

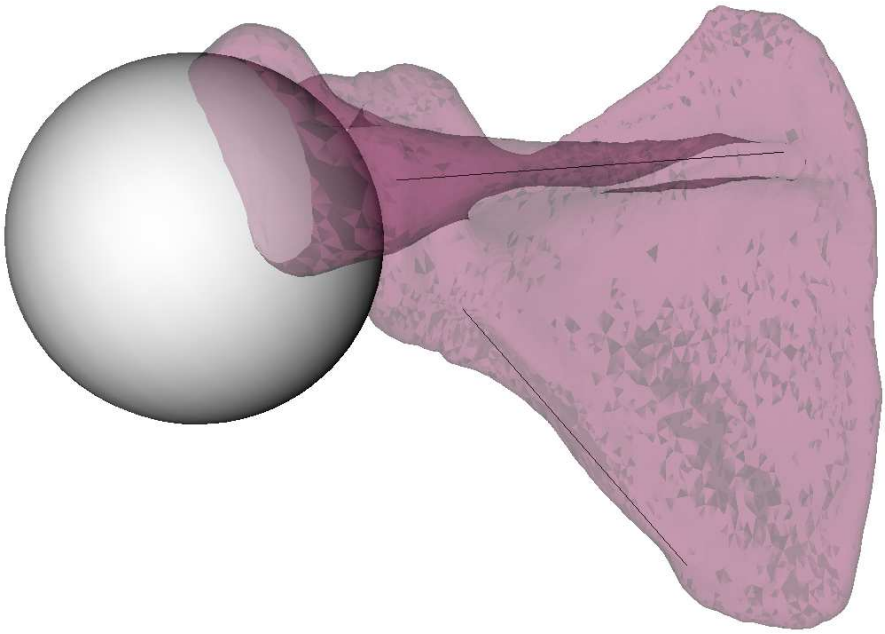

Figure 4.28: Approximation axes constructed on a *Homo* scapula

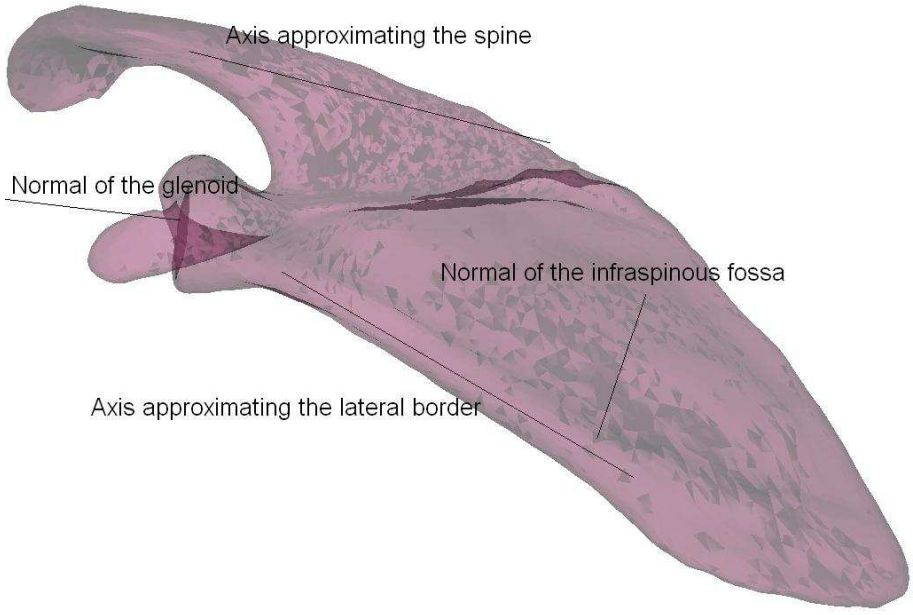

Figure 4.29: Demonstration of the scapula axes

(S_g): radius of fitted sphere	43.63mm
(D_{gn}): angle between glenoid axis and fossa normal	96.50°
(D_{sn}): angle between spine axis and fossa normal	78.60°
(D_{sb}): angle between spine axis and lateral border axis	52.20°
(D_{gb}): angle between glenoid normal and lateral border axis	127.96°
(D_{gs}): angle between glenoid normal and spine axis	175.02°

Table 4.4: Morphological parameters of a *Homo* scapula

Monkeys	*Cebus*		*Colobus*		*Macaca*		*Papio*		*Presbytis*	
	mean	std	mean	std	mean	std	mean	std	mean	std
$S_g(mm)$	9.7	1.5	20.0	6.5	12.7	3.3	20.3	3.2	12.6	1.5
$D_{gn}(°)$	85.0	6.4	87.8	3.7	81.9	9.9	74.5	17.3	87.3	7.0
$D_{sn}(°)$	85.6	6.1	85.8	5.3	87.6	2.9	88.3	2.2	89.1	3.3
$D_{sb}(°)$	31.1	7.7	32.8	1.4	31.3	2.0	35.9	5.3	31.8	3.0
$D_{gb}(°)$	35.1	3.5	52.0	3.7	35.6	7.7	46.7	3.6	81.8	3.7
$D_{gs}(°)$	11.5	3.1	21.2	3.4	13.1	5.4	22.9	2.0	75.4	2.5
Great apes	*Pan*		*Gorilla*		*Homo*		*Pongo*			
	mean	std	mean	std	mean	std	mean	std		
$S_g(mm)$	34.8	7.5	36.8	2.1	40.6	10.2	22.9			
$D_{gn}(°)$	86.9	2.0	83.3	8.6	85.8	5.2	82.5			
$D_{sn}(°)$	62.2	6.2	83.7	9.1	79.9	10.9	82.3			
$D_{sb}(°)$	40.1	6.6	33.1	6.7	46.7	6.3	25.0			
$D_{gb}(°)$	32.3	2.0	32.3	9.4	51.1	13.4	20.4			
$D_{gs}(°)$	35.8	2.1	10.7	1.4	11.2	5.7	5.0			

Table 4.5: Average morphological parameters of scapulae of all the present genera

All the 30 scapulae in the dataset were analysed. The average estimations of geometrical parameters are listed in Table 4.5. The parameters vary greatly across the dataset without obvious commonality within the great apes or within the monkeys. The difference of the radii of the fitted spheres on the glenoid is the only direct difference between the monkeys and the great apes.

4.5 Redefinitions of the Coordinate Frames

Crest lines are utilised to differentiate feature areas on the surfaces to semi-automatically construct the coordinate frames. Instead of working on every single 2D slice, the proposed definitions obtain geometrical parameters from 3D shapes directly.

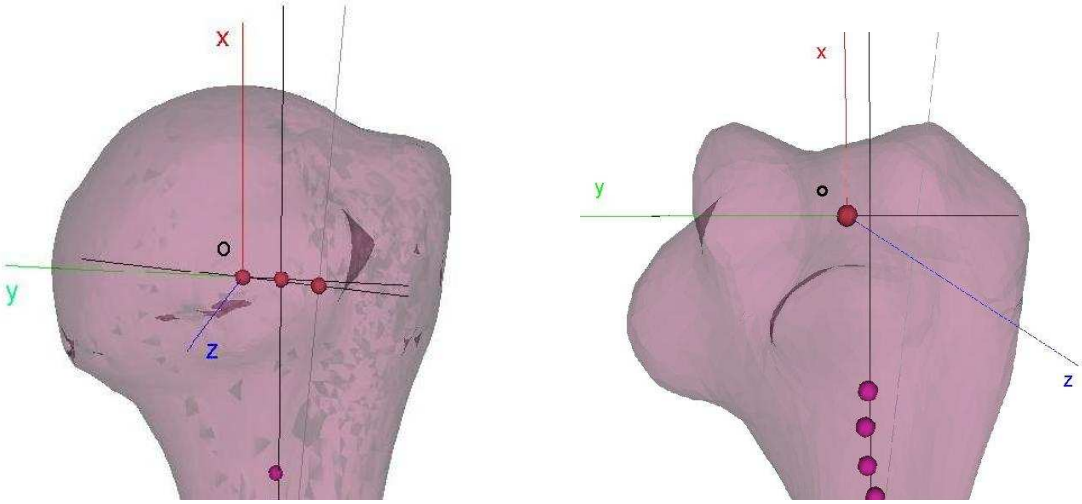

(a) Proximal humerus frame ($frame_{h1}$) (b) Distal humerus frame ($frame_{h2}$)

Figure 4.30: Two coordinate frames on a *Homo* humerus

4.5.1 Coordinate Frames on the Humerus

Two coordinate frames on the humerus were established, one for the proximal humerus referred to as $frame_{h1}$ (Figure 4.30(a)) and the other for the distal humerus referred to as $frame_{h2}$ (Figure 4.30(b)).

Frame One - Proximal Humerus

The origin $\mathbf{o}_{h1}$ of frame one is set as the centre of the humeral head. It is the centre of the sphere which is fitted to the surface of humeral head. Details of how to obtain this centre were described in Section 4.3.2. The first axis $\mathbf{x}_{h1}$ is set to be parallel to the medial axis L_{h1} of the humeral shaft near the proximal end, pointing laterally. The second axis $\mathbf{y}_{h1}$ is perpendicular to the line L_{h1} and it passes through the origin $\mathbf{o}_{h1}$. The third axis $\mathbf{z}_{h1}$ is perpendicular to the plane defined by $\mathbf{x}_{h1}$ and $\mathbf{y}_{h1}$, passing through the origin $\mathbf{o}_{h1}$. It is obtained by calculating the cross product of $\mathbf{x}_{h1}$ and $\mathbf{y}_{h1}$.

Frame Two - Distal Humerus

Two methods constructing the elbow rotation axis were described in Section 4.3.1. Since the structure of the capitulum does not always resemble a sphere, especially in non-

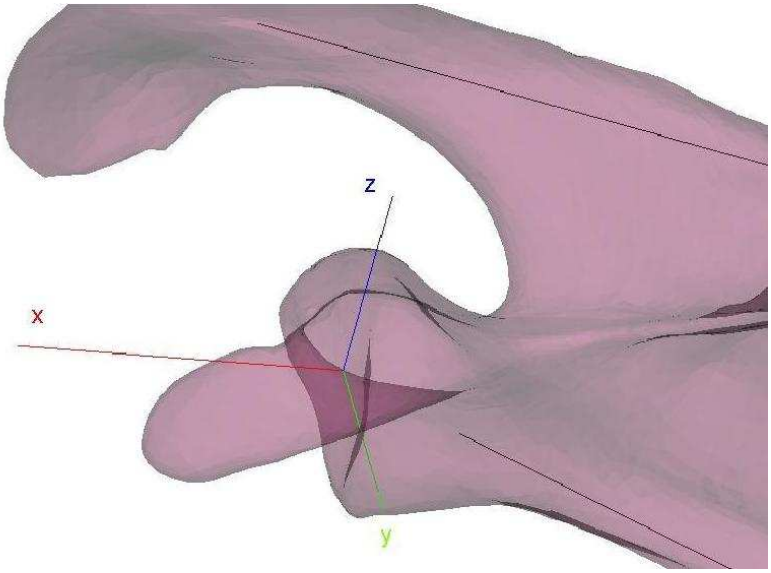

Figure 4.31: Scapular coordinate frame

human primate humeri, the rotation axis was constructed using method two - the clipped cylinder method. The unit vector of the constructed rotation axis, pointing to the medial epicondyle, is taken as the second axis $\mathbf{y}_{h2}$ of the coordinate frame $frame_{h2}$. The origin $\mathbf{o}_{h2}$ is defined as the projection point from axis L_{h2} to the second axis $\mathbf{y}_{h2}$. The first axis $\mathbf{x}_{h2}$ is parallel to axis L_{h2}. The third axis $\mathbf{z}_{h2}$ is thus the perpendicular line to the plane defined by $\mathbf{x}_{h2}$ and $\mathbf{y}_{h2}$. Axis $\mathbf{z}_{h2}$ lies on the perpendicular line l between axes L_{h2} and $\mathbf{y}_{h2}$.

4.5.2 Coordinate Frames on the Scapula

The origin of the scapular coordinate frame is set at the centre of the glenoid, which is defined as the average point of the surface points obtained from the glenoid (region growing points in Figure 4.13). The direction of the first axis $\mathbf{x}_s$ points to the centre of the sphere that fitted to the glenoid surface points. Let $\mathbf{n}_s$ be the normal vector of the plane fitted to the fossa, the second axis $\mathbf{y}_s$ is defined as the perpendicular vector to both axes $\mathbf{x}_s$ and $\mathbf{y}_s$ (cross product between them), pointing proximally. The cross product between axis $\mathbf{x}_s$ and axis $\mathbf{y}_s$ thus gives the third coordinate axis $\mathbf{z}_s$. A demonstration is shown in Figure 4.31.

4.6 Summary

An improved method to extract crest lines on the shoulder bone surfaces has been proposed. The implementation sequence was determined so that the surface curvatures can be estimated more accurately. The crest lines automate the calculation of the bony geometrical parameters, such as glenoid size and its orientation. With the constructed axes inside the bones, other geometrical parameters can be easily obtained.

The chapter also redefines the coordinate frames on both of the shoulder bones. The proposed definitions are based on automatic calculation instead of relying on massive manual labelling as in traditional methods. Little manual manipulation was involved and the resulting variations due to this manual intervention affect the parameter calculations only slightly. The surface local features (such as the edge of the trochlea) used to extract global shape information were chosen carefully so that they can not only describe shape information from human datasets but also from non-human datasets.

The proposed definitions are applicable to all the shoulder bones in the present datasets. The chosen features are reliable and the extracted parameters are comparable across the genera. However, the tradeoff is the lack of information on some specific bony morphological features which are uniquely present in human shoulders.

The methods developed in this chapter will be used in Chapter 6 to assess the accuracy of the shape prediction method.

Chapter 5

3D Statistical Shape Modelling of Shoulder Bones

5.1 Introduction

This chapter proposes and uses robust methods for the construction of 3D statistical shape models (SSM) of the primate humeri and scapulae. The point-to-point correspondence establishment is addressed by the B-spline multi-resolution free form deformation (FFD) algorithm proposed by Rueckert *et al* [RSH+99]. Two applications of the constructed shape models of the primate shoulder bone shapes are demonstrated. The first application is the classification of a shoulder bone without taxonomical information by using principal component analysis (PCA). The results demonstrate significant variability between clusters of the great apes and the monkeys, clearly distinguishable in the coordinate systems formed by the principal axes. Leave-one-out validations were conducted. The second application is the description of morphological variations of the shoulder bones. No prior knowledge about anatomy was required or used.

Recent studies on bony morphology have demonstrated methodologies of building an SSM of human femora [CBE+04, RNS04]. An application of the SSM is to reconstruct a whole femur shape using a set of sparse points on the bone surface. This application is also called bone morphing and it is highly useful for intra-operative visualisation of bone

structures in image-free surgery [RNS04, SBM+02]. An iterative optimisation method was developed to reconstruct a complete surface by fitting a constructed shape model to a set of sparse surface points. Leave-one-out validations were also performed to assess the accuracy of the surface reconstruction.

5.2 Correspondence Establishment

The basic idea of establishing point-to-point correspondences between two surfaces is similar to the one proposed by Frangi *et al* [FRSN02], which is to relate the position of features or coordinate space in a source shape with the position of the corresponding feature or coordinate space in its target shape. A shape in the dataset is chosen as the reference (atlas), and it is transformed globally and deformed locally with regard to the remainders of the shapes (targets).

The deformed reference shape is thus close enough to one of its target shapes so that the corresponding surface point set can be identified. For a global transformation, rigid surface registration based on the iterative closest point (ICP) algorithm [BM92] was used to align the reference to its target; for local transformations, non-rigid registration based on the B-spline multiresolution FFD, an extension of the image-based registration algorithm proposed by Rueckert *et al* [RSH+99] and further developed by Schnabel *et al* [SRQ+01], was used.

5.2.1 Humerus Dataset

Since the present datasets include various genera, the size of the bones is very different. For example, a *Gorilla* humerus can be about five times longer than a *Cebus* humerus in the dataset. A direct rigid transformation, followed by an affine transformation, may fail to align the reference shape properly for further local non-rigid registration. An easy and appropriate way to deal with this is to initialise the rigid deformation by scaling the reference shape to the same size as its current target shape. A shape satisfying the following two conditions is chosen as the reference shape: its number of surface points is

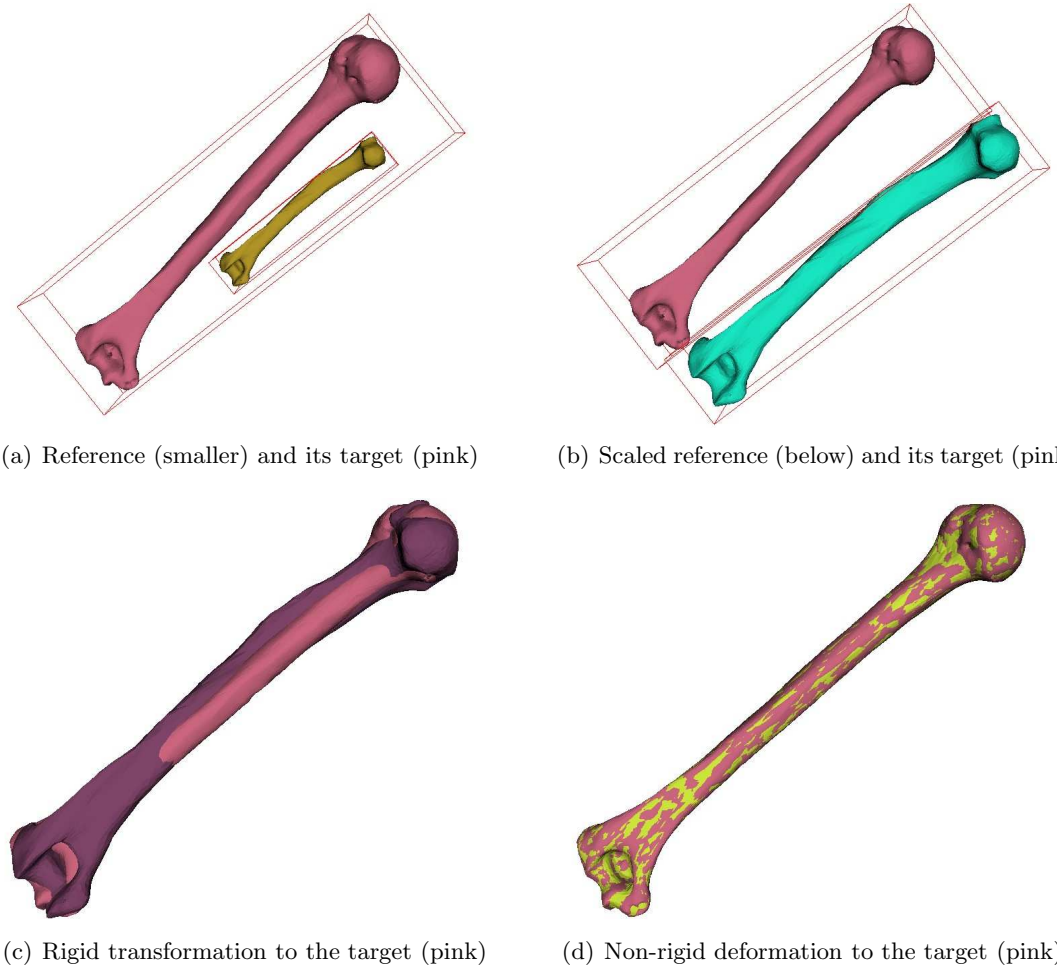

(a) Reference (smaller) and its target (pink)

(b) Scaled reference (below) and its target (pink)

(c) Rigid transformation to the target (pink)

(d) Non-rigid deformation to the target (pink)

Figure 5.1: Scaling, alignment and deformation of the reference shape. The target shape (pink) is unchanged from (a) to (d).

close to the average number of surface points across the dataset; its surface is visually smooth.

Assuming the reference shape and the current target shape are in a common coordinate system and that the longest axes of their bounding boxes lie on the same or similar directions (direction difference must be less than 90 degrees), the scaling factors in x, y and z directions are all defined with regard to the difference between the reference shape and the target shape on the longest axes of their bounding boxes. The scaled reference shape is only changed in size but not in the shape. The scaled reference shape is then aligned to the target shape using rigid surface registration based on the ICP algorithm [BM92].

Figure 5.1 shows the procedure by which the reference humerus shape (from a *Macaca*) is aligned and deformed to the current target humerus shape (from a *Homo*). As can be seen, the surface of the reference shape is very close to the surface of the target shape after scaling and rigid alignment. Therefore, a local multi-resolution B-spline deformation without global affine registration is sufficient to deform the source shape to the target shape finely. The deformation shown in Figure 5.1(d) is completed by an initial control grid resolution of $40mm \times 40mm \times 40mm$ and four control grid subdivisions. The resolution of the control point grid and the number of subdivisions are determined empirically, so that the values provide a compromise between smoothness and accuracy.

One can either use the deformed reference shape directly as one of training samples, or find the closest surface point set of the target shape to the reference shape. The first method produces very smooth surfaces for training whilst the latter produces sometimes very bumpy but comparatively accurate surfaces. Shapes produced by these two methods are shown in Figure 5.2, where the left shape is constructed using the closest point set to the deformed reference shape and the right one is the deformed reference. No obvious differences between these two surfaces can be identified. As such the deformed reference shapes were taken as the training samples.

5.2.2 Scapula Dataset

The humerus belongs to the catalogue of long bones, which is a relatively simple anatomical form, whilst the scapula belongs to the catalogue of flat bones, which have complex structures expanding into broad, flat plates. The other three types of bones in the human body include short bones, irregular bones and sesamoid bones. The flat and irregular bony structures challenge all non-rigid deformation methods which utilise closest point analysis. Figures 3.5 and 3.6 in Chapter 3 (on pages 73 and 74) display all scapulae of the present datasets. They were aligned into the same position. Both size and the shape vary significantly from one genus to the other. As in the humerus set, the reference scapula shape was scaled to the current study shape using their bounding boxes during correspondence establishment.

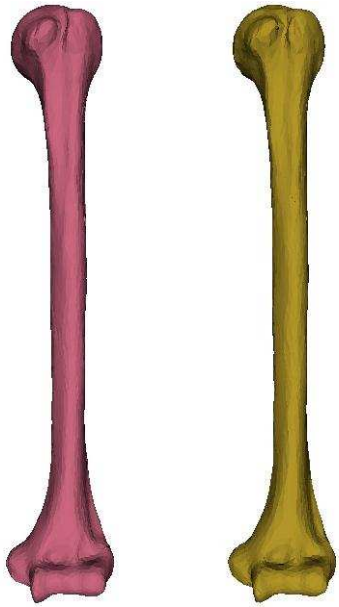

(a) (b)

Figure 5.2: Two representations of the same bone shape that are almost identical. (a) Deformed reference shape (b) Closest point set to the reference shape (they are surface points on the target shape)

In the present dataset, scapulae are similar at the acromion, the coracoid and the glenoid areas within the category of monkeys or within the category of great apes. A global transformation T_{global} and a local surface-based FFD are sufficient to deform a monkey scapula shape to another monkey scapula shape (Figure 5.3 shows a *Macaca* scapula shape being deformed to a *Papio* scapula shape which is in the same coordinate system), or a great ape scapula shape to another great ape scapula shape. However, these scapulae have very different acromion, coracoid and glenoid features in different categories, which make it insufficient to use a direct surface-based B-spline FFD following a global transformation. For example, a *Gorilla* scapula has a more extended acromion surrounding the humeral head than a *Macaca* scapula. The highlighted area in Figure 5.4 shows the incorrect registration area when deforming a *Macaca* scapula shape to a *Gorilla* scapula shape using a surface-based FFD.

To establish correct correspondences, this thesis proposes to initialise the B-spline deformation by matching a few point landmarks on the reference shape to their corresponding point landmarks on the target shape. These landmarks are the anatomical landmarks

(a) After global transformation, including rigid and affine transformations. The *Papio* scapula is in khakis and it is the target shape.

(b) Subdivision level one to level four (left to right). The *Papio* scapula (in khakis) is the target shape, and it is unchanged from left to right.

Figure 5.3: Multiresolution free form deformation. The control point resolution is $40mm \times 40mm \times 40mm$ in subdivision level one. A *Macaca* scapula is transformed and deformed to a *Papio* scapula (in khakis and unchanged in all subfigures). With more subdivisions, the reference shape is closer to the target shape.

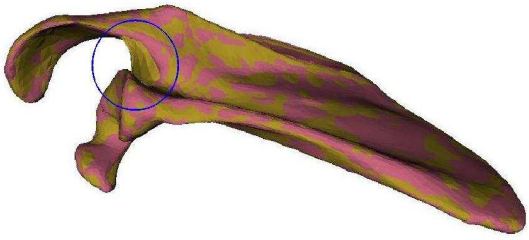

(a) Deformed shape (in khakis) shown in surface

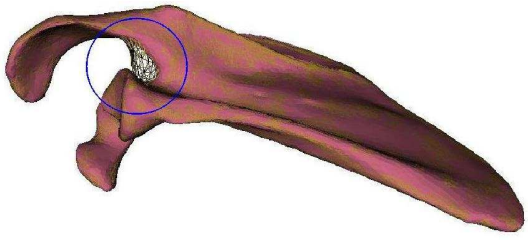

(b) Deformed shape (in khakis) shown in mesh

Figure 5.4: A *Macaca* scapula (in khakis) incorrectly deformed to a *Gorilla* scapula (target, in pink)

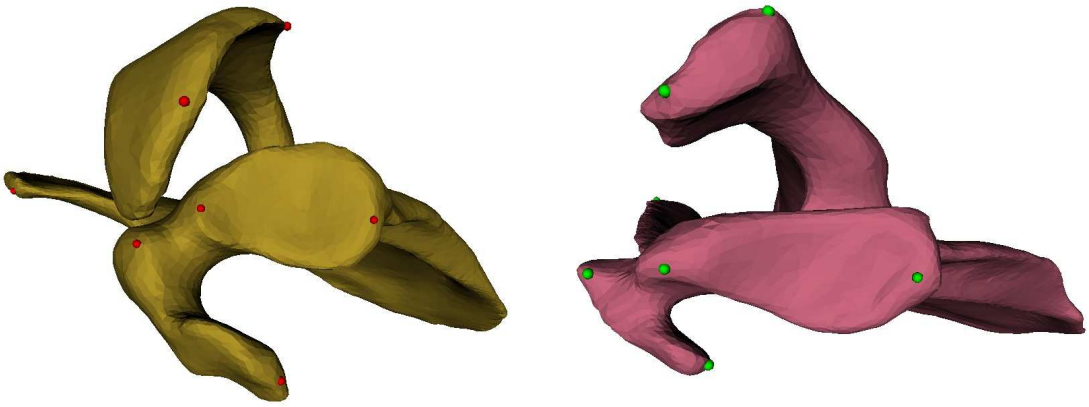

(a) Anatomical landmarks on a study shape (from a *Gorilla*)

(b) Anatomical landmarks on the reference shape (from a *Macaca*). It is transformed rigidly and affinely to the study shape.

Figure 5.5: Corresponding anatomical landmarks labelled on two aligned scapulae. They were selected manually.

located on the medial angle, the glenoid rim near the supraglenoid and the infraglenoid tubercles, the lateral edge of the acromion, and the region on the coracoid process attached to the biceps brachii. A demonstration of these anatomical landmarks is shown in Figure 5.5. The points in the figure were labelled manually on both the target (left) and the reference (right) scapula shapes. After the initialisation procedure, the reference shape resembles the target shape at the areas which contain those anatomical landmarks. A further refined surface-based B-spline deformation was then applied to the initialised shape. In the present work, the scapula from *Macaca* 2 was selected as the reference shape. Therefore, the initialisation step was only utilised when establishing correspondences of scapula shapes from the great apes in the dataset.

Given a reference shape S_r and a study shape S_s which is in a different category (category of the monkeys versus category of the great apes) from shape S_r, the implementation procedure is listed as follows:

- S_r was firstly scaled with regard to S_s and then transformed rigidly to S_s: $S_{r-global} = T_{global}(S_r)$. The scaling factor is determined by the size difference between their bounding boxes (Section 5.2.1). A rigid transformation is performed based on the ICP algorithm.

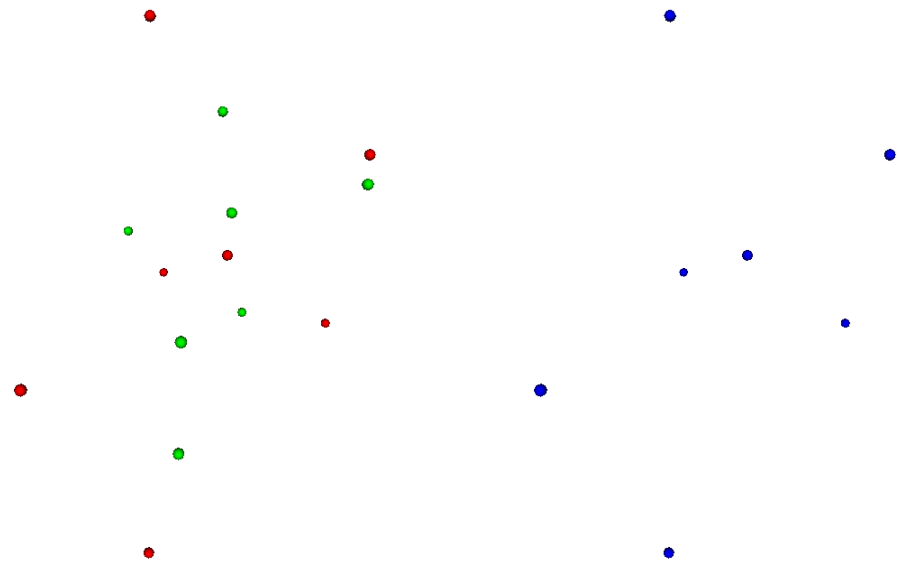

(a) Two sets of anatomical landmarks. Red points are on the target shape; green points are on the transformed reference shape.

(b) One landmark set deformed to the other. Green points (become blue points in the figure) are deformed to the red points. Red points are almost invisible.

Figure 5.6: Matching corresponding landmarks using B-spline free form deformation. The two point sets in (a) are the same point sets shown in Figure 5.5

- Manual selection of the corresponding anatomical landmarks, mainly selected on the acromion and the coracoid process, was conducted on S_s and $S_{r-global}$. Figure 5.5 shows an example of the two sets of corresponding landmarks, LM_s (red points) and LM_r (green points), which were manually selected on S_s and $S_{r-global}$.

- The two sets of corresponding anatomical landmarks were matched. In Figure 5.6, LM_r (the green point set in Figure 5.6(a), the blue point set in Figure 5.6(b)) is deformed to LM_s (the red point set in both subfigures) non-rigidly using multiresolution B-spline FFD with a $20mm \times 20mm \times 20mm$ control point grid and four subdivisions. The red points are selected from the study shape; the green points are selected from the rigidly and affinely transformed reference shape. In Figure 5.6(b) the green points are deformed to the red points, and the blue points are the anatomical landmarks after the deformation.

- $S_{r-global}$ is embedded into the deformation field of the control point mesh, which is obtained by matching the two sets of landmarks, so that the acromion and the

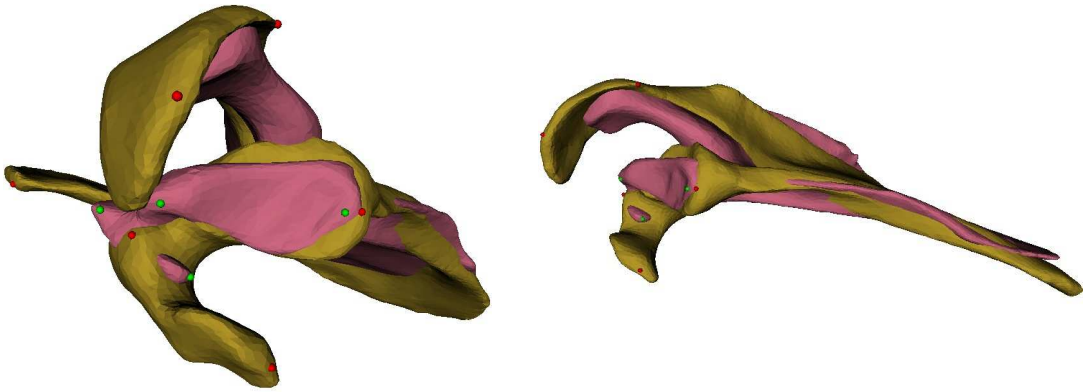

(a) Two shapes and their point landmarks from two angles of view. These are the same shapes and point sets as shown in Figure 5.5

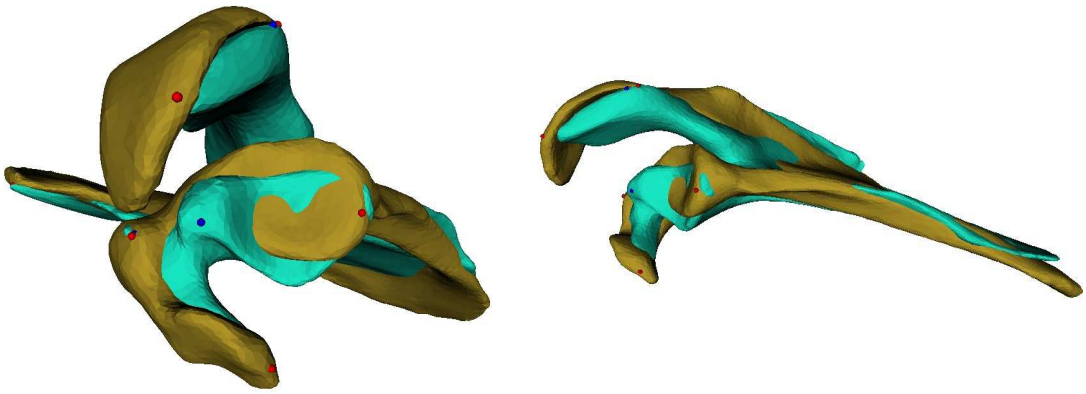

(b) The reference shapes are embedded into the deformation field defined by matching the anatomical landmarks. The green scapulae are the deformed reference shape from two angles of view.

Figure 5.7: Initialising surface-based free form deformation. The reference shape (pink shape in (a)) is deformed approximately to a study shape (in khakis)

coracoid are extended to those of S_s. Other areas (e.g. vertebral border) remain the same (Figure 5.7).

- The embedded shape S_{r-em} is now morphometrically close enough to S_s. A further refined surface-based FFD is able to deform S_{r-em} to S_s accurately. The deformation results shown in Figure 5.8 were attained using four control points subdivisions and a starting resolution $40mm \times 40mm \times 40mm$. The selected landmarks on both shapes do not necessarily match each after the surface-based deformation.

As in building the humerus training set, one can either use the deformed reference

Figure 5.8: Illustration of surface-based B-spline free form deformation from two angles of view. The khakis shape is the same *Gorilla* scapula shape in Figures 5.5 and 5.7. The purple shape is the final deformation.

scapula shape (for example the purple scapula in Figure 5.8) directly as one of the training samples, or find the closest surface point set of the target scapula shape (the khakis scapula in Figure 5.8) to the reference shape. No obvious differences between these two types of scapula surfaces can be identified. This thesis uses the deformed reference scapula shapes as the training samples.

5.3 Rigid Alignment

Size information is comparatively easy to obtain, but represents a significant portion of variance, and shape variability is of more importance yet more subtle in magnitude. Due to the substantial size variation in the datasets, other (shape) variations are comparatively less explicit. To better understand both size variation and shape variation, two models were built in this thesis: in model one, the training set was built from the bone shapes in their original size; in model two, all the bones were scaled to the reference shape so that there is no size variation in the training set.

Before constructing the two models, it is assumed that point-to-point correspondences have been established. This section explains how to align all the shapes into the common coordinate systems. The two training sets (with point-to-point correspondences) are used in the classification application in this chapter and will be used in Chapter 6.

5.3.1 Model One - Including Size Variation

Although bones were fixed in a certain position during CT scanning, there are still large location errors due to the manual positioning. Given a set of shapes with n corresponding surface points, in order to minimize the variations caused by different positions, they are aligned to a pre-defined coordinate system.

Humerus Model

The centre of the humeral head $\mathbf{o}_{h1}$ (definition of $\mathbf{o}_{h1}$ is in Chapter 4, Section 4.5.1) is defined as the origin of the local coordinate system of a humerus. All humerus shapes in the training set were aligned in a way such that (*i*) the centres of their humeral heads are fixed to a certain point (origin), (*ii*) the humeral shaft, which is represented by a line connecting the centre of the humeral head and the middle point between the two epicondyles in this section, were aligned, and (*iii*) the epicondylar axis, determined by the medial epicondyle and lateral epicondyles, are placed on the same plane. The humeral shaft representation in point (*ii*) is different from the one described in Chapter 4. It is only used for alignment purposes only in this chapter.

More specifically, let's assume $P1$, $P2$ and $P3$ (origin) are three points on the reference shape, denoting the medial epicondyle, the middle point of the two epicondyles and the centre of the humeral head respectively, and $Q1$, $Q2$ and $Q3$ denote the three corresponding points on a study shape. The study shape was aligned to the reference shape so that $Q3$ was moved to the origin, $Q2$ was located on line $P2$ - $P3$ and $Q3$ was placed on the plane determined by $P1$, $P2$ and $P3$. A demonstration of the alignment is shown in Figure 5.9.

The three points are obtained semi-automatically. The calculation of the centre of the humeral head is described in Chapter 4, Section 4.3.2. The two outermost points on the epicondyles were obtained by getting two points with extreme coordinates. Figure 5.9(d) shows a *Cebus* humerus shape being aligned to a *Macaca* humerus shape using the three alignment points.

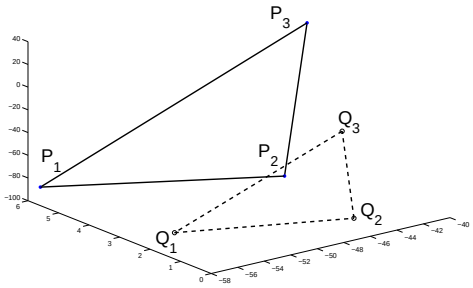

(a) Before alignment

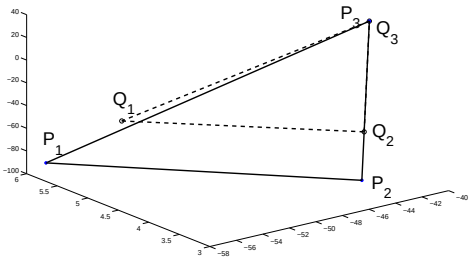

(b) After alignment

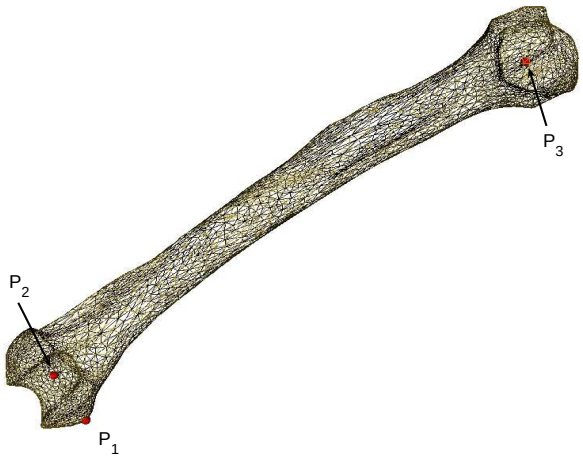

(c) Alignment points on a *Macaca* humerus

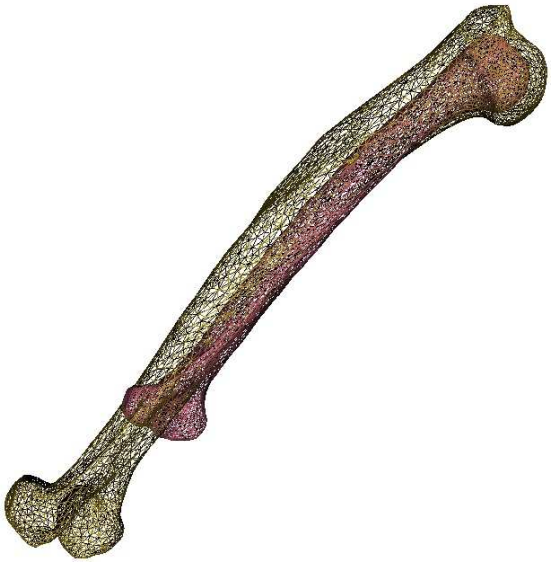

(d) A *Cebus* humerus (smaller) aligned to a *Macaca* humerus using the two alignment point sets

Figure 5.9: Alignment based on three alignment points

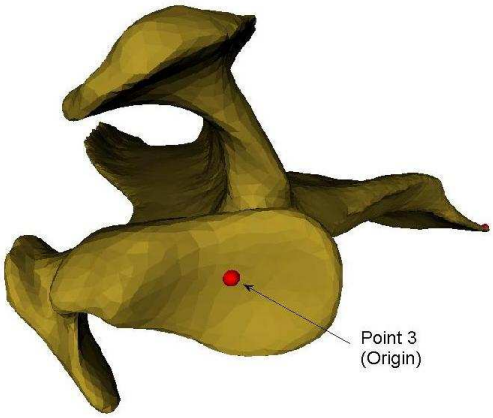

(a) Origin

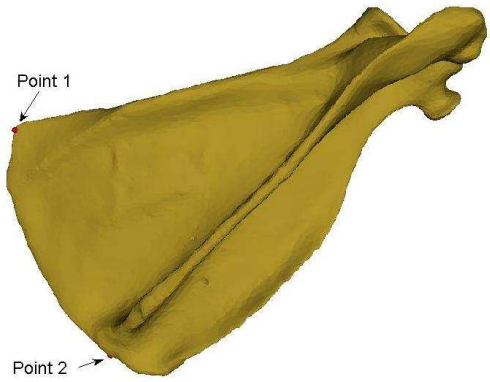

(b) Two of the three alignment points

(c) A *Presbytis* scapula (smaller) is aligned to a *Papio* scapula

Figure 5.10: Three points defining alignment coordinate system

Scapula Model

A study scapula shape was aligned to the reference scapula shape with its centre of the glenoid cavity located at the predefined origin (Figure 5.10(a)). The other two points determining alignment are located at the inferior angle and the intersection shared by the medial border and the scapular spine. The three alignment points shown in the figure were selected manually. The idea of alignment is the same as that in the humerus model, which is shown in Figure 5.9. $P1$, $P2$ and $P3$ (origin) are the three alignment points on the reference shape whilst $Q1$, $Q2$ and $Q3$ are the three corresponding points on the study shape. The study shape was aligned to the reference shape so that $Q3$ was moved to the origin, $Q2$ was located on line $P2$ - $P3$ and $Q3$ was placed on the plane determined by $P1$,

$P2$ and $P3$. The result of aligning a *Presbytis* scapula shape to a *Papio* scapula shape is shown in Figure 5.10(c).

5.3.2 Model Two - Excluding Size Variation

Before aligning the shapes into the same coordinate system, they were scaled into the same size as the reference shape. Alignment in model two is implemented automatically using a rigid transformation. The solution for the transformation function T_{rigid}, which is known as the solution to the *orthogonal Procrustes* problem, can be obtained using the Procrustes algorithm [KIMW00].

Humerus Model

Two humeri are considered to have the same size if they have the same length from the humeral head to the trochlea. To scale a study humerus shape to the reference humerus shape, the bounding box was utilised (described in Section 5.2.1). If the reference humerus R is in a $\Delta x \times \Delta y \times \Delta z$ bounding box with Δz denoting the length of its longest axis, and the study humerus H_i is in a $\Delta x_i \times \Delta y_i \times \Delta z_i$ bounding box with Δz_i denoting the length of its longest axis, H_i is scaled with a scaling factor $t = \Delta z / \Delta z_i$ in all the three directions. The scaled study humerus shape H_i was thereafter aligned to the reference humerus shape using the ICP algorithm.

The scaling method using bounding boxes is a rough method to eliminate size variation in the humerus dataset, because the longest axis of a humerus' bounding box is not equal to the longest axis of the local coordinate system of the humerus. To remove more size effect, the procedure of scaling and alignment was repeated twice (Figure 5.11).

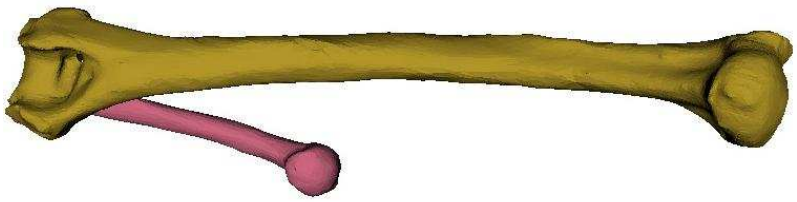

(a) A *Colobus* humerus (pink) and a *Papio* humerus

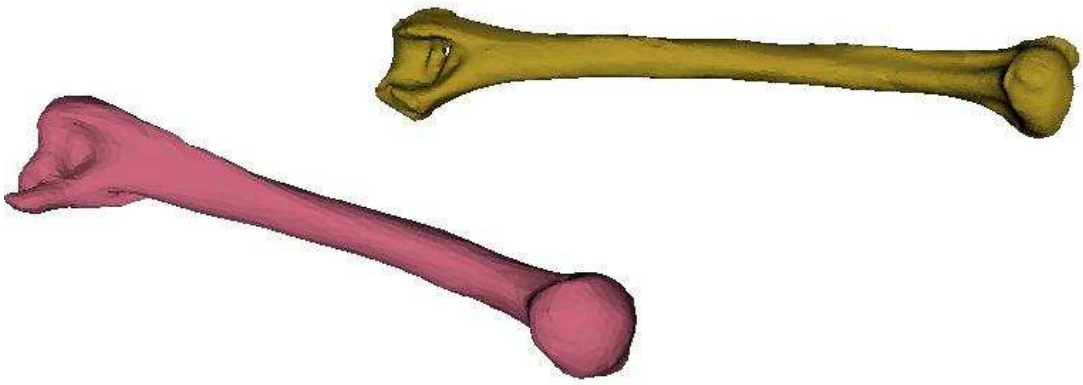

(b) The *Colobus* humerus (pink) is scaled using its current bounding box; the *Papio* humerus is unchanged.

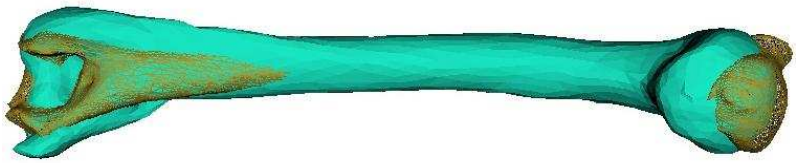

(c) The scaled *Colobus* humerus (in green) is aligned to the *Papio* humerus, which is shown in khakis triangular mesh surface.

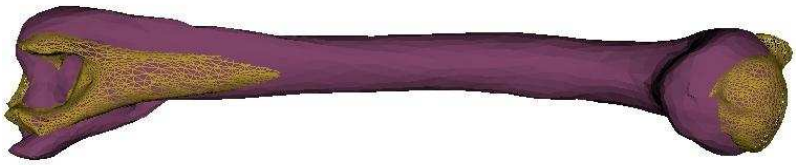

(d) The *Colobus* humerus (in purple) is scaled a second time using its modified bounding box. Then it is aligned rigidly again to the *Papio* humerus, which is shown in khakis triangular mesh surface.

Figure 5.11: Repeated scaling and alignment of a *Colobus* humerus

Scapula Model

The scaling factor is computed in a such way that any two scapulae have the same length between point 2 and point 3 as shown in Figure 5.10. That is to say, line $Q2 - Q3$ in Figure 5.9 is scaled so that it has the same length as line $P2 - P3$. The scaling factor obtained was then applied to the other two directions. In Figure 5.12, a *Colobus* scapula is firstly scaled to a *Papio* scapula using the manually selected points defined in Figure 5.10, and then aligned to the *Papio* scapula rigidly using the ICP algorithm.

5.4 Results and Applications

Once the surface point correspondences are identified and the shapes are aligned in a common coordinate system, a shape $\mathbf{x}_i (i = 0, 1, \cdots, n-1)$ is denoted by a column vector of all its surface point coordinates: $\mathbf{x}_i = (x_{i1}, y_{i1}, z_{i1}, x_{i2}, y_{i2}, z_{i2}, \cdots, x_{in}, y_{in}, z_{in})^T$.

The eigenvalues of the covariance matrix C are the measurements of the variations described by the corresponding eigenvectors. They decrease rapidly, which means the variations described by the corresponding principal axes also decrease rapidly. The cumulative percentage of eigenvalues of the first few principal components in model one (including size variation) is much greater when compared to model two (excluding size variation), which can be seen in Figure 5.13. In the humerus models, the first three principal modes of model one contribute more than 99% of the shape variability whilst the first three principal modes of model two contribute 73%. In the scapula models, the first three principal modes of model one contribute 97% of the scapula shape variability whilst the first three principal modes of model two contribute 83%.

Since different genera in the datasets have different numbers of samples, the overall mean shape $\overline{\mathbf{x}}$ in Equation 2.16 was calculated from the mean shapes of every genus. Projections of all the humerus shapes onto the first three principal axes (transformed shape vectors) are shown in Figures 5.14 and 5.15 and projections of all the scapula shapes are shown in Figures 5.16 and 5.17. Each point in the figures represents a humerus or a scapula shape.

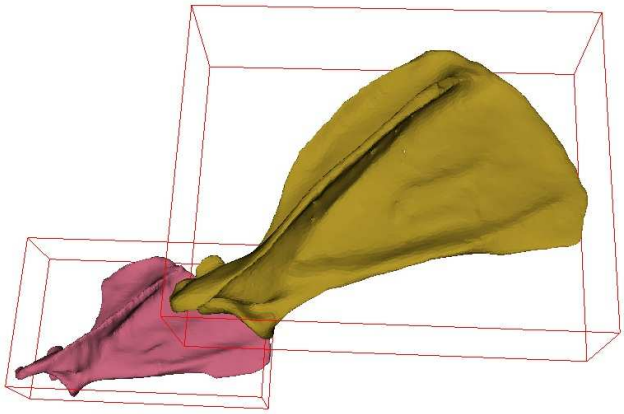

(a) A *Papio* scapula (right) and a *Colobus* scapula in their bounding boxes

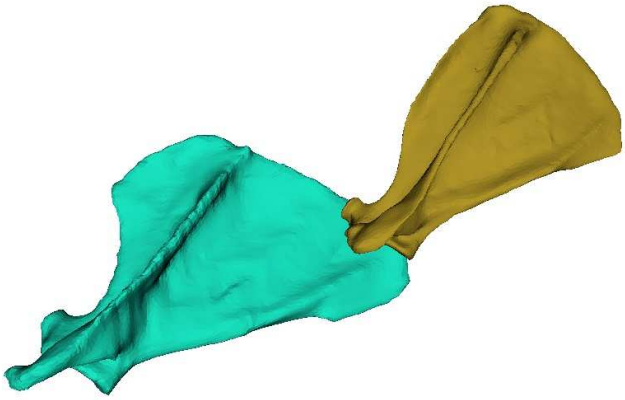

(b) The *Colobus* scapula (left) is scaled using its bounding box

(c) The scaled *Colobus* scapula (in purple) is aligned to the *Papio* scapula

Figure 5.12: Scaling and alignment of a *Colobus* scapulae. The reference shape is a *Papio* scapula shape.

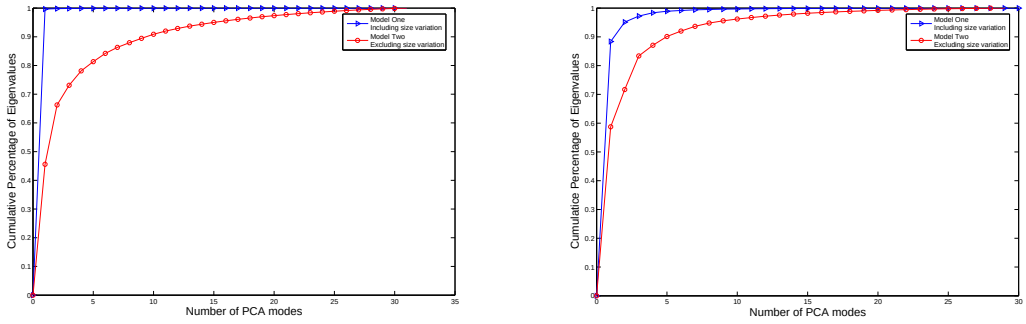

(a) Humerus dataset (b) Scapula dataset

Figure 5.13: Cumulative percentages of eigenvalues of the humerus models and the scapula models

Figure 5.14(a) shows three clusters, one of which contains four types of the great apes including the humans, one of which contains only the *Papio* humeri and one of which consists of all the remaining monkey humeri. The great ape cluster can be further classified into two sub-clusters, one of which consists of only the *Gorilla* humeri. This clustering pattern is consistent with the locomotor grouping in Table 3.3 (page 67). The *Homo* and the *Pongo* in the figure can be categorised into group three according to Table 3.3. In Figure 5.14(b), the group of *Papio* which encompasses the fewest locomotor types (quadrupedalism and vertical climbing), separates itself from all the other genera in the dataset.

When size variation is excluded, the first principal components distinguish the great apes from all the monkeys (Figure 5.15(a)). The genera encompassing bipedalism and brachiation locomotor types are different in morphology from the genera that do not encompass these locomotor types. No obvious clusters can be identified from the projections on the second and the third principal axes (Figure 5.15(b)).

In scapula model one, the human scapulae are distinguishable in both Figures 5.16(a) and 5.16(b), and they separate themselves from all the remaining genera in the dataset on the plane formed by the second and the third components (Figure 5.16(b)). The *Gorilla* are separated by the first principal component (Figure 5.16(a)). The *Pongo*, primarily arboreal, in Figure 5.16(b) belong neither to the *Homo* group, nor to that of any other genus.

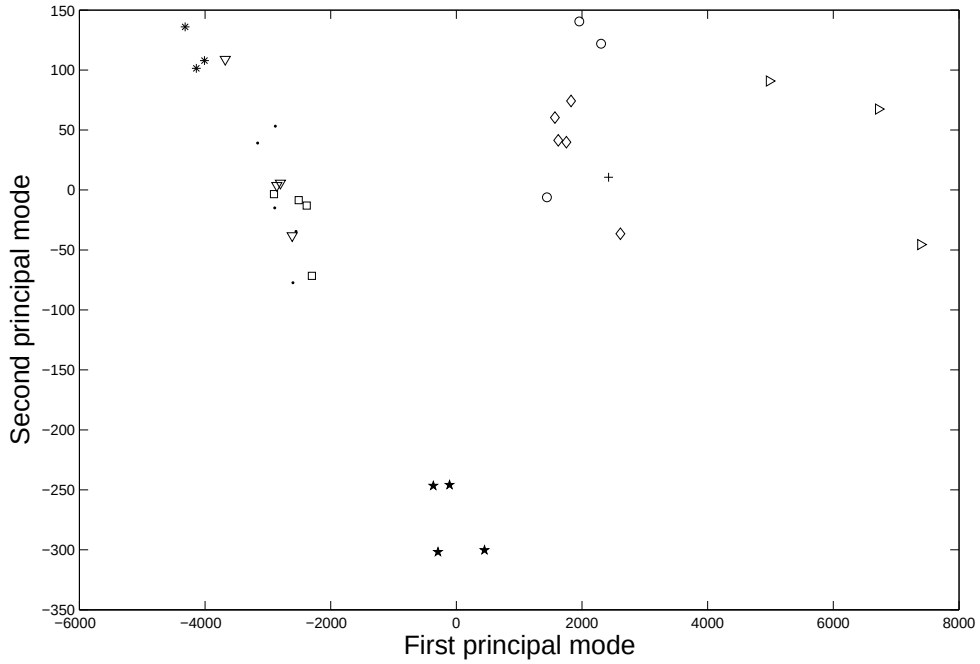

(a)

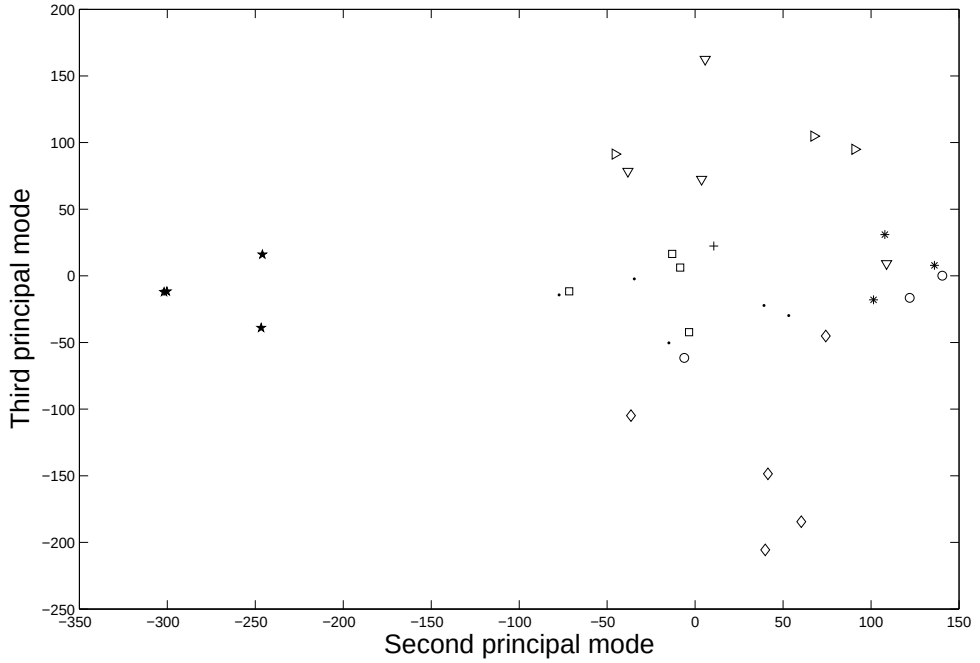

(b)

∗ *Cebus*; ∘ *Pan*; □ *Colobus* ▷ *Gorilla*; ♢ *Homo*; ▽ *Macaca*; + *Pongo*; ⋆ *Papio*; • *Presbytis*

Figure 5.14: Quantification of the humeri - Model One (Including size variability)

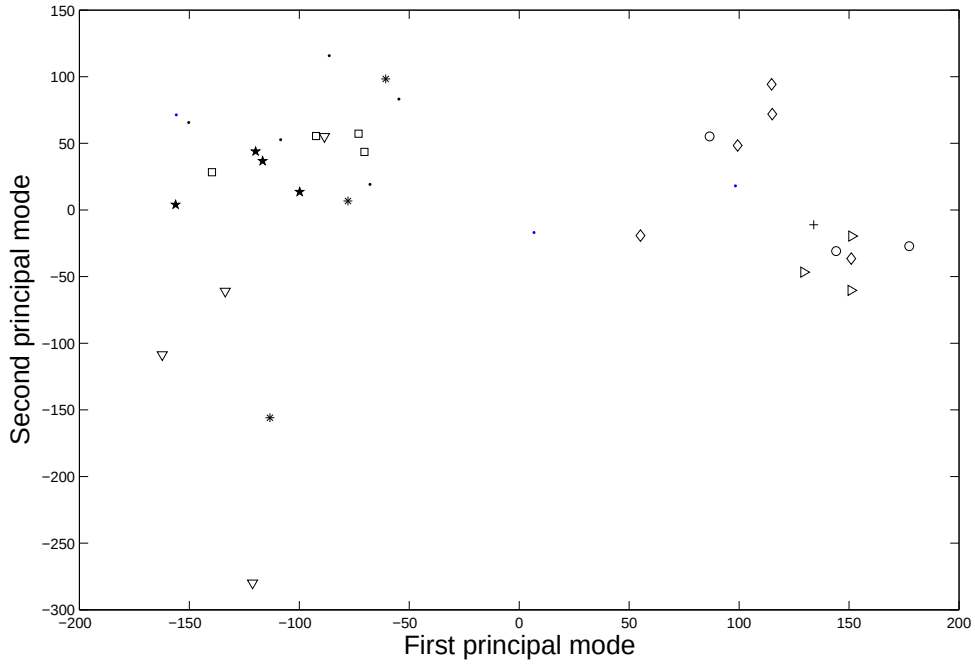

(a)

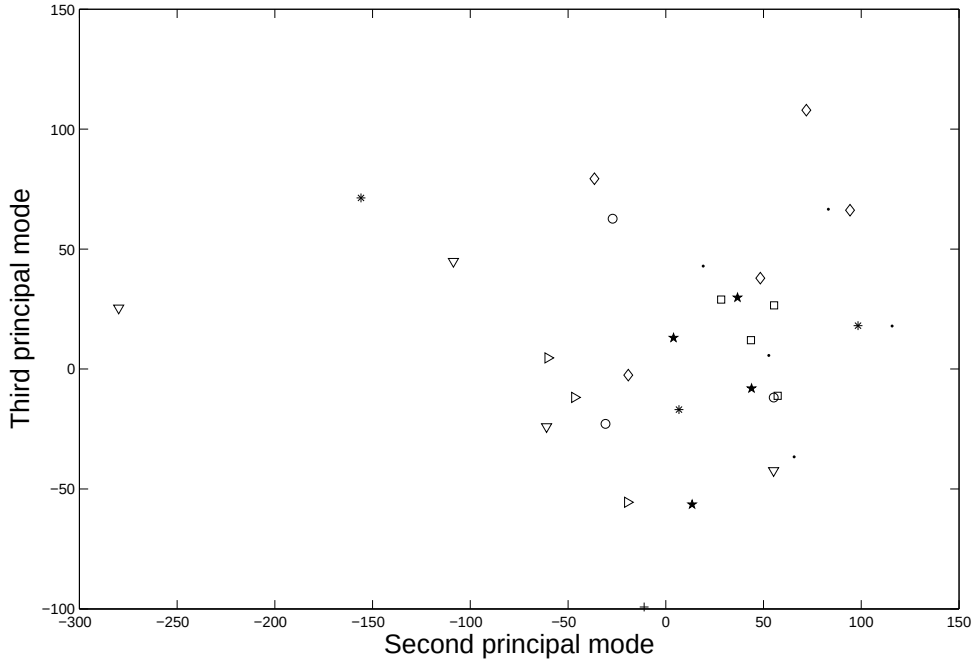

(b)

∗ *Cebus*; ∘ *Pan*; □ *Colobus* ▷ *Gorilla*; ♢ *Homo*; ▽ *Macaca*; + *Pongo*; ⋆ *Papio*; • *Presbytis*

Figure 5.15: Quantification of the humeri - Model Two (Excluding size variability)

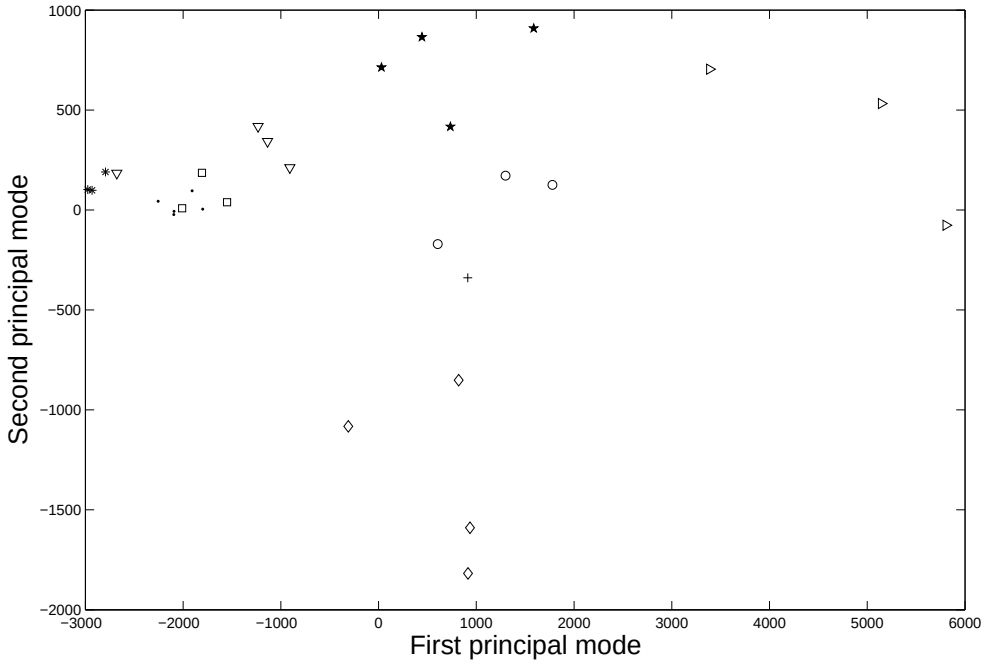

(a)

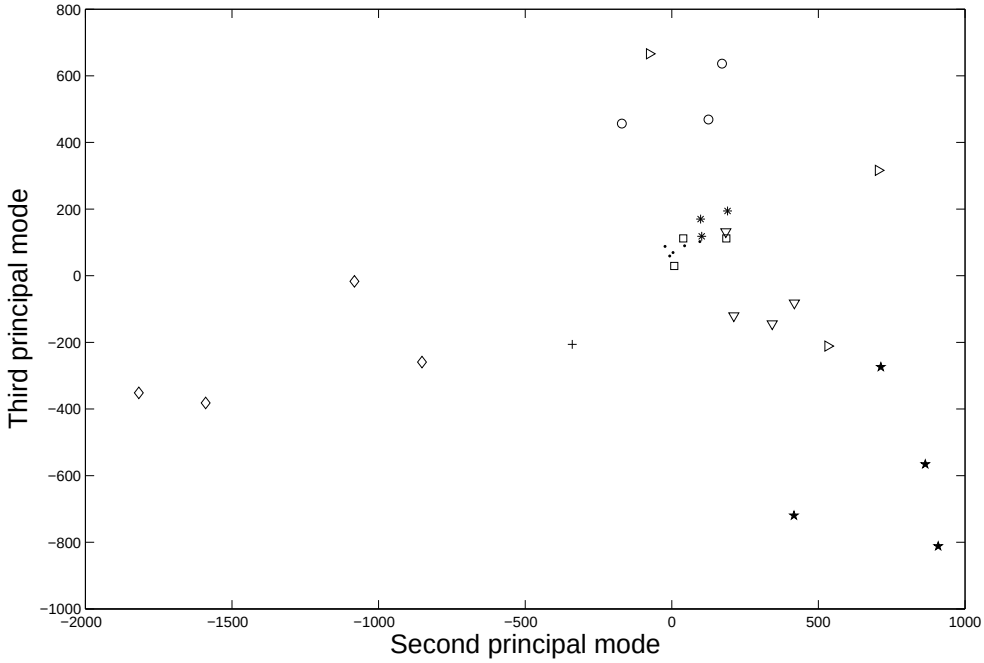

(b)

$*$ *Cebus*; $\circ$ *Pan*; $\square$ *Colobus* $\triangleright$ *Gorilla*; $\diamondsuit$ *Homo*; $\bigtriangledown$ *Macaca*; $+$ *Pongo*; $\star$ *Papio*; $\bullet$ *Presbytis*

Figure 5.16: Quantification of the scapulae - Model One (Including size variability)

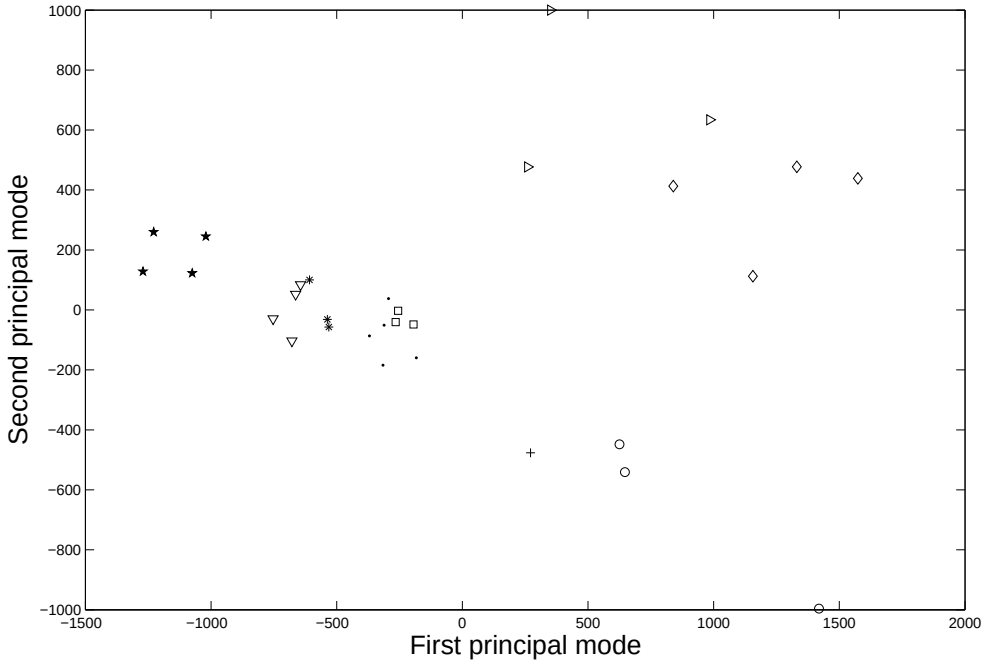

(a)

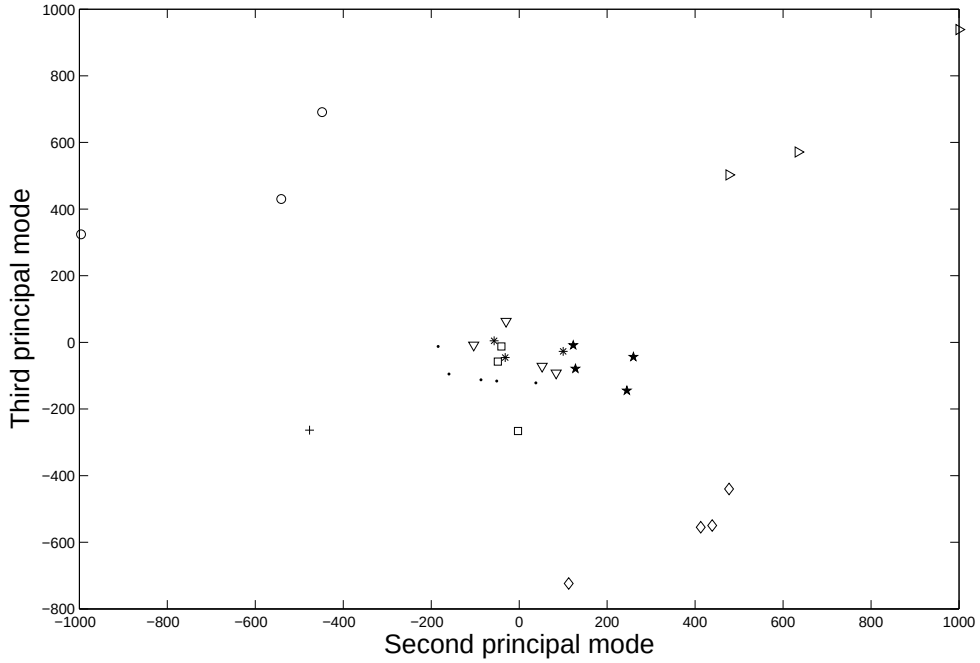

(b)

∗ *Cebus*; ∘ *Pan*; □ *Colobus* ▷ *Gorilla*; ♢ *Homo*; ▽ *Macaca*; + *Pongo*; ⋆ *Papio*; • *Presbytis*

Figure 5.17: Quantification of the scapulae - Model Two (Excluding size variability)

In scapula model two, the group consisting of the great apes is located on the positive side of the first principal axis whist the group consisting of monkeys is located on the negative side (Figure 5.17(a)). Four clusters can be identified: one consists of the *Papio* only, one consists of all the remaining monkeys, one contains the *Pongo* and the *Pan*, and one contains the other two types of great ape, the *Homo* and the *Gorilla*. If we group the remaining two clusters (both located on the positive size of the first principal axis), the clustering pattern is also consistent with the locomotion grouping in Table 3.3. On the plane formed by the second and the third principal axes (Figure 5.17(b)), the monkey scapulae tend to gather at the centre of the cluster whilst the great ape scapulae take up a larger area around the monkey scapulae. This suggests that the morphological variation of large primate genera is greater than those from smaller primate genera.

The present datasets contain a large number of variables. Each coordinate of a surface point is a variable (number of variables = 3 × number of surface points). However, the sample size of the dataset is small. Validation of applying PCA to this kind of dataset is out of the scope of this thesis. To assess the robustness of the proposed methodologies, all applications involving PCA results (including shape models, genus classifications, and the prediction models in Chapter 6) are validated instead.

5.4.1 Classification

Using a transformed shape vector in the coordinate system formed by the principal axes (b in Equation 2.16, page 44), a given shoulder bone shape B without any prior knowledge can be classified. Assuming M_i ($i = 1, 2, \cdots, 9$) is the mean projection of each genus, and B_p is the transformed B vector, the most possible group that B belongs to is the genus whose mean vector M_i is closest to vector B_p (the shortest Euclidean distance along the first three principal axes).

Due to orthogonality of the eigenvectors P in Equation 2.16, distribution b_i on the principal axes P_i can be calculated as $b_i = P_i^T(\mathbf{x} - \overline{\mathbf{x}})$ and scaled by $b_i = b_i/\sqrt{\lambda_i}$, where λ_i is the eigenvalue corresponding to eigenvector P_i. Scaling of b is linear and it does not change the pattern of distribution. Two identical distribution patterns, with and without

the eigenvalue scaling, are shown in Figure 5.18. The Euclidean distance between any two points in projection space is calculated based on the scaled axes.

Leave-one-out validations of the classification were conducted. In each validation, one of the humerus shapes was taken out and an SSM was built on the remainder of the shapes. The left-out humerus shape was then classified based on the constructed model. Since there are 32 humeri and 30 scapulae and there is only one pair of *Pongo* shoulder bones available, 31 humerus classifications and 29 scapula classifications were conducted.

Classifying the Humeri

As mentioned above, two clusters, but no further sub-clusters, are distinguishable in the coordinate system constructed by the principal axes of humerus model two. Consequently, classification of the humeri without size variation shows poor results, with only 12 accurate classifications out of 31 (38.7% correctness). Though most of the humeri are inaccurately classified to genus, they were classified to a genus belonging to the same higher taxon (the monkey category or great ape category). For example, in model two, *Cebus* 1 was classified as *Papio* but both of them belong to the monkey category. *Pan* 1 was classified as *Gorilla* but they both belong to the great apes. All 31 primate humeri are classified within the correct higher taxon.

When size variation is included, humerus shapes from the same genus tend to group together in the coordinate system (Figure 5.15) and, consequently, the classification based on model one shows much more promising results, with 25 accurate classifications out of 31 (80.6% correctness). Table 5.1 gives the classification results on the humerus dataset.

Classifying the Scapulae

Table 5.2 gives the classification results of the scapula dataset. 21 out of 29 classifications are accurate when size variation is included and 23 out of 29 classifications are correct when it is excluded, claiming 72% and 79% correctness. For those scapulae that are inaccurately classified, they are classified to the genus which belongs to the same higher taxon (the monkeys or the great apes) of themselves. In model two, only *Papio* 4 (the

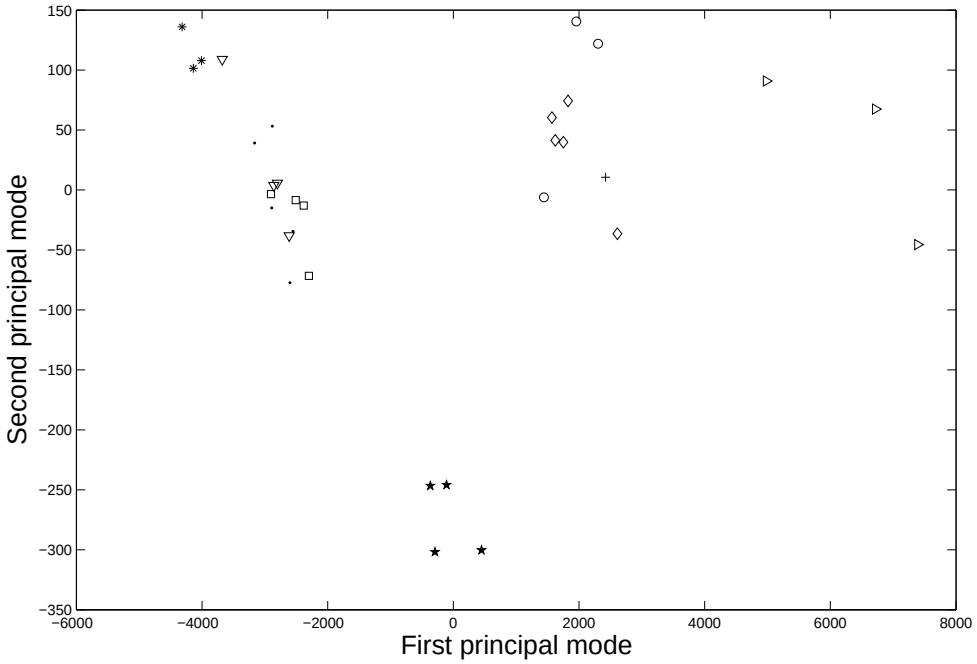

(a) Distribution without scaling

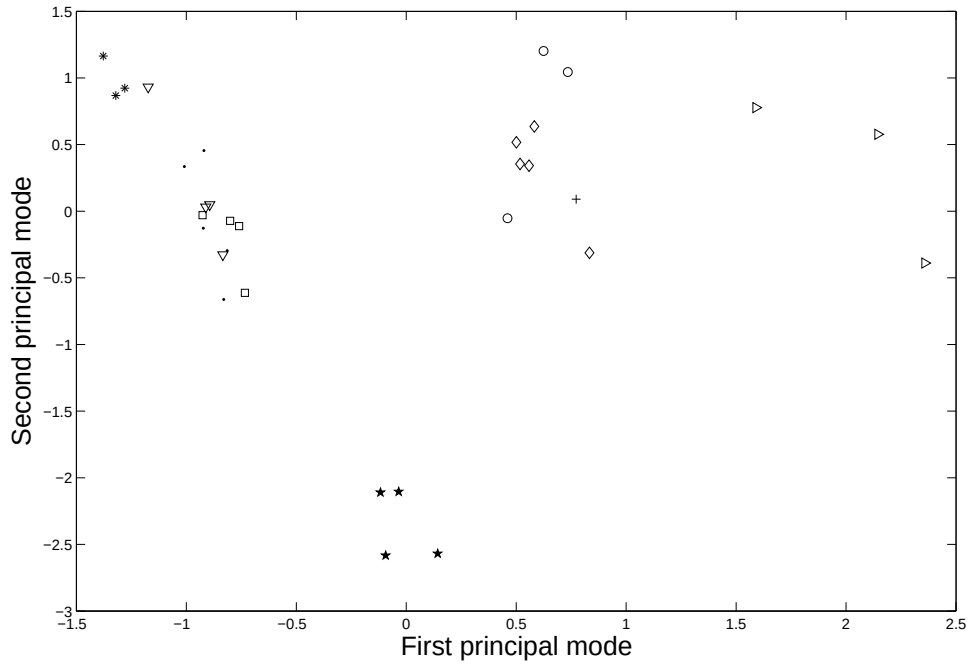

(b) Distribution with scaling

∗ *Cebus*; ∘ *Pan*; □ *Colobus* ▷ *Gorilla*; ♢ *Homo*; ▽ *Macaca*; + *Pongo*; ⋆ *Papio*; • *Presbytis*

Figure 5.18: Comparison of the quantification distribution patterns with and without scalings. In (a), the coordinates b_i on the principal axes are calculated by $b_i = P_i^T(\mathbf{x}-\overline{\mathbf{x}})$; in (b), the coordinates are scaled by $b_i = b_i/\sqrt{\lambda_i}$.

Specimen	Model One (Excluding size)	Model Two (Including size)
Cebus 1	*Cebus*	*Papio*
Cebus 2	*Cebus*	*Macaca*
Cebus 3	*Cebus*	*Presbytis*
Colobus 1	*Presbytis*	*Presbytis*
Colobus 2	*Colobus*	*Colobus*
Colobus 3	*Colobus*	*Papio*
Colobus 4	*Colobus*	*Presbytis*
Macaca 1	*Macaca*	*Macaca*
Macaca 2	*Macaca*	*Macaca*
Macaca 3	*Cebus*	*Papio*
Macaca 4	*Macaca*	*Macaca*
Papio 1	*Papio*	*Colobus*
Papio 2	*Papio*	*Cebus*
Papio 3	*Papio*	*Colobus*
Papio 4	*Papio*	*Papio*
Presbytis 1	*Presbytis*	*Presbytis*
Presbytis 2	*Colobus*	*Colobus*
Presbytis 3	*Colobus*	*Papio*
Presbytis 4	*Presbytis*	*Colobus*
Presbytis 5	*Presbytis*	*Cebus*
Pan 1	*Pan*	*Gorilla*
Pan 2	*Homo*	*Gorilla*
Pan 3	*Pan*	*Homo*
Gorilla 1	*Gorilla*	*Gorilla*
Gorilla 2	*Gorilla*	*Gorilla*
Gorilla 3	*Gorilla*	*Pan*
Homo 1	*Homo*	*Homo*
Homo 2	*Homo*	*Homo*
Homo 3	*Homo*	*Homo*
Homo 4	*Pan*	*Homo*
Homo 5	*Homo*	*Pan*

Table 5.1: Leave-one-out validations of the humerus classification

Specimen	Model One (Excluding size)	Model Two (Including size)
Cebus 1	*Cebus*	*Cebus*
Cebus 2	*Cebus*	*Macaca*
Cebus 3	*Cebus*	*Cebus*
Colobus 1	Prebytis	*Colobus*
Colobus 2	*Macaca*	*Presbytis*
Colobus 3	*Colobus*	*Presbytis*
Macaca 1	*Macaca*	*Macaca*
Macaca 2	*Macaca*	*Macaca*
Macaca 3	*Cebus*	*Macaca*
Macaca 4	*Macaca*	*Cebus*
Papio 1	*Papio*	*Papio*
Papio 2	*Papio*	*Papio*
Papio 3	*Papio*	*Papio*
Papio 4	*Pongo*	*Papio*
Presbytis 1	*Presbytis*	*Presbytis*
Presbytis 2	*Colobus*	*Colobus*
Presbytis 3	*Colobus*	*Presbytis*
Presbytis 4	*Presbytis*	*Colobus*
Presbytis 5	*Presbytis*	*Presbytis*
Pan 1	*Pan*	*Pan*
Pan 2	*Pongo*	*Pan*
Pan 3	*Pan*	*Pan*
Gorilla 1	*Gorilla*	*Gorilla*
Gorilla 2	*Gorilla*	*Gorilla*
Gorilla 3	*Gorilla*	*Gorilla*
Homo 1	*Homo*	*Homo*
Homo 2	*Homo*	*Homo*
Homo 3	*Pongo*	*Homo*
Homo 4	*Homo*	*Homo*

Table 5.2: Leave-one-out validations of the scapula classification

monkeys) was classified as *Pongo* (great apes), giving 96.6% correct classification of the categories. Classification accuracy of the scapula dataset is much higher than that of the humerus dataset when size is included, and it is slightly worse when size is excluded.

5.4.2 Plausible Shapes

According to Equation 2.16, changes of the latent variable b within a certain range of distribution can reconstruct the plausible shapes. These reconstructed shapes are able to demonstrate the morphological variation visually corresponding to each principal mode.

The results show that, in model one (including size), the first principal modes in the humerus model and the scapula model are related to size variation (Figures 5.19 and 5.20).

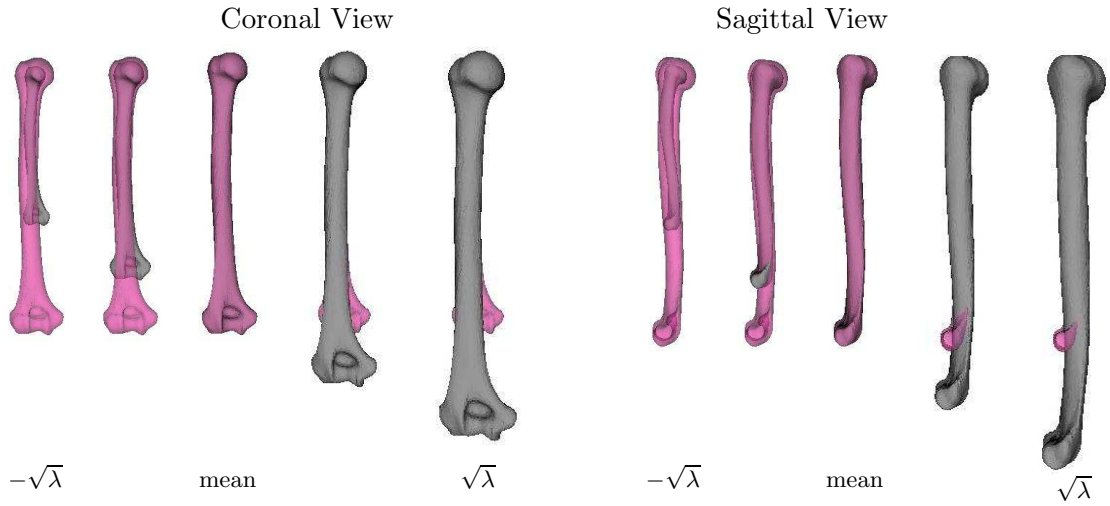

Figure 5.19: Humerus morphological variation described by the first principal mode (model one - including size)

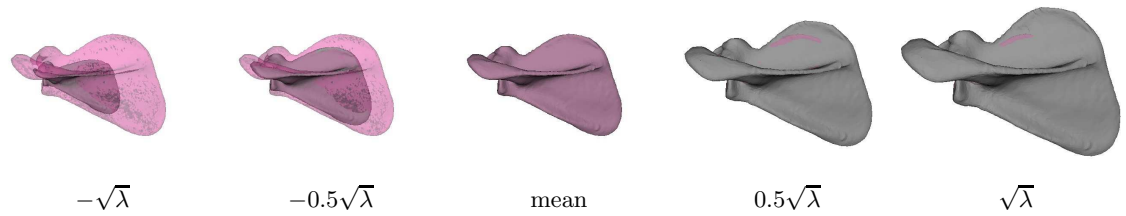

Figure 5.20: Scapula morphological variation described by the first principal mode (model one - including size)

Humerus Model

Size is an important variable in the analysis of the primate humerus shape. It claims 99.7% of variability in the present humerus shape model. When size was removed, the humerus shapes within the same category (the monkeys or the great apes) are barely distinguishable. When comparing Figure 5.21 with Figure 5.22, it can be seen that the variation of the first principal mode in model two (excluding size) is similar to that of the second principal mode in model one (including size), which is related to bending of the humeral shaft. Furthermore, the variation of the second principal mode in model two

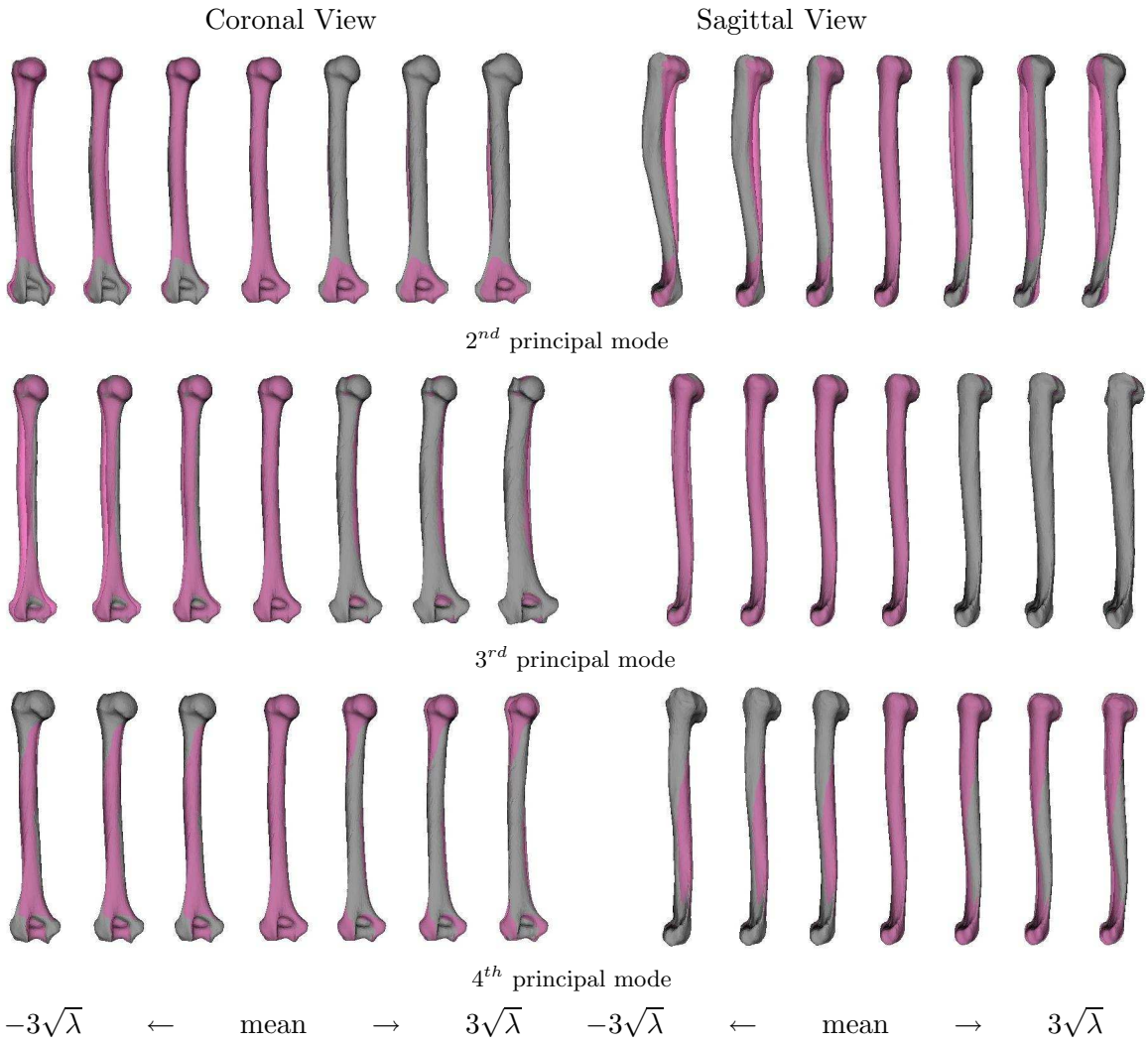

Figure 5.21: Humerus morphological variations described by the 2^{nd}, 3^{rd} and 4^{th} principal modes (model one - including size)

(excluding size) is similar to that of the third principal mode in model one (including size), regarding the width of the humeral shaft.

According to the morphological variations and the distribution patterns (Figures 5.14 and 5.15), one can tell that bending is the main morphological variation distinguishing the humeri from the monkeys and the humeri from the great apes. This can be a key element in analysing shape changes relating to the development of bipedalism and brachiation. Relating Figure 5.19 to Table 3.3 and Figure 5.14 shows that difference in humerus size is an important variable characterising to the three locomotor groups.

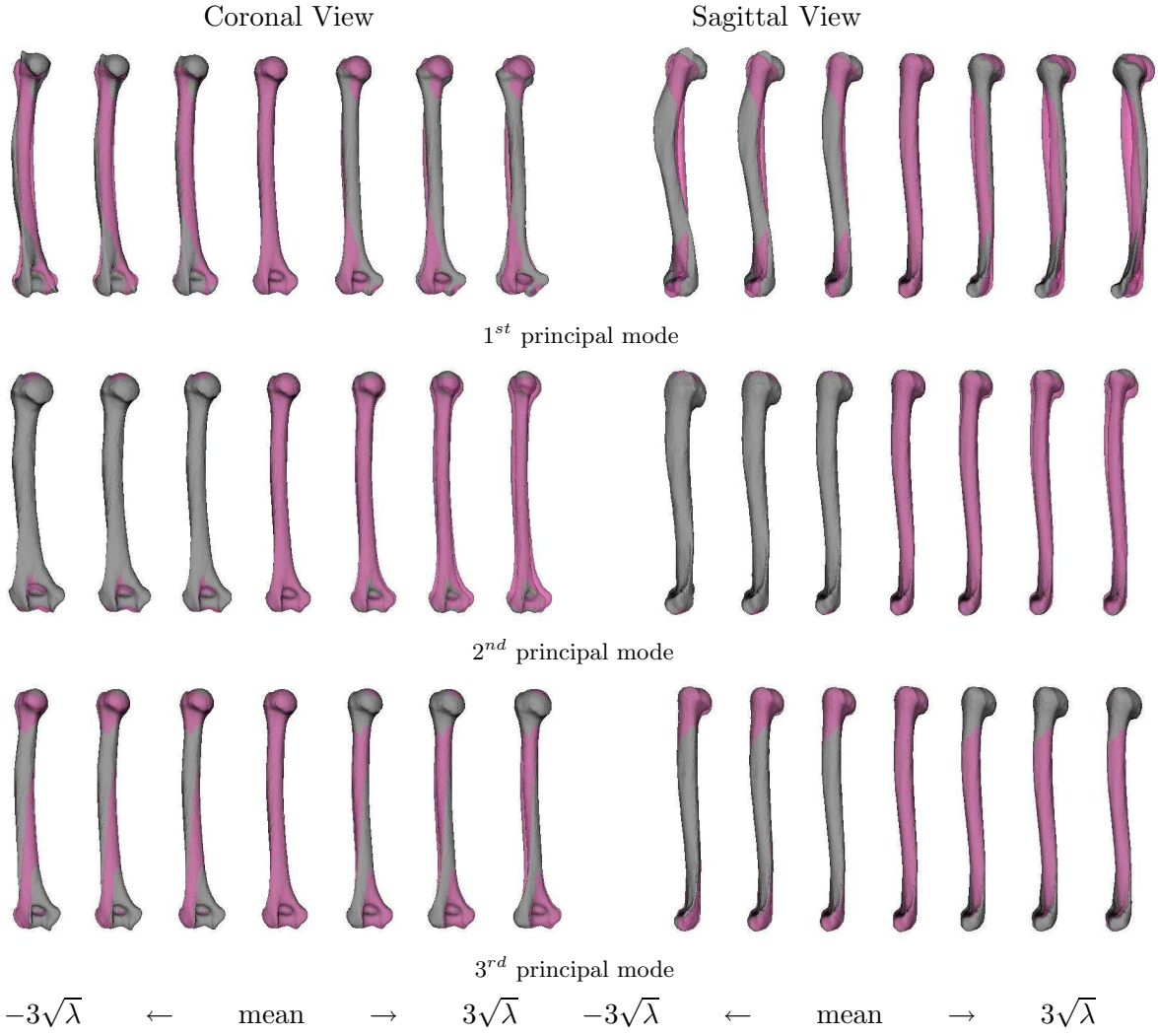

Figure 5.22: Humerus morphological variations of the first three principal modes (model two - excluding size)

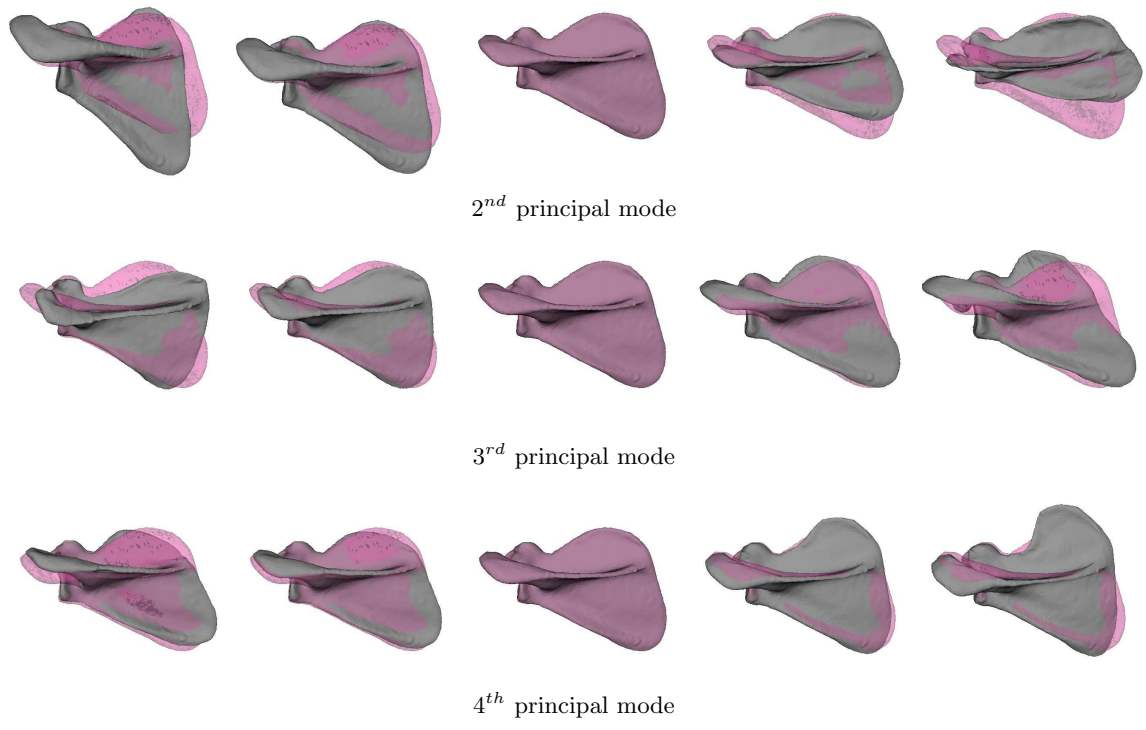

Figure 5.23: Scapula morphological variations described by the 2^{nd}, 3^{rd} and 4^{th} principal modes (model one - including size)

Scapula Model

Morphological variations of the scapulae are demonstrated in Figures 5.23 and 5.24. In model one (including size), the shape variations of the second principal mode are related to the relationship of length to breadth of the bone, and to the extent of the acromion. The long, narrow scapula becomes progressively broader, primarily due to the increase of size of the infraspinous fossa, and the acromion becomes more extended. This is consistent with the alterations of the scapula shape with the change from pronograde to orthograde posture as suggested by Inman *et al* [ISDA44]. In model two (excluding size), the first principal mode corresponds to the size of the infraspinous and supraspinous fossae. Similar to the second principal mode in model one, the acromion becomes more extended as the scapula blade becomes broader.

Compared to the humerus-shape model, the size of the scapulae in the dataset is less dominant although the first principal mode accounts for 88.4% total variance. When

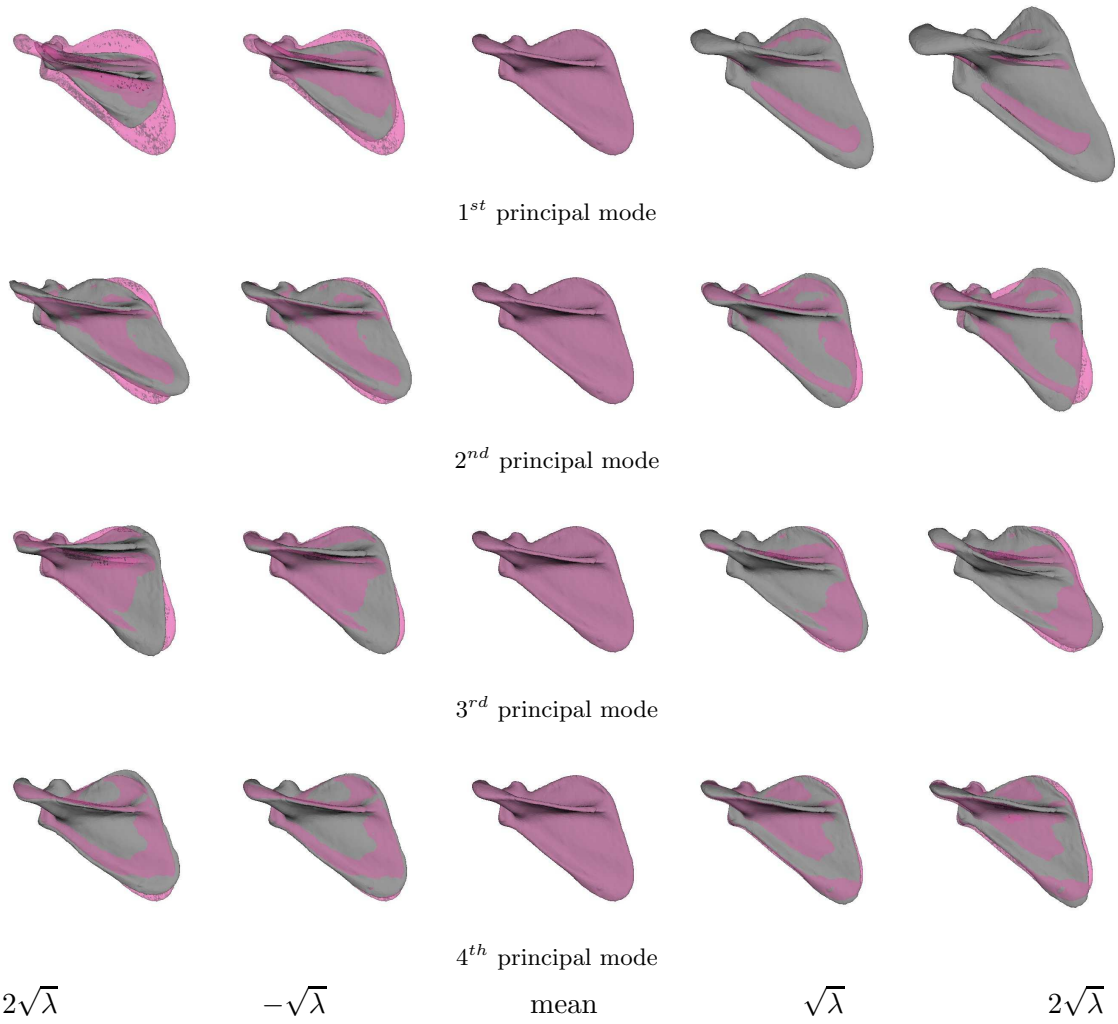

Figure 5.24: Scapula morphological variations of the first four principal modes (model two - excluding size)

size variation is excluded, the classification of the scapulae shows 71% accuracy in the leave-one-out validations (Table 5.2), which is more accurate than was the classification of the humeri (Table 5.1). When analysing correlations between shoulder bone morphology and locomotion, the scapulae are likely to provide more morphological information than the humeri, since they are more distinguishable between genera.

5.5 Statistical Shape Models of the Human Femora

The methodology developed to build a 3D SSM for the humeri was applied to a set of human femora. Size variation is essential and therefore included in the model. Point-to-point

correspondence establishment of the bone surfaces are obtained using multi-resolution B-spline FFD (Section 5.2). Two shape models were built - one aligned the training shapes with the centres of femoral heads fixed, and the other without the centres being fixed. Both alignments utilised the ICP algorithm. In the former model, ICP was applied using the centre of the femoral head as the centre of rotations and translations; in the latter model, the centroid of all surface points was taken as the centre of rotations and translations. Assuming the femoral head is a perfect sphere, the centre point can be calculated by fitting a sphere to the femoral head (implementation in Chapter 4, Section 4.3.2). The alignments of both models are displayed in Figure 5.25.

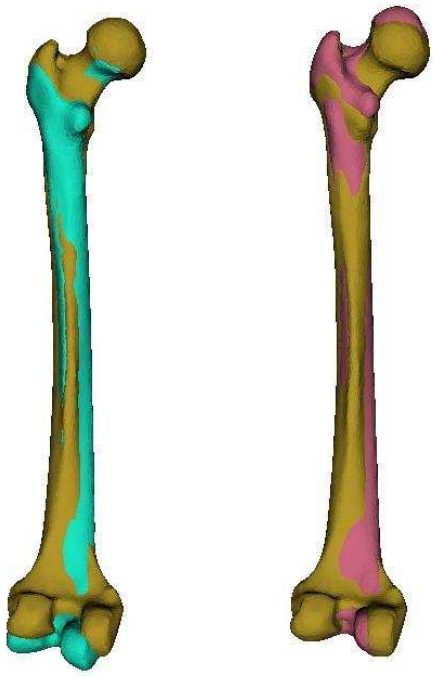

(a) (b)

Figure 5.25: ICP alignment of the femur shapes. Khakis shapes in both (a) and (b) are reference shapes. (a) centre of the femoral head fixed, (b) ICP rigid alignment.

The two models are built from 24 adult human femora, 17 left femora and seven right femora. They were CT scanned with imaging parameters as follows: slice thickness $1mm$; image matrix dimension 512×512, with in-plane resolution $0.39mm \times 0.39mm$. The outline of each femur was segmented manually using the software *Amira*® and then converted into a 3D triangulated mesh surface using the marching cubes algorithm in the

software *Image Registration Toolkit*. Decimation and smoothing were both implemented using *Amira*®. The seven right femora were flipped to the left femora using their mirror shapes.

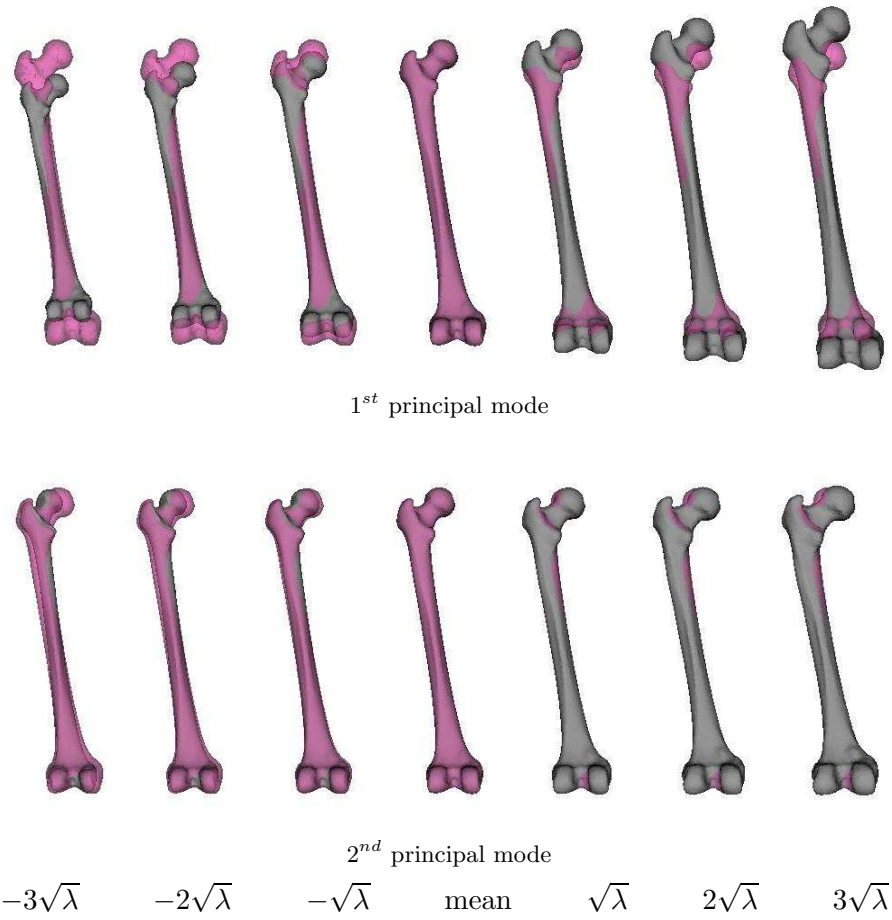

Figure 5.26: Femur morphological variations of the first two principal modes (model one - without fixing the femoral head)

The initial resolution of the mesh grid in the multi-resolution B-spline FFD was $40mm \times 40mm \times 40mm$ with four subdivisions. Shape variations of the femora, corresponding to the first two principal modes, are shown in Figures 5.26 and 5.27. In model one (with the centre of the femoral head fixed), the first three principal modes represent 98% shape variance and its first principal mode accounts for 94% of the total variance. According to Figure 5.26, size is the most prominent variation and the extension of the femoral neck is the second most important component. In model two, the first three principal modes explain 95% of the total shape variations and the first principal mode describes

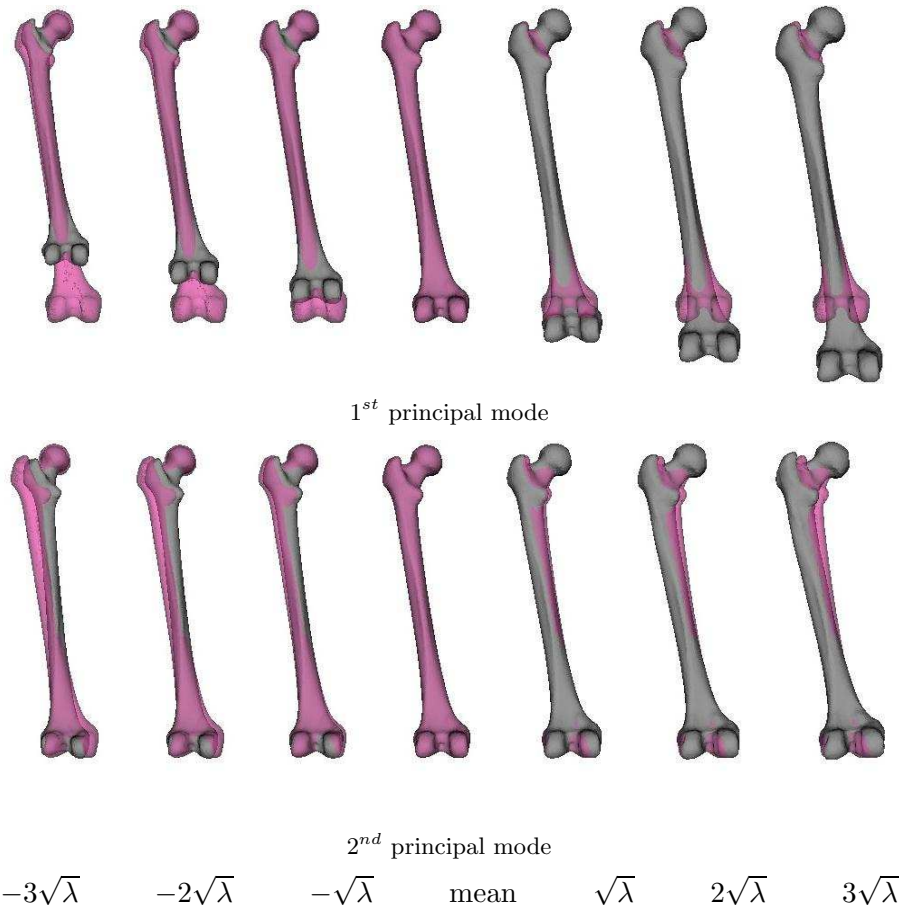

Figure 5.27: Femur morphological variations of the first two principal modes (model two - fixing the femoral head)

89% of the total variance. The first component is also related to size of the femora and the second component is related to the extension of the femoral head.

5.6 Bone Morphing with Statistical Shape Models

Bone morphing enables a complete surface to be reconstructed from a set of extremely sparse 3D digitised anatomical landmarks or surface points on the bone. Only a set of points on the bone surface is required to instantiate its bony structure without scanning the complete bone. This technique is useful in reconstructing a whole bone with discrete bone segments or with bone tumors. This section simulates the surface point digitisation procedure and describes how to reconstruct a complete femur surface on the sparse surface points.

5.6.1 Simulation of Digitising Surface Points

The reproduction of the surface around the femoral neck, the greater trochanter and the anterior border of the femoral notch is of importance and geometric surface points are therefore digitised on those areas. To reduce a massive manual digitising work, surface points are obtained automatically using the skeleton of the crest points. Details concerning the extraction of crest points and the skeletonisation are in Chapter 4, Section 4.2. A demonstration of the selected surface points is shown in Figure 5.28.

Figure 5.28: Simulation of digitised point landmarks

5.6.2 Methodology

The morphing procedure involves two steps: global rigid registration and local morphological deformations. Given a set of sparse points on a femur surface which was not used in the shape model construction, the ICP algorithm was applied to rigidly register the point cloud to the mean shape of the training set. Starting from the mean shape which has zero weights on all principal components, a new shape fitting the point cloud is reconstructed by changing the weights of the principal components (latent variables) so that the root mean square (RMS) distance between the point cloud and the resulting surface is smaller than a pre-defined threshold.

Global Registration

Two different rigid alignments, corresponding to the two models described in Section 5.5, were applied in different circumstances. If the centre of the femoral head is not provided (for example the femoral head is incomplete), the point cloud is translated and rotated to the mean shape with the centroid of the point cloud (result shown in Figure 5.29(a)).

When the centre of the femoral head is available (if the hip joint is not widely opened, this centre can be considered as the centre of the sphere that best fits the cloud of points obtained during motions (this is known as the *functional method* [SBM+02]; if the joint is physically opened, the digitisation of geometric surface points is easy), it acts as the translation and rotation centre in global rigid registration (Figure 5.29(b)). To obtain the centre of the femoral head from a study-femur shape, 20 surface points were randomly picked to simulate the digitised surface points (right top sub-figure in 5.29(b)). To obtain the centre of the femoral head of the mean femur shape of the training set, a sphere can be fitted to surface points on the femoral head, which can be obtained by region-growing of a few manually-selected seed points (seed points are shown in green in the right bottom sub-figure in Figure 5.29(b)).

(a) Without centre of the femoral head fixed (model one)

(b) Centre of the femoral head fixed (model two)

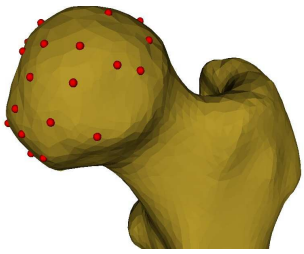

Manually selected geometric surface points on a study femur

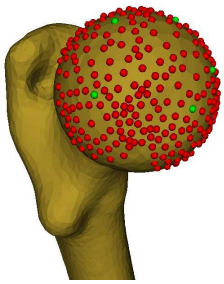

Region growing from the green seed points on the mean shape

Figure 5.29: Global rigid registration in femur morphing

Local Deformations

The surface of the mean shape (starting shape) is deformed to the point cloud iteratively until convergence. The deformation procedure is formulated as a linear equation system and the solution to the system is a set of weights on the principal components that best fit the deformed shape to the point cloud. The objective function to minimise the surface-points distance is defined as [rSJ04]

$$f = \gamma \sum_{k,j=1}^{N} \|\vec{Y}_k - (\vec{X}_j + \sum_{i=1}^{m} \alpha_i \vec{p}_i(j))\|^2 + \sum_{i=1}^{m} \frac{\alpha_i^2}{\lambda_i^2} \tag{5.1}$$

where N the number of points that are digitised, $\vec{Y}_i$ is the k^{th} digital point, $\vec{X}_i$ is the point in the starting shape that closest to $\vec{Y}_i$, $\vec{p}_i(j)$ is the j^{th} tuple of the i^{th} shape basis vector, λ_i is the i^{th} eigenvalue and α_i are the weights on principal modes of the m shape. The first term minimises the distance between the reconstructed shape and the cloud of points; the second term controls the probability of the reconstructed shape. The factor γ is a parameter that balances the two terms of the function. Its optimal value is dependent on individual applications and it is determined empirically as $1e-5$ in the present work.

To solve this equation and determine the weights α_i, function f is differentiated with respect to α_i and equated to zero, which gives

$$2\gamma \sum_{k,j=1}^{N} (\vec{Y}_k - \vec{X}_j - \sum_{i=1}^{m} \alpha_i \vec{p}_i(j))(-\vec{p}_i(j)) + \frac{2\alpha_i}{\lambda_i^2} = 0 \tag{5.2}$$

The linear equation system can be written as $A\alpha = b$, where

$$A = \begin{pmatrix} 2\gamma \sum_{j=1}^{N} (\vec{p}_1(j))^2 + \frac{2}{\lambda_1^2} & 2\gamma \sum_{j=1}^{N} \vec{p}_2(j)\vec{p}_1(j) & \cdots & 2\gamma \sum_{j=1}^{N} \vec{p}_m(j)\vec{p}_1(j) \\ 2\gamma \sum_{j=1}^{N} \vec{p}_1(j)\vec{p}_2(j) & \ddots & & \vdots \\ \vdots & & \ddots & \vdots \\ 2\gamma \sum_{j=1}^{N} \vec{p}_1(j)\vec{p}_m(j) & \cdots & \cdots & 2\gamma \sum_{j=1}^{N} (\vec{p}_m(j))^2 + \frac{2}{\lambda_m^2} \end{pmatrix}$$

and

$$b = \begin{pmatrix} 2\gamma \sum_{k,j=1}^{N} \vec{p}_1(\vec{Y}_k - \vec{X}_j) \\ \vdots \\ \vdots \\ 2\gamma \sum_{k,j=1}^{N} \vec{p}_m(\vec{Y}_k - \vec{X}_j) \end{pmatrix} \tag{5.3}$$

A method to iteratively generate a surface to best fit the selected point set has been developed (implementation described in Algorithm 5 shown below). In each iteration, a surface is reconstructed by minimising the linear equation system $A\alpha = b$. Given a cloud of digitised points (surface points or anatomical landmarks) $\vec{Y}$ and a shape model $\vec{X}$, the iterative morphing procedure can be described as the following algorithm. ϵ is the threshold deciding if the a local minimum is reached (convergent) and it is determined empirically.

Algorithm 5 Morphing procedure

1: Initialization: $i = 0$. $\alpha^i = 0$. Align the point cloud to the mean shape of the model using ICP algorithm. The mean shape is set as the starting shape $\vec{X}^i$.
2: $i = i + 1$. $\vec{X}^i = \vec{X}^{i-1}$. Calculate the weights α^i that best fit $\vec{X}^i$ to $\vec{Y}$ by minimising Equation 5.1.
3: Deform $\vec{X}^i$ to $\vec{X}^{i*}$: $\vec{X}^{i*} = \vec{X}^i + \vec{p}\alpha$, where α the weight vector calculated from step 2.
4: Calculate the RMS distance between α^i and α^{i-1}: $E^i = RMS(\alpha^i - \alpha^{i-1})$.
5: **if** $E^i \leq \epsilon$ **then**
6: End of algorithm. Result is $\vec{X}^{i*}$.
7: **else**
8: Goto step 2.
9: **end if**

5.6.3 Results

A femur $F_i (i = 1, 2, \cdots, 24)$ was taken out of the dataset whilst the 23 remaining femora were used to build the SSM. F_i is digitised (simulative digitisation described in Section 5.6.1) using the crest line technique. A reconstructed surface fitting the aligned sparse point set is shown in Figure 5.30. The threshold ϵ of convergence is 0.15 here.

Figure 5.30(b) shows the reconstructed surface with incorporation of the centre of the femur whilst Figure 5.30(a) shows the reconstructed surface without incorporation of this point. The weights on the first five principal modes, describing 96.6% and 98.9%

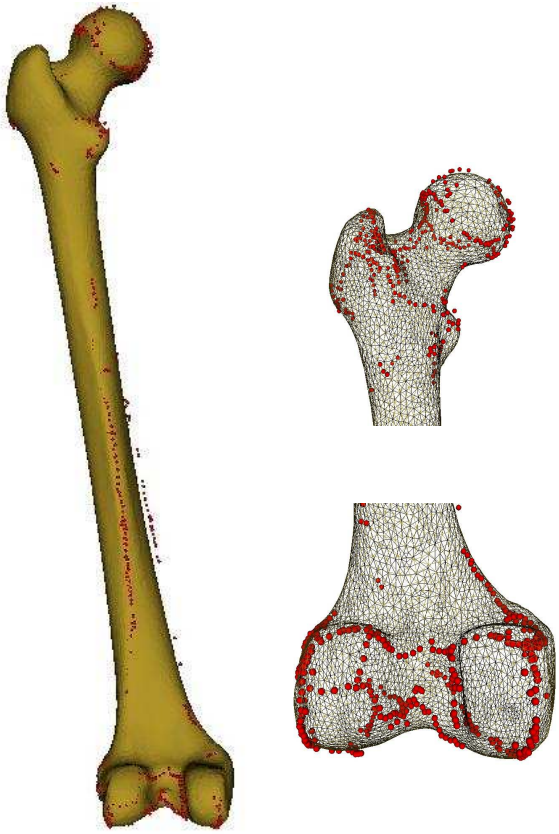

(a) Without centre of the femoral head fixed (model one)

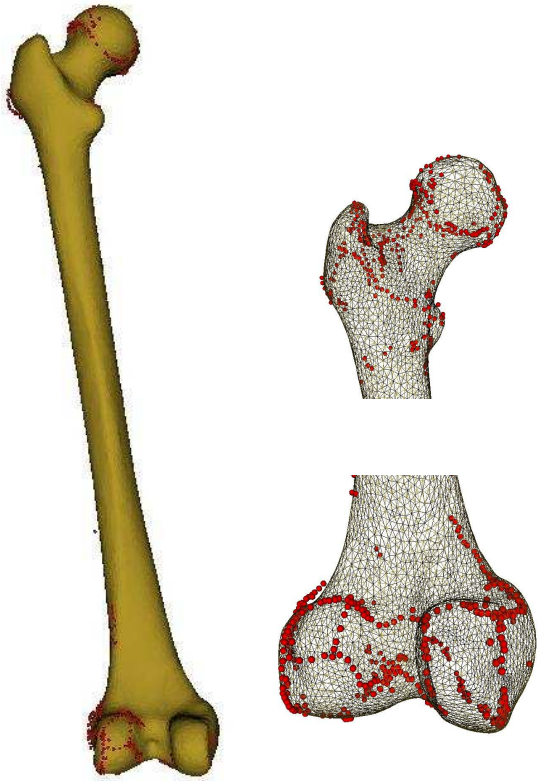

(b) Centre of the femoral head fixed (model two)

Figure 5.30: Femur morphing

total variance respectively, were calculated to generate the surfaces in both models. The reconstructed femur surface was compared to the real surface (the one left out from the model construction) to assess accuracy. RMS distance between the reconstructed shape and the real shape was estimated. Results shown in Figures 5.30(a) and 5.30(b) have RMS distances $2.09mm$ and $2.69mm$ respectively.

Leave-one-out validations were performed. Since changes of ϵ and λ in Equation 5.1 within a certain range do not generate much variability in the resulting surface, they are set as 0.15 and $1e-5$, respectively. The average RMS distances of the reconstructed femur shapes are $2.35mm$ using femur model one and $2.82mm$ using femur model two. The standard deviations of the distances in the two models are $1.24mm$ and $1.11mm$ respectively.

5.7 Summary

This chapter demonstrates methodologies to build an SSM for long bones and for complex plate-like bones. Point-to-point correspondences amongst a training set are established by applying multi-resolution B-spline FFD. Due to the large size variation across different primate genera in this thesis, two models were built for each shoulder bone, one includes size variation using bones in their original size, the other removes size variation by scaling the bones to the same size.

The major advantage of building shape models based on all available surface points compared with estimating morphological variations using traditional geometric morphometrics, which utilises a few corresponding anatomical landmarks on the subjects, is that the shape model measures the overall variation as a whole bone instead of the areas of interest defined by landmarks, which can be different from individual studies. As a result, the estimated shape variations using the shape models are not restricted to specific locations with landmarks. Another advantage is that no prior knowledge about anatomy and no manual selections are required. Even in the initialisation of deforming a monkey scapula to an ape scapula, or vice versa, labelling of the corresponding landmark sets does

not have to be very accurate. Moreover, the use of bone surfaces enables visualisation of the estimated variations (Figures 5.19 to 5.24), such that prominent variability in the training set can be easily identified. However, disadvantages come from the automation of the model construction. Since there are no correspondences provided from the bone shapes, the registration procedure is likely to miss-match some important anatomical areas, although the matching error is small.

Quantification based on PCA implies that the humeri from the different genera in the datasets cannot be easily classified if size variation is eliminated. Although the scapulae in the same size can be better classified compared with the humeri, the classification using size variation has higher accuracy. Leave-one-out validations of the classification were performed. The shapes of the shoulder bones are nearly 100% correctly classified between great apes and monkeys. By changing the weights on the PCA axes, one can see that the principal component corresponds to size variation if the shapes in the training set are in their original size. Bending of the humeral shaft and the extension of the scapular acromion are very important variations.

The methodology developed to build the SSM for long bones is applied to a set of human femora. Consideration of the centre of the femoral head provides important surgical information; all femora in the training set were aligned to the reference femur in a such way that the centre of the femoral head is taken as the translation and rotation centroid. Another alignment method was also applied, with the average surface point as the centre of translations and rotations.

An improved optimisation method for bone morphing was introduced. It iteratively deforms the shape of the model to a cloud of selected surface points until convergence. A simulation of digitising surgical anatomical landmarks is implemented using the crest line technique. It largely reduces the time involved to select landmarks. RMS errors between the reconstructed surfaces and their real surfaces were calculated in leave-one-out validations. Results of the validations indicate that the reconstructed surfaces can predict the whole surface from a set of sparse points.

Chapter 6

Predicting the Shape of a Shoulder Bone from the Adjoining Segment

6.1 Introduction

The ability to predict the shape of one bone from its neighbour at a joint could be beneficial in many areas, such as orthopaedics, palaeontology and taxonomy. In particular, the morphological variation of the humerus and scapula are important in the analysis of joint mechanics in anatomy and pathology. The intrinsic morphological relationship between these two bones has previously not been described in a numerical way and neither has a method been devised for predicting the shape of one bone from its neighbour. Recent studies on bony morphology have focused on the hip [CBE$^+$04, RNS04, SBM$^+$02, LSHD04, MK04]. The application of the studies to the shoulder are limited largely due to its complexity, high mobility and much greater range of movement than other synovial joints.

The geometry of the shoulder articulation provides little passive stabilising effect to the joint. An additional osteological constraint is provided superiorly by the acromion and the coracoid process of the scapula. Because of this intimate relationship between the two bones, the hypothesis of this study is that the shape of one would be able to predict the shape of the other.

The aims of this chapter are to (i) devise and test a new computational approach

to extract the linear correlations between a set of humeri and its corresponding set of scapulae using their respective shape variation which is described by a statistical shape model (SSM); and (*ii*) develop a robust method to construct a bone shape from the adjoining segment.

To address the two main aims, canonical correlation analysis (CCA) was chosen as the tool to represent the visible and hidden correlations between how the changes in the shape of a certain part of the scapula affect the humerus as an entire shape or vice versa. Assuming that the humerus dataset and the scapula dataset are described by two sets of multivariables, partial least square (PLS) regression was chosen to predict a set of response variables from a set of predictor variables.

A neighbour-conditional shape model was also built on the datasets. Given a scapula shape, a shape model of its adjacent humerus can be constructed conditioned on this scapula. Instead of describing morphological variation within the humerus dataset, the conditional shape model predicts the shape variation of an unknown shoulder bone based on the morphology of the other segment.

6.2 Methodology

The methodological framework is presented in Figure 6.1. The size of the shoulder bones across the present datasets varies by approximately 500%. Since shape variation is the key factors of interest in this study, CCA was applied to the shoulder bone shapes both in their original size and in their scaled size. Similar to Chapter 5, Section 5.3, two types of models were constructed, one includes size variation (model one) while the other excludes size variation (model two). Point-to-point correspondences are required in both CCA and PLS, which can be obtained using multiresolution B-spline free form deformation (FFD) (details explained in Chapter 5, Section 5.2).

Each shape in the training sets contains a large number of surface points. The number of the shoulder bone pairs (number of observations) is too small compared with the number of surface points (number of variables). As underlined in Chapter 2, Section

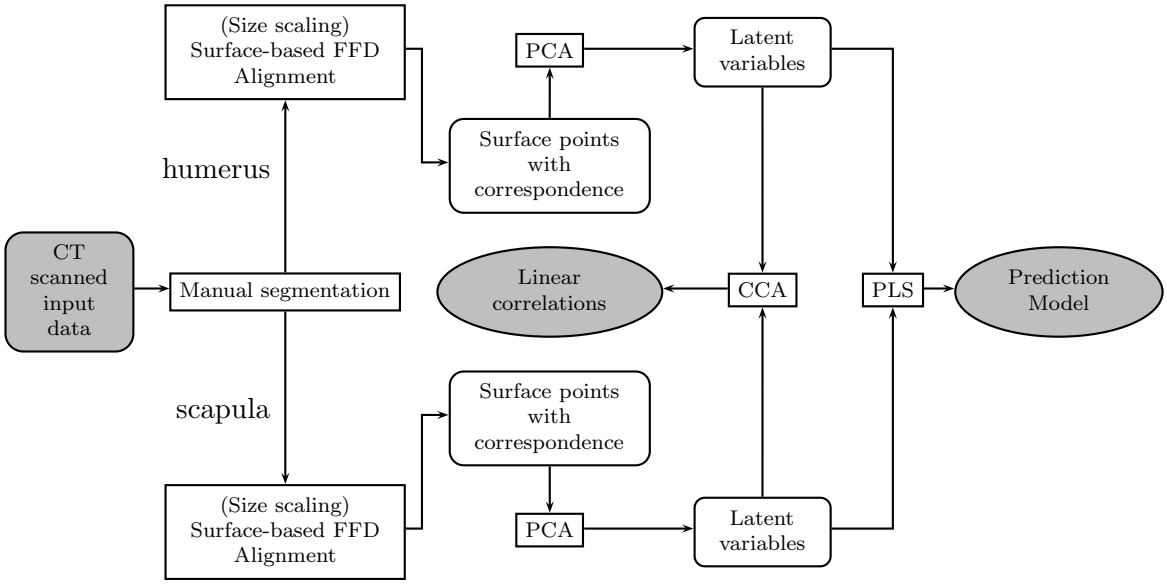

Figure 6.1: Implementation framework of canonical correlation analysis and partial least squares regression to predict bone shapes

2.7.1 and Section 2.7.2, the large number of variables makes it difficult for the analysis to be conducted using both PLS and CCA. If all the surface points are considered directly as the variables, the resulting linear equation system is indeterminate. In principal component regression (PCR), principal component analysis (PCA) is performed on the observation data matrix so that the high dimensional samples can be described by a few orthogonal (uncorrelated or independent) components. The number of predictor variables is thus reduced in the linear system and is less than the number of equations. Based on this idea, PCA was applied to reduce dimensionality of both the observation and the response data matrices.

6.2.1 Extracting Linear Correlations

A shape with surface point correspondences across the training set can be defined by a data vector $\mathbf{x}$. Assuming $\overline{\mathbf{x}}$ is the mean vector of the humerus or scapula training set, C is the corresponding covariance matrix and P is the eigenvectors of matrix C, a shape x can be transformed to the orthogonal coordinate system defined by the principal axes: $b = P^T(\mathbf{x} - \overline{\mathbf{x}})$. Components of b are the coordinates in the orthogonal system. In Chapter 5, Section 5.4.1, b was utilised to quantify bone shapes in the training set. Details

concerning calculations of $\overline{\mathbf{x}}$, C and P (from indeterminate data vectors) are explained in Chapter 2, Section 2.5.1.

Suppose there are n pairs of shoulder bone shapes (each pair consists of the two shoulder bones from the same subject), one pair is left out for testing and PCA is conducted separately on the remaining $n-1$ humeri and scapulae. The resulting PCA latent variables of the humerus set and the scapula set, which can be denoted as $\mathbf{b}_{h(n-1\times m_h)}$ $(1 \leq m_h < n-1)$ and $\mathbf{b}_{s(n-1\times m_s)}$ $(1 \leq m_s < n-1)$, are used as the observation variables and the response variables, respectively, for CCA and PLS calculations.

Let $X = \mathbf{b}_h$ and $Y = \mathbf{b}_s$, the maximal canonical correlation ρ between variables $\mathbf{b}_h$ and $\mathbf{b}_s$ can be calculated by Equation 2.37. The solution to this equation is provided in Chapter 2, Section 2.7.1. The value of ρ is between zero and one inclusive, with zero indicating no correlation and one indicating perfect linear correlation.

6.2.2 Implementation of Shape Prediction

PLS regression is widely used as a prediction technique based on correlations between two sets of variables. Similarly, the linear correlations extracted from CCA can be also used for prediction purposes. Both prediction methods are discussed in this section.

Based on PLS Model

Given a training set of humerus shapes X, a training set of scapula shapes Y and an individual humerus shape $\mathbf{x}$, implementation of the PLS regression method is described in the following steps:

I Apply a PCA to X and a PCA to Y. The reduced data vectors (also called latent variables in this thesis) for X and Y are denoted by $\mathbf{b}_x$ and $\mathbf{b}_y$.

II Establish surface point-to-point correspondences between the humerus shape $\mathbf{x}$ and the mean shape $\overline{\mathbf{x}}$ of the humerus shape model (correspondence identification is described in Chapter 5, Section 5.2).

III Align shape $\mathbf{x}$ to $\overline{\mathbf{x}}$ using rigid registration or by defining three anatomical points (these alignment methods are explained in Sections 5.3.1 and 5.3.2 in Chapter 5).

IV Transform the shape $\mathbf{x}$ onto the orthogonal coordinate system defined by the principal axes calculated from X: $b_x = P_x^T(X - \overline{\mathbf{x}})$ where b_x is the reduced data vector representing X.

V Implement PLS regression using the NIPALS algorithm described on page 62. Obtain the regression coefficient matrix B_{pls}.

VI Predict the response variable b_y by $b_y = b_x B_{pls}$. Since the regression coefficient matrix B_{pls} is calculated from the principal scores of the observation and response variables, b_y is the reduced data vector of the response scapula shape $\mathbf{y}$. Transform b_y to the Cartesian coordinate system by $\mathbf{y} = \overline{\mathbf{y}} + P_y b_y$.

Based on Linear Correlations

If the linear relationship between the two sets of variables can be modelled, the variables can be predicted given the relationship. Graphical demonstrations of the linear correlations (canonical scores) are shown from Figures 6.2 to 6.7 (pages 166 to 171), which correspond to the largest canonical correlation ρ between the two sets of variables. This linear property can be expressed by a linear equation system using least square regression. Let A be the coefficient matrix, the linear equation is in the form $b_y w_y = A b_x w_x$. A can be estimated by $A = C_{xy}/C_{xx}$ where C_{xy} is the cross covariance matrix between $\mathbf{b}_x$ and $\mathbf{b}_y$, C_{xx} is the covariance matrix of $\mathbf{b}_x$. Therefore, the predicted value of b_y from the predictor b_x is

$$b_y = (A b_x w_x) w_y^{-1} \tag{6.1}$$

6.3 Results

As shown in Tables 3.1 and 3.2, there are 32 humeri and 30 scapulae in total, but only 28 complete pairs of shoulder bones. To perform the leave-one-out validations, one pair

of shoulder bones, for example the pair from *Cebus* 1, was taken out of the model constructions. PCA was applied to the remaining 31 humeri and 29 scapulae respectively. The resulting latent variables, $\mathbf{b}'_h$ and $\mathbf{b}'_s$, of these two shape models are in the dimensionalities of 31×31 and 29×29. 27 pairs of corresponding latent variables were extracted from $\mathbf{b}'_h$ and $\mathbf{b}'_s$ to form the two blocks of variables, $\mathbf{b}_{h(27\times i)}$ $(i = 1, \cdots, 26)$ and $\mathbf{b}_{s(27\times j)}$ $(j = 1, \cdots, 26)$. To solve the indeterminate problem of the linear system, only the first 26 principal modes are used at most.

The results in the remainder of this section are based on the 27 pairs of primate shoulder bone shapes, with one pair of the *Cebus* shoulder bone shapes being taken out of the model constructions.

6.3.1 Linear Correlations

According to Equation 2.37, page 59, scalings of variables $\mathbf{b}_h$ and $\mathbf{b}_s$ do not change the results of correlation coefficient ρ. This is to say, using the standard deviations, denoted as $\mathbf{d}$, of variables $\mathbf{b}$ as the CCA input gives the same result as using the variables $\mathbf{b}$. $\mathbf{d}$ is defined as $\mathbf{d} = \mathbf{b}/\sqrt{\lambda}$, where λ is the corresponding eigenvalues to eigenvectors P.

PCA describes variability within the training set whilst CCA describes the linear interrelationships between two training sets. Therefore, the i^{th} principal mode of the humerus model (the i^{th} column of $\mathbf{b}_h$) is not necessarily correlated to the i^{th} principal mode of the scapula model (the i^{th} column of $\mathbf{b}_s$). As shown in Table 6.1, the percentage of total variance described by principal modes decreases rapidly, but the canonical correlation coefficient ρ between each pair of principal modes does not decrease. Only the first pairs of the principal modes are considered to be linearly correlated in both models according to their correlation coefficients 0.96 and 0.85. The correlation coefficients of other pairs are too small to claim their linear interrelationships. However, it is possible that $b_{h(i)}$ and $b_{s(j)}$ $(i \neq j, j = 1, 2, ..., n)$ are linearly correlated.

Correlations between all first i pairs of principal modes were also calculated. Tables 6.2 and 6.3 show the first ten coefficients as different numbers of principal modes were applied. Apparently, more principal modes improved the extracted linear relationship

Modes	Model One (Including size)			Model Two (excluding size)		
	humerus PTV [b] (%)	scapula PTV (%)	CC [a]	humerus PTV (%)	scapula PTV (%)	CC
1^{st}	99.67	87.82	0.96	45.82	58.63	0.85
2^{nd}	0.14	7.10	0.32	21.15	13.11	0.12
3^{rd}	0.06	2.20	0.14	6.80	11.83	0.38
4^{th}	0.04	1.19	0.40	4.99	3.73	0.07
5^{th}	0.02	0.55	0.16	2.99	3.05	0.23
6^{th}	0.02	0.28	0.60	2.95	1.86	0.23
7^{th}	0.01	0.23	0.12	2.14	1.58	0.06
8^{th}	0.01	0.13	0.19	1.57	1.16	0.32
9^{th}	0.01	0.10	0.02	1.47	0.77	0.41
10^{th}	0.01	0.08	0.22	1.43	0.62	0.38

[a] Correlation Coefficient
[b] Percentage of Total Variance

Table 6.1: Percentage of the variation described by each principal mode and the correlation coefficient of each pair of the principal modes

	1^{st}	2^{nd}	3^{rd}	4^{th}	5^{th}	6^{th}	7^{th}	8^{th}	9^{th}	10^{th}
1^a	0.9596									
2	0.9829	0.3352								
3	0.9856	0.8340	0.6732							
4	0.9895	0.8563	0.7731	0.3118						
5	0.9926	0.8902	0.8340	0.7015	0.0832					
6	0.9965	0.9672	0.9032	0.8448	0.7736	0.0023				
7	0.9980	0.9714	0.9338	0.9040	0.8165	0.5225	0.4356			
8	0.9982	0.9860	0.9668	0.9194	0.8678	0.6633	0.5209	0.3893		
9	0.9988	0.9883	0.9802	0.9584	0.9211	0.8223	0.6818	0.4026	0.2115	
10	0.9992	0.9961	0.9868	0.9787	0.9563	0.9221	0.8190	0.4383	0.3083	0.1455
⋮	⋮	⋮	⋮	⋮	⋮	⋮	⋮	⋮	⋮	⋮
26	1.0000	1.0000	1.0000	1.0000	1.0000	1.0000	1.0000	1.0000	1.0000	1.0000

[a] Number of principal modes used

Table 6.2: Canonical correlation coefficients between shoulder bone shapes (model one - including size)

	1^{st}	2^{nd}	3^{rd}	4^{th}	5^{th}	6^{th}	7^{th}	8^{th}	9^{th}	10^{th}
1^a	0.8451									
2	0.8611	0.1332								
3	0.8989	0.5403	0.1568							
4	0.9462	0.7787	0.2618	0.0702						
5	0.9745	0.8196	0.6532	0.3289	0.0340					
6	0.9832	0.8338	0.7251	0.5834	0.2031	0.1050				
7	0.9923	0.8966	0.8464	0.7254	0.5782	0.2532	0.0976			
8	0.9971	0.9283	0.8705	0.8277	0.602	0.2665	0.2466	0.0646		
9	0.9971	0.9753	0.9193	0.8458	0.7028	0.6118	0.2611	0.1956	0.0620	
10	0.9979	0.9880	0.9752	0.8489	0.8182	0.6491	0.5931	0.2888	0.1987	0.0738
⋮	⋮	⋮	⋮	⋮	⋮	⋮	⋮	⋮	⋮	⋮
26	1.0000	1.0000	1.0000	1.0000	1.0000	1.0000	1.0000	1.0000	1.0000	1.0000

[a]Number of principal modes used

Table 6.3: Canonical correlation coefficients between shoulder bone shapes (model two - excluding size)

between them, and the coefficients increase along with the number of principal modes. With the current input, the first coefficient became one when at least 14 principal modes were used.

Figures 6.2 to 6.7 plot the relations between the first pair of canonical variates (S_h and S_s in Equation 2.37, page 59). S_h and S_s are the projections of the principal modes onto the first column of the linear transformation matrices w_h and w_s. Each point in the figures states the projection of one pair of shoulder bones. These points lie on straight lines when the number of principal modes is large enough (Figures 6.4 and 6.7).

Figures 6.2, 6.3, 6.5 and 6.6 also demonstrate a clustering pattern of the projected variables. There are three obvious clusters in Figures 6.2 and 6.3 when size variation is included, one belonging to all the monkeys in the present datasets, one being formed by the *Pan*, the *Homo* and the *Pongo*, and one only containing the *Gorilla*. When size variation is excluded, the plots show two clear clusters, one being formed by the great apes and the other being formed by monkeys (Figures 6.5 and 6.6). This result illustrates CCA's ability to act as a data classifier.

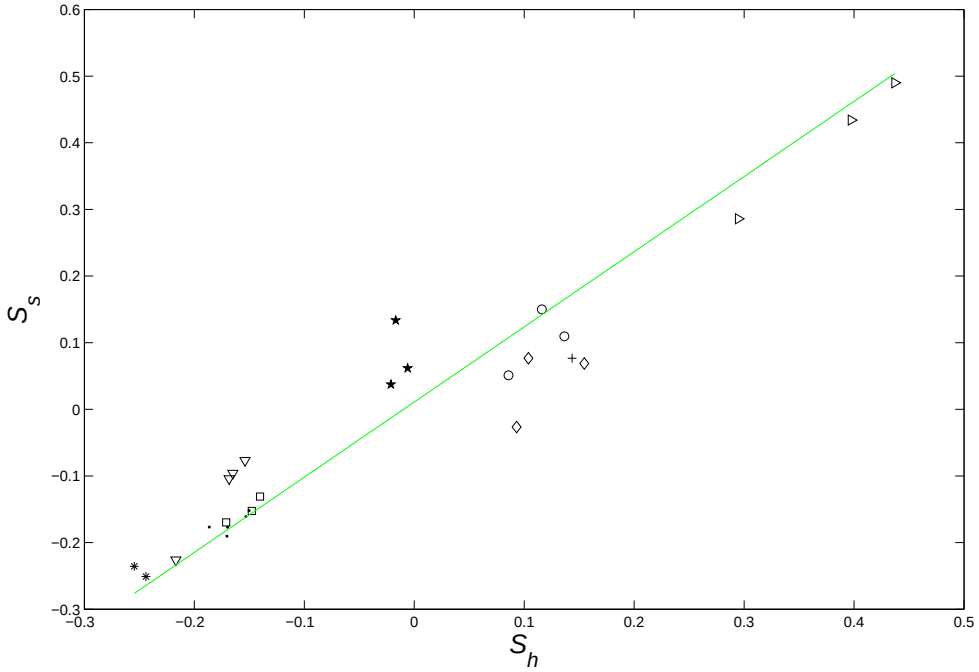

First pair of principal modes

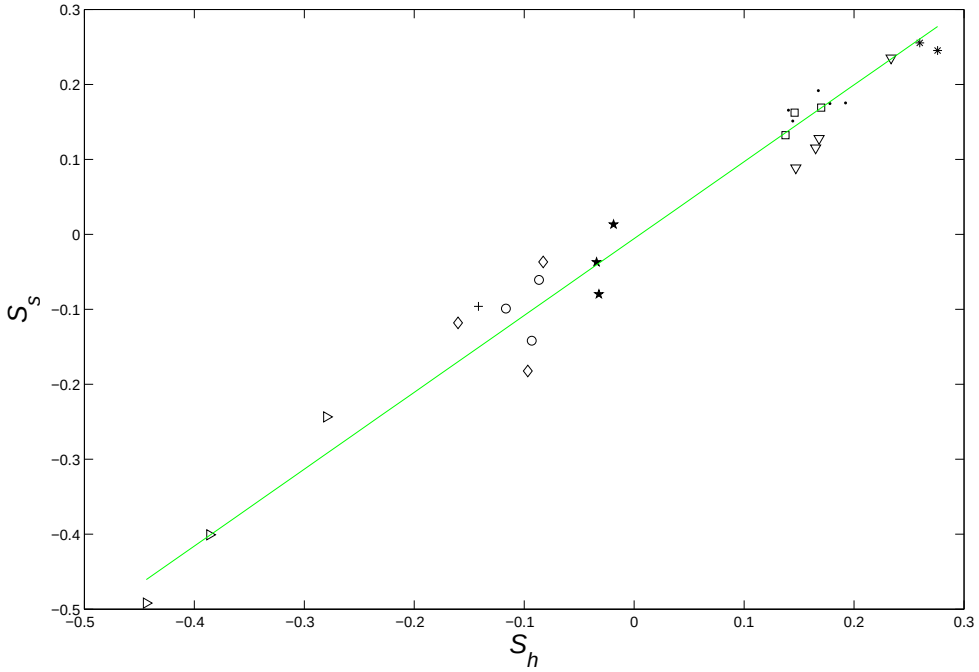

First two pairs of principal modes

∗ *Cebus*; ∘ *Pan*; □ *Colobus* ▷ *Gorilla*; ♢ *Homo*; ▽ *Macaca*; + *Pongo*; ⋆ *Papio*; • *Presbytis*

Abscissa: canonical scores for the humerus set; ordinate: canonical scores for the scapula set; lines obtained by ordinary least squares regression.

Figure 6.2: Linear correlation representations of the first canonical variate using one and two pairs of principal modes (model one - including size)

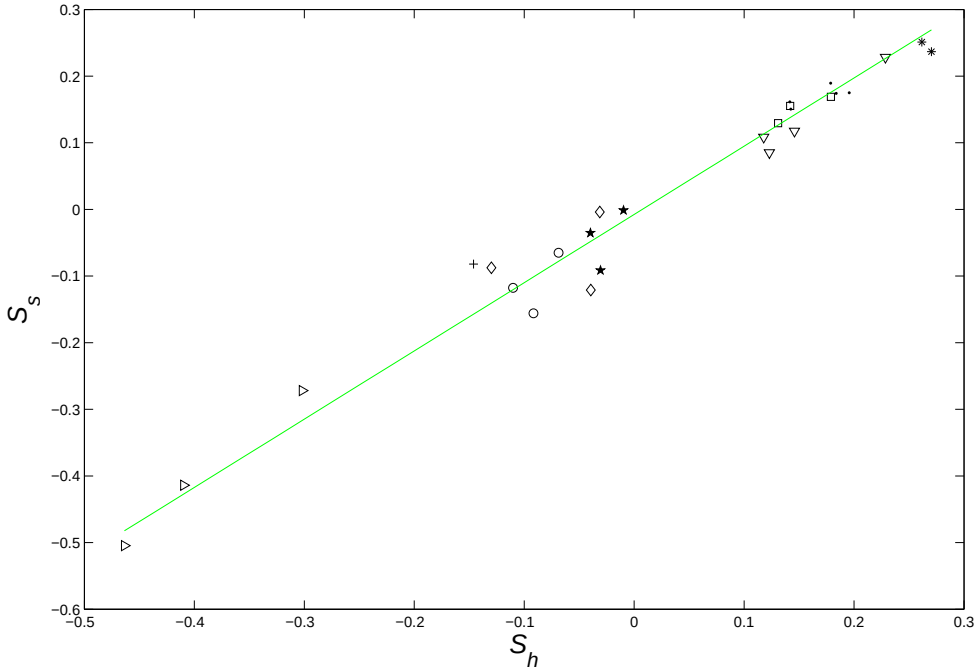

First three pairs of principal modes

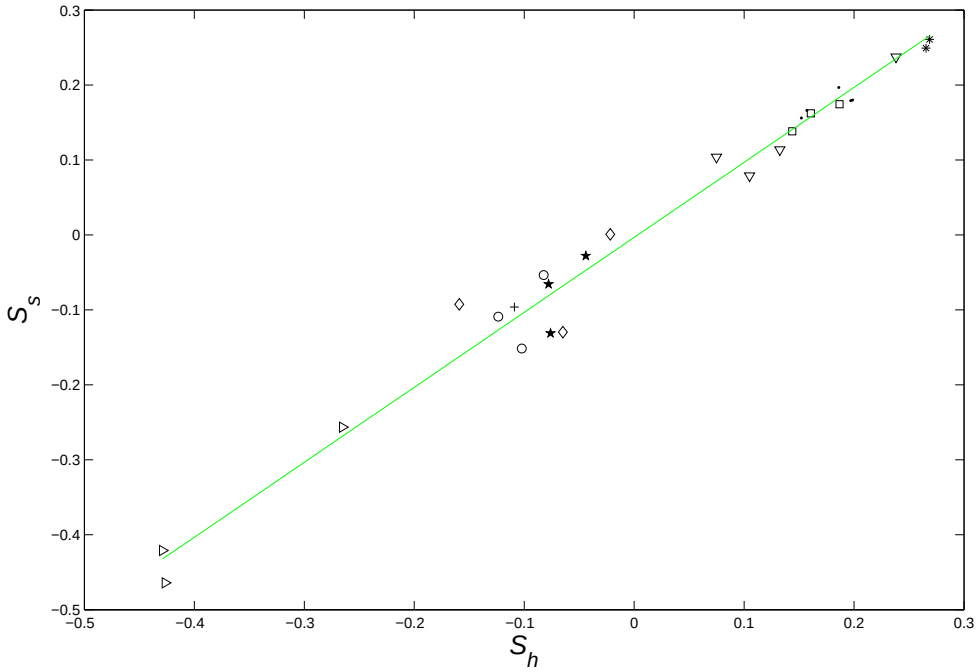

First four pairs of principal modes

⋮

∗ *Cebus*; ∘ *Pan*; □ *Colobus* ▷ *Gorilla*; ♢ *Homo*; ▽ *Macaca*; + *Pongo*; ⋆ *Papio*; • *Presbytis*

Abscissa: canonical scores for the humerus set; ordinate: canonical scores for the scapula set; lines obtained by ordinary least squares regression.

Figure 6.3: Linear correlation representations of the first canonical variate using three and four pairs of principal modes (model one - including size)

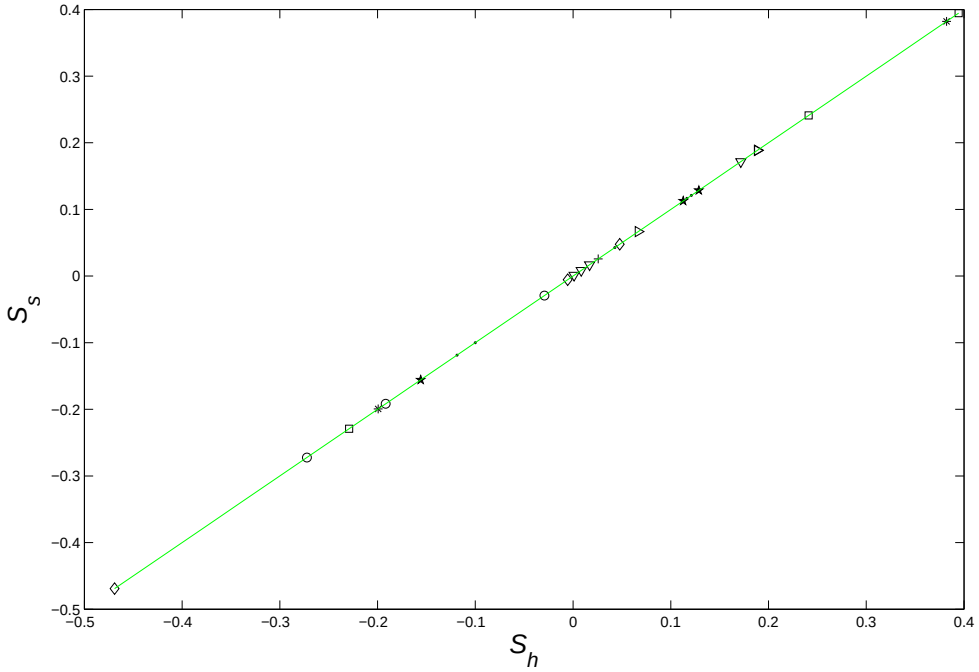

First 24 pairs of principal modes

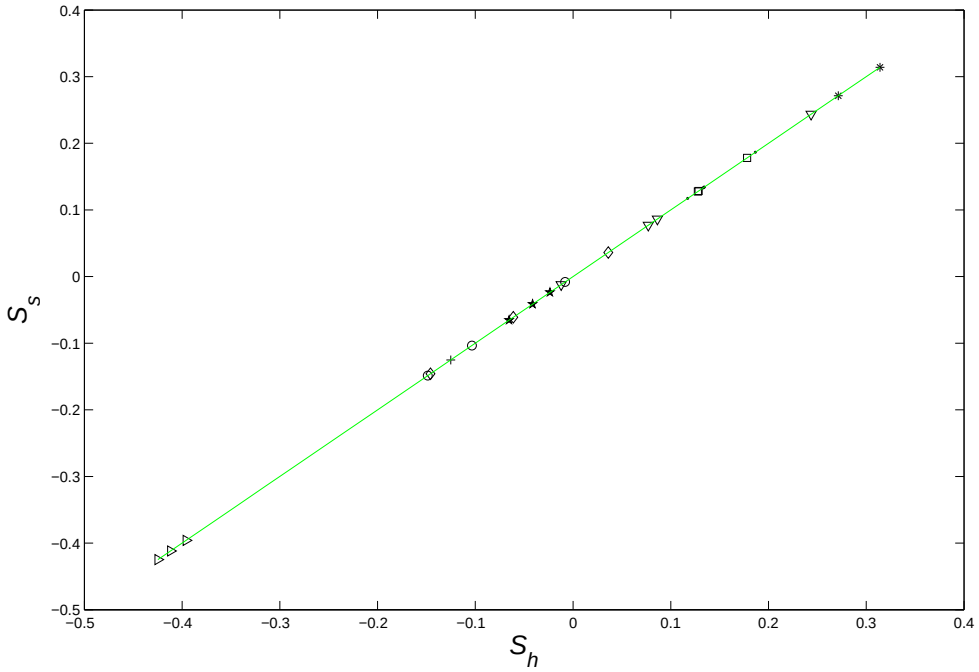

First 25 pairs of principal modes

$*$ *Cebus*; $\circ$ *Pan*; $\square$ *Colobus* $\triangleright$ *Gorilla*; $\diamondsuit$ *Homo*; $\triangledown$ *Macaca*; $+$ *Pongo*; $\star$ *Papio*; $\bullet$ *Presbytis*

Abscissa: canonical scores for the humerus set; ordinate: canonical scores for the scapula set; lines obtained by ordinary least squares regression.

Figure 6.4: Linear correlation representations of the first canonical variate using 24 and 25 pairs of principal modes (model one - including size)

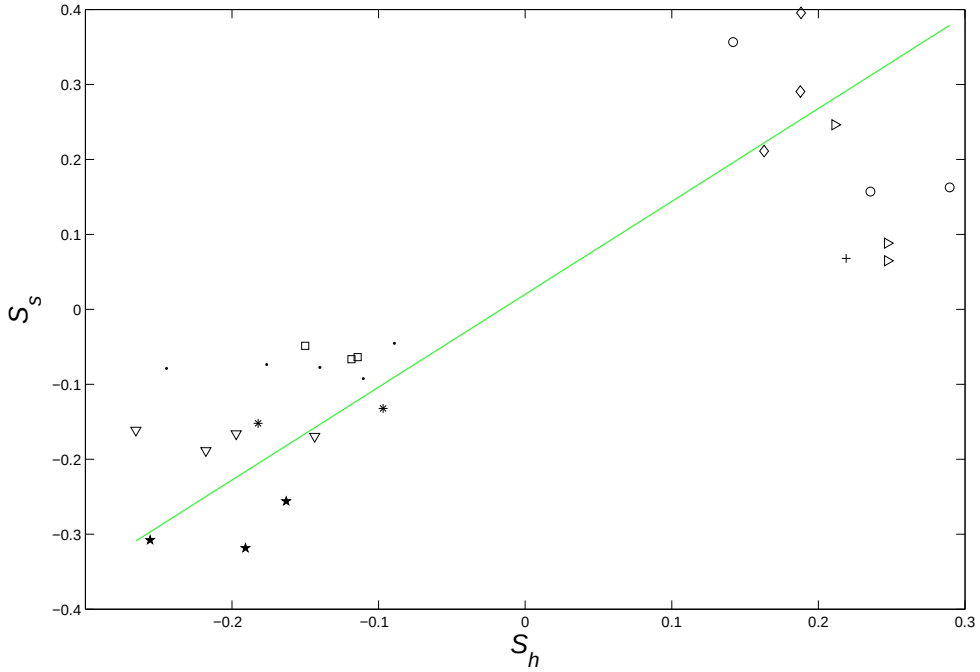

First pair of principal modes

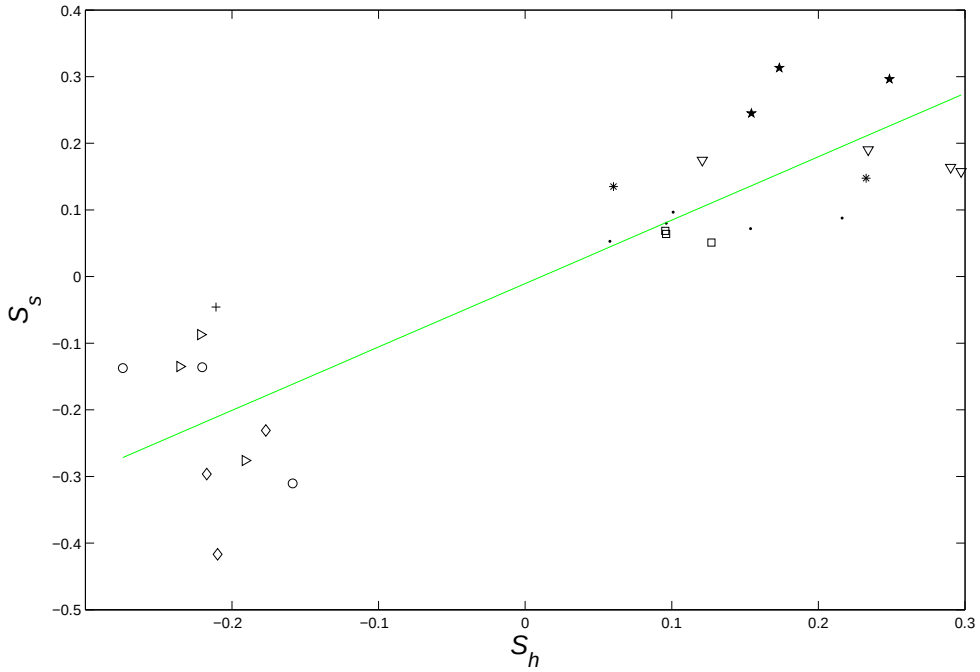

First two pairs of principal modes

∗ *Cebus*; ∘ *Pan*; □ *Colobus* ▷ *Gorilla*; ♢ *Homo*; ▽ *Macaca*; + *Pongo*; ⋆ *Papio*; • *Presbytis*

Abscissa: canonical scores for the humerus set; ordinate: canonical scores for the scapula set; lines obtained by ordinary least squares regression.

Figure 6.5: Linear correlation representations of the first canonical variate using one and two pairs of principal modes (model two - excluding size)

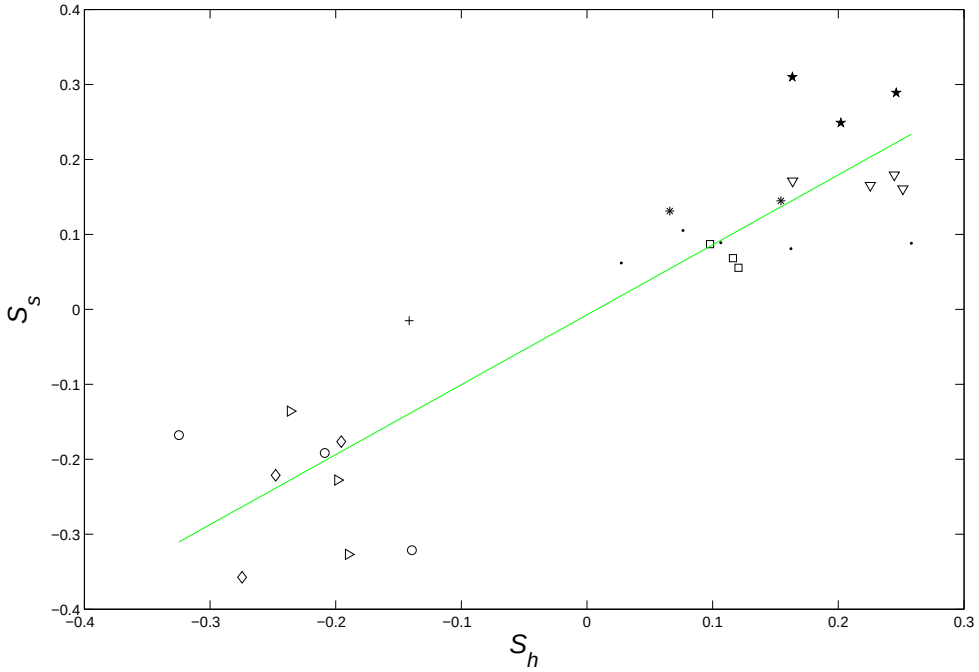

First three pairs of principal modes

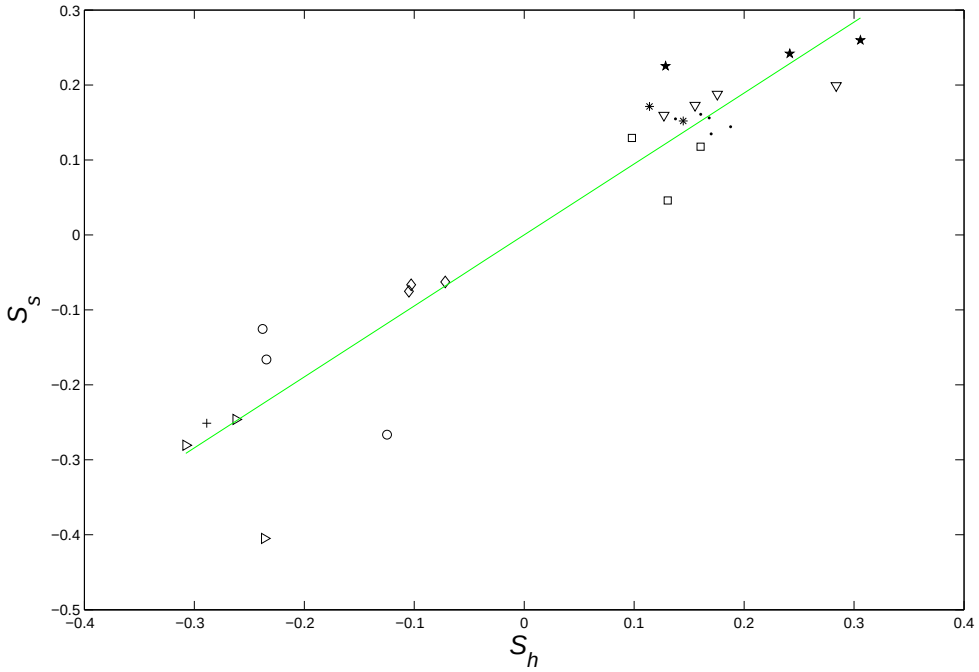

First four pairs of principal modes

⋮

∗ *Cebus*; ∘ *Pan*; □ *Colobus* ▷ *Gorilla*; ♢ *Homo*; ▽ *Macaca*; + *Pongo*; ⋆ *Papio*; • *Presbytis*

Abscissa: canonical scores for the humerus set; ordinate: canonical scores for the scapula set; lines obtained by ordinary least squares regression.

Figure 6.6: Linear correlation representations of the first canonical variate using three and four pairs of principal modes (model two - excluding size)

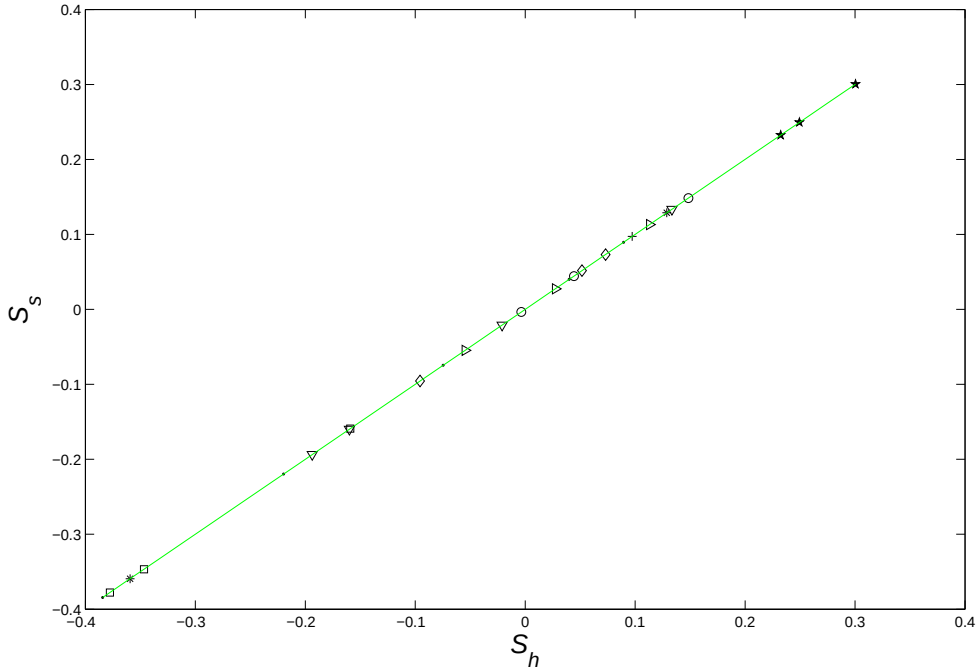

First 24 pairs of principal modes

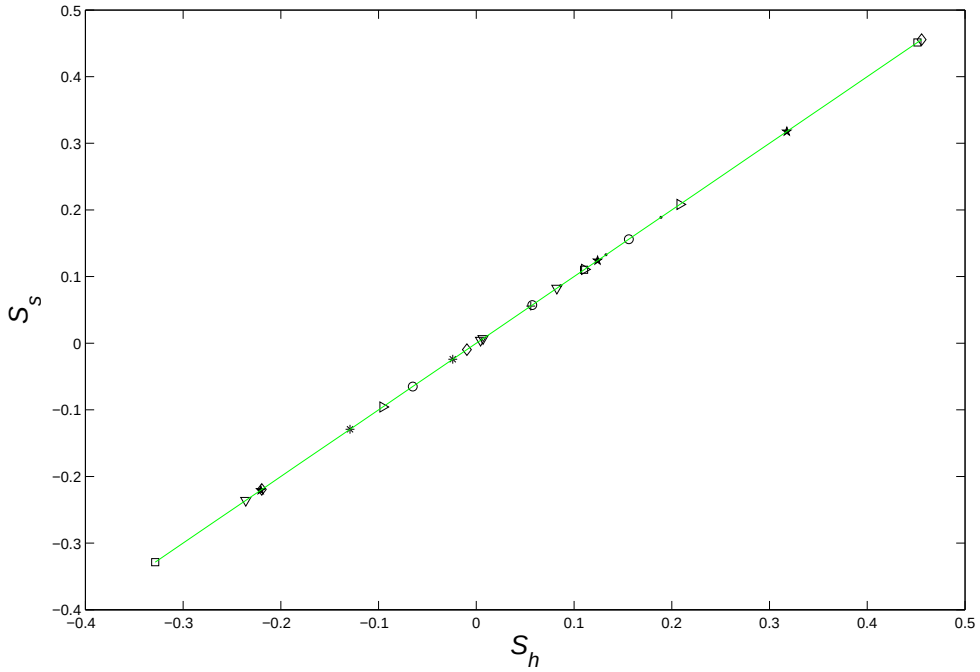

First 25 pairs of principal modes

∗ *Cebus*; ∘ *Pan*; □ *Colobus* ▷ *Gorilla*; ♢ *Homo*; ▽ *Macaca*; + *Pongo*; ⋆ *Papio*; • *Presbytis*

Abscissa: canonical scores for the humerus set; ordinate: canonical scores for the scapula set; lines obtained by ordinary least squares regression.

Figure 6.7: Linear correlation representations of the first canonical variate using 24 and 25 pairs of principal modes (model two - excluding size)

6.3.2 Predictions

The shape prediction method based on PLS regression contains three main steps: 1) obtain projected data vectors b by transforming the shape vectors onto the PCA axes, 2) apply PLS regression and 3) project the predicted data vectors onto the original Cartesian coordinate system. Figures 6.8 and 6.9 show the predicted humerus shape from *Cebus* 1, which was left out during the model construction. Figures 6.10 and 6.11 show the predicted shape of the *Cebus* scapula from its humerus. The number of principal modes used are, from left to right, one, two and three. The graphical results demonstrate that the shape prediction model based on model two (excluding size variation) gives better prediction results.

Linear correlations between the two shoulder bone shapes based on CCA, combined with least square regression (or a PLS regression) on the canonical variates, were also utilised to predict one shape from the other (details are in Section 6.2.2). The two results show the same prediction results as those obtained using the NIPALS algorithm.

The linear relationship can be used to explore the pattern of variation between the two datasets. Recreating the humerus shapes by changing their principal modes, the corresponding scapula shapes were predicted from the reconstructed humerus shapes. Figures 6.12 and 6.13 show the morphological relationship based on the first and second canonical variates (also called CCA modes in this thesis) using the first three principal modes. In the first canonical variate, the volume of the scapular socket and size of the supraspinous and infraspinous fossae increase as the degree of bending decreases. In the second canonical variate, the width of the humeral shaft is mostly related to the shape of the supraspinous and infraspinous fossae. From Table 6.3, the canonical coefficients of these two figures are 0.8989 and 0.5403.

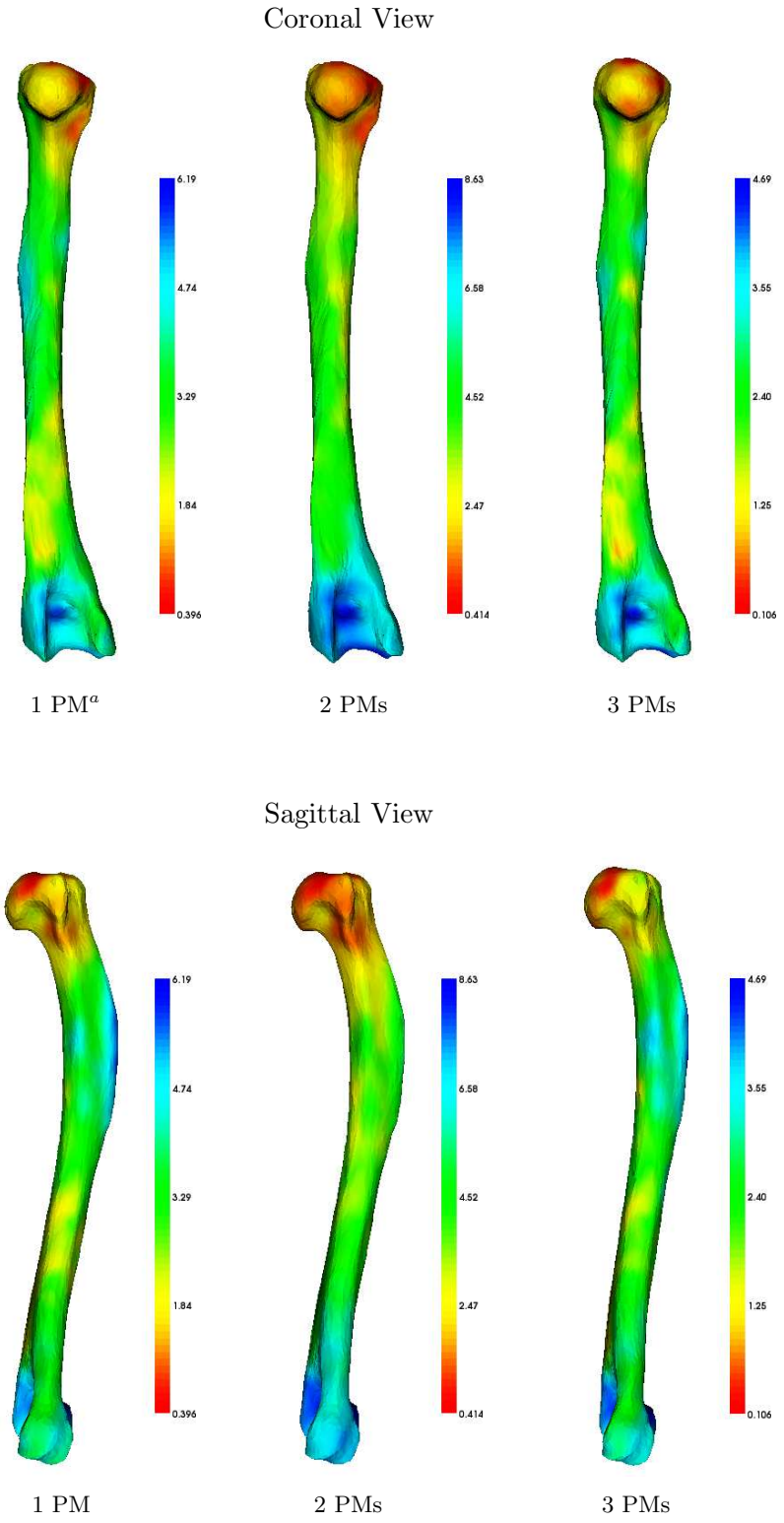

[a]principal mode

Figure 6.8: Predicted *Cebus* humerus shapes (model one - including size). Warmer colour indicates closer point-to-point distance to the real *Cebus* humerus shapes.

Coronal View

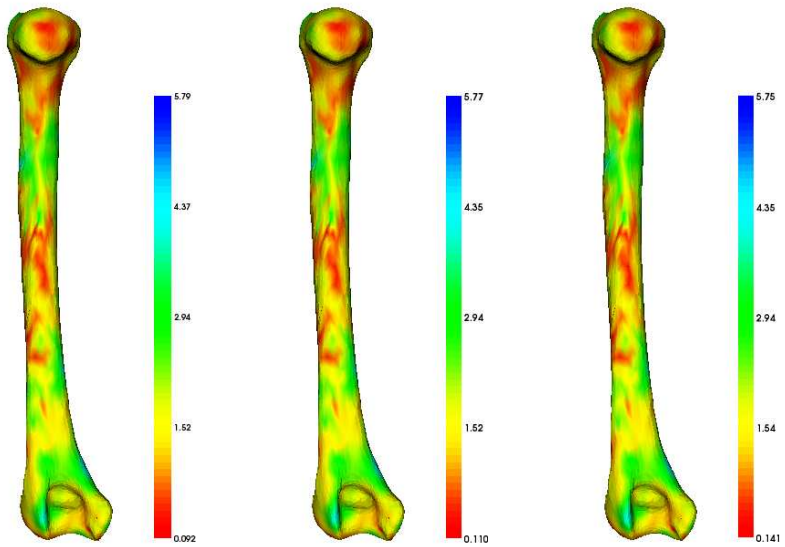

1 PM[a] 2 PMs 3 PMs

Sagittal View

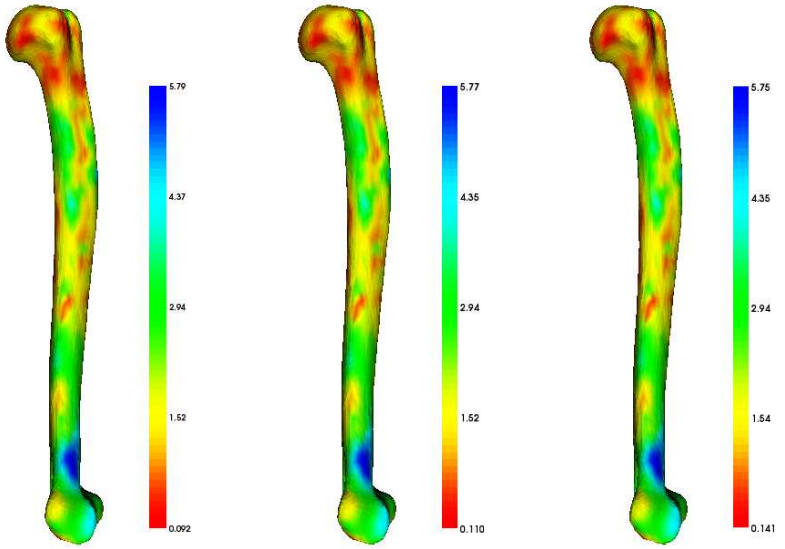

1 PM 2 PMs 3 PMs

[a]principal mode

Figure 6.9: Predicted *Cebus* humerus shapes (model two - excluding size). Warmer colour indicates closer point-to-point distance to the real *Cebus* humerus shapes.

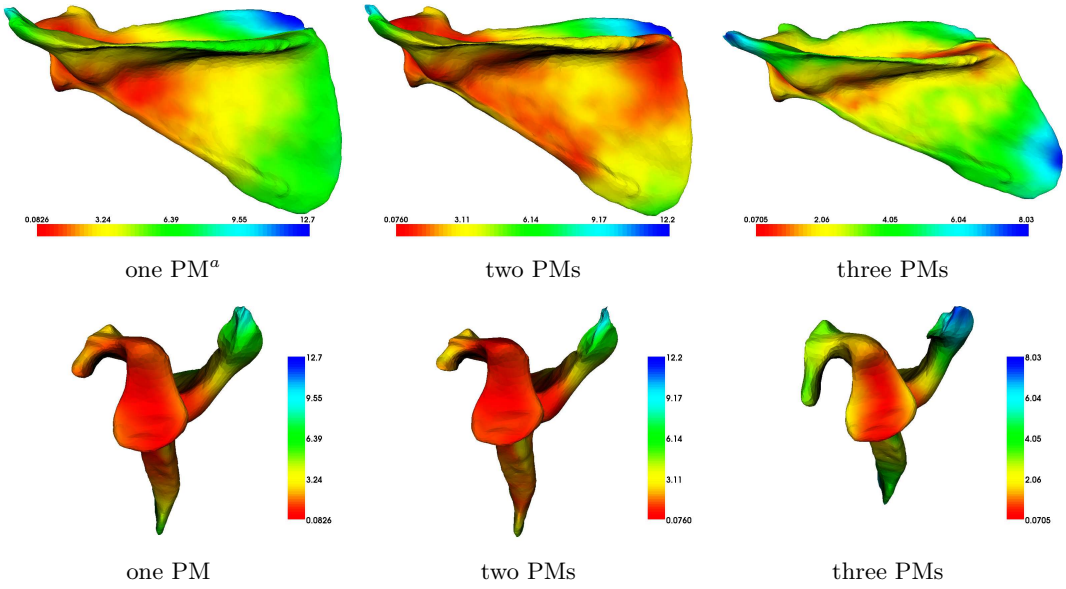

[a]principal mode

Figure 6.10: Predicted *Cebus* scapula shapes (model one - including size). Warmer colour indicates closer point-to-point distance to the real *Cebus* scapula shapes.

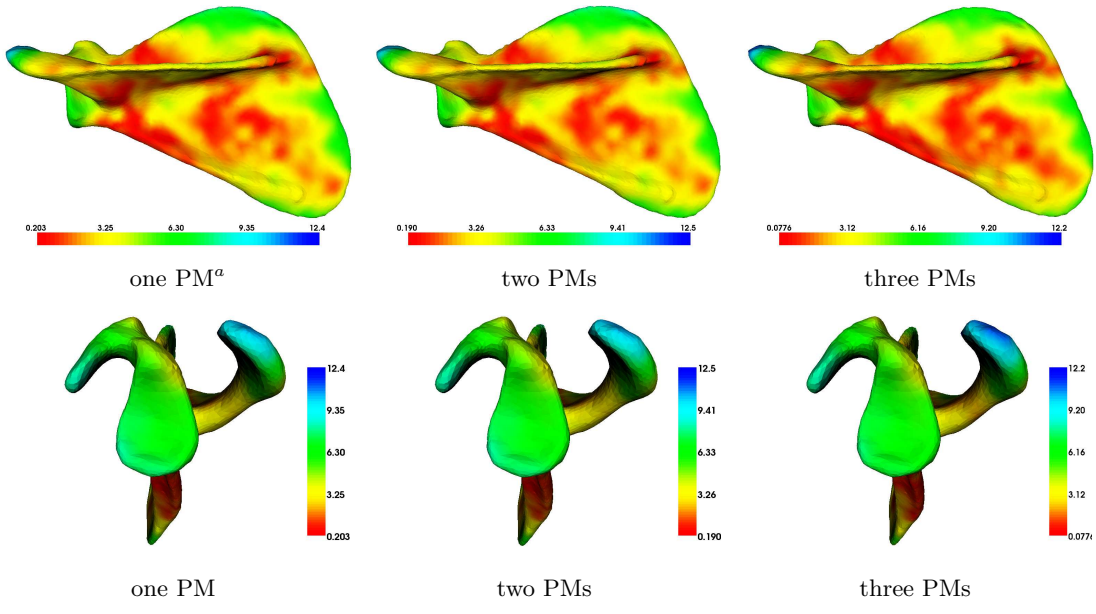

[a]principal mode

Figure 6.11: Predicted *Cebus* scapula shapes (model two - excluding size). Warmer colour indicates closer point-to-point distance to the real *Cebus* scapula shapes.

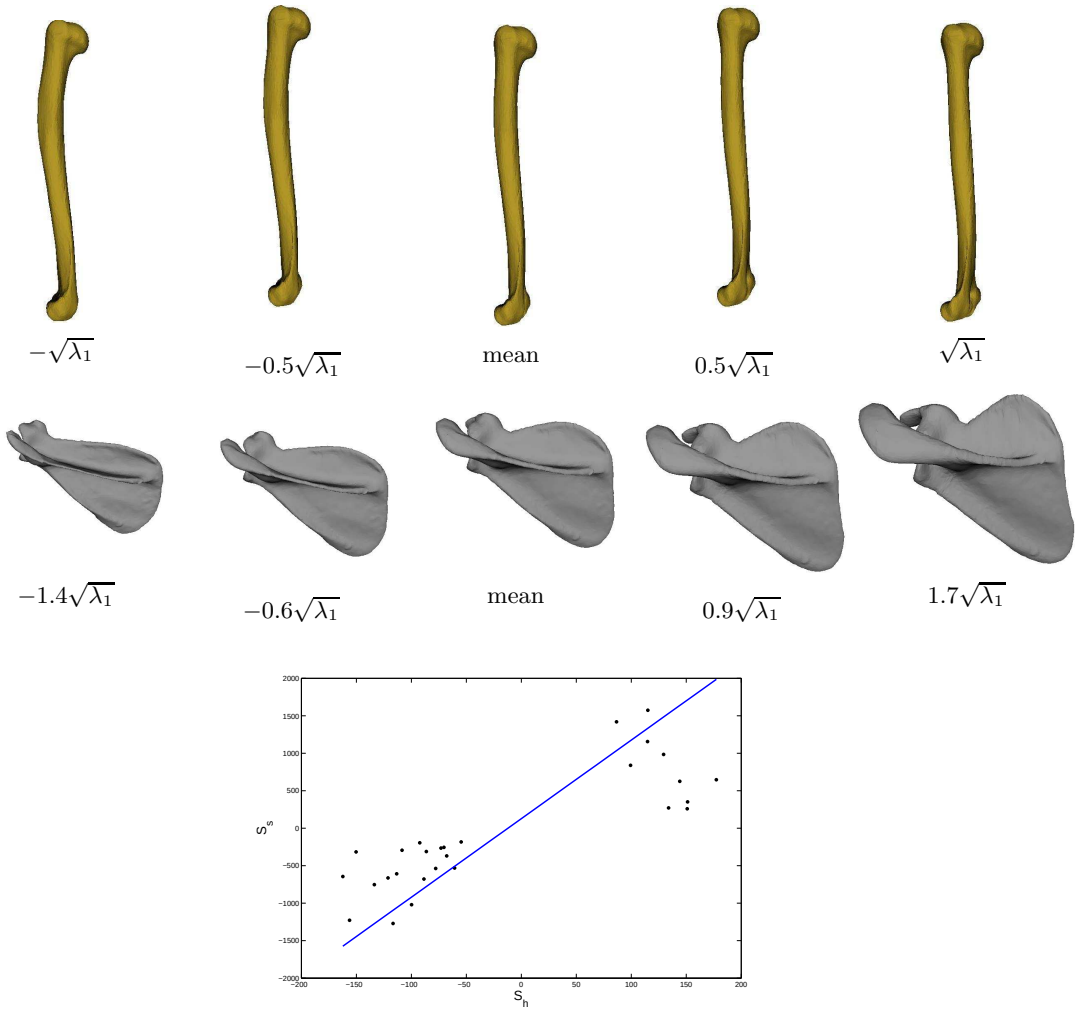

Figure 6.12: Corresponding linear morphological variation based on the first CCA mode using the first three principal modes

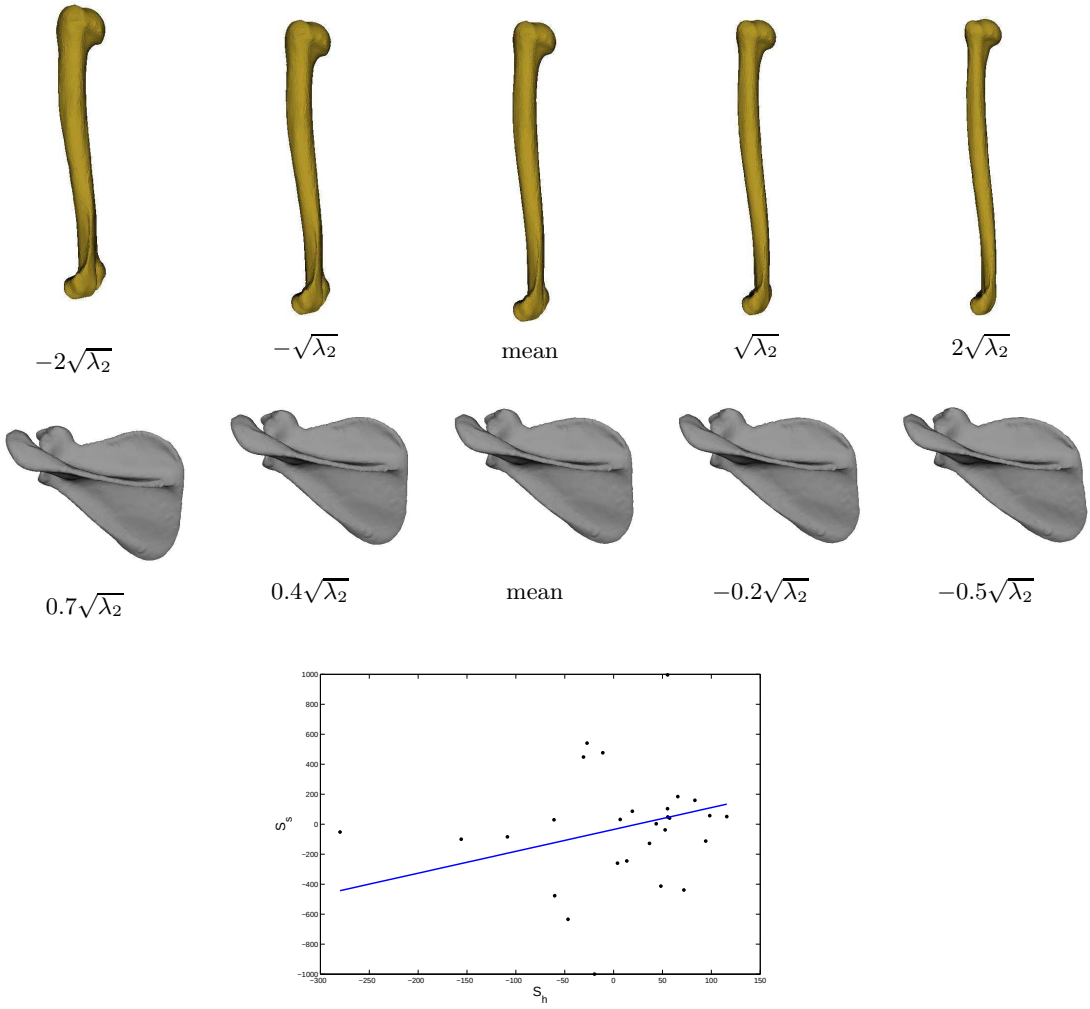

Linear correlation

Figure 6.13: Corresponding linear morphological variation based on the second CCA mode using the first three principal modes

6.3.3 Discussion

Results have shown that both the PLS regression method and the CCA method combined with a least square regression gave the same predicted shapes with the present datasets. It is not true that the two methods always produce the same results if PCA is not performed to reduce data dimensionality.

For example, there is a function f that maps a point set in a cubic to a point set on a 3D line (as shown in Figure 6.14). PLS regression is able to capture the nonlinear correlations between the two point sets but CCA cannot. Take a random point in the cubic (the star in Figure 6.14(a)) as the predictor, its corresponding point on the 3D line predicted using PLS regression is shown as the star on the line in Figure 6.14(b). However, least square regression on the extracted canonical variates (projections shown in Figure 6.15) and PLS regression on the canonical variates are both unable to estimate a correct function f. Their corresponding prediction estimations, shown as the circle and the square, respectively, in Figure 6.14(b), do not lie on the line. In this example, the PLS regression prediction method alone is superior to the CCA method with least square regression.

Only one pair of latent vectors is extracted for each iteration in the NIPALS algorithm. This is based on the inequality ${s_i}^2(A-B) \geq {s_{i+k}}^2(A)$ [Rao79], where $s_i(A)$ is the i^{th} singular value of A and B is a matrix of rank k. Replacing matrices A and B by the described variables, E^2 and F, respectively, the following equation is obtained:

$$ {S_i}^2({E_{i+1}}^2F) = s^2({E_i}^TF - p_i{t_i}^TF) \geq {S_2}^2({E_i}^TF) \tag{6.2} $$

The second largest singular value of E^TF at iteration i is smaller than the largest singular value at iteration $i+1$. Therefore, the selection of one pair of latent vectors at each time gives maximum variance of the weighted covariance matrix.

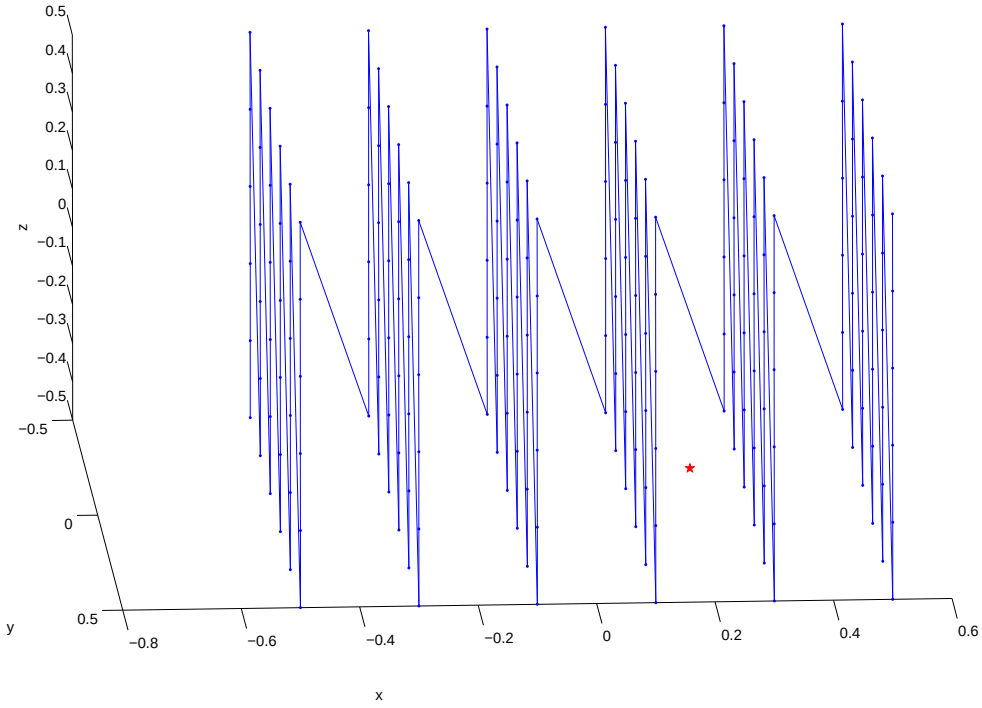

(a) Ordered point set (the star is the predictor point)

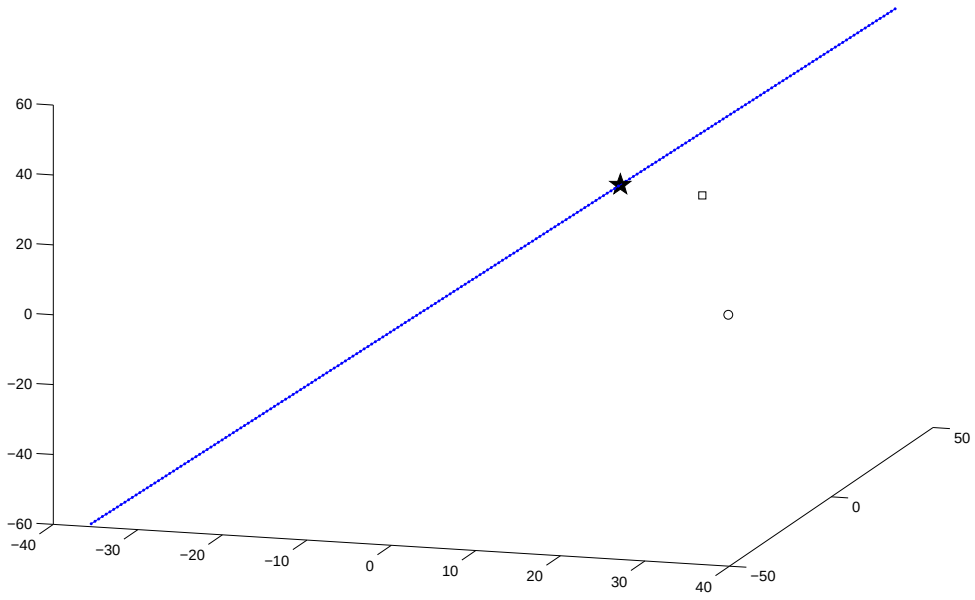

(b) Another ordered point set on a 3D line ($\star$ predicted point based on PLS regression; $\square$ partial least squares regression on canonical variates; $\circ$ least squares regression on canonical variates)

Figure 6.14: A prediction example of two sets of variables

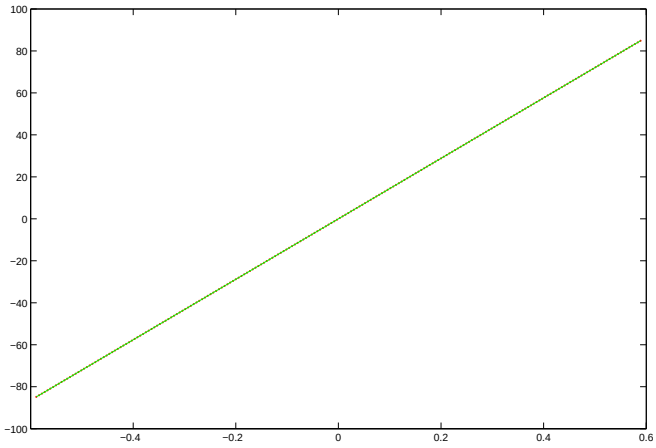

(a) 1^{st} canonical variate

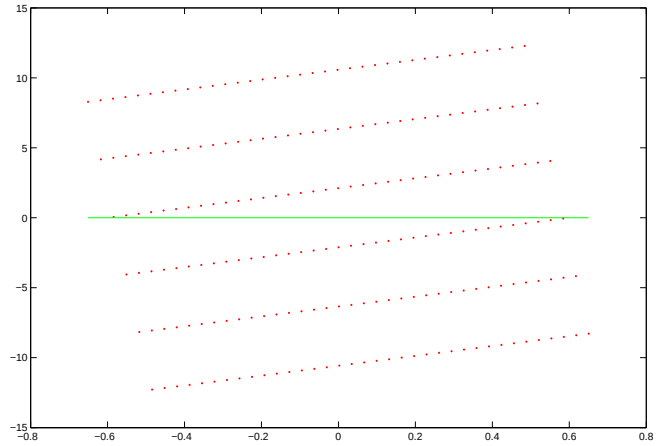

(b) 2^{nd} canonical variate

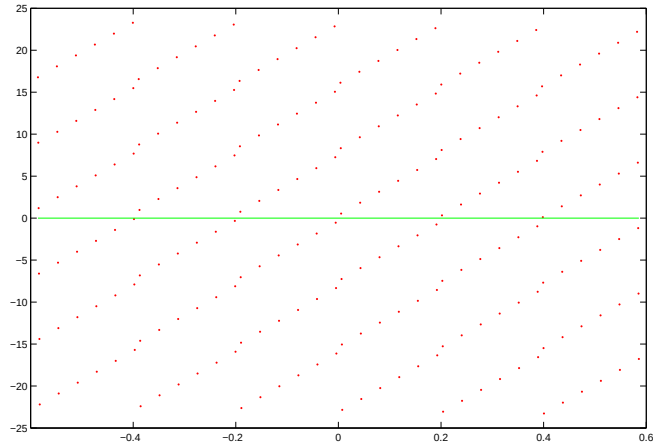

(c) 3^{rd} canonical variate

Figure 6.15: Canonical variates of the two sets of variables and their least squares lines

6.4 Prediction Validation

Apart from visually viewing the results of the shape prediction models, the prediction errors were also estimated by root mean square (RMS) distance between surface points. When RMS distance (error) between the real shape and the predicted shape is less than the RMS error between the real shape and the mean shape of the training set, it means that the PLS method is better than using the mean shape as an estimate of this specific shape. In order to assess the robustness of the PLS prediction method, two prediction models were validated using leave-one-out validations.

6.4.1 Root Mean Square Errors

In the training sets constructed earlier, a humerus or a scapula shape $\mathbf{x}$ is denoted by a column vector of all its surface points coordinates: $\mathbf{x} = (x_1, y_1, z_1, x_2, y_2, z_2, \cdots, x_n, y_n, z_n)^T$, where n is the number of surface points on each humerus or scapula shape in the training set. Let $\mathbf{x}' = (x'_1, y'_1, z'_1, x'_2, y'_2, z'_2, \cdots, x'_m, y'_m, z'_m)^T$ be a predicted shape, the RMS error between this predicted shape and the real shape $\mathbf{x}$ in the training set is estimated by

$$e = \sqrt{\frac{1}{n}\sum_{i=1}^{n}[(x_i - x'_i)^2 + (y_i - y'_i)^2 + (z_i - z'_i)^2]} \tag{6.3}$$

A comparison between the RMS errors from the predicted shapes and the RMS errors from the mean shapes can be seen in Figures 6.16 and 6.17, the abscissa representing the 28 specimens. The first three principal modes were used for the PLS prediction in these figures. The order of the genera from left to right is: *Cebus* (three pairs), *Colobus* (three pairs), *Pan* (three pairs), *Gorilla* (three pairs), *Homo* (three pairs), *Macaca* (four pairs), *Pongo* (one pair), *Papio* (three pairs) and *Presbytis* (five pairs).

When size variation is included in the models, there are 25 better predictions using the PLS method to predict a humerus shape from a scapula shape among the 28 leave-one-out validations, whilst there are 28 better predictions predicting a scapula shape from a humerus shape. As mentioned above, size varies largely from genus to genus, the mean

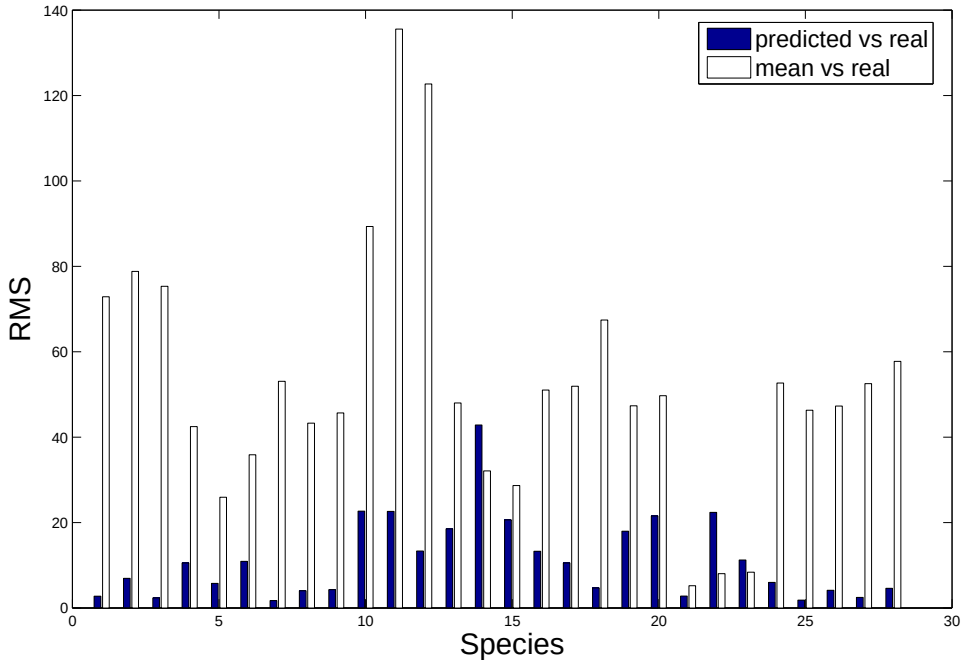

(a) Predicted humerus shapes

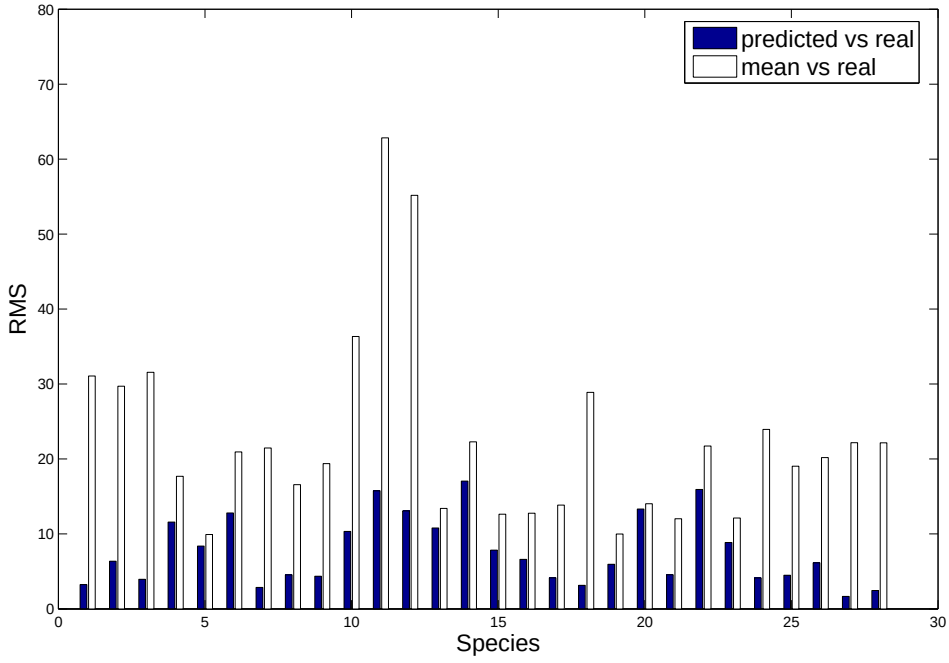

(b) Predicted scapula shapes

Figure 6.16: RMS errors between the predicted shape and the real shape, compared to RMS errors between the mean shape of the shape mode and the real shape. The order of the genus from left to right is: *Cebus* (three pairs), *Colobus* (three pairs), *Pan* (three pairs), *Gorilla* (three pairs), *Homo* (three pairs), *Macaca* (four pairs), *Pongo* (one pair), *Papio* (three pairs) and *Presbytis* (five pairs). (model one - including size)

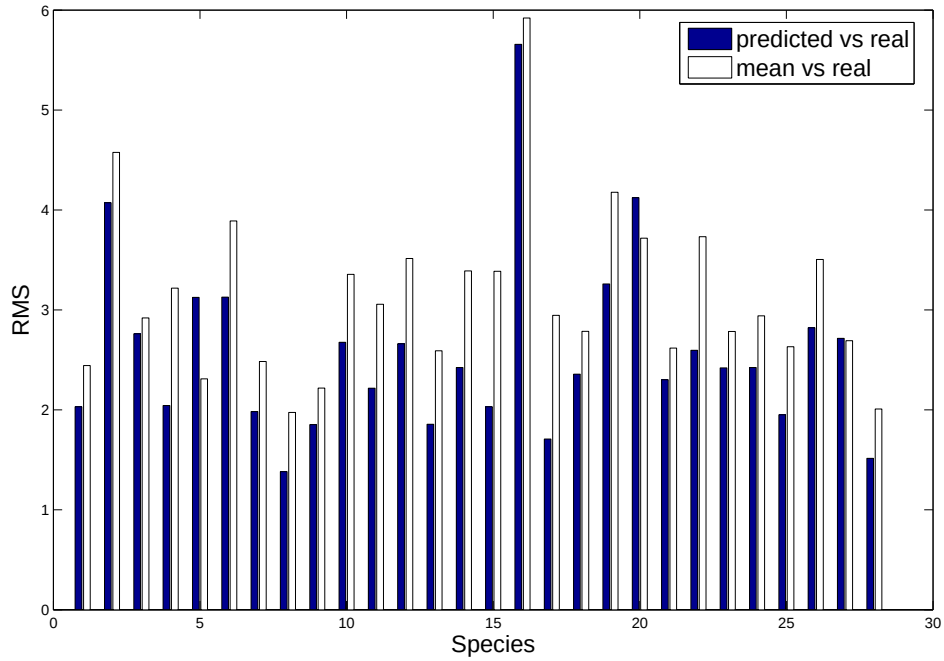

(a) Predicted humerus shapes

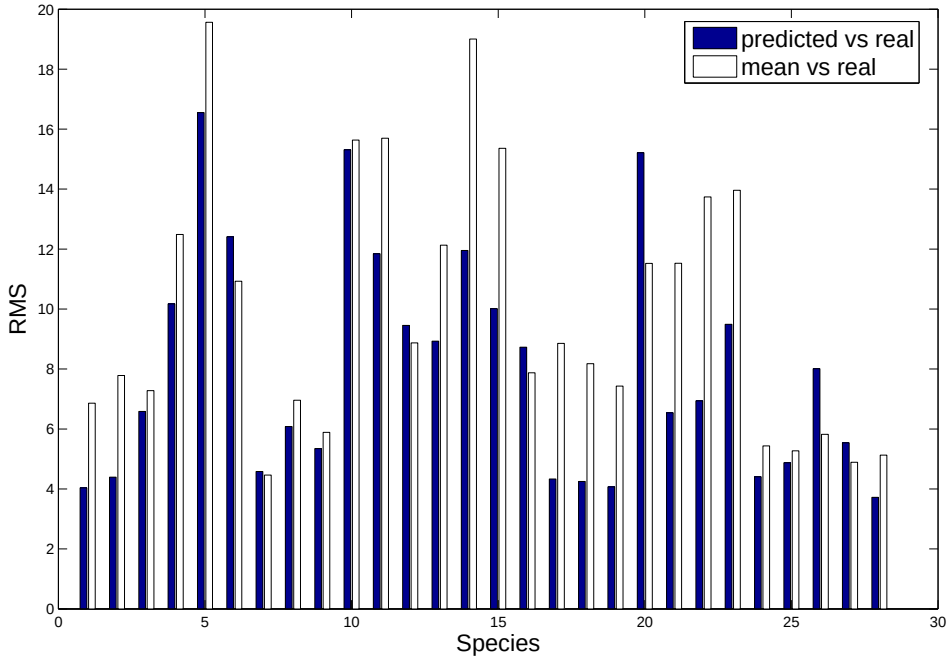

(b) Predicted scapula shapes

Figure 6.17: RMS errors between the predicted shape and the real shape, compared to RMS errors between the mean shape of the shape mode and the real shape. The order of the genus from left to right is: *Cebus* (three pairs), *Colobus* (three pairs), *Pan* (three pairs), *Gorilla* (three pairs), *Homo* (three pairs), *Macaca* (four pairs), *Pongo* (one pair), *Papio* (three pairs) and *Presbytis* (five pairs). (model two - excluding size)

shapes of the models can be very different from some bone shapes in the datasets due to the size difference. As such, RMS error between the mean shape and those shapes can be large. Once size variation is predicted correctly, the predicted shape is very likely to have much less RMS error compared to the mean shape. In the models without size variation, there are also 25 better-predicted humerus shapes. Although there are less better predicted scapula shapes (showing 21 better predictions), the RMS errors have shown that this model produces more accurate prediction results.

The prediction behaviour is different when different numbers of principal modes were applied. Jeffers suggested that the number of samples should always exceed the number of variables, and, ideally, should be at least four times the number of variables [Jef02]. Most authors recommend that one should have at least ten to 20 times as many observation samples as one has variables, otherwise the estimates of the regression line are probably very unstable and unlikely to replicate if one were to repeat the study [tex08]. Since there are only 27 shoulder bone pairs in the datasets, the recommended number of principal modes applied is thus one or two according to this theory.

Figures 6.18 and 6.19 show the RMS errors of the predicted humerus shape and scapula shape of *Cebus* 1 using different numbers of principal modes, the abscissa representing the number of principal modes applied and the ordinate representing the values of RMS errors. The prediction results of this shoulder pair become inaccurate as there are more than a certain number of principal modes being used in PLS regression. To explore the relationship between the prediction behaviour and the number of principal modes applied to the prediction, the average RMS error of the predicted shapes were calculated for each specimen when different numbers of principal modes were used in PLS regression. A demonstration of these average errors is shown in Figure 6.20, with the abscissa representing the number of principal modes.

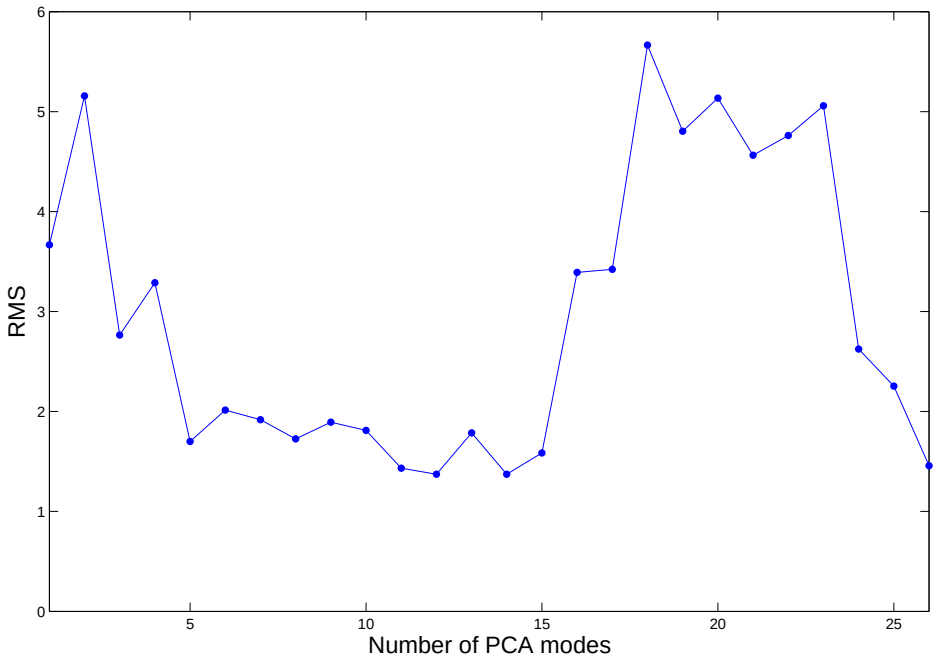

(a) Predicted humerus shape

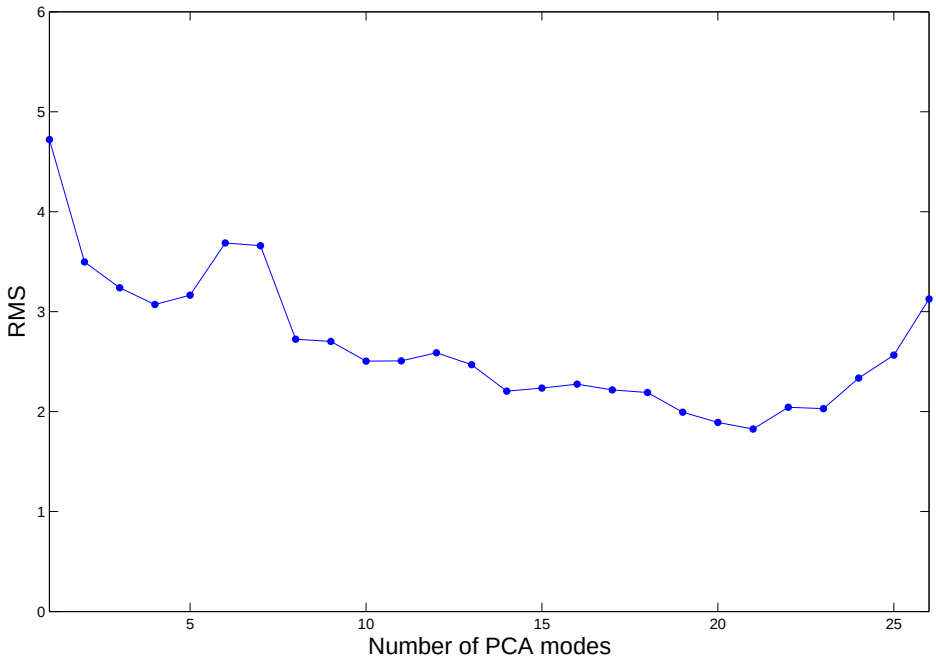

(b) Predicted scapula shape

Figure 6.18: RMS errors of the predicted *Cebus* humerus and scapula using different numbers of principal modes (model one - including size)

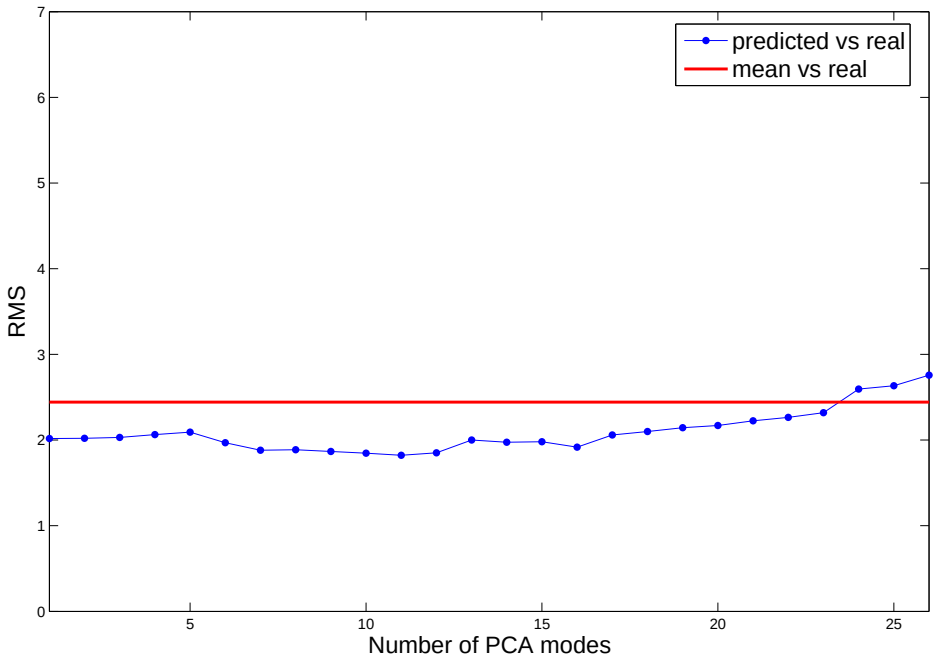

(a) Predicted humerus shape

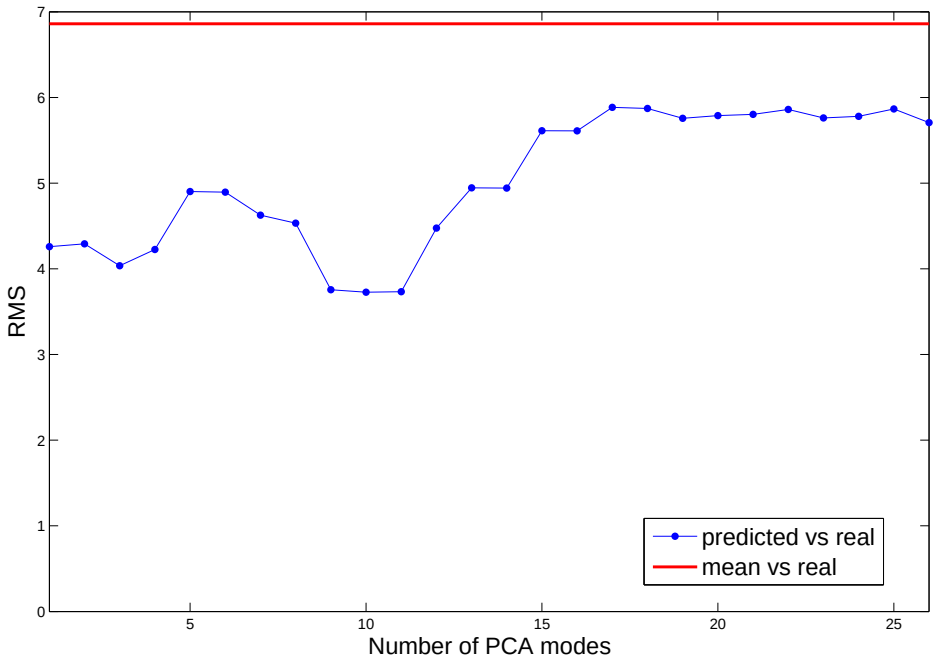

(b) Predicted scapula shape

Figure 6.19: RMS errors of the predicted *Cebus* humerus and scapula using different numbers of principal modes (model two - excluding size)

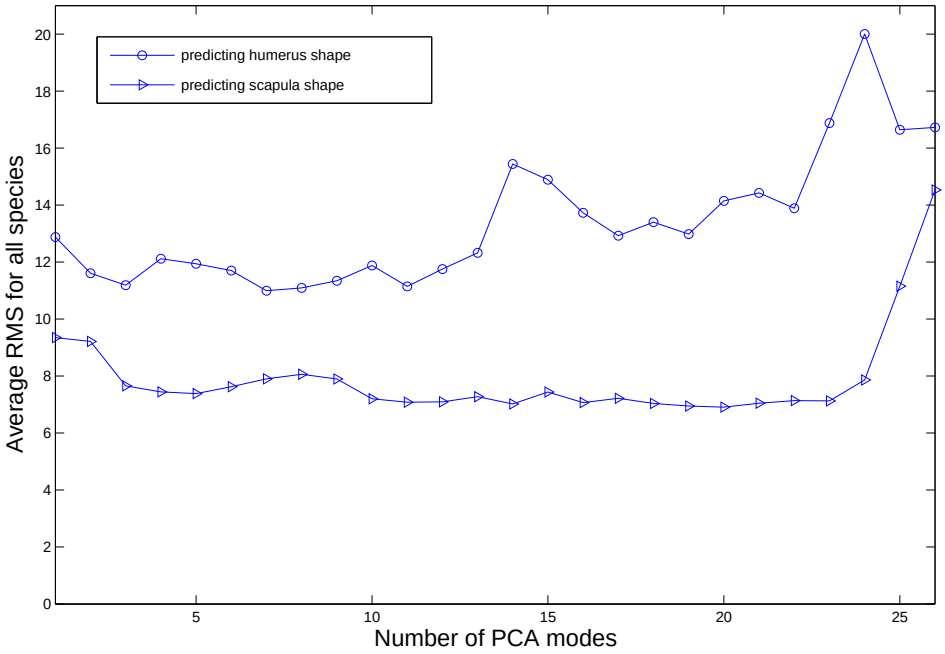

(a) Model One (Including size)

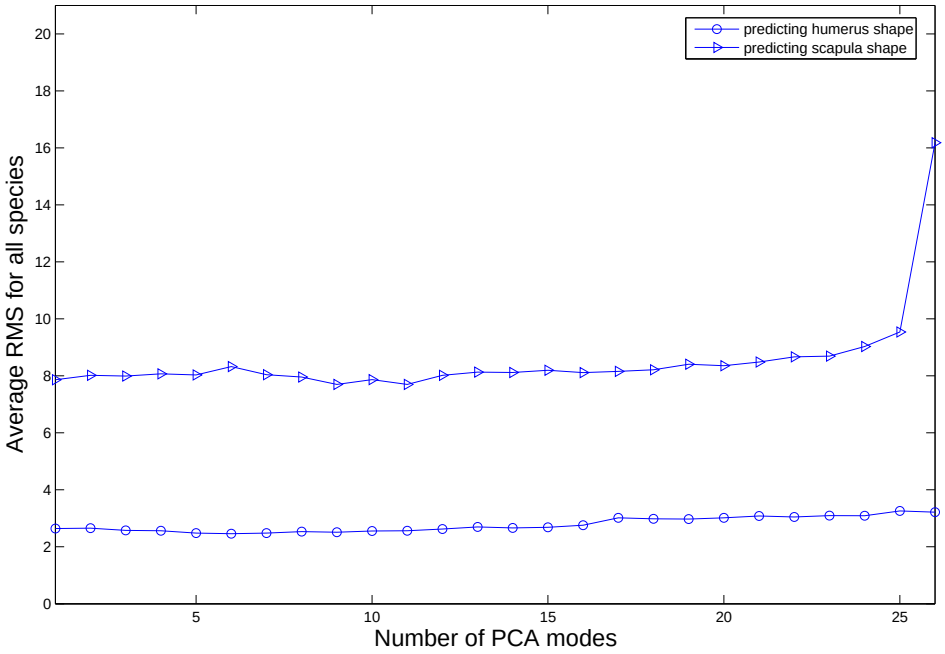

(b) Model Two (Excluding size)

Figure 6.20: Average RMS errors when different numbers of principal modes are applied

In the leave-one-out validations, RMS errors of the mean shapes of the models were calculated. Table 6.4 lists the RMS errors of the mean shapes of the models. It can be seen that the mean shapes are not good prediction estimations when size variation is included in the models. In the present datasets, the mean shapes of the scapula models have larger RMS errors than those of the humerus models. All RMS errors of the predicted shapes were calculated to compare to the RMS errors of the mean shapes. They are listed from Tables C.1 to C.4 in Appendix C. The number of principal modes applied in PLS regression ranges from one to 20 in those tables.

Specimen	Model One (mm) (Including size)		Model Two (mm) (Excluding size)	
	humerus	scapula	humerus	scapula
Cebus 1	72.8547	31.0723	2.4433	6.8595
Cebus 2	78.8011	29.7106	4.5760	7.7828
Cebus 3	75.3217	31.5684	2.9200	7.2789
Pan 1	42.4614	17.6824	3.2185	12.4867
Pan 2	25.9162	9.9278	2.3103	19.5621
Pan 3	35.8626	20.9433	3.8902	10.9274
Colobus 1	53.0795	21.4632	2.4840	4.4637
Colobus 2	43.2643	16.5659	1.9738	6.9576
Colobus 3	45.6630	19.3828	2.2180	5.8869
Gorilla 1	89.3229	36.3328	3.3561	15.6347
Gorilla 2	135.5530	62.8350	3.0565	15.6951
Gorilla 3	122.6820	55.1760	3.5151	8.8711
Homo 1	47.9850	13.4010	2.5910	12.1306
Homo 2	32.0940	22.2910	3.3905	19.0028
Homo 3	28.6469	12.6299	3.3862	15.3608
Macaca 1	51.0209	12.7612	5.9201	7.8730
Macaca 2	51.9230	13.8414	2.9463	8.8560
Macaca 3	67.4287	28.8807	2.7857	8.1758
Macaca 4	47.3334	9.9949	4.1768	7.4291
Pongo 1	49.6868	14.0315	3.7174	11.5234
Papio 1	5.1874	12.0186	2.6181	11.5251
Papio 2	8.0394	21.7337	3.7323	13.7378
Papio 3	8.3631	12.1293	2.7847	13.9590
Presbytis 1	52.6649	23.9471	2.9415	5.4356
Presbytis 2	46.3060	19.0304	2.6313	5.2733
Presbytis 3	47.2642	20.1852	3.5049	5.8198
Presbytis 4	52.5121	22.1631	2.6917	4.8911
Presbytis 5	57.7301	22.1521	2.0083	5.1300

Table 6.4: RMS errors of the mean shapes of the models

Although the more principal modes are used the more morphological variation of the training set are described, this does not mean that the more principal modes applied to PLS regression the better prediction behaviour we will have. The number of better predictions is plotted in Figure 6.21, the abscissa representing the number of principal modes.

When predicting the humerus shapes from their corresponding scapula shapes without size variation, the best prediction results are attained when the first two principal modes are used, claiming 28 better predictions out of the 28 leave-one-out experiments (100%) than using mean shapes. However this number drops when more principal modes were applied, 15 better predictions remaining when the first 17 principal modes are used. When predicting the scapula shapes from their corresponding humerus shapes, the figure shows that the first 11 principal modes produce the best prediction behaviour, with 24 better predictions (86%) than using the mean shape. According to the figures, there is a descending tendency when more principal modes are applied. In model one (including size variation), since the mean shape of the model differs from many single shapes in the training set due to the large size difference, the comparison between the RMS from the PLS predicted shapes and the RMS from the mean shapes does not directly reflect prediction accuracy.

If the number of samples is relatively small, PLS regression cannot extract sufficient correlations due to the lack of data description. This results in worse prediction behaviour when more principal modes are applied to the correlation analysis.

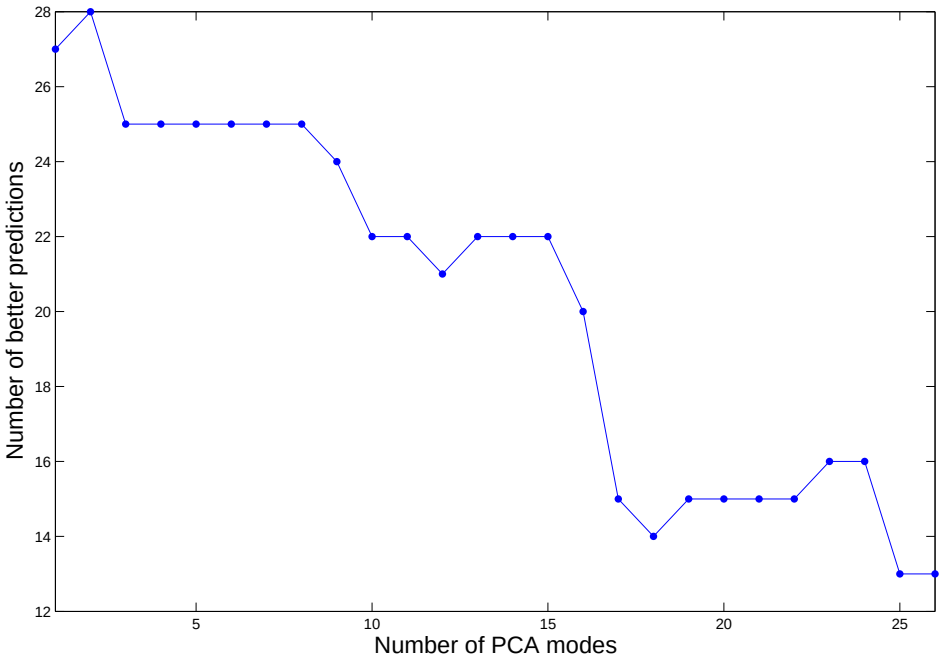

(a) Predicting humerus shapes

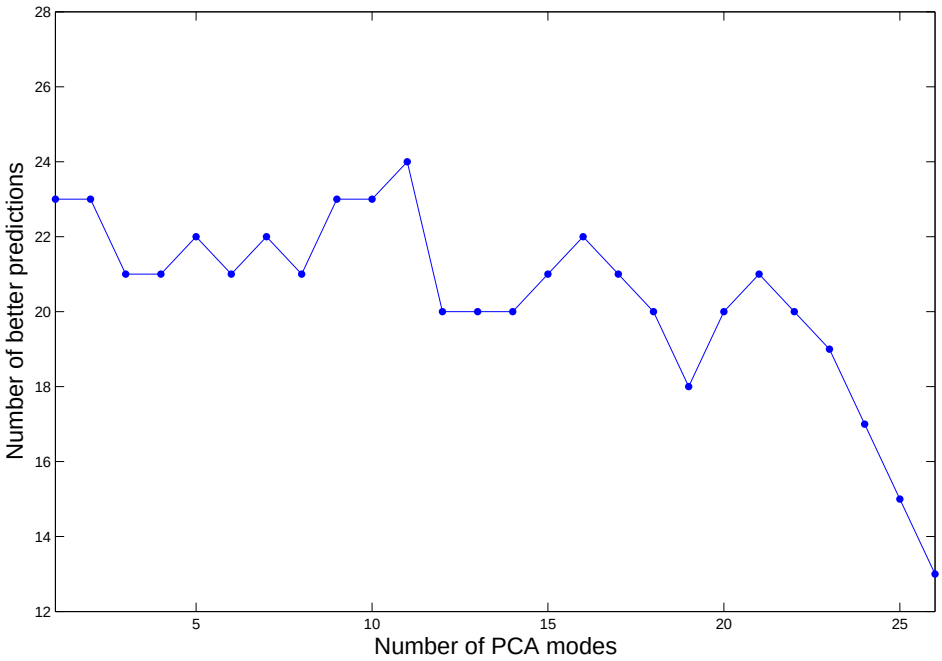

(b) Predicting scapula shapes

Figure 6.21: Number of better predictions using the PLS regression method when different numbers of principal modes were applied (model two - excluding size)

6.4.2 Standard Morphological Measurements

The RMS error of the surface points can measure closeness between two surfaces but cannot estimate the anatomical differences in a way that relates joint mechanics. To validate the accuracy of the prediction models in terms of joint mechanics, the bony features (such as bending of the humeral shaft and size of the scapular glenoid) of the predicted shapes were measured to compare to those of the real shapes. The morphological measurement method is described in Chapter 4, Sections 4.3 and 4.4.

Predicting the Humerus

The radius of the fitted sphere on the humeral head is used to describe size of the humeral head, and the radius of the fitted sphere on the scapular glenoid is used to describe size of the glenoid. The radii were calculated from the predicted shapes to compare with those of the real shapes. Table 6.5 lists the calculated radii of the predicted shapes, the real shapes, and of the mean shapes of the training sets. The predicted shapes were based on the first three principal modes.

Figure 6.22 compares the size differences between the predicted shapes based on prediction model one (including size variation) and the real shapes, and the differences between the mean shapes and the real shapes. The minimum error of size of the predicted humeral head is $0.01mm$ (from *Presbytis* 1), and the minimum error of size of the predicted glenoid is $0.02mm$ (from *Cebus* 2). The average errors of the predicted humeral head and the predicted glenoid are $1.51mm$ and $3.42mm$ respectively. *Homo* 1 and *Homo* 2 have the greatest prediction errors. 26 predicted humerus shapes in the 28 leave-one-out validations (93%) have a humeral head size closer to the real humerus shapes than the mean shapes of the training sets; 27 predicted scapula shapes (96%) are closer in glenoid size to the real scapula shapes than the mean shapes of the training sets.

Specimen	Humeral head (mm)			Scapular glenoid (mm)		
	Predicted	Real	Mean	Predicted	Real	Mean
Cebus 1	6.32	6.73	15.11	8.16	11.32	20.50
Cebus 2	6.22	10.38	14.99	6.38	9.51	20.56
Cebus 3	6.05	5.35	15.22	8.37	8.35	20.53
Pan 1	19.38	23.04	14.79	33.38	42.18	20.92
Pan 2	18.10	15.98	14.69	25.06	34.83	19.95
Pan 3	21.18	20.96	14.92	27.08	27.25	20.22
Colobus 1	8.94	9.00	15.22	12.44	12.59	19.45
Colobus 2	10.09	8.47	14.63	13.31	13.89	20.41
Colobus 3	9.34	8.95	15.14	12.59	12.53	19.30
Gorilla 1	24.41	26.07	15.54	31.32	34.98	19.27
Gorilla 2	35.44	33.25	15.07	42.89	39.04	19.23
Gorilla 3	27.76	31.65	15.23	40.64	36.41	19.38
Homo 1	18.06	22.78	14.95	28.42	34.02	20.43
Homo 2	23.03	21.26	15.36	27.65	49.53	19.50
Homo 3	16.70	18.97	15.50	31.31	29.74	20.61
Macaca 1	9.80	13.10	14.92	13.00	13.93	20.61
Macaca 2	9.81	9.76	15.02	13.75	12.70	20.62
Macaca 3	6.40	6.74	14.73	11.37	8.20	21.94
Macaca 4	10.70	9.90	14.52	14.04	16.01	20.56
Pongo 1	17.98	18.29	14.89	28.49	21.48	20.23
Papio 1	13.19	11.73	14.63	20.49	15.99	20.75
Papio 2	15.87	12.56	14.62	18.99	18.80	20.61
Papio 3	11.68	12.38	14.56	20.33	17.92	20.65
Presbytis 1	7.66	6.96	14.66	13.65	11.09	20.42
Presbytis 2	9.58	9.06	15.00	12.84	12.71	20.65
Presbytis 3	9.16	8.34	14.98	13.77	13.38	21.33
Presbytis 4	8.22	8.13	15.22	13.21	11.09	20.75
Presbytis 5	8.64	8.63	15.30	12.05	14.65	21.28

'Predicted' column: size of the predicted shapes
'Real' column: size of the real shapes
'Mean' column: size of the mean shapes of the training sets

Table 6.5: Size (radius of the best fitted sphere) of humeral head and scapular glenoid. The first three principal modes were used in the prediction models. (Model one - including size)

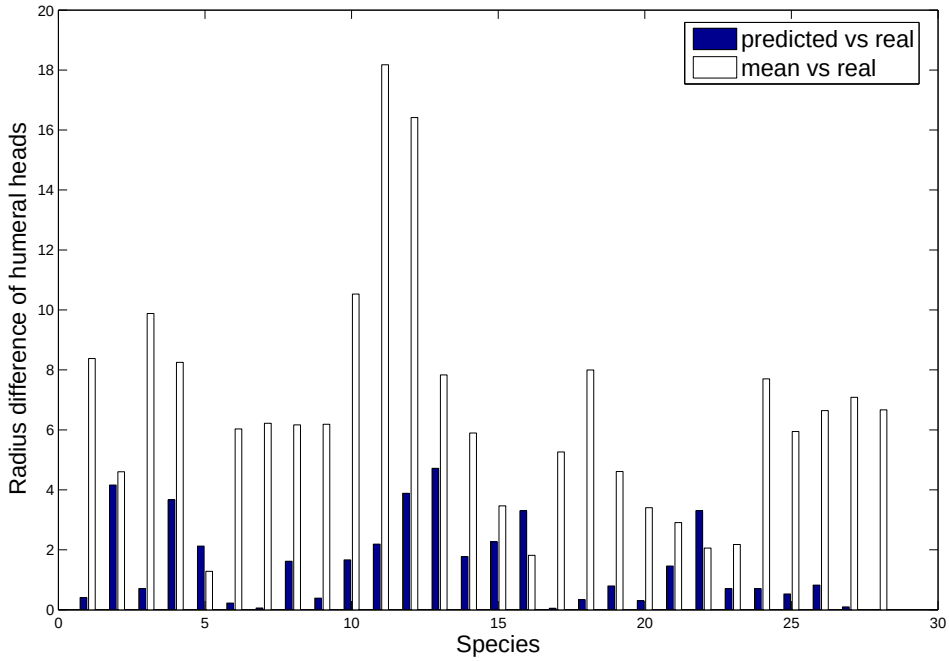

(a) Humeral head

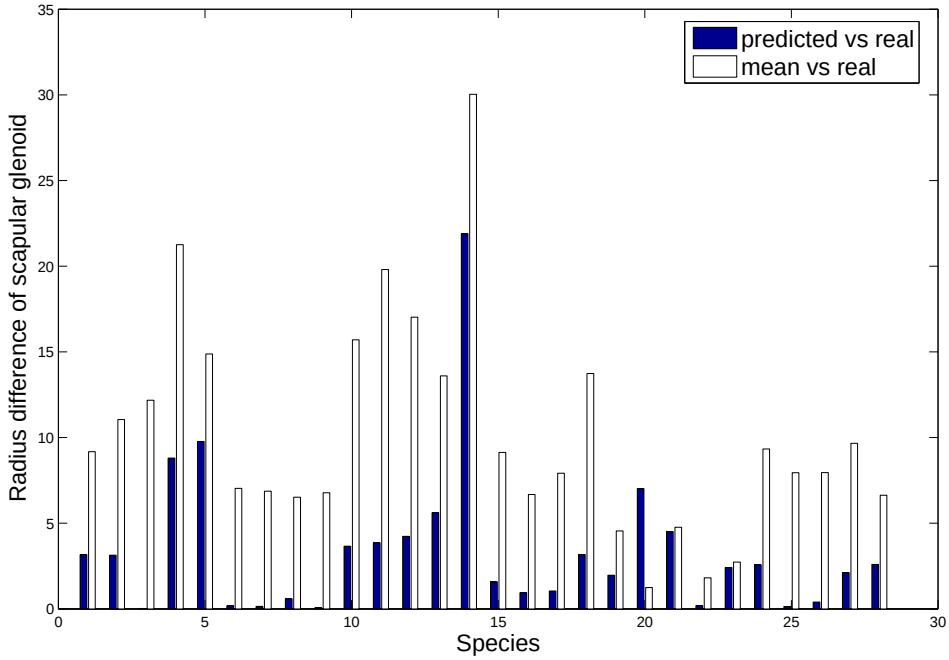

(b) Scapular glenoid

The order of the genus from left to right is: *Cebus* (three pairs), *Colobus* (three pairs), *Pan* (three pairs), *Gorilla* (three pairs), *Homo* (three pairs), *Macaca* (four pairs), *Pongo* (one pair), *Papio* (three pairs) and *Presbytis* (five pairs)

Figure 6.22: Size differences when the first three principal modes were used (model one - including size)

Other geometrical parameters were calculated when size variation was excluded. In the humeri, bending of the humeral shaft was estimated on the proximal end (angle between axis L_{shaft} and axis L_{h1}). Torsion was estimated by the angle between axis L_r and axis L_c (definitions are in Chapter 4, Section 4.3.3). In the scapulae, the spatial relationship between the glenoid and the infraspinous fossa was investigated by the angle between the normal vector of the glenoid and the normal vector of the infraspinous fossa.

Degrees of torsion, mid-shaft bending and proximal bending of the predicted humerus shapes are listed in Tables 6.6 to 6.8. These parameters were calculated based on different numbers of principal modes - from one mode to eight. Parameters from the real shapes and the mean shapes are also presented in these tables. Table 6.9 shows the numbers of better predictions of the humerus shapes. There are 22 predicted humeri that have a torsion feature closer to the targets than the mean shapes when four or six principal modes were used (78.6% better prediction). There are 21 (75%) predictions having closer mid-shaft bending when four, five, six or seven principal modes were applied, while there are 25 (89.3%) predictions having closer proximal bending when the first or the first two principal modes were applied. From these tables, the PLS regression method provides the best humerus prediction from the scapula when the first four principal modes were applied.

Figure 6.23 shows the morphological differences between the predicted humerus shapes and the real shapes. The first four principal modes were used in the prediction validations as the prediction model behaves best in terms of torsion when the first four principal modes were applied. The figure shows that the predicted humerus shapes have more accurate degrees of bending than degrees of torsion. Degrees of proximal bending is more accurate compared to mid-shaft bending.

Specimen	Degrees of torsion of the predicted shapes (°)								Real	Mean
	1	2	3	4	5	6	7	8	(°)	(°)
Cebus 1	76.62	76.80	77.22	77.53	74.68	74.97	75.07	75.10	66.02	64.97
Cebus 2	77.54	76.73	77.26	77.16	68.30	67.44	65.72	64.69	76.99	63.36
Cebus 3	76.97	77.70	78.16	79.79	80.55	83.70	88.86	87.02	66.09	64.54
Pan 1	55.91	60.13	51.43	56.71	44.05	37.73	38.00	34.70	13.77	64.58
Pan 2	31.02	37.41	22.49	30.10	36.52	45.25	49.26	30.42	37.17	62.75
Pan 3	55.29	61.89	55.60	60.73	55.19	54.98	59.77	61.68	21.98	64.19
Colobus 1	69.69	70.49	71.55	72.19	78.80	81.17	82.32	82.56	74.42	63.56
Colobus 2	73.01	73.17	76.04	71.50	81.19	85.79	85.42	90.97	79.81	64.28
Colobus 3	71.09	71.55	72.39	72.96	78.46	78.70	80.45	81.87	89.33	63.82
Gorilla 1	60.46	62.76	37.97	40.59	28.15	28.86	26.12	9.89	28.71	63.88
Gorilla 2	42.39	48.00	26.08	20.91	35.20	45.47	51.12	39.54	49.69	63.23
Gorilla 3	62.33	64.64	54.77	50.17	48.79	54.85	59.71	57.70	15.92	64.37
Homo 1	46.51	45.47	59.38	57.76	45.47	43.47	42.01	46.41	51.84	63.83
Homo 2	22.20	19.25	30.23	53.94	40.24	33.56	30.19	26.50	48.27	64.21
Homo 3	39.20	39.79	53.89	56.03	53.12	49.20	40.83	45.32	30.72	63.99
Macaca 1	78.45	78.23	79.20	78.96	77.44	74.67	74.62	71.64	61.22	64.90
Macaca 2	80.01	80.06	79.44	80.26	78.02	74.20	74.33	73.95	87.37	63.58
Macaca 3	79.31	79.67	79.69	78.97	78.80	80.37	79.88	77.48	67.83	64.56
Macaca 4	75.53	74.71	75.53	77.16	77.32	76.72	77.43	76.97	78.50	62.53
Pongo 1	56.41	58.76	63.88	66.62	54.54	49.42	48.65	32.78	74.03	64.45
Papio 1	83.10	80.85	82.49	81.22	80.17	76.75	78.62	76.61	68.62	63.48
Papio 2	86.11	83.60	83.97	83.87	77.90	77.95	76.12	76.61	76.90	64.07
Papio 3	82.94	80.88	81.59	79.16	75.45	68.38	66.97	66.54	80.43	63.57
Presbytis 1	65.31	65.75	65.88	67.57	73.11	77.86	77.38	76.99	91.66	63.79
Presbytis 2	71.33	71.29	72.95	74.27	79.94	79.44	80.21	81.39	92.41	63.86
Presbytis 3	70.26	71.36	71.99	72.89	78.34	81.59	83.03	84.75	73.74	62.72
Presbytis 4	68.60	69.12	69.28	71.85	72.06	71.95	71.14	71.09	75.43	64.32
Presbytis 5	74.84	75.30	77.91	78.24	81.07	80.63	81.45	81.72	78.92	64.64

Table 6.6: Degrees of torsion of the predicted humeri using one to eight principal modes (model two - excluding size)

Specimen	Degrees of mid-shaft bending of the predicted shapes (°)								Real	Mean
	1	2	3	4	5	6	7	8	(°)	(°)
Cebus 1	11.83	11.91	11.69	11.60	11.34	11.14	10.85	10.83	14.15	8.87
Cebus 2	12.18	12.43	12.14	12.11	11.04	10.90	10.80	10.63	13.44	8.80
Cebus 3	12.27	12.36	12.18	12.11	12.05	12.48	13.46	13.15	40.64	9.22
Pan 1	8.12	7.45	9.84	9.62	10.08	8.40	8.68	9.87	6.15	8.89
Pan 2	9.46	8.37	11.69	11.94	11.35	11.73	11.48	12.26	5.59	8.78
Pan 3	8.21	7.51	9.29	8.97	9.09	8.73	8.67	9.11	9.02	9.17
Colobus 1	10.14	10.14	9.54	9.38	10.03	10.68	10.32	10.34	10.95	9.03
Colobus 2	10.10	10.11	9.54	9.69	11.46	11.80	12.17	12.89	11.40	8.86
Colobus 3	10.65	10.59	10.31	10.11	10.73	10.91	10.16	9.98	11.67	8.98
Gorilla 1	8.47	8.00	9.61	8.94	9.27	10.48	11.98	12.54	11.68	8.87
Gorilla 2	7.63	6.93	9.09	10.26	11.06	11.07	11.00	8.18	11.71	8.95
Gorilla 3	8.49	8.41	8.67	10.64	10.44	11.17	11.67	11.34	12.42	9.09
Homo 1	7.69	7.52	3.56	4.14	4.68	5.72	6.02	6.53	5.98	8.91
Homo 2	10.79	11.02	9.20	6.09	8.21	7.78	9.02	6.60	6.98	9.19
Homo 3	8.67	8.39	3.62	3.95	4.38	3.33	2.09	3.01	4.96	9.03
Macaca 1	12.19	12.35	12.39	12.15	11.87	11.83	11.84	12.03	13.50	8.92
Macaca 2	12.88	13.03	12.97	12.99	12.53	12.05	12.08	11.77	16.87	8.84
Macaca 3	12.60	12.82	12.83	12.72	12.69	13.05	13.47	13.43	11.79	9.18
Macaca 4	12.17	12.29	11.97	11.93	11.73	11.64	11.59	11.55	16.94	9.00
Pongo 1	7.07	7.09	6.82	7.28	6.57	6.29	5.95	3.46	15.58	8.33
Papio 1	14.91	14.87	14.71	14.66	14.54	14.59	14.54	14.94	15.07	8.91
Papio 2	15.80	15.86	15.99	15.86	15.22	14.39	14.53	14.50	17.64	8.92
Papio 3	16.73	16.94	17.26	17.25	16.44	16.44	16.67	17.66	11.00	9.08
Presbytis 1	11.00	11.13	10.55	10.39	11.33	11.53	11.56	11.52	9.43	8.96
Presbytis 2	10.42	10.42	9.83	9.58	10.52	10.72	10.86	10.67	13.35	8.89
Presbytis 3	10.30	10.44	10.31	10.26	10.92	11.06	10.79	10.80	16.47	8.81
Presbytis 4	11.22	11.55	12.37	13.16	14.03	14.03	13.71	13.69	6.27	9.12
Presbytis 5	11.25	11.34	11.20	11.08	11.53	11.55	11.49	11.47	7.68	9.09

Table 6.7: Degrees of mid-shaft bending of the predicted humeri using one to eight principal modes (model two - excluding size)

Specimen	Degrees of proximal bending of the predicted shapes (°)								Real	Mean
	1	2	3	4	5	6	7	8	(°)	(°)
Cebus 1	11.04	11.16	11.23	11.42	11.06	10.85	11.22	11.25	10.46	7.74
Cebus 2	11.35	11.48	11.54	11.63	10.69	10.63	10.88	10.74	9.73	7.64
Cebus 3	11.13	11.31	11.17	11.78	11.85	11.62	12.24	12.14	9.38	7.81
Pan 1	5.09	5.34	4.22	4.32	3.04	3.20	2.95	2.47	1.20	7.83
Pan 2	1.83	1.21	3.81	3.50	2.89	2.88	3.11	4.87	3.46	7.60
Pan 3	4.97	5.55	4.87	5.37	5.10	5.33	5.40	5.13	1.06	7.78
Cobolus 1	9.17	9.20	9.33	9.63	10.75	10.65	10.43	10.48	10.80	7.79
Cobolus 2	9.49	9.54	10.27	9.35	10.81	10.66	10.87	10.82	10.47	7.76
Cobolus 3	9.66	9.71	9.72	10.11	10.88	10.87	10.65	10.48	8.68	7.87
Gorilla 1	6.60	6.66	3.92	3.99	3.14	3.23	3.69	4.86	2.65	7.68
Gorilla 2	3.13	3.02	1.39	2.17	2.16	1.90	1.67	0.91	5.26	7.74
Gorilla 3	6.96	6.96	5.38	4.86	4.58	4.58	4.58	5.11	3.80	7.83
Homo 1	3.77	3.09	4.66	4.47	3.14	2.56	2.79	2.99	3.19	7.76
Homo 2	2.57	2.93	1.50	1.68	1.53	1.84	1.56	1.46	1.89	7.84
Homo 3	2.41	1.96	3.49	3.42	3.16	3.48	4.52	5.69	3.41	7.75
Macaca 1	11.59	11.64	11.79	11.85	11.56	11.82	11.78	11.82	12.27	7.72
Macaca 2	12.17	12.36	12.11	12.40	12.04	12.17	12.21	12.01	14.52	7.72
Macaca 3	12.02	12.24	12.27	12.20	12.14	11.98	12.34	12.41	11.11	7.87
Macaca 4	11.59	11.65	11.86	12.28	12.26	12.30	12.17	12.15	14.47	7.70
Pongo 1	6.44	6.64	8.24	8.39	7.83	7.59	7.32	2.64	5.00	8.15
Papio 1	14.08	14.07	14.45	14.07	13.97	14.27	14.24	14.58	10.98	7.80
Papio 2	14.70	14.59	14.69	14.51	13.50	13.15	13.60	13.69	17.49	7.62
Papio 3	15.66	15.78	16.01	15.35	14.56	15.02	15.42	15.95	10.87	7.86
Presbytis 1	9.93	10.10	10.41	10.88	11.96	11.75	11.95	11.85	10.78	7.77
Presbytis 2	9.69	9.68	9.93	10.37	11.44	11.58	11.39	11.25	12.99	7.71
Presbytis 3	9.70	9.84	9.86	10.25	11.27	10.96	10.71	10.53	15.52	7.61
Presbytis 4	10.25	10.42	10.88	11.34	12.01	12.01	11.88	11.87	9.70	7.84
Presbytis 5	10.22	10.35	10.61	11.02	11.54	11.48	11.35	11.34	10.21	7.83

Table 6.8: Degrees of proximal bending of the predicted humeri using one to eight principal modes (model two - excluding size)

number of modes	torsion	bending	
		mid-shaft	proximal
1	21	17	25
2	20	18	25
3	20	18	22
4	22	21	23
5	21	21	23
6	22	21	22
7	21	21	22
8	21	20	22
9	19	19	23
10	21	20	23

Table 6.9: Number of predicted humerus shapes that have closer torsion and bending features to the real shapes than the mean humerus shapes of the training sets to the real shapes. Result vary when different numbers of principal modes were used. (model two - excluding size)

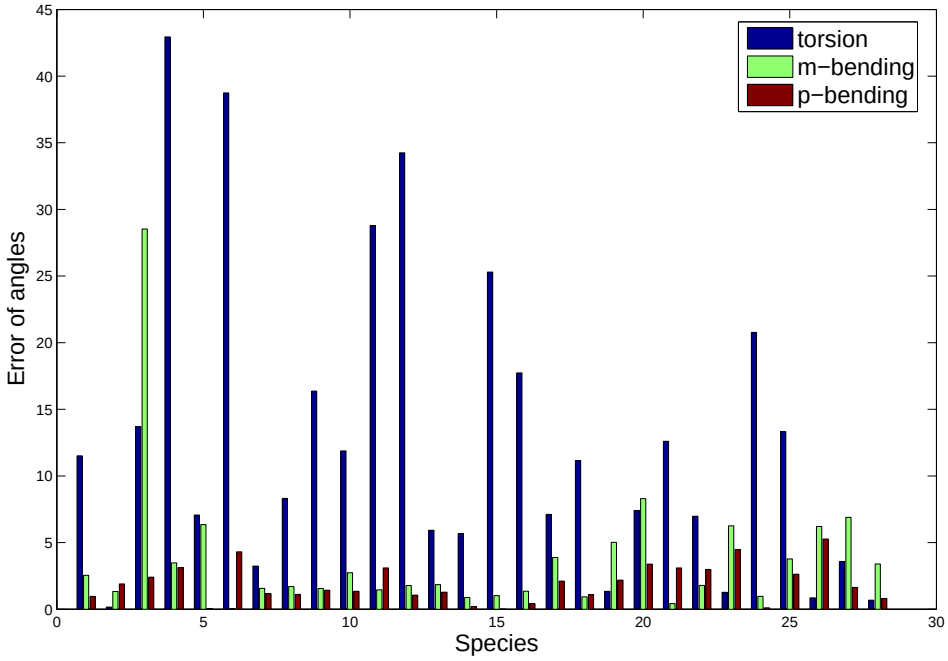

m-bending: mid-shaft bending; p-bending: proximal bending

The order of the genus from left to right is: *Cebus* (three pairs), *Colobus* (three pairs), *Pan* (three pairs), *Gorilla* (three pairs), *Homo* (three pairs), *Macaca* (four pairs), *Pongo* (one pair), *Papio* (three pairs) and *Presbytis* (five pairs)

Figure 6.23: Morphological differences between the predicted humerus shapes and the real shapes (model two - excluding size)

Predicting the Scapula

In order to validate the predictions of the scapula shapes, D_{gn} (angle between the normal of the glenoid and the normal of the infraspinous fossa) and D_{gb} (angle between the glenoid normal and the lateral border axis) of the predicted shapes were calculated. The definitions of D_{gn} and D_{gb} are shown in Table 4.4, page 111; a demonstration of these normal vectors and anatomical axes is shown in Figure 4.29.

Tables 6.10 and 6.11 list the angles of the predicted scapulae using different numbers of principal modes - from one mode to eight modes. Parameters of the real scapula shapes and the mean shapes are listed, to compare with those of the predicted shapes.

Specimen	Predicted shapes (°)								Real	Mean
	1	2	3	4	5	6	7	8	(°)	(°)
Cebus 1	83.36	83.39	83.11	83.79	83.95	84.69	86.33	86.66	83.76	85.03
Cebus 2	82.69	81.02	81.95	86.21	86.80	87.05	87.02	89.56	89.32	85.27
Cebus 3	84.50	85.07	86.19	88.14	86.50	87.29	88.97	89.40	84.65	85.73
Pan 1	87.23	86.82	86.08	84.42	84.80	84.53	84.89	85.21	89.46	84.24
Pan 2	86.24	86.42	86.10	85.56	85.76	85.97	87.34	87.01	84.97	84.35
Pan 3	87.37	87.26	88.07	88.12	88.14	87.45	89.68	87.17	89.05	84.19
Colobus 1	82.26	82.53	82.94	84.83	84.10	84.77	84.65	85.76	88.50	84.71
Colobus 2	83.66	84.46	85.06	86.11	85.96	85.05	85.81	86.43	84.58	85.83
Colobus 3	83.76	84.09	83.40	84.75	84.07	84.26	84.11	84.30	88.42	85.50
Gorilla 1	88.93	88.69	87.57	86.06	85.30	85.40	84.96	85.22	87.24	85.79
Gorilla 2	88.15	87.80	87.92	87.35	87.72	85.85	86.37	84.88	85.16	85.50
Gorilla 3	87.13	86.81	87.25	87.02	87.00	86.74	86.32	87.44	78.31	84.15
Homo 1	86.80	86.86	87.14	87.76	88.10	87.90	88.23	89.27	83.50	85.03
Homo 2	87.20	87.70	88.43	89.85	89.27	89.19	89.04	86.15	86.05	85.39
Homo 3	87.73	88.03	88.58	89.73	89.91	89.04	89.42	89.77	87.67	85.38
Macaca 1	82.96	79.53	82.15	81.82	82.27	79.86	80.84	78.98	79.34	85.52
Macaca 2	82.31	82.15	81.56	81.69	81.89	80.83	81.00	78.95	80.40	85.71
Macaca 3	83.39	83.66	82.94	83.16	83.22	83.75	84.53	84.01	83.16	85.65
Macaca 4	81.46	80.44	80.59	80.49	80.55	77.30	77.06	77.18	84.73	85.56
Pongo 1	88.69	88.60	85.69	85.66	85.35	86.47	87.18	88.06	82.96	85.65
Papio 1	83.52	83.54	82.76	82.51	82.35	81.99	81.89	80.81	71.04	85.69
Papio 2	82.41	82.44	81.87	81.65	81.63	81.64	81.47	81.11	71.39	85.64
Papio 3	82.23	82.40	82.53	84.20	83.52	83.02	82.96	82.33	70.96	85.08
Presbytis 1	83.11	83.78	83.86	85.80	85.35	86.12	86.85	87.36	85.28	85.32
Presbytis 2	82.08	82.20	82.11	83.97	83.07	83.67	84.25	85.05	83.22	85.07
Presbytis 3	81.53	81.82	80.59	81.36	80.65	80.75	80.61	80.27	81.02	85.61
Presbytis 4	84.47	84.84	86.27	87.99	87.96	87.17	87.89	88.00	89.38	85.50
Presbytis 5	84.13	84.22	85.64	86.71	85.86	85.40	85.41	86.34	83.49	85.47

Table 6.10: Angles between the normals of the glenoid and the normals of the infraspinous fossa (D_{gn}) on the predicted scapulae. One to eight principal modes were applied. (model two - excluding size)

Specimen	Predicted shapes (°)								Real	Mean
	1	2	3	4	5	6	7	8	(°)	(°)
Cebus 1	34.90	35.00	35.02	35.84	36.15	33.63	35.55	35.27	29.91	36.09
Cebus 2	37.15	37.25	37.75	43.07	43.96	42.76	41.49	41.22	31.85	38.81
Cebus 3	37.50	37.41	40.00	43.97	43.00	44.79	42.80	42.49	32.70	37.89
Pan 1	39.06	40.20	35.75	31.70	34.49	32.73	30.77	31.22	33.72	38.45
Pan 2	36.36	35.98	35.08	35.22	36.41	36.81	32.24	32.22	31.89	35.80
Pan 3	38.45	39.13	40.47	40.60	42.57	46.10	45.04	45.78	25.45	37.40
Colobus 1	33.43	33.84	36.58	39.97	40.01	38.94	39.28	38.70	40.71	36.94
Colobus 2	36.66	39.56	38.14	39.85	40.11	37.83	41.63	41.73	40.80	40.51
Colobus 3	39.12	39.24	38.07	40.58	38.05	36.47	36.33	36.23	35.85	40.51
Gorilla 1	38.97	37.41	34.05	29.87	28.47	28.25	29.44	30.49	32.09	39.11
Gorilla 2	38.64	37.53	35.73	32.66	34.71	30.56	32.68	30.65	33.18	36.97
Gorilla 3	36.61	36.19	35.64	35.18	32.94	32.57	39.04	36.87	21.02	35.92
Homo 1	37.79	38.00	36.86	38.76	41.39	40.56	40.44	40.07	52.04	35.80
Homo 2	32.54	33.95	34.10	36.14	38.61	39.69	42.31	45.79	58.85	33.95
Homo 3	36.03	36.00	36.40	38.62	39.46	40.46	42.30	43.21	38.36	33.86
Macaca 1	32.91	33.55	26.36	26.09	27.85	34.40	36.81	38.98	42.66	36.40
Macaca 2	32.27	32.67	32.50	33.19	32.92	34.37	35.70	33.69	38.08	37.60
Macaca 3	32.24	32.46	31.77	32.56	32.47	33.30	35.87	36.45	35.69	36.47
Macaca 4	31.89	31.79	33.10	40.06	37.80	36.46	37.98	38.59	30.90	37.14
Pongo 1	36.62	36.43	29.35	28.90	29.76	29.49	27.77	29.92	10.84	34.58
Papio 1	33.03	32.98	30.33	31.23	29.50	30.46	31.58	33.04	42.92	36.67
Papio 2	31.67	31.66	33.00	39.30	39.34	42.87	44.34	44.41	48.06	36.46
Papio 3	33.18	33.17	35.98	42.40	40.75	43.00	43.49	42.33	35.80	37.66
Presbytis 1	31.72	32.02	35.37	38.07	38.10	37.85	38.89	38.86	37.27	35.04
Presbytis 2	34.16	33.91	35.38	37.94	37.42	35.73	37.50	37.65	36.53	38.52
Presbytis 3	30.69	30.50	31.35	32.32	50.16	27.76	27.56	20.39	30.24	35.79
Presbytis 4	35.76	35.85	41.04	46.12	46.27	44.47	41.87	40.85	36.27	36.44
Presbytis 5	34.25	34.41	37.84	39.72	37.62	36.84	35.52	35.59	37.59	35.36

Table 6.11: Angles between the normals of the glenoid and the axes approximating the lateral border (D_{gb}) on the predicted scapulae. One to eight principal modes were applied (model two - excluding size)

number of modes	D_{gn}	D_{gb}
1	16	11
2	16	11
3	17	19
4	21	15
5	18	14
6	19	16
7	16	18
8	20	16
9	21	18
10	20	17

D_{gn}: the angle between the normal of the glenoid and the normal of the infraspinous fossa
D_{gb}: the angle between the normal of the glenoid and the axis approximating the lateral border

Table 6.12: Number of predicted scapula shapes that have closer D_{gn} and D_{gb} to the real shapes than the mean scapula shapes of the training sets to the real shapes. The results vary when different numbers of principal modes were used. (model two - excluding size)

Table 6.12 shows the number of predicted shapes which have closer D_{gn} and D_{gb} to the real shapes than the mean shapes. There are 21 predictions (75%) that have closer D_{gn} when four or nine principal modes were applied, while there are 19 predictions (68%) that have closer D_{gb} when the first three principal modes were used. Results show that the predicted scapula shapes are less accurate than the predicted humerus shapes.

6.4.3 Summary

Two prediction validation methods are provided, one calculating the RMS distance of surface points whilst the other utilises morphological features. Leave-one-out validations on both error estimations show that the prediction method using PLS regression is able to predict a shoulder bone shape from its adjacent segment. In the latter validation method, 3D angles between anatomical axes were used to indicate the relationship between the axes. However, these angles are insufficient to describe the spatial relationship. For example, the angle between an axis and any axis on its perpendicular plane is 90 degrees. A potential problem of the use of 3D axes is the lack of spatial information.

Since the humerus and the scapula are more related to each other around the regions

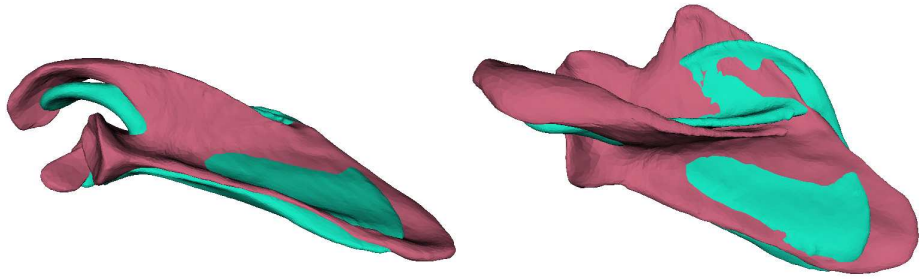

(a) mean shape (green) vs real shape (pink)

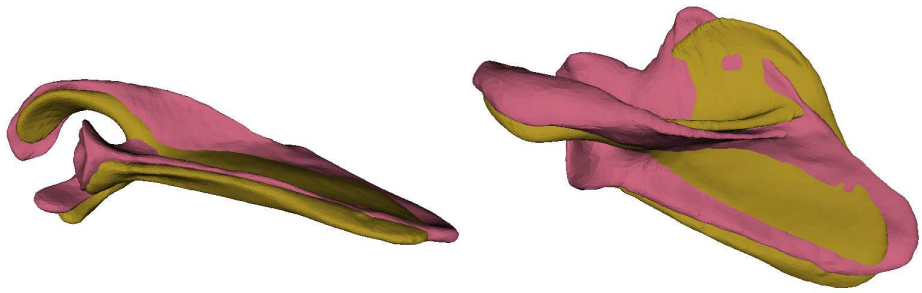

(b) predicted shape (khakis) vs real shape (pink)

Figure 6.24: A *Pan* scapula shape and its predicted shape using the first three principal modes. The mean shape of the training set (built without this *Pan* scapula shape) is displayed. The predicted shape has a more similar area around the glenoid, acromion and coracoid process.

of the humeral head and the glenoid but not of the distal humerus and the scapular blade, it is feasible to estimate the RMS distance on the region of interest, instead of the whole bone, between the predicted shapes and the real shapes. Figure 6.24 shows a predicted *Pan* scapula and the mean scapula from the training set over the real scapula. Although the scapular blade of the predicted shape does not match the real one, the region of the glenoid, the acromion and the coracoid process is very close to the real one. The RMS distance on this region is much less than that of the blade. A remaining question is how to define those regions across different genera.

6.5 Neighbour-Conditional Shape Models

Chapter 5 has built SSMs for the humerus dataset and the scapula dataset. To describe the morphological variations of a shoulder bone conditioned on the adjoining segment, a neighbour-conditional shape model was applied. Given two training sets of shoulder bone shapes and a predictor shape, the mean shape ($\overline{\mathbf{x}}$ in Equation 2.16, page 44) of the neighbour-conditional shape model is the maximum likelihood estimation conditioned on the predictor shape, using Equation 2.17 (page 45). The conditional covariance matrix C is calculated by Equation 2.18. Eigenvalues P (in Equation 2.16) and eigenvectors λ of matrix C can be obtained.

As underlined above, the number of variables compared to the number of observation samples has an influence on multivariate regression. Therefore, PCA was applied to reduce dimensionality of the data vectors. In the construction of the conditional shape model, the described method is numerically unstable if the number of variables is greater than the number of samples. To build a numerically stable model, each shape was described by the PCA scores of its surface points instead of the vectors of all surface points. Details about reducing dimensionality using PCA are explained in Section 6.2. As in the PLS prediction method, the estimated PCA scores can be transformed to its corresponding shape vectors.

Morphological variation demonstrations of the conditional shape models are shown in Figures 6.25 and 6.26, conditioned on a *Homo* scapula and a *Homo* humerus. In these demonstrations, size variation was excluded and the first three principal modes were applied to construct the models. The first shape variation of the estimated humerus is the width and the second variation is bending, which are different from the variation obtained in Chapter 5, Section 5.3.2.

In conditional shape models, the recreated shapes are only plausible in a small range of distribution. Once a conditional shape model is built, the corresponding real shape can be fitted into the model to calculate its distribution in the PCA orthogonal coordinate system (parameter b in Equation 2.16). The distance between b and the origin

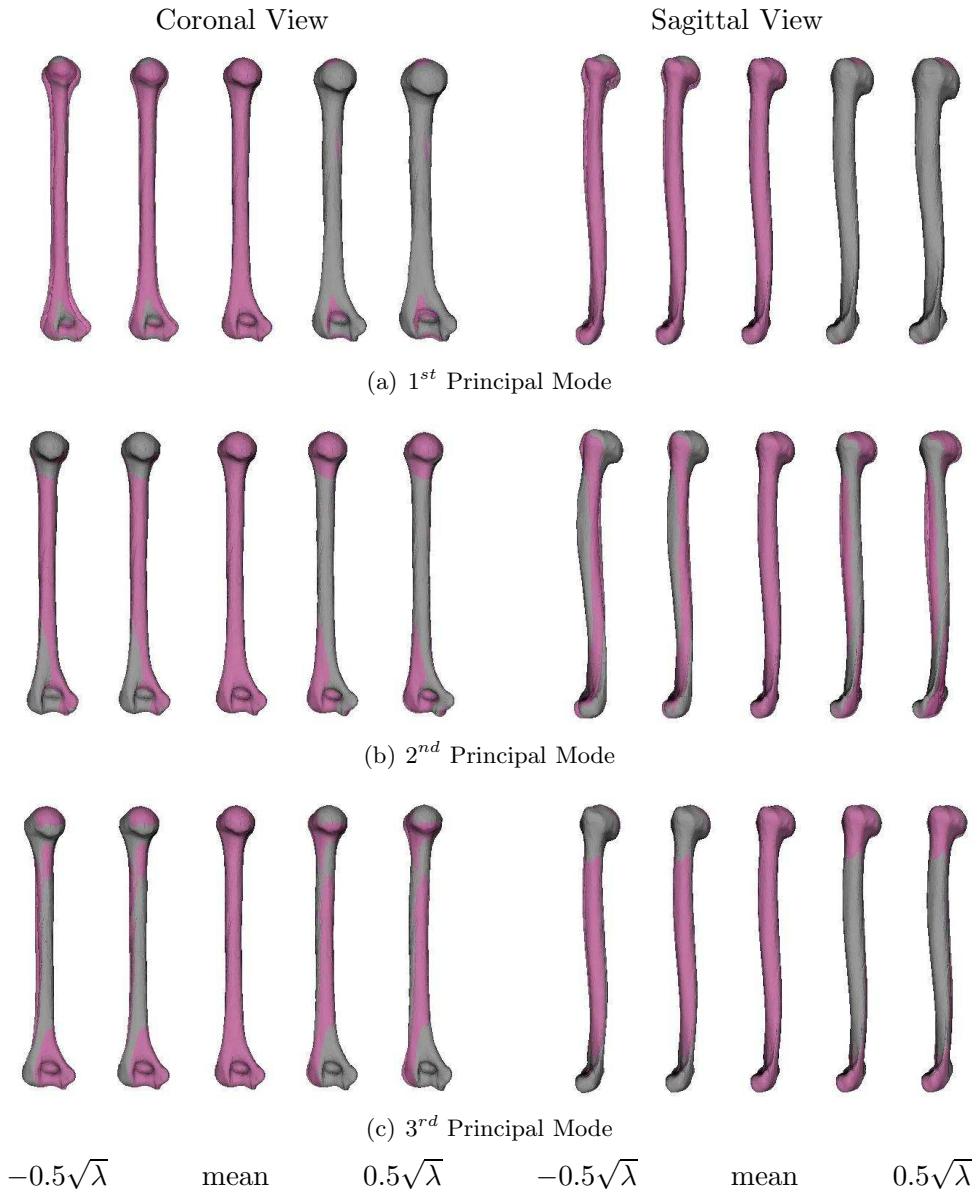

Figure 6.25: Morphological variations of a *Homo* humerus given the adjoining scapula shape. The first three principal modes were used. (model two - excluding size)

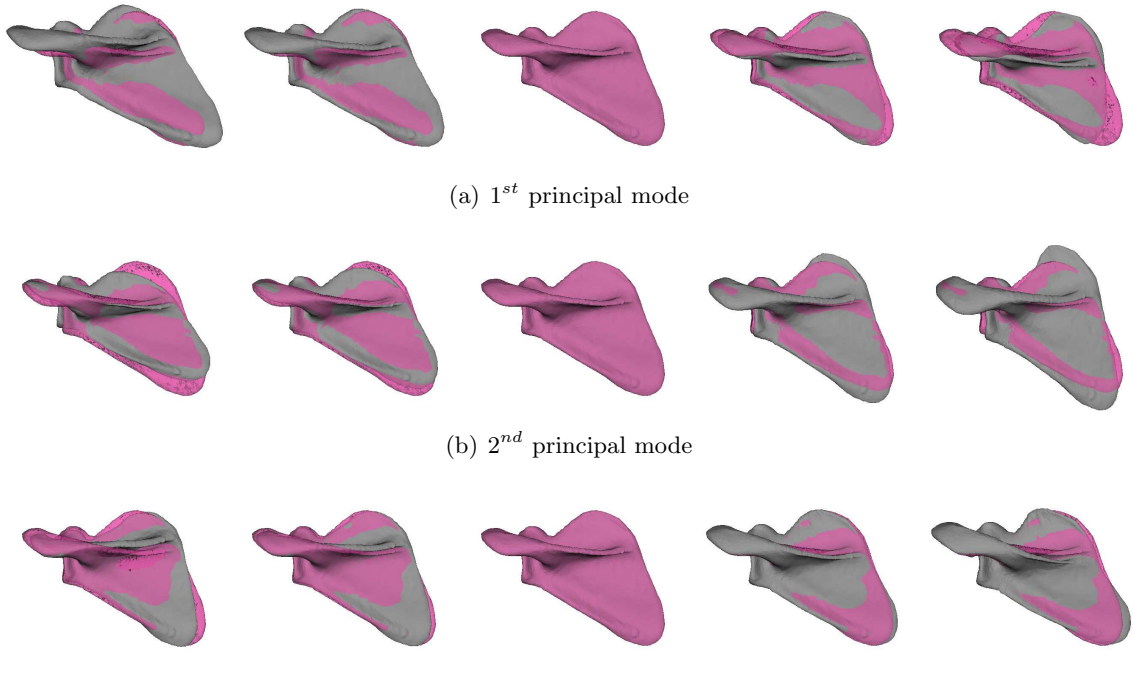

(a) 1^{st} principal mode

(b) 2^{nd} principal mode

(c) 3^{rd} principal mode

$-0.5\sqrt{\lambda}$ $-0.25\sqrt{\lambda}$ mean $0.25\sqrt{\lambda}$ $0.5\sqrt{\lambda}$

Figure 6.26: Morphological variations of a *Homo* scapula given the adjoining humerus shape. The first three principal modes were used. (model two - excluding size)

of the system indicates how close the maximum likelihood estimation is to the real shape.

Leave-one-out validations were performed. The distribution of the estimated humerus and scapula shapes on principal axes were scaled by multiplying $1/\sqrt{\lambda}$ (Figures 6.27 and 6.28 show the distribution patterns). The average b vectors are $\{-0.039, 0.008, -0.063\}^T$ and $\{-0.018, 0.013, -0.063\}^T$. Both are very close to the origin $\{0.0, 0.0, 0.0\}^T$.

The maximum likelihood estimations (or the mean shapes of the conditional shape models) were compared to the predicted shapes using PLS regression method. The results show that there is no difference between the estimated shapes and the predicted shapes in the present work.

A potential application of the neighbour-conditional shape model is to combine the model with the bone-morphing technique. Deformation of the mean shape to a set of sparse points, which can be obtained from an incomplete bone, can be constrained by

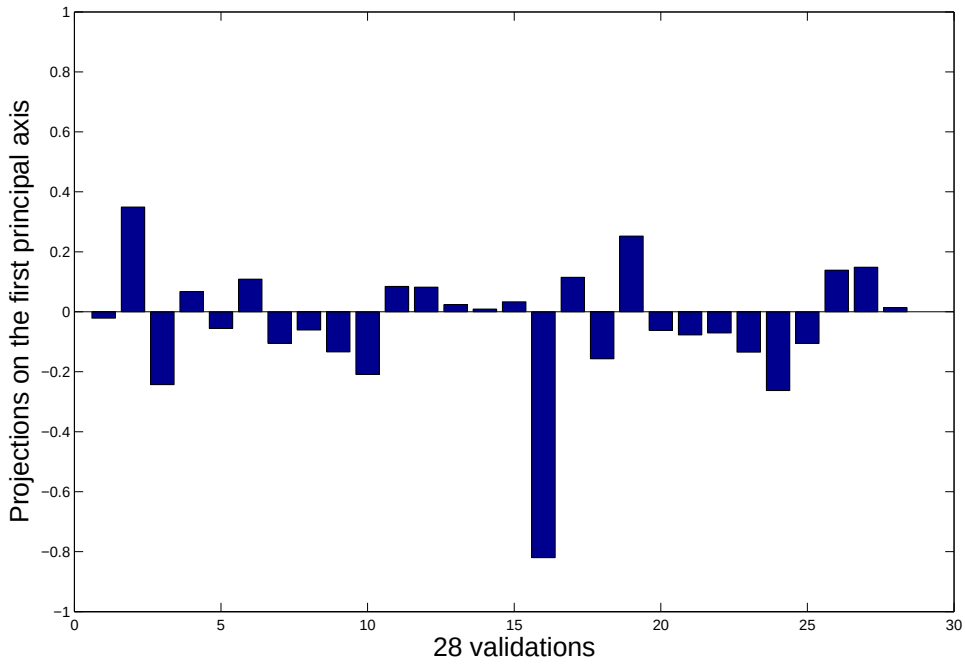

(a) mode one

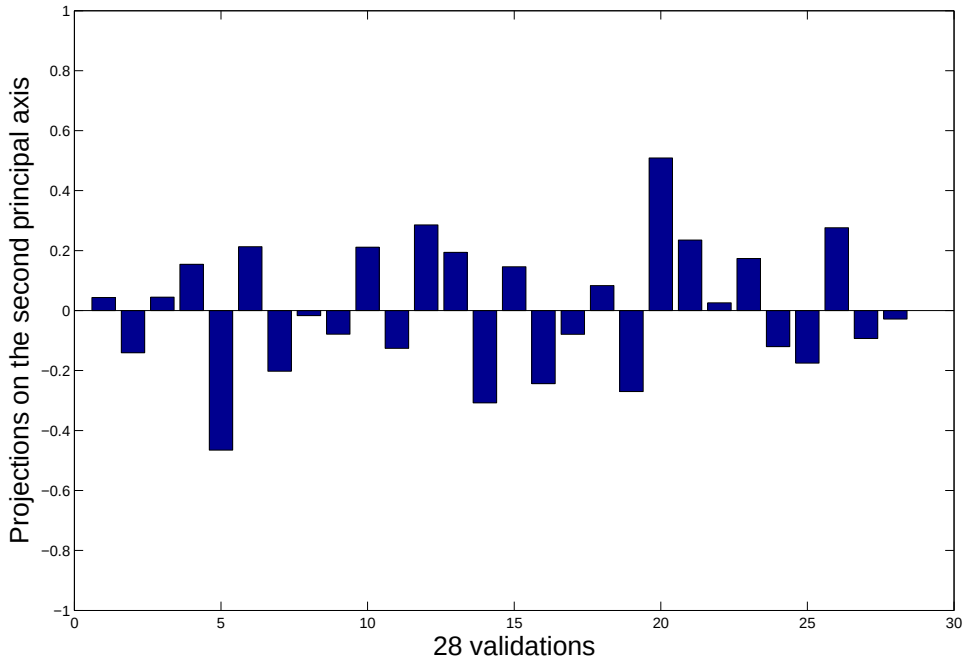

(b) mode two

Figure 6.27: Distributions of the maximum likelihood estimations of humeri conditional on the corresponding scapulae

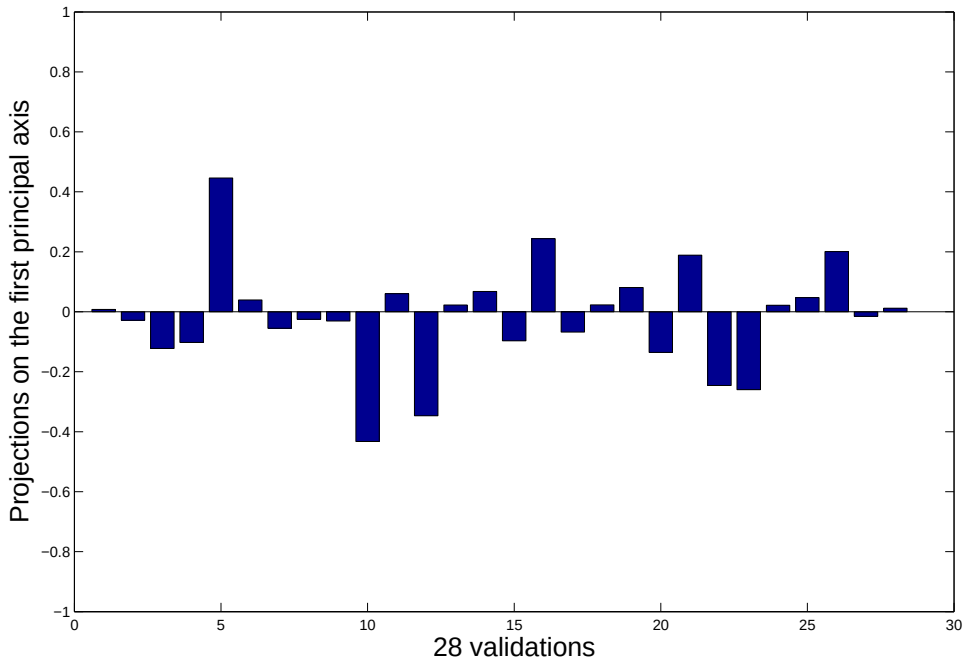

(a) mode one

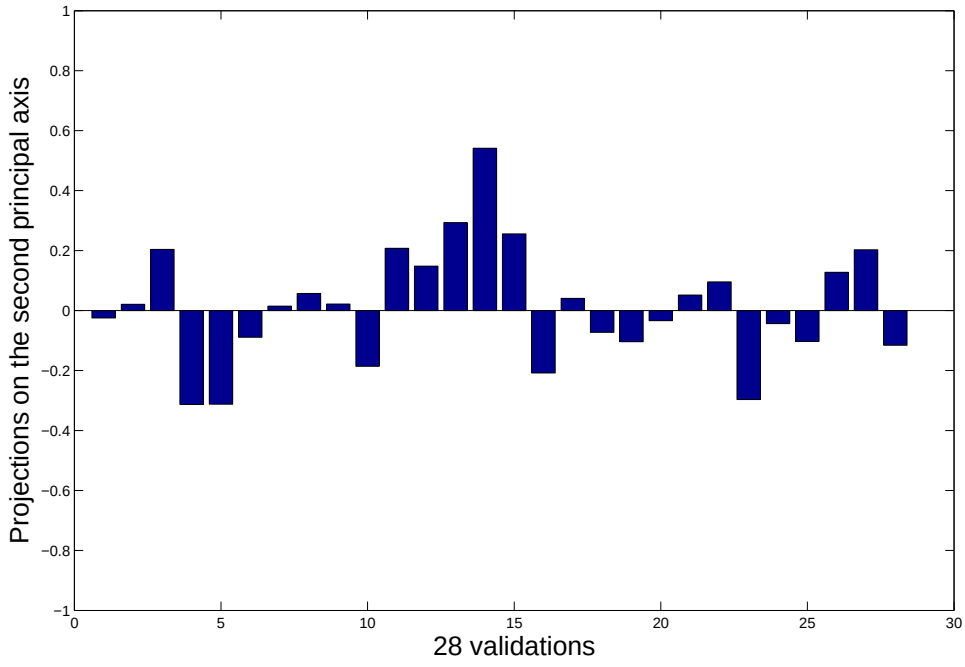

(b) mode two

Figure 6.28: Distributions of the maximum likelihood estimations of scapulae conditional on the corresponding humeri

variance of the maximum likelihood estimation.

6.6 Summary

This chapter has described a method to derive the morphological relationship between the glenohumeral joint bones using CCA and a method to predict one bone shape efficiently from its neighbour using PLS regression. The proposed methods are totally automatic apart from a semi-manual labelling procedure of surface points in the establishment of surface point-to-point correspondences of the scapulae. No prior knowledge about anatomy of shoulder bones is required or incorporated in these methods.

PCA was applied to both training sets to reduce the dimensionality of the data vectors before performing CCA, PLS regression and conditional shape modelling. There are two main reasons for regressing the predictor variables on the principal components rather than directly on the explanatory variables. Firstly, the explanatory variables are often highly correlated (multi-collinearity) which may cause inaccurate estimations of the least square regression coefficients. This can be avoided by using the principal components in place of the original variables since the principal components are uncorrelated. Secondly, the dimensionality of the regressors is reduced by taking only a subset of principal components for prediction.

The shoulder bones in the training sets show highly linear morphological interrelationship according to the canonical coefficients ρ. The first shape variation of the two datasets were correlated and the relationship between their principal modes were able to estimate how one shape was influenced by the other numerically. Clusters of different genera can be identified lying approximately on a line defined by two canonical variates. Therefore, a classifier could be trained and the morphological parameters were predictable from each other.

The prediction results demonstrate that the two shoulder bones can be predicted from each other. In statistical shape analysis, the mean shape is an estimation of a single data sample. The leave-one-out validations have shown that the overall prediction

behaviour using PLS regression on PCA latent variables was better than using the mean as an estimation. In RMS distance validations of predictions without size variation, the best humerus and scapula prediction results were obtained when the first two principal modes (66.3% humerus shape variability) and the first 11 principal modes (96.2% scapular shape variability) were used to form the PLS data blocks. In validations using morphological features, the size of humeral head and size of scapular glenoid of the predicted shapes are very close to those of the real shapes, claiming 89.3% and 96.4% better estimations than the mean shapes when the first three principal modes were applied. Other features (torsion and bending of the humerus, the relationship between the glenoid normal vector and orientation of the infraspinous fossa) were also maintained in the predicted shapes.

Neighbour-conditional shape models were constructed with the present shoulder bone pairs. Instead of describing variations within the same bones, the models described bony morphological variability conditioned on the adjoining segment. The models provide a range of possible shapes given the neighbour bone shape. The maximum likelihood shape estimations were taken as the mean shapes of the models. They are the same as the predicted shapes using PLS regression. Leave-one-out validations have shown that the real shapes are very close to the likelihood estimations.

The applications of this chapter can be generally extended to human-only datasets and other joint shapes predictions (such as the knee joint and the hip joint). Moreover, the large variations of the scapula's thin blade in the dataset, which has an influence on the humerus analysis, induced errors in the prediction results. If the dataset only contains human shoulder bones, it is likely that the prediction behaviour will be better.

The method could be also applied to reconstruct fossil shapes. Given a complete fossil of a joint bone from an extinct primate would allow its adjoining segment to be predicted. The problem is that the method requires a good training set, which can be difficult to construct due to the lack of available sample fossils. Moreover, the method is not constrained to determining morphological interrelationships and it can be applied to many other fields, such as exploring the relationship between morphology and kinematics.

Chapter 7

Discussion and Perspectives

7.1 Conclusions

This thesis applied some mathematical methods and models to analyse the morphology of the two main shoulder bones, the humerus and the scapula, from nine genera of primates that encompass terrestrial and arboreal locomotor types. Many techniques were used, including crest line extraction, rigid and non-rigid registration, principal component analysis (PCA), statistical shape models (SSM), bone morphing, canonical correlation analysis (CCA), partial least square (PLS) regression and neighbour-conditional shape models.

Morphological features of the bones can be extracted robustly and automatically. Manual manipulation was highly reduced compared to traditional bone shape measurements in morphometrics and therefore minimised resulting variations. Redefined local coordinate frames were proposed that utilise stable bony structure instead of a few manually labelled anatomical landmarks.

The shape variations of the humerus set and the scapula set can be described by a few principal modes based on which a classification model can be built. Size is a very important variation when distinguishing genera in the present datasets. Bending of the humeral shaft plays a significant role across specimens, representing the first component. The region composed of the glenoid, the acromion and the coracoid process is the major difference amongst these primate scapulae, providing valuable information for taxonomy.

To verify the robustness of the proposed SSM construction method, an SSM was built on a set of human femora using the methodology pipeline applied to the humerus dataset. According to the plausible shapes, length is the first component and the extension of the femoral neck is the second component. An iterative optimisation method was proposed to implement bone morphing, which is a technique to reconstruct a whole bone surface using a set of sparse surface points.

Morphological interrelationships between the two shoulder bones can be extracted. Prediction models were built so that one bone shape can be predicted from its neighbour bone shape. Leave-one-out validations of the RMS distance between surface points has shown that the prediction method provides the best results when the first two principal modes were applied to the model. This is similar to the recommendation by many authors (Chapter 6, Section 6.4.1). Validation of the morphological features has shown that the predicted shapes have more accurate degrees of bending compared to the real shapes than the mean shapes of the training sets do. Neighbour-conditional shape models were also constructed to investigate shape variations of a shoulder bone conditioned on its adjoining segment.

7.2 Future Work

A major limitation of this thesis is the lack of observation samples. There are only maximally five samples for each genus and only one pair of *Pongo* shoulder bones available. To analyse primate shoulder bone shapes statistically, more samples should be provided in the future. The remainder of this section mainly discusses two parts of future work, one relating to methodology developments and the other relating to applications.

7.2.1 Methodology

In the current study, proximal and distal axes describing the humeral shaft were constructed using predefined portions of the shaft (Chapter 4, Figure 4.18). Due to the different locations of the deltoid tuberosity (the point of insertion of the deltoid muscle,

see Figure 2.2 on page 27), humeri in the current dataset have different bending points on the humeral shaft. A disadvantage of this axis construction method using a predefined portion on the humeral shaft is that the shaft within the predefined portion may have different anatomical meaning across the dataset. For example (see Figure 3.4 on page 71), the proximal third of the proximal shaft of a *Macaca* humerus contains the deltoid tuberosity but the same portion of the proximal shaft of a *Papio* humerus does not. Definitions of the axes describing the humeral shaft can be further improved by fitting a curve to the centres along the humeral shaft. Humeri from different genera tend to bend at different positions along the shaft, which can be seen in Figures 4.7 (page 90, the middle and the right humeri) and 4.19 (page 98). Therefore, the areas used to approximate two axes, L_{h1} and L_{h2}, shown in Figure 4.18 on page 97 are not accurate enough to differentiate the two parts of the humeral shaft. To describe bending and to obtain the largest bending point, local curves can be fitted to approximate the centres along the humeral shaft and the principal curvatures of the curves can be calculated.

PLS is an essential technique utilised in Chapter 6. In PLS regression, PCA was applied to reduce data dimensionality and the reduced data vectors were used to build the prediction model. PCA is a linear technique, and nonlinear (or kernel) PCA would be desirable in the future.

Some other studies have been performed concerning non-rigid registration and the construction of SSM, but they are not robust enough for the present datasets, which include large shape variations. Details of implementation of these studies are described below.

Automation

When establishing correspondences among flat bones or complex bones, one problem is that the flat or irregular bony structures challenge all non-rigid deformation methods which utilise the closest point analysis. Section 5.2.2 in Chapter 5 addressed this problem by initialising non-rigid registration by matching a few manually selected surface points. Since crest points are detected on a surface where there is large curvature, they contain

most of the anatomical landmarks. A more automatic method can be developed utilising the crest points on the bone surface.

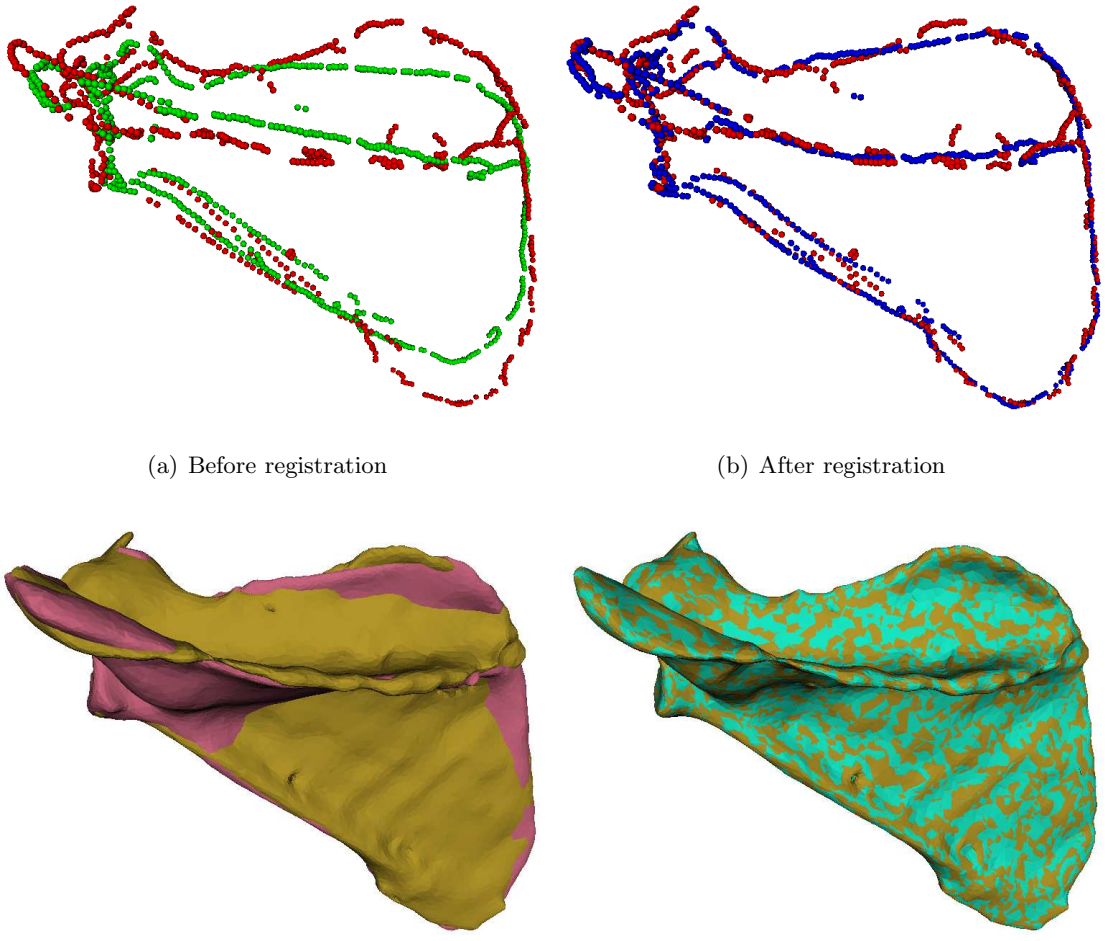

(a) Before registration

(b) After registration

(c) Registration initialisation

(d) After non-rigid registration

Figure 7.1: Initialising surface-based registration by matching two sets of crest points

Instead of using the manually selected surface points, two sets of crest points can be extracted from the source shape and the target shape. Surface-based non-rigid registration can be initialised by matching the two sets of crest points. The TPS-RPM method proposed by Chui and Rangarajan is a point matching algorithm to register two clouds of point sets [CR03]. However, this method only works on point clouds with simple structures. It is also prone to generate incorrect correspondences. Landmark-based registration with B-spline FFD was applied. Subsol *et al* proposed a line matching method to match the crest lines on two skulls [STA98]. The method requires point correspondences before

identifying line correspondences. B-spline FFD is capable of registering a cloud of points to another point cloud (Figure 7.1). A shape can be initialised using the deformation field of the registered points.

However, this method still failed to register a complex bone shape to its target bone shape which has different morphological features (for an extreme example, to register a triangle to a star). Point matching is thus error prone in the registration initialisation and further introduces problems in non-rigid surface deformation. Further development in deforming a very complex bone shape to its target can be beneficial.

7.2.2 Extension in Total Shoulder Replacement

Image-free techniques that build mathematical models to provide surgical guidance are applicable in surgeries such as total knee arthroplasty (TKA), total hip arthroplasty (THA), anterior cruciate ligament reconstruction (ACL) and total shoulder replacement (TSR). TSR is much less common than TKA and THA. In UK approximately 2400 - 2500 shoulder prostheses are implanted every year and the number of replacements is increasing only slowly [RC04, MHW01].

Implantation of a total shoulder system involves replacement of the glenohumeral joint. The limited applications of studies of the glenohumeral joint is largely due to its complexity, high mobility and much greater range of movement than other synovial joints, and therefore high susceptibility to soft tissue pathology and instability. Contrary to the widespread belief, total surgical replacement of arthritic shoulder joints carries no greater risk of complications than replacement of other major joints. This was recently suggested by a research group in Johns Hopkins Hospital after their analysis on anonymous patient information provided by the Maryland Health Services Cost Review Commission [Ven07].

Traditional joint replacement surgeries require X-rays to be taken pre-operatively. Conventional image-guided joint replacement surgery require expensive CT scans for planning purposes, but have the potential to minimise invasive procedures and surgical exposure of bone, and therefore reduce disruption of the soft tissues. Although they increase accuracy and reduce failure rate, they deliver a high radiation dose to the patient.

To obtain a good guidance system for TSR with minimally invasive methods and to overcome some of the problems encountered frequently in the system, analysis of shoulder bony morphology is important for better understanding of the shoulder joint. Accurate computer models for shoulder bone shapes can be built using the techniques described in this thesis, which provides information for patient-specific models.

7.2.3 Bone Morphing

Bone morphing is an extrapolation procedure for intra-operative visualisation of bony structures in image-free surgeries. Bone morphing enables a complete surface to be reconstructed from extremely sparse 3D digitised landmarks or surface points on the bone. Reconstruction of the 3D bone shapes from a set of sparse points provides valuable information to the surgeon during arthroplasty. SSM has been successfully incorporated with bone morphing techniques to provide accurate surface models in hip and knee replacements [FL98, SBM$^+$02, YT03, CBE$^+$04]. In practice, landmarks can be collected by a optical pointer [FL98, SBM$^+$02] easily since the hip or knee joint is widely opened. However, image-free techniques such as bone morphing and SSM are not as developed in shoulder replacements as those in the hip and knee replacements because shoulder replacement is less common. The developed methodologies in Chapter 5, Section 5.6, can be extended to shoulder bone morphing.

For a more accurate surface reconstruction, the local deformation step in bone morphing can be modified by incorporating a neighbour-conditional shape model (details are explained in Chapter 6, Section 6.5) instead of an SSM. Given a set of sparse surface points on an incomplete bone, the deformation of the mean shape to the sparse point set can be constrained by variance (calculated from Equation 2.19 in Chapter 2) of the maximum likelihood estimation.

References

[AGK+04] N. A. Ablitt, J. Gao, J. Keegan, L. Stegger, D. N. Firmin, and G. Z. Yang. Predictive cardiac motion modelling and correction with partial least square regression. *IEEE Trans. Medical Imaging*, 23(10), 2004.

[Ama06] H. O. Amadi. *Glenohumeral joint kinematics and ligament loading.* PhD thesis, Imperial College London, May 2006.

[Ane93] R. L. Anemone. *Postcranial Adaptation in Nonhuman Primates*, chapter The functional anatomy of the hip and thigh in primates, pages 150–174. Northern Illinois University Press, Dekalb, 1993.

[ANK98] P. R. Andresen, M. Nielsen, and S. Kreiborg. 4d shape-preserving modelling of bone growth. *Proc. Conf. Medical Image Computing and Computer-Assisted Intervention*, 1998.

[AOS65] E. H. Ashton, C. E. Oxnard, and T. F. Spence. Scapular shape and primate classification. *Proceedings of the Zoological Society*, 145:125–142, 1965.

[ARS04] D. C. Adams, F. J. Rohlf, and D. E. Slice. Geometric morphometrics: ten years of progress following the "revolution". *Ital. J. Zool.*, 71(1):5–16, 2004.

[Bag83] A. R. Baggaley. Deciding on the ratio of number of subjects to number of variables in factor analysis. *Multivariate Experimental Clinical Research*, 6(2):81–85, 1983.

[BF04] P. Buchler and A. Farron. Benefits of an anatomical reconstruction of the

humeral head during shuolder arthroplasty: a finite element analysis. *Clinical Biomechanics*, 19:16–23, 2004.

[BGK95] C. Brechbuhler, G. Gerig, and O. Kubler. Parametrization of closed surfaces for 3d shape description. *Computer Vision and Image Understanding*, 61(2):154–170, March 1995.

[BHT99] A. D. Brett, A. Hill, and C. J. Taylor. A method of 3d surface correspondence and interpolation for merging shape examples. *Image and Vision Computing*, 17(8):635–642, June 1999.

[BLT+06] M. Bruijne, M. T. Lund, L. B. Tanko, P. C. Pettersen, and M. Nielsen. Quantitative vertebral morphometry using neighbor-conditional shape models. *LNCS*, 4190:1–8, 2006.

[BM92] P. J. Besl and N. D. McKay. A method for registration of 3d shapes. *IEEE Trans. Pattern Anal. Mach. Intell.*, 14:239–356, 1992.

[Boe] W. Boehm. *Curves and surfaces for CAGD: a practical guide*, chapter 22, pages 348–362. Academic Press, 4 edition.

[Boo89] F. L. Bookstein. Principal warps: thin-plate splines and the decomposition of deformations. *IEEE Transactions on Pattern Analysis and Machine Intelligence*, 11(6), 1989.

[Boo96a] F. L. Bookstein. Biometrics, biomathematics and the morphometric synthesis. *Bulletin of Mathematical Biology*, 58(21):313–365, 1996.

[Boo96b] F. L. Bookstein. *Combining the tools of geometric morphometrics*, pages 131–151. Plenum Press, New York, 1996.

[Boo97] F. L. Bookstein. Landmark methods for forms without landmarks: morphometrics of group differences in outline shape. *Medical Image Analysis*, 1(3):225–243, April 1997.

[Bor84] G. Borgefors. Distance transformations in arbitrary dimensions. *Comput. Vision Graph. Image Processing*, 27:321–345, 1984.

[Bri02] R. J. Britten. Divergence between samples of chimpanzee and human dna sequences is 5%, counting indels. *Proceedings of the National Academy of Sciences U.S.A.*, 99(21):13633–13635, October 2002.

[BS84] P. Bobko and F. M. Schemmer. Eigen value shrinkage in principal component based factor analysis. *Applied Psychological Measurement*, 8:439–451, 1984.

[BSGM04] F. L. Bookstein, D. Slice, P. Gunz, and P. Mitteroecker. Anthropology takes control of morphometrics. *Coll. Antropol.*, 28(Suppl. 2):121–132, 2004.

[BSP+91] F. L. Bookstein, K. Schafer, H. Prossinger, Seidler H., and M. Fieder. *Morphometric tools for landmark data: geometry and biology.* Cambridge Univ.Press, London, 1991.

[BSP+99] F. L. Bookstein, K. Schafer, H. Prossinger, Seidler H., and M. Fieder. Comparing frontal cranial profiles in archaic and modern homo by morphometric analysis. *Anat. Rec. (New Anat.)*, 257(6):217–214, 1999.

[BT00a] A. D. Brett and C. J. Taylor. Construction of 3d shape models of femoral articular cartilage using harmonic maps. *MICCAI*, 1935/2000:1205–1214, 2000.

[BT00b] A. D. Brett and C. J. Taylor. A method of automated landmark generation for automated 3d pdm construction. *Image and Vision Computing*, 18(9):739–748, 2000.

[CBE+04] C. S. K. Chan, D. C. Barratt, P. J. Edwards, G. P. Penney, M. Slomczykowski, T. J. Carter, and D. J. Hawkes. Cadaver validation of the use of ultrasound for 3d model instantiation of bony anatomy in image guided orthopaedic surgery. *MICCAD, LNCS 3217*, pages 397–404, 2004.

[CBET99] T. F. Cootes, C. Beeston, G. J. Edwards, and C. J. Taylor. A unified framework for atlas matching using active appearance models. *Information Processing in Medical Imaging*, 1613:322–333, 1999.

[CCD+02] A. T. Chinwalla, L. L. Cook, K. D. Delehaunty, G. A. Fewell, L. A. Fulton, and et al. Initial sequencing and comparative analysis of the mouse genome. *Nature*, 420:520–562, 2002.

[CCTG95] T. F. Cootes, D. Cooper, C. J. Taylor, and J. Graham. Active shape models: their training and application. *Computer Vision and Image Understanding*, 61(1):38–59, January 1995.

[Cha03] I. W. Charlton. *A model for the prediction of the forces at the glenohumeral joint*. PhD thesis, University of Newcastle upon Tyne, UK, 2003.

[Cli70] N. Cliff. The relation between sample and population characteristic vectors. *Psychometrika*, 35:163–178, 1970.

[CLJ+94] C. S. Carlson, R. F. Loeser, M. J. Jayo, D. S. Weaver, M. R. Adams, and C. P. Jerome. Osteoarthritis in cynomolgus macaques: A primate model of naturally occurring disease. *J. Orthop. Res.*, 12:331–339, 1994.

[Cor87] R. Corruccini. Shape in morphometrics: comparative analyses. *Am. J. Phys. Anthropol.*, 73:289–303, 1987.

[CR03] H. Chui and A. Rangarajan. A new point matching algorithm for non-rigid registration. *Computer Vision and Image Understanding*, 89:114–141, February 2003.

[CTCG92] T. F. Cootes, C. J. Taylor, D. H. Cooper, and J. Graham. Training models of shape from sets of examples. *In Proc. British Machine Vision Conference*, pages 266–275, 1992.

[DCT01] Rh. H. Davies, T. F. Cootes, and C. J. Taylor. A minimum description length approach to statistical shape model. *IPMI*, 2082/2001:18–22, June 2001.

[DDKJ03] C. E. Dunning, T. R. Duck, G. J. W. King, and J. A. Johnson. Quantifying translations in the radiohumeral joint: application of a floating axis analysis. *Journal of Biomechanics*, 36:1219–1223, August 2003.

[DFS03] D. DeCarlo, A. Finkelstein, and A. Santella. Suggestive contours for conveying shape. *ACM Transactions on Graphics*, 22(3):845–855, 2003.

[DM98] I. L. Dryden and K. V. Mardia. *Statistical Shape Analysis*. Wiley, 1998.

[DTA+03] Rh. H. Davies, C. J. Twining, P. D. Allen, T. F. Cootes, and C. J. Taylor. Shape discrimination in the hippocampus using and mdl model. *IPMI 2003, LNCS 2732*, pages 38–50, 2003.

[EBN00] Novotny J. E., B. D. Beynnon, and C. E. Nichols. Modeling the stability of the glenohumeral joint during external rotation. *Journal of Biomechanics*, 33:345–354, 2000.

[FL98] M. Fleute and S. Lavallee. Building a complete surface model from sparse data using statistical shape models: Application to computer assisted knee surgery. *MICCAI*, pages 878–887, 1998.

[FRSN02] A. F. Frangi, D. Rueckert, J. A. Schnabel, and W. J. Niessen. Automatic construction of multiple-object three-dimensional statistical shape models: Application to cardiac modeling. *IEEE Transactions on Medical Imaging*, 21(9):1151–1161, 2002.

[FWMJ98] J. Fitzpatric, J. West, and C. Maurer Jr. Predicting error in rigid-body, point-based registration. *IEEE Trans, on Medical Imaging*, 15(5):694–702, 1998.

[GA92] A. Gueziec and N. Ayache. Smoothing and matching of 3d space curves. *LNCS (Proc. European Conf. Computer Vision)*, 588:620–629, 1992.

[GD04] J. C. Gower and G. B. Dijksterhuis. *Procrustes Problems*. Oxford Univ. Press, New York, 2004.

[GFP06] L. M. Galantucci, R. Ferrandes, and G. Percoco. Digital photogrammetry for facial recognition. *Journal of Computing and Information Science in Engineering*, 6(4):390–396, December 2006.

[GG91] D. Geiger and F. Girosi. Parallel and deterministic algorithms from mrfs: Surface reconstruction. *IEEE Trans. Patt. Anal. Mach. Intell.*, 13(5):401–412, May 1991.

[GI04] J. Goldfeather and V. Interrante. A novel cubic-order algorithm for approximating principal direction vectors. *ACM Transactions on Graphics*, 23(1):45–63, January 2004.

[Gou71] H. Gouraud. Continuous shading of curved surfaces. *IEEE Transactions on Computers*, 20(6):623–629, June 1971.

[Gow75] J. C. Gower. Generalized procrustes analysis. *Psychometrika*, 40(1):33–51, 1975.

[GRL+98] S. Gold, A. Rangarajan, C. P. Lu, S. Pappu, and E. Mjolsness. New algorithms for 2d and 3d point matching: pose estimationa and correspondence. *Pattern Recognition*, 31(8):1019–1031, 1998.

[GS83] E. S. Grood and W. J. Suntay. A joint coordinate system for the clinical descritption of three-dimensional motions: application to the knee. *Trans. ASME Journal of Biomechanical Engineering*, 105:136–144, 1983.

[GV88] E. Guadagnoli and W. F. Velicer. Relation of sample size to the stability of component patterns. *Psychological Bulletin*, 103:265–275, 1988.

[Ham93] B. Hamann. Curvature approximation for triangulated surfaces. *Computing Suppl.*, (8):139–153, 1993.

[Har89] S. E. Hartman. Stereophotographic analysis of occlusal morphology of extant hominoid molars: phenetics and function. *Am. J. Phys. Anthropol.*, 80(2):145–166, 1989.

[Haw00] D. Hawkes. *Medical Image Registration*. 2000.

[HG01] A. Hubeli and M. Gross. Multiresolution feature extration from unstructured meshes. *Proceedings of the IEEE Visualization*, pages 287–294, 2001.

[Hil06] A. M. Hill. *Passive stability of the glenohumeral joint*. PhD thesis, Imperial College, University of London, 2006.

[HK70] A. Hoerl and R. Kennard. Ridge regression: biased estimation for nonorthogonal problems. *Technometrics*, 12(1):55–67, 1970.

[HK02] R. Hertel and F. T. Knothe, U. andBallmer. Geometry of the proximal humerus and implications for prosthetic design. *J Shoulder Elbow Surg*, 11:331–338, 2002.

[Hos92] M. Hosaka. *Modeling of curves and surfaces in CAD/CAM*. Springer, Berlin, 1992.

[HR85] D. D. Hoffman and W. A. Richards. Parts of recognition. *Cognition*, 18:65–96, 1985.

[ISDA44] V. T. Inman, J. B. Saunders, M. DeC, and L. C. Abbott. Observations on the function of the shoulder joint. *JBJS*, 26:1–30, 1944.

[JCR+94] C. P. Jerome, C. S. Carlson, T. C. Register, F. T. Bain, M. J. Jayo, D. S. Weaver, and M. R. Adams. Bone functional changes in intact, ovariectomized, and ovariectomized, hormone-supplemented adult cynomolgus monkeys (macaca fascicularis) evaluated by serum markers and dynamic histomorphometry. *J. Bone Miner. Res.*, 9:527–540, 1994.

[Jef02] J. N. R. Jeffers. Multivariate analysis - statistical inference. *URL http://www.sawleystudios.co.uk/jnrj/StatisticalCheck/Multivariate.htm*, 2002.

[JFW95] W. Jungers, A. Falsetti, and C. Wall. Shape, relative size, and size-adjustments in morphometrics. *Yearbook Phys. Anthropol.*, 38:137–161, 1995.

[JM05] A. Jagannathan and E. L. Miller. Unstructured point cloud matching within graph-theoretic and thermodynamic frameworks. *Proceedings of the 2005*

IEEE Computer Society Conference on Comput. Vis. and Pattern Recognition, 2:1008–1015, 2005.

[JRH92] H. Jiang, R. A. Robb, and K. S. Holton. A new approach to 3d registration of multi-modality medical images by surface matching. *Visualization in Biomedical Computing*, pages 196–213, 1992.

[Kap82] I. A. Kapandji. *The physiology of the joints*. Elsevier Health Sciences, 1982.

[Ken77] D. G. Kendall. The diffusion of shape. *Advances in Applied Probability*, 9:428–430, 1977.

[Kim85] T. Kimura. Bipedal and quadrupedal walking of primates: Comparative dynamics. *Primate Morphophysiology, Locomotor Analysis and Human Bipedalism*, pages 81–104, 1985.

[Kim92] T. Kimura. Hindlimb dominance during primate high-speed locomotion. *Primates*, 33:465–476, 1992.

[KIMW00] K. Kneoaurek, M. Ivanovic, J. Machac, and D. A. Weber. Medical image registration. *Europhysics News*, 31(4), 2000.

[Kir85] J. K. Kirkwood. Patterns of growth in primates. *J. Zool. Lond.*, 205:123–136, 1985.

[KK06] S. K. Kim and C. H. Kim. Finding ridges and valleys in a discrete surface using a modified mls approximation. *Computer-Aided Design*, 38:173–180, 2006.

[KMG98] N. Khaneja, M. I. Miller, and U. Grenander. Dynamic programming generation of curves on brain surfaces. *IEEE Trans. Patt. Anal. Mach. Intell.*, 20(11):1260–1265, November 1998.

[KSB98] T. Y. Kuo, J. G. Skedros, and R. D. Bloebaum. Comparison of human, primate, and canine femora : Implications for biomaterials testing in total hip replacement. *J. Biomed. Mater. Res*, 40(3):475–489, 1998.

[KT98] A. C. W. Kotcheff and C. J. Taylor. Automatic construction of eigenshape models by direct optimisation. *Medical Image Analysis*, 2(4):303–314, December 1998.

[LK00] C. Lorenz and N. Krahnstover. Generation of point-based 3d statistical shape models for anatomical objects. *Comput. Vis. Image Understand.*, 77:175–191, 2000.

[LP00] R. J. A. Lapeer and R. W. Prager. 3d shape recovery of a newborn skull using thin-plate splines. *Computerized Medical Imaging and Graphics*, 24:193–204, 2000.

[LPC+88] D. N. Levin, C. A. Pelizzari, G. T. Y. Chen, C. T. Chen, and M. D. Cooper. Retrospective geometric correlation of mr, ct and pet images. *Radiology*, 169:817–823, 1988.

[LR04] S. R. Lele and J. T. Richtsmeier. *An invariant approach to statistical analysis of shapes*. Chapman and Hall/CRC, 2004.

[LSHD04] H. Lamecker, M. Seebass, H. C. Hege, and P. Deuflhard. A 3s statistical shape model of the pelvic bone for segmentation. *In proc. of SPIE Medical Imaging: 5370, Image Processing*, pages 1341–1351, 2004.

[LV95] S. Lobregt and M. A. Viergever. Discrete dynamic contour model. *IEEE Trans. Med. Imaging*, 14(1), March 1995.

[LWCS96] Y. Lee, S, G. Wolberg, K. Y. Chwa, and S. Y Shin. Image metamorphosis with scattered feature constraints. *IEEE Trans. on Vis. and comput. Graph.*, 2(4), December 1996.

[LWS97] S. Lee, G. Wolberg, and S. Y. Shin. Scattered data interpolation with nultilevel b-splines. *IEEE Trans. Vis. Comput. Graph.*, 3:228–244, September 1997.

[MAM97] O. Monga, N. Armande, and P. Montesinos. Thin nets and crest lines:

application to satellite data and medical images. *Comuter Vision and Image Understanding*, 67(3):285–295, September 1997.

[Max99] Nelson Max. Weights for computing vertex normal from facet normal. *Journal of Graphics tools*, 4(2):1–6, 1999.

[MB92] O. Monga and S. Benayoun. From partial derivatives of 3d density images to ridge lines. *In Proc. CVPR92, IEEE*, pages 354–359, 1992.

[MH02] S. J. H. McGraw-Hill. *Basic Biomechanics*. 0-07-255241-7. 4 edition, 2002.

[MHW01] D. C. Mackay, B. Hudson, and J. R. Williams. Which primary shoulder and elbow replacement? a review of the results of prostheses available in the uk. *Ann Roy Coll Surg Engl*, 83:258–265, 2001.

[Mil32] R. A. Miller. Evolution of the pectoral girdle and forelimb in primates. *American Journal of Physical Anthropology*, 18:1–56, 1932.

[MK04] S. Meller and W. A. Kalender. Building a statistical shape model of the the pelvic. *International Congress, 1268*, pages 561–566, 2004.

[mmg03] A patient's guide to shoulder anatomy. eOrthopod.com, 228 West Main St., Suite D, Missoula, MT 59802-4345, 2003.

[Mye] P. Myers. Primates (on-line). *Animal Diversity Web. http://animaldiversity.ummz.umich.edu/site/accounts/information/Primates.html*.

[OBS04] Y. Ohtake, A. Belyaev, and H. P. Seidel. Ridge-valley lines on meshes via implicit surface fitting. *ACM Transactions on Graphics (TOG)*, 23(3):609–612, August 2004.

[O'H00] P. O'Higgins. The study of morphological variation in the hominid fossil record: biology, landmarks and geometry. *J. Anat.*, 197:103–120, 2000.

[OJ98] P. O'Higgins and N. Jones. Facial growth in cercocebus torquatus: an application of three dimensional geometric morphometric techniques to the study of morphological variation. *J. Anat.*, 193:251–272, 1998.

[OL07] J. B. Ogston and P. W. Ludewig. Differences in 3-dimensional shoulder kinematics between persons with multidirectional instability and asymptomatic controls. *The American Journal of Sports Medicine*, 35(8), 2007.

[PAT00] X. Pennec, N. Ayache, and J. P. Thirion. Landmark-based registration using features identified through differenctial geometry. *Handbook of Medical Imaging*, pages 499–513, 2000.

[PK03] M. Pauly and R. Keiser. Multi-scale feature extraction on point-sampled surfaces. *Proceedings of the Eurographics*, pages 281–289, 2003.

[PTVF92] W. H. Press, S. A. Teukolsky, W. T. Vetterling, and B. P. Flannery. *Numerical Recipes in C*, chapter Minimization or Maximization of Functions, pages 394–455. Cambridge University Press, 2nd edition, 1992.

[PV95] M. L. Pearl and A. G. Volk. Retroversion of the proximal humerus in relationship to prosthetic replacement arthroplasty. *J Shoulder Elbow Surg*, 4:286–289, 1995.

[Rao79] C. R. Rao. Separation theorems for singular values of matrices and their applications in multivariate analysis. *J. Multivariate Anal.*, 9:362–377, 1979.

[RC90] F. J. Rohlf and M. Corti. Morphometrics. *Annu. Rev. Ecol. Syst.*, 21:299–316, 1990.

[RC00] F. J. Rohlf and M. Corti. Use of two-block partial least-squares to study covariation in shape. *Syst. Biol*, 49(4):740–753, 2000.

[RC02] F. J. Rohlf and M. Corti. *Geometric morphometrics and phylogeny.* Taylor and Francis, London, 2002.

[RC04] M. Ravenscroft and P. Calvert. Utilisation of shoulder arthroplasty in the uk. *Ann R Coll Surg Engl*, 86:25–28, 2004.

[RDL02] J. T. Richtsmeier, V. B. Deleon, and S. R. Lele. The promise of geometric morphometrics. *Yearbook Phys. Anthropol.*, 45:63–91, 2002.

[RK06] R. Rosipal and N. Kramer. Overview and recent advances in partial least squares. *LNCS*, 3940:34–51, 2006.

[RKS00] C. Rossl, L. Kobbelt, and H. P. Seidel. Extraction of feature lines on triangulated surfaces using morphological operators. *Proc. of the 2000 AAAI Symposium*, pages 71–75, 2000.

[RM93] F. J. Rohlf and L. F. Marcus. A revolution in morphometrics. *Trends Ecol. Evol.*, 8:129–132, 1993.

[RNS04] K. T. Rajamani, L. Nolte, and M. Styner. A novel approach to anatomical structure morphing for intraoperative visualization. *MICCAI*, 2004.

[Rob74] D Roberts. *Primate Locomotion*. Academic Press, 1974.

[RPW05] M. Rang, M. E. Pring, and D. R. Wenger. *Rang's children's fractures*. Lippincott Willians and Wilkins, 2005.

[RS98] C. R. Rao and S. Suryawanshi. Statistical analysis of shape through triangulation of landmarks: a study of sexual dimorphism in hominids. *Proc. Natl. Acad. Sci.*, 95(8):4121–4125, 1998.

[RSH+99] D. Rueckert, L. I. Sonoda, C. Hayes, D. L. G. Hill, M. O. Leach, and D. J. Hawkes. Non-rigid registration using free-form deformations: application to breast mr images. *IEEE Trans. Med. Img.*, 18:712–721, August 1999.

[rSJ04] K. T. rajamani, M. Styner, and S. C. Joshi. Bone model morphing for enhanced surgical visualization. *ISBI*, (1255-1258), 2004.

[RTSGB05] K. T. Rajamani, H. Talib, M. A. Styner, and M. A. Gonzalez Ballester. Evaluation and initial validation studies of anatomical structure morphing. *Proc. IEEE Eng Med Biol Soc.*, September 2005.

[SBM+02] E. Stindel, J. L. Briard, P. Merloz, S. Plaweski, F. Dubrana, C. Lefevre, and J. Troccaz. Bone morphing: 3d morphological data for total knee arthroplasty. *Computer Aidded Surgery*, 7:156–168, 2002.

[SBSB93] A. P. Streissguth, F. L. Bookstein, P. D. Sampson, and H. M. Barr. The enduring effects of prenatal alcohol exposure on child development: British through seven years. a partial least squares solution. *Yearbook Phys. Anthropol.*, 1993.

[SC05] G. Stylianou and Y. Chrysanthou. Crest line extraction from point clouds. *Proc. of Graphicon*, 2005.

[SF86] B. A. Sigmon and D. L. Farslow. *Comparative Primate Biology (Systematics, Evolution, and Anatomy)*, volume 1, chapter The primate hindlimb, pages 671–718. Alan R. Liss, Inc., New York, 1986.

[SF03] G. Stylianou and G. Farin. Crest lines extraction from 3d triangulated meshes. *Hierarchical and Geometrical Methods in Scientific Visualization*, pages 269–281, 2003.

[SF04] G. Stylianou and G. Farin. Crest lines for surface segmentation and flattening. *IEEE Trans. Vis. Comput. Graph.*, 10(5), 2004.

[SJ97] R. J. Smith and W. L. Jungers. Body mass in comparative primatology. *J. Hum. Evol.*, 32:523–559, 1997.

[SL92] D. Schmitt and S. G. Larsom. Heel contact as a function of substrate type and speed in primates. *Am. J. Phys. Anthropol.*, 96:39–50, 1992.

[SL96] R. Szeliski and S. Lavallee. Matching 3d anatomical surfaces with non-rigid deformations using octree-splines. *Int. J. Comp. Vision*, 18(2):171–186, 1996.

[Sli07] D. E. Slice. Geometric morphometrics. *Annu. Rev. Anthropol.*, 36:261–281, 2007.

[SLM+06] K. Schafer, T. Lauc, P. Mitteroecker, M. Bernhard, and Bookstein F. L. Dental arch asymmetry in an isolated adriatic community. *Am. J. Phys. Anthropol.*, 129(1):132–142, 2006.

[SML89] D. R. Sumner, M. E. Morbeck, and J. J. Lobick. Apparent age-related bone loss among adult female gombe chimpanzees. *Am. J. Phys. Anthropol.*, 79:225–234, 1989.

[SP86] T. W. Sederberg and S. R. Parry. Free form deformation of solid geometric models. *Dallas*, 20(4), August 1986.

[SRQ+01] J. A. Schnabel, D. Rueckert, M. Quist, J. M. Blackall, A. D. Casterllano-Smith, T. Harkens, G. P. Penney, W. A. Hall, H. Liu, C. L. Truwitt, F. A. Gerritsen, D. L. G. Hill, and D. J. Hawkes. A generic framework for nonrigid registration based on nonuniform unlit-level free-form deformations. *Medical Image Comuting and Computer Science*, 2208:573–581, 2001.

[SSBB89] P. D. Sampson, A. P. Streissquth, H. M. Barr, and F. L. Bookstein. Neurobehavioral effects of prenatal alcohol: part ii. partial least squares analysis. *Neurotoxicol Teratol*, 11(5):477–491, 1989.

[STA98] G. Subsol, J. P. Thirion, and M. Ayache. A scheme for automatically building three-dimensional morphometric anatomical atlases: application to a skull atlas. *Medical Image Analysis*, 2(1):37–60, March 1998.

[Tag99] H. Tagare. Shape-based nonrigid correspondence with application to heart motion analysis. *IEEE Transactions on Medical Imaging*, 18(7), July 1999.

[tex08] Electronic textbook. *Multiple regression - Assumptions, Limitations, and Practical Considerations.* StatSoft Inc. URL http://www.statsoft.com/textbook/stmulreg.html, 1984 - 2008.

[TG93] J. P. Thirion and A. Gourdon. The marching lines algorithm: new results and proofs. Technical Report 1881, Institut National de Recherche en Informatique et en Automatique, April 1993.

[TG96] J. P. Thirion and A. Gourdon. The marching lines algorithm. *Graphical Models and Image Processing*, 58(6):503–509, 1996.

[Try98] P. Tryfos. *Methods for Business Analysis and Forecasting: Text and Cases*, chapter 14. Wiley, 1998.

[TW98] G. Thurmer and C. Wuthrich. Computing vertex normals from polygonal facets. *Journal of Graphics Tools*, 3(1):43–46, 1998.

[vdEV93] P. A. van den Elsen and M. A. Viergever. Automated ct and mr brain image registration using geometrical feature correlation. *Nuclear science symposium and medical imaging conference IEEE*, pages 1827–1830, 1993.

[vdH97a] F. C. T. van der Helm. Analysis of the kinemaics and dynamic behavior of the shoulder mechanism. *Journal of Biomechanics*, 27:527–550, 1997.

[vdH97b] F. C. T. van der Helm. A standardized protocol for motions recordings of the shoulder. *In Proc. 1st Conf. Int. Shoulder Group*, pages 7–12, 1997.

[vdHCM+04] F. C. T. van der Helm, S. Chair, M. Makhsous, P. van Roy, C. Angilin, J. Nagels, A. Karduna, D. J. Veeger, K. McQuade, and X. Wang. Isb recommendation of definitions of joint coordinate system of various joints for the reporting of human joint motion - part ii: Shoulder. *Journal of Biomechanics*, January 2004.

[Ven07] J. Ventura. 'shrug off' shoulder surgery myth, johns hopkins study suggests. *The JHU Gazette (The newspaper of The Johns Hopkins University)*, 36(33), 7 May 2007.

[VHK94] M. Van Herk and H. M. Kooy. Automated three-dimensional correlation of ct-ct, ct-mri and ct-spect using chamfer matching. *Med. Phys.*, 21:1163–1178, 1994.

[Weg00] J. A. Wegelin. A survey of partial least wquares (pls). Technical Report 371, Department of Statistics, University of Washington, 2000.

[Wol84] H. Wold. *Encyclopaedia of statistical sciences*, chapter PLS regression. Wiley, New York, 1984.

[WPS00] Y. Wang, B. S. Peterson, and L. H. Staib. Shape-based 3d surface correspondence using geodesics and local geometry. *CVPR*, 2:644–651, 2000.

[WR00] B. Wood and B. G. Righmond. Human evolution: taxinomy and paleobiology. *J. Anat.*, 196:19–60, 2000.

[WvdHV+05] G. Wu, F. C. T. van der Helm, H. E. J. Veeger, M. Makhsous, P. V. Roy, C. Anglin, J. Nagels, A. R. Karduna, K. McQuade, X. Wang, F. W. Werner, and B. Buchholz. Isb recommedation on definitions of joint coordinate systems of various joints for the reporting of human joint motion - part ii: shoulder, elbow, wrist and hand. *Journal of Biomechanics*, 38:981–992, 2005.

[YBS05] S. Yoshizawa, A. G. Belyaev, and H. P. Seidel. Fast and robust detection of crest lines on meshes. *ACM Symposium of Solid and Physical Modeling (SPM)*, pages 227–232, June 2005.

[YT03] J. Yao and R. Taylor. A multiple-layer flexible mesh template matching method for nonrigid registration between a pelvis model and ct images. *SPIE Medical Imaging: Image Processing*, 5032:1117–1124, May 2003.

Appendix A

Anatomical Planes and ISB Definitions of a Shoulder Joint Coordinate System

A.1 Anatomical Directions and Planes

Directional terms used in describing anatomy:

- **Superior** Closer to the Head

  Inferior Closer to the Feet

- **Anterior** Towards the Front

  Posterior Towards the Back

- **Medial** Closer to the Median Plane

  Lateral Farther from the Median Plane

- **Proximal** Closer to the Trunk

  Distal Farther from the Trunk

- **Superficial** Closer to the Surface

  Deep Farther from the Surface

- **Dorsum** Posterior aspect of the hand or Anterior aspect of the foot

  Palmar Anterior aspect of the hand

  Plantar Posterior aspect of the foot

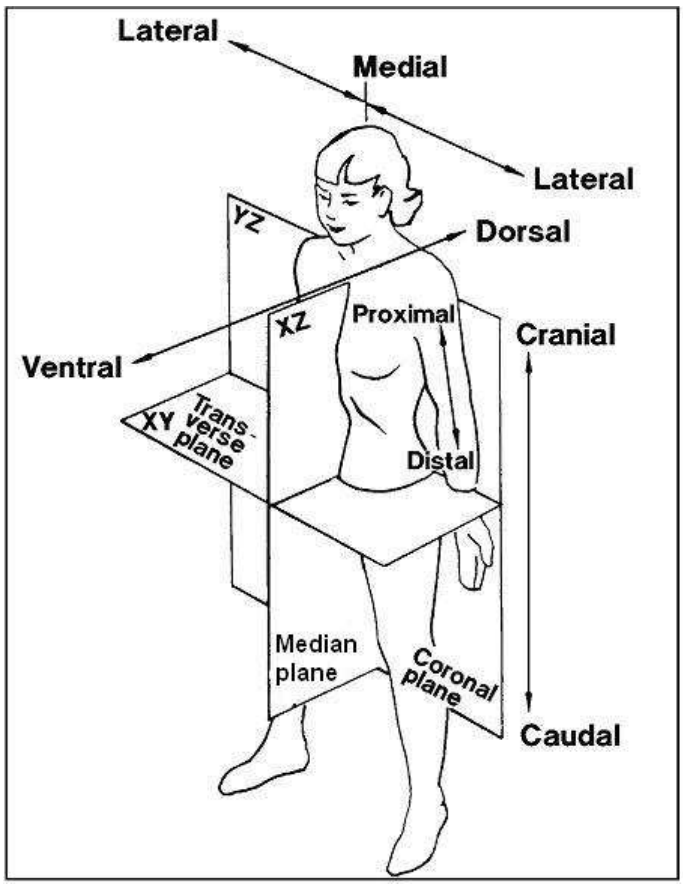

Figure A.1: Anatomical reference planes

A.2 ISB Recommendation on Definitions of Joint Coordinate System of Shoulder

For interpretation of Euler angles, it is suggested that two coordinate systems (*proximal* and *distal*) are initially (by introduction of *anatomical* orientations of these coordinate systems) aligned to each other. The rotation method is exactly equal to the method of Grood and Suntay [GS83] using floating axes. The anatomical landmarks used are shown in Figure A.2.

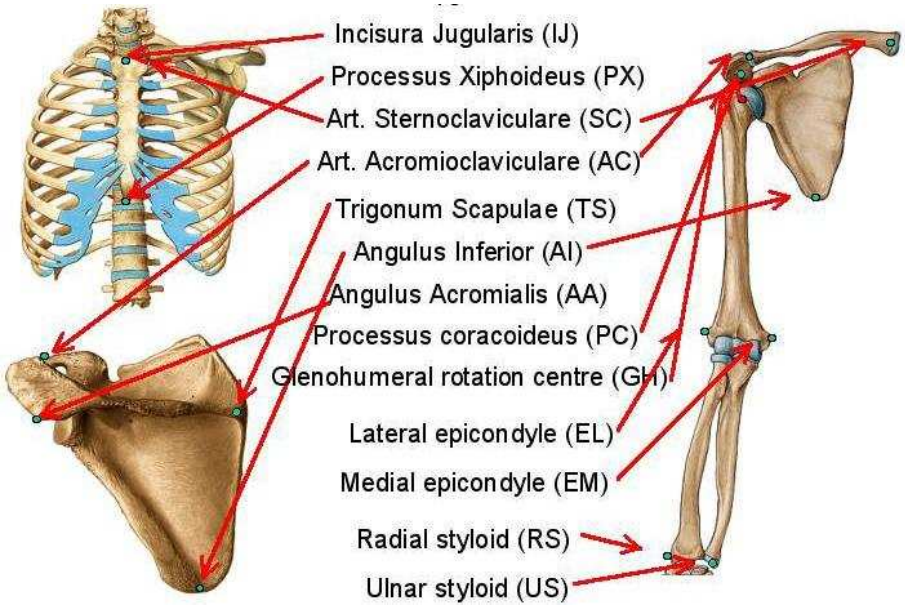

Figure A.2: Illustration of anatomical landmarks used for the definition of shoulder joint coordinate system [vdHCM$^+$04]

Humerus

GH: Glenohumeral rotation centre, estimated by regression or motion recordings

EM: Most caudal point on Medial Epicondyle

EL: Most caudal point on Lateral Epicondyle

Scapula

AC: Most dorsal point on Acromioclavicular joint (shared with clavicula)

TS: Trigonum Spinae Scapulae, mid point of triangular surface on medial border of the scapula in line with the scapula spine

AI: Angulus Inferior, most caudal point of scapula

AA: Angulus Acromialis, most latero-dorsal point of scapula

PC: Most ventral point of processus coracoideus

A.2.1 Scapula Coordinate System - $X_sY_sZ_s$

O_s: The origin coincident with AA

Z_s: The line connecting AA and TS, pointing to AA

X_s: The line perpendicular to the plane formed by AI, AA and Z_s, pointing forward

Y_s: The common line perpendicular to X_s- and Y_s- axis

A.2.2 Humerus First Degree Coordinate System - $X_{h1}Y_{h1}Z_{h1}$

O_{h1}: The origin coincident with GH

Y_{h1}: The line connecting GH and the midpoint of EL and EM, pointing to GH

X_{h1}: The line perpendicular to the plane formed by EL, EM and Y_{h1}, pointing forward

Z_{h1}: The common line perpendicular to $Y_{h1}-$ and $X_{h1}-$ axis

A.2.3 Humerus Second Degree Coordinate System - $X_{h2}Y_{h2}Z_{h2}$

O_{h2}: The origin coincident with GH

Y_{h2}: The line connecting GH and the midpoint of EL and EM

Z_{h2}: The line perpendicular to the plane formed by Y_{h2} and Y_{h2} (see below), pointing laterally

X_{h2}: The common line perpendicular to $X_{h2}-$ and $Y_{h2}-$ axis

N.B.1. The Z_{h2} axis depends on the position of the upper arm and forearm, since it can not assured that it is equal to the joint rotation axis. Therefore, by definition, the Z_{h2} axis is taken with 90 degrees flexed elbow

N.B.2. The 1^{st} and 2^{nd} degree definitions of the humerus coordinate system do not exactly agree, since the longitudinal axis of the forearm is not necessarily per-

pendicular to the flexion-extension axis, and the line EM - EL is not necessarily perpendicular to the longitudinal axis of the humerus

A.2.4 JCS and Motion for the Glenohumeral Joint (X - Y - Z Order)

For joint displacements one common point to both proximal and distal coordinate system and preferably the (initial) rotation centre (or a point on the fixed rotation axis in case of a hinge joint), should be taken.

e1: The axis fixed to the scapula and coincident with the Y_s axis of the scapula coordinate system. Rotation β_{GH1}: GH pole angle or plane of elevation

e2: The axis fixed to the humerus and coincident with the X_h axis of the humerus coordinate system. Rotation α_{GH}: GH elevation (negative)

e3: Axial rotation around the Y_h axis. Rotation β_{GH2}: GH axial rotation, endorotation (positive) and exorotation (negative)

Appendix B

Library Packages and Software

B.1 C++ Library Packages

- Visualisation Toolkit (VTK) 5.1.0
- Fast Light Toolkit (FLTK) 1.1.7
- Image Registration Toolkit (VTK) by Daniel Rueckert and Julia Schnabel

B.2 Software Used

- Amira 3.1.1 – for surface segmentation, decimation and smoothing
- ParaView 1.4 – for cylinder clipping on a humerus shape

B.3 Software Developed in C++

- BonBon (Figure B.1)

  Tab *View* – compares maximally five shapes, with transparent function.

  Tab *SemiLabel* – displays shapes and surface points.

  Tab *Setting* – functions including landmark labelling, manual transformation (rotations and translations), bone size scaling, identifying humeral epicondyle, etc.

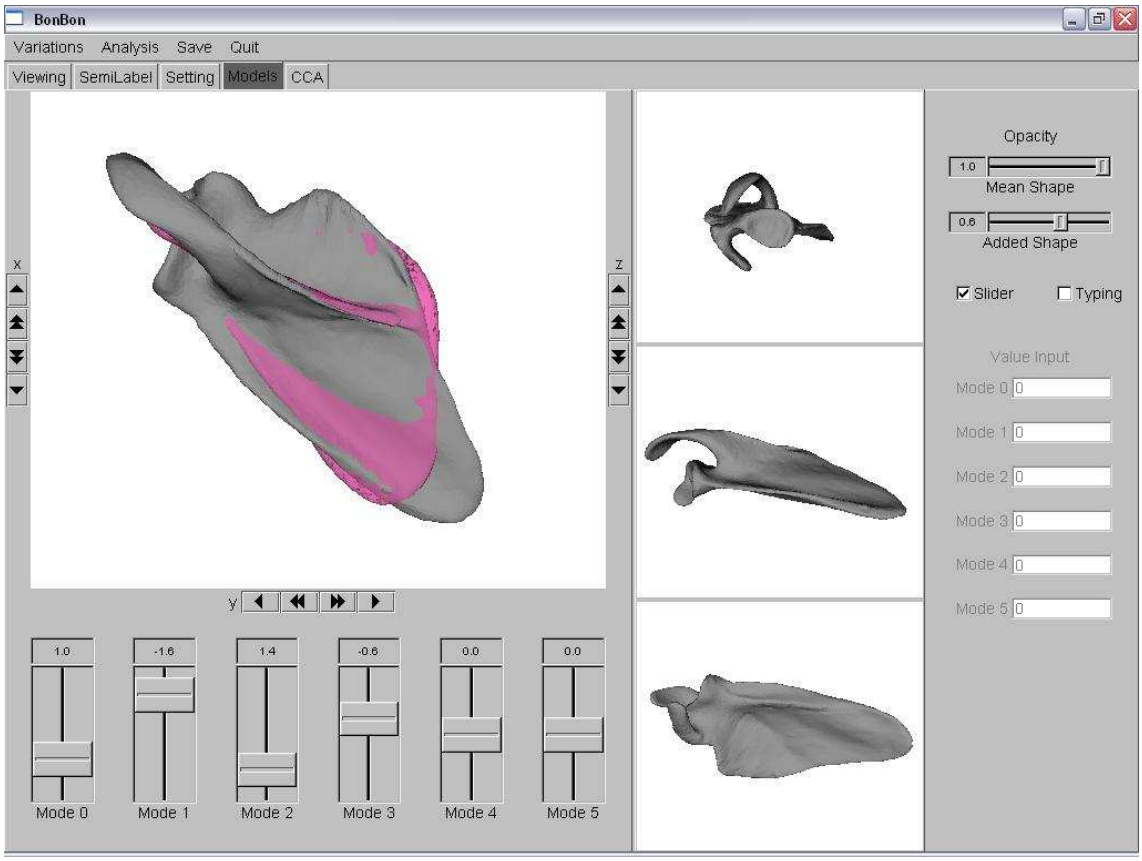

Figure B.1: Interface of the visualisation tool developed in this work

Tab *Models* – creates SSM plausible shapes.

Tab *CCA* – performs CCA and predicts a shapes from its neighbour segment.

- Snack

  The software package mainly includes the following executable files:

  align_h – Use three manually selected point landmarks to align a humerus (Section 5.3.1, Chapter 5)

  cca_loo – implement CCA and predict a shoulder bone from its adjacent segment based on the extracted linear correlation; perform leave-one-out experiment to each pair of shoulder bones

  conditionSSM – implement conditional shape models

  consAxis_H – construct and show morphological axes for a humerus based on Dun-

ning's method [DDKJ03]

consAxis_H_cyl – construct and show morphological axes for a humerus based on the cylinder clipping method

consAxis_S_moreLM – construct morphological axes for a scapula

conv2points – convert all kinds of vtk data formats to vtkPoints

fitCylinder – fit a cylinder to the point set of the clipped surface using the method described in Section 4.3.2, Chapter 4

formshape – reconstruct a shape given the mean shape, eigenvectors and PCA scores

getaxis_h – get the long axis and the elbow joint axis from a humerus shape

getClosestPnt – given two shapes or two sets of point, find the closest point sets from the other shape or point set

getcrest – get the crest lines of a shape

getdiff – calculate the RMS distance between two shapes

getsingleb – calculate the PCA scores of a shape given the mean shape and the eigenvectors of a shape model

manualalign_S – use three manually selected point landmarks to align the source scapula shape to its target shape

morphing – implement bone morphing

mymirror – get the mirror shape of a shape

mypca – implement PCA using the weighted mean shape

regionGrow – implement region growing on a shape

rreg_f – align the source humerus/femur shape to its target shape using ICP with the humeral/femoral head fixed

smoothShape – get the smoothed shape

stl2vtk – convert stl format to vtk format

vq – vector quantisation

writeSTL – convert vtk format to stl format

Appendix C

Root Mean Squares Errors in Leave-one-out Validation of the Shoulder Bone Shape Prediction Models

	1	2	3	4	5	6	7	8	9	10	11	12	13	14	15	16	17	18	19	20
ce1	3.67	5.16	2.77	3.29	1.70	2.01	1.92	1.73	1.89	1.81	1.43	1.37	1.79	1.37	1.59	3.39	3.42	5.67	4.80	5.14
ce2	8.01	4.83	6.94	6.55	5.34	9.84	8.31	7.33	7.23	11.91	12.34	12.49	11.72	10.58	9.72	11.20	14.04	13.88	16.62	20.32
ce3	2.68	3.98	2.34	2.93	2.46	2.76	1.87	1.91	2.07	1.95	1.77	1.79	3.36	3.07	6.05	3.45	3.26	3.33	3.70	3.31
ch1	13.89	15.84	10.54	4.84	18.56	14.20	8.74	10.30	12.02	14.56	12.73	12.80	13.13	23.78	24.73	26.35	26.04	32.18	32.29	30.97
ch2	14.91	10.43	5.76	4.64	6.04	4.56	7.98	8.80	15.26	14.88	6.98	7.04	6.42	18.27	13.55	10.24	10.36	13.28	11.83	11.72
ch3	7.04	6.39	10.92	20.46	17.46	17.32	12.59	13.69	13.63	15.24	12.57	11.85	11.03	16.67	15.13	15.35	19.37	19.74	19.44	17.82
co1	1.55	1.68	1.72	1.56	2.89	2.30	2.36	2.30	2.29	3.83	3.08	3.49	3.26	2.06	3.04	4.08	3.17	5.11	4.33	4.99
co2	2.79	2.68	4.01	3.52	5.15	3.65	9.27	10.99	11.69	10.49	11.72	11.91	11.92	10.79	9.06	14.24	14.09	14.45	14.64	10.97
co3	2.61	5.74	4.27	4.55	4.34	4.83	4.10	4.41	4.63	4.59	9.11	10.16	11.41	15.99	14.30	12.18	13.17	14.50	14.53	11.44
go1	12.10	26.60	22.68	23.77	27.17	27.04	16.81	15.42	11.90	10.74	10.57	13.59	19.40	34.22	31.03	28.17	25.55	23.09	22.54	14.15
go2	8.79	13.67	22.60	40.00	36.02	34.10	35.38	31.80	23.05	23.46	22.96	21.35	22.59	40.80	35.79	34.80	13.22	10.50	11.48	24.23
go3	5.12	9.45	13.32	13.78	8.33	6.00	6.39	5.21	5.36	8.16	4.79	10.10	14.29	34.00	30.74	20.39	21.85	23.44	20.87	22.74
ho1	31.66	13.59	18.53	19.20	17.26	14.65	11.44	9.05	4.29	5.42	7.81	12.86	12.00	20.60	22.60	18.86	18.80	18.56	18.26	23.91
ho2	13.91	46.26	42.83	43.23	36.55	41.03	33.80	33.32	46.00	48.27	41.84	41.86	43.56	41.11	35.18	31.02	29.79	34.49	31.20	41.80
ho3	40.56	19.59	20.63	21.02	28.85	26.67	23.38	22.75	23.08	23.18	22.51	22.28	22.16	21.01	19.24	20.93	16.67	17.40	18.07	16.53
ma1	21.33	15.14	13.28	13.06	11.44	14.31	12.46	12.55	12.43	15.13	13.73	14.63	14.23	14.97	14.55	13.41	14.02	13.74	13.73	10.82
ma2	19.56	11.59	10.53	10.53	10.20	9.22	7.51	8.25	8.21	10.12	8.46	8.55	7.85	10.12	8.61	10.30	3.22	2.23	2.95	2.80
ma3	3.57	6.67	4.67	5.23	4.14	3.41	3.96	4.78	4.60	4.65	5.20	5.24	4.76	7.27	6.70	5.95	6.10	6.24	4.31	4.01
ma4	23.23	19.63	17.97	18.23	15.55	13.41	16.68	16.07	16.07	15.35	14.37	15.31	15.50	15.49	20.37	15.03	13.75	15.99	14.31	21.69
or1	25.77	18.02	21.54	22.04	16.27	20.25	15.39	16.21	18.53	18.92	17.13	17.75	18.45	9.35	8.49	6.19	15.00	17.24	6.97	14.33
pa1	18.70	12.11	2.79	2.60	2.87	5.82	14.25	15.55	15.47	14.64	15.74	16.85	17.09	17.46	16.67	14.98	13.25	9.45	10.70	8.85
pa2	44.43	30.99	22.39	23.82	18.38	10.99	12.87	16.15	16.03	13.46	17.10	17.84	18.63	19.44	19.42	14.33	15.14	12.88	14.92	19.29
pa3	16.12	4.46	11.22	11.13	18.23	16.98	16.54	16.83	16.54	15.42	13.30	13.23	14.11	16.25	18.96	17.33	19.35	19.55	19.48	21.49
pr1	6.71	7.18	5.99	6.46	6.15	6.39	7.22	7.25	7.47	9.31	7.17	7.09	6.24	6.25	7.55	4.82	5.46	3.84	2.37	2.50
pr2	1.68	1.62	1.83	1.75	2.01	2.97	4.84	5.61	5.48	5.19	6.01	5.96	7.89	7.65	6.45	6.21	5.24	2.92	4.55	4.74
pr3	3.81	5.13	4.13	4.16	4.52	6.66	5.27	6.08	6.04	5.66	5.10	5.05	5.69	6.33	7.27	9.21	8.35	7.90	12.69	13.83
pr4	3.06	2.74	2.46	2.49	2.95	3.27	2.93	3.66	3.59	4.69	2.90	2.74	2.79	2.38	2.97	3.75	2.95	4.41	3.62	3.48
pr5	3.30	3.89	4.60	4.48	3.50	3.02	3.54	2.68	2.76	1.64	3.65	3.94	3.82	5.19	7.16	8.27	7.27	9.20	8.28	8.32

ce - *Cebus*; ch - *Pan*; co - *Colobus*; go - *Gorilla*; ho - *Homo*; ma - *Macaca*; or - *Pongo*; pa - *Papio*; pr - *Presbytis*

Table C.1: RMS errors of the predicted humerus shapes when using different numbers of principal modes (model one - including size)

	1	2	3	4	5	6	7	8	9	10	11	12	13	14	15	16	17	18	19	20
ce1	4.72	3.50	3.24	3.07	3.17	3.69	3.66	2.72	2.70	2.51	2.51	2.59	2.47	2.20	2.24	2.28	2.22	2.19	1.99	1.89
ce2	4.68	7.30	6.37	5.60	6.60	7.95	7.74	8.19	7.71	6.71	6.48	6.30	5.21	5.77	6.04	5.74	5.50	5.66	5.98	6.01
ce3	4.47	3.53	3.95	3.95	4.17	4.46	4.48	4.53	3.98	4.00	4.08	4.11	4.12	3.62	3.52	3.31	3.34	3.83	3.44	2.61
ch1	11.97	11.91	11.58	11.87	10.53	10.26	10.64	10.05	10.10	9.74	9.60	9.60	9.11	7.92	7.96	7.95	8.22	8.35	8.11	8.09
ch2	9.42	9.51	8.38	8.91	8.62	8.79	8.41	7.13	7.06	7.07	7.05	7.50	7.75	7.37	8.82	8.96	9.10	9.04	9.08	8.07
ch3	9.71	13.25	12.80	11.75	11.71	11.91	13.70	13.99	13.34	7.86	8.30	7.59	6.55	6.89	9.10	8.95	9.12	9.06	9.15	9.42
co1	2.95	3.28	2.87	3.00	3.34	3.34	3.08	3.38	2.66	2.18	2.41	2.48	2.61	2.78	2.52	2.28	2.29	2.31	2.06	1.94
co2	3.53	3.67	4.54	3.45	4.58	4.57	4.47	4.64	4.54	4.62	5.07	4.72	3.91	4.01	3.98	3.54	4.33	4.17	3.83	3.93
co3	4.18	3.95	4.36	2.69	2.58	2.74	3.18	3.19	3.29	3.42	3.48	3.05	2.91	2.89	2.89	2.86	3.80	4.06	4.02	3.64
go1	11.14	13.86	10.34	10.08	9.97	10.18	10.93	12.17	12.06	11.02	10.64	10.69	13.19	13.25	13.16	13.17	13.51	14.86	14.80	15.08
go2	17.49	16.78	15.75	16.42	16.17	16.62	18.25	21.30	19.74	17.06	16.87	17.60	19.41	19.13	17.09	18.13	18.27	18.14	17.15	16.50
go3	12.70	16.15	13.07	11.62	12.09	12.01	11.49	11.21	10.76	11.27	11.22	11.21	10.32	10.35	9.34	9.08	9.57	9.66	9.98	9.53
ho1	15.61	16.88	10.79	13.08	13.18	13.02	12.99	13.09	11.22	8.39	8.53	8.57	7.81	8.35	9.77	8.76	8.88	7.87	7.02	7.88
ho2	20.61	20.28	17.05	16.54	13.35	13.87	13.62	12.76	12.90	12.92	13.05	13.14	12.92	13.04	13.45	13.15	13.13	12.92	12.94	12.89
ho3	20.20	18.85	7.84	7.28	7.30	6.53	6.35	10.00	9.49	9.41	9.47	10.64	11.73	10.29	11.49	9.41	8.51	8.25	8.32	7.78
ma1	8.97	8.66	6.61	11.38	11.26	12.29	12.13	13.30	14.00	9.55	7.79	8.39	10.08	7.55	16.65	15.12	16.08	13.12	13.25	14.80
ma2	8.60	8.14	4.14	3.14	3.07	3.10	3.85	3.77	4.04	4.34	4.58	4.34	4.36	3.97	3.96	3.69	3.71	3.77	3.91	4.07
ma3	4.59	3.87	3.14	2.93	3.02	3.16	4.59	4.53	4.35	4.46	4.13	3.85	3.82	4.04	4.33	4.35	3.96	4.02	3.38	3.89
ma4	9.36	7.95	5.96	5.52	5.69	5.95	5.99	5.18	5.43	5.53	4.94	4.88	5.20	5.17	5.35	4.58	3.63	3.64	3.05	3.60
or1	12.95	12.52	13.31	13.43	13.52	14.25	15.75	15.88	16.05	16.00	14.02	13.77	13.70	13.69	13.52	11.67	11.91	11.78	11.88	10.83
pa1	12.11	8.32	4.55	4.84	5.25	6.57	7.44	7.12	10.18	9.27	8.00	6.57	6.68	6.93	5.52	5.52	6.38	6.18	6.37	8.29
pa2	22.92	17.42	15.93	14.18	13.99	13.75	13.63	12.24	11.53	11.10	11.06	10.84	13.90	11.83	11.51	11.29	12.03	10.32	10.33	8.52
pa3	13.04	9.16	8.85	8.87	7.80	7.96	7.92	8.03	6.86	6.64	7.95	8.96	8.85	8.99	9.06	9.37	9.39	9.37	9.54	9.09
pr1	4.85	5.44	4.12	2.95	2.76	2.83	3.14	3.00	2.64	2.63	2.77	2.46	2.50	2.26	2.26	2.22	2.40	2.39	3.02	3.02
pr2	2.80	4.00	4.49	2.87	2.79	2.86	2.93	3.08	3.37	3.41	3.58	3.41	3.45	3.35	3.56	2.42	2.60	2.60	2.63	3.00
pr3	3.36	5.73	6.14	3.82	4.45	4.68	4.79	5.52	5.57	5.24	5.43	5.74	5.57	5.17	5.28	3.99	4.02	2.81	3.16	2.85
pr4	3.03	2.01	1.67	2.60	3.33	3.73	3.71	3.40	3.54	2.98	3.18	3.50	3.30	3.16	3.17	3.31	3.35	3.62	3.59	3.56
pr5	1.85	2.11	2.46	2.59	2.48	2.42	2.34	2.35	1.97	2.39	2.12	2.19	2.22	2.67	2.82	2.84	2.89	3.16	2.49	2.67

ce - *Cebus*; ch - *Pan*; co - *Colobus*; go - *Gorilla*; ho - *Homo*; ma - *Macaca*; or - *Pongo*; pa - *Papio*; pr - *Presbytis*

Table C.2: RMS errors of the predicted scapula shapes when using different numbers of principal modes (model one - including size)

	1	2	3	4	5	6	7	8	9	10	11	12	13	14	15	16	17	18	19	20
ce1	2.02	2.02	2.03	2.06	2.09	1.97	1.88	1.89	1.87	1.85	1.82	1.85	2.00	1.98	1.98	1.92	2.06	2.10	2.14	2.17
ce2	4.20	4.08	4.07	4.06	4.03	4.09	4.28	4.28	4.25	4.70	4.71	4.98	4.95	4.64	4.52	4.57	4.68	4.68	4.73	4.70
ce3	2.76	2.75	2.76	2.73	2.73	2.57	2.44	2.48	2.27	2.35	2.33	2.33	2.56	3.08	2.82	2.70	3.00	2.85	3.11	3.20
ch1	2.43	2.73	2.04	2.38	2.01	2.06	2.07	2.25	2.27	2.25	2.24	2.12	2.12	2.11	2.68	3.06	3.70	3.69	3.75	3.88
ch2	2.36	1.93	3.13	2.93	2.67	2.70	2.76	3.16	2.86	3.05	2.78	3.29	3.29	3.00	2.99	3.00	3.36	3.39	3.40	3.79
ch3	3.02	3.47	3.13	3.34	3.23	3.20	3.10	3.09	2.95	2.94	2.93	2.88	2.98	2.90	3.10	3.13	3.74	3.79	3.79	3.85
co1	2.14	2.08	1.98	1.85	1.50	1.43	1.42	1.42	1.48	1.57	1.60	1.60	1.61	1.56	1.56	1.66	1.70	1.70	1.72	1.97
co2	1.62	1.60	1.38	1.61	1.42	1.40	1.38	1.48	1.64	1.65	1.63	1.62	1.73	2.17	1.98	2.06	1.62	2.84	2.80	2.72
co3	1.88	1.84	1.85	1.80	1.62	1.61	1.70	1.68	1.68	1.66	1.65	1.71	2.10	1.75	2.20	2.37	2.55	2.36	2.50	2.22
go1	3.01	3.14	2.68	2.79	3.19	2.96	2.83	3.32	3.77	3.70	3.92	3.88	4.06	2.72	3.21	3.87	4.56	3.77	3.68	3.68
go2	2.09	2.45	2.22	2.30	2.67	2.43	2.60	2.75	2.59	2.82	2.82	3.10	3.23	2.35	2.31	2.70	4.80	4.44	4.18	3.89
go3	3.28	3.42	2.66	2.41	2.31	2.34	2.33	2.44	2.38	2.21	2.28	2.22	2.47	2.93	2.43	2.67	3.39	3.85	3.93	3.44
ho1	1.91	1.81	1.86	1.81	1.59	1.52	1.72	1.78	1.77	1.87	1.88	1.98	2.27	2.39	2.18	2.11	2.29	2.07	1.91	2.14
ho2	3.23	3.24	2.42	1.97	1.82	1.79	1.68	1.34	1.58	1.85	1.88	2.28	3.11	2.94	3.77	3.06	4.92	3.53	3.84	4.30
ho3	2.82	2.57	2.03	2.03	2.01	2.12	2.29	2.71	2.67	2.50	2.48	2.70	2.52	3.40	3.62	3.63	3.66	3.84	3.36	3.47
ma1	5.68	5.60	5.66	5.67	5.60	5.45	5.44	5.44	5.41	5.59	5.58	5.59	5.54	5.48	5.25	5.25	4.85	4.84	4.97	4.51
ma2	1.81	1.75	1.71	1.75	1.73	1.63	1.63	1.66	1.53	1.49	1.45	1.48	1.49	1.51	1.67	1.77	1.68	1.85	1.80	1.81
ma3	2.33	2.34	2.36	2.35	2.37	2.29	2.26	2.28	2.26	2.25	2.49	2.46	2.65	2.52	2.54	2.82	2.86	2.84	2.83	2.73
ma4	3.35	3.28	3.26	3.24	3.24	3.22	3.21	3.19	3.16	3.26	3.28	3.36	3.22	3.18	3.02	2.92	2.98	2.94	2.81	2.85
or1	3.32	3.38	4.12	4.20	3.72	3.71	3.66	3.17	3.12	3.09	3.08	3.11	2.90	3.22	3.35	3.53	3.94	3.91	3.68	4.22
pa1	2.12	2.17	2.30	2.17	2.17	2.36	2.43	2.56	2.56	2.70	2.70	2.66	2.69	2.54	2.22	2.27	2.29	2.25	2.42	2.43
pa2	2.55	2.60	2.60	2.64	2.72	2.87	2.90	2.97	2.97	3.04	3.02	2.98	2.86	2.59	2.37	2.47	2.62	2.60	2.56	2.54
pa3	2.24	2.40	2.42	2.43	2.55	2.92	3.13	3.35	3.19	3.00	2.99	3.00	2.64	2.65	2.80	3.09	3.02	3.12	3.13	3.09
pr1	2.62	2.58	2.42	2.33	2.07	1.81	1.79	1.79	1.71	1.59	1.57	1.60	1.71	1.92	1.56	1.56	1.42	1.34	1.44	1.54
pr2	2.10	2.10	1.95	1.84	1.55	1.63	1.74	1.73	1.72	1.67	1.67	1.68	1.69	1.69	1.69	1.72	1.67	1.68	1.67	1.84
pr3	2.90	2.80	2.82	2.73	2.33	2.21	2.28	2.28	2.21	2.23	2.20	2.18	2.12	2.30	2.36	2.35	2.20	2.21	2.10	2.40
pr4	2.53	2.55	2.72	2.86	3.01	3.02	2.99	2.99	2.90	3.03	3.15	3.16	3.33	3.36	3.28	3.28	3.32	3.33	3.34	3.30
pr5	1.62	1.61	1.52	1.48	1.52	1.54	1.50	1.49	1.58	1.60	1.68	1.64	1.65	1.68	1.66	1.65	1.66	1.65	1.66	1.75

ce - *Cebus*; ch - *Pan*; co - *Colobus*; go - *Gorilla*; ho - *Homo*; ma - *Macaca*; or - *Pongo*; pa - *Papio*; pr - *Presbytis*

Table C.3: RMS errors of the predicted humerus shapes when using different numbers of principal modes (model two - excluding size)

	1	2	3	4	5	6	7	8	9	10	11	12	13	14	15	16	17	18	19	20
ce1	4.26	4.29	4.04	4.23	4.90	4.90	4.63	4.53	3.76	3.73	3.73	4.48	4.94	4.94	5.61	5.61	5.88	5.87	5.76	5.79
ce2	4.54	4.70	4.39	5.70	6.16	6.48	6.58	6.73	6.76	7.09	6.78	8.19	10.10	9.43	9.56	9.76	9.37	9.69	9.82	8.46
ce3	5.40	6.16	6.58	6.70	7.56	7.89	7.50	7.30	5.91	5.97	5.63	5.69	3.87	3.77	3.81	4.73	4.89	5.37	6.38	6.89
ch1	11.24	11.61	10.17	10.85	11.23	11.90	11.14	11.56	11.58	11.84	10.91	10.93	10.88	11.58	11.74	11.77	11.98	12.22	12.23	12.31
ch2	16.46	16.15	16.55	16.85	16.71	16.84	16.06	16.04	16.64	16.67	16.73	16.80	16.58	16.65	16.13	15.33	14.90	14.84	14.57	14.52
ch3	9.88	10.73	12.41	12.31	12.75	13.67	13.86	13.84	10.44	10.10	9.70	11.05	11.11	11.22	10.56	10.63	10.87	12.40	18.63	17.45
co1	5.02	4.65	4.58	4.10	3.70	3.63	3.75	3.56	3.67	3.57	4.07	3.94	4.27	4.24	4.09	3.80	3.96	4.45	4.76	4.67
co2	6.52	6.46	6.08	6.39	6.28	6.12	5.92	5.84	5.93	5.83	6.03	5.96	6.19	6.23	6.16	6.19	6.73	6.60	6.57	6.61
co3	5.30	5.19	5.35	5.05	5.07	5.13	5.02	5.00	4.94	4.92	4.77	4.74	5.74	5.80	5.84	5.71	5.50	5.51	5.67	5.51
go1	16.61	16.58	15.31	15.83	14.83	14.78	14.39	15.40	15.35	15.22	14.87	14.91	14.56	14.52	14.50	13.92	13.60	13.30	13.41	13.38
go2	12.42	12.77	11.84	11.81	11.80	11.68	10.46	11.56	11.51	11.50	11.59	11.22	11.20	11.12	10.78	10.79	10.94	11.15	11.05	10.83
go3	10.98	10.67	9.45	9.63	9.16	9.24	9.95	10.02	9.92	9.86	10.32	10.30	10.95	10.88	10.63	10.25	10.43	10.42	10.23	10.32
ho1	9.21	8.98	8.93	9.02	8.99	9.06	8.44	8.35	8.32	8.43	8.38	8.95	8.70	8.48	8.88	9.85	9.76	9.86	9.35	9.43
ho2	14.38	13.83	11.95	11.86	11.47	11.81	10.52	8.93	9.05	9.08	9.23	10.25	10.25	10.22	10.25	9.78	9.77	9.70	9.93	9.79
ho3	11.48	11.01	10.01	10.28	9.83	10.40	10.06	9.93	9.06	9.38	8.78	8.93	8.08	8.08	8.11	8.02	8.28	8.57	8.78	8.56
ma1	4.26	7.13	8.73	8.52	7.67	8.83	8.77	8.26	8.06	7.77	7.52	9.45	9.63	9.73	10.31	8.52	9.02	7.93	8.40	8.54
ma2	4.05	4.08	4.33	4.30	4.49	4.47	4.57	4.54	4.53	4.49	4.50	4.45	4.61	4.82	4.08	4.96	4.70	4.60	4.56	4.31
ma3	4.79	5.19	4.25	4.13	4.57	4.62	4.47	4.16	4.16	3.85	4.29	4.56	5.92	6.24	6.48	5.86	5.34	4.87	5.00	5.03
ma4	3.56	5.03	4.07	4.41	4.70	6.18	6.04	5.71	5.68	7.76	7.02	7.63	7.69	9.37	8.63	8.44	8.30	8.62	8.01	7.71
or1	12.48	12.32	15.21	15.07	14.29	15.22	15.19	15.01	15.17	15.65	15.68	15.68	14.76	14.16	14.19	14.24	14.46	14.55	13.48	13.94
pa1	7.21	7.35	6.54	6.30	6.30	7.14	6.45	6.47	6.39	7.03	6.65	7.18	6.51	6.54	7.10	7.72	7.58	6.98	7.15	7.50
pa2	6.85	6.93	6.94	7.80	7.96	7.75	7.30	7.32	6.72	8.63	6.25	8.46	9.74	8.35	8.20	8.40	8.99	8.88	8.82	9.69
pa3	8.48	8.98	9.49	9.83	9.69	9.48	9.56	9.05	8.28	7.66	7.54	6.70	6.60	6.06	6.93	6.96	6.95	7.25	6.83	7.48
pr1	4.52	4.33	4.41	4.05	3.46	3.26	3.39	3.45	3.59	3.60	3.68	3.92	4.58	4.54	4.16	4.26	4.67	4.75	4.74	5.02
pr2	5.21	4.92	4.87	4.39	3.94	4.13	4.29	3.89	3.81	3.77	4.30	4.30	4.06	4.00	4.72	4.13	4.43	4.46	4.68	4.70
pr3	7.10	6.55	8.01	7.76	8.59	9.03	8.85	8.19	8.02	7.69	7.69	7.14	7.21	7.50	8.03	7.95	7.12	7.11	6.49	5.43
pr4	4.59	4.47	5.54	5.24	5.02	5.72	4.74	4.90	4.94	5.60	5.39	5.33	5.08	5.22	4.74	4.50	4.83	4.79	4.96	4.97
pr5	3.35	3.42	3.72	3.52	3.71	3.77	3.18	3.33	3.44	3.54	3.53	3.39	3.85	3.67	5.22	5.10	5.13	5.25	5.21	5.12

ce - *Cebus*; ch - *Pan*; co - *Colobus*; go - *Gorilla*; ho - *Homo*; ma - *Macaca*; or - *Pongo*; pa - *Papio*; pr - *Presbytis*

Table C.4: RMS errors of the predicted scapula shapes when using different numbers of principal modes (model two - excluding size)